Dublin City University
Ollscoil Chathair Bhaile Átha Cliath

Vapour and Electro-deposited Metal Films on Copper: Structure and reactivity

by

Mr. Thomas F. McEvoy B.Sc.

Thesis submitted for the Degree of Doctor of Philosophy

Supervisors:
Prof. Robert J. Forster
&
Dr. Colin J. Barnes

Dublin City University **August 2004**

This thesis is dedicated to my late supervisor Dr. Colin J. Barnes

Doubt sees the obstacle,
Faith sees the way,
Doubt sees the long dark night,
Faith sees the day,
Doubt dreads to take a step,
Faith soars on high,
Doubt thunders 'who believes?',
Faith answers 'I'.

- *prayer*

'It does not matter how slowly you go once you do not stop'

-Confucius

I hereby certify that the material, which I now submit for assessment on the programme of study leading to the award of doctor of philosophy, is entirely of my own work and has not been taken from the work of others, save and to the extent that such work has been cited and acknowledged within the text of my work.

Signed: Thomas M'Enroy ID: 50162225

Date: 8/9/2004

PUBLICATIONS & PRESENTATIONS

- **McEvoy, T.**, Barnes, C.J., Pussi, K., Al Shameileh, E., Lindroos, M. "Determination of the structure of Cu{100}-c(4x4)-In by TLEED", Surface Science 526 (2003) 141-148.

- **McEvoy, T.**, Guaino, Ph., Barnes, C.J., Al Shameileh, E., McLoughlin, E., Cafolla, A.A. "Observation of an anti-phase domain structure in the Cu{100}/Sn surface alloy system", Surface Science 544 (2003) 121-133.

- **McEvoy, T.**, Al Shameileh, E., Cafolla, A.A. "Structural Study of the Cu{100}-p(2x2)-Sb Surface Alloy Using Low Energy Electron Diffraction" accepted for publication by Surface Science.

- Inaugural Conference of the National Centre for Plasma Science and Technology, Dublin City University, July 7^{th}-12^{th} 2001.
  Poster presentation: "Indium on Cu{100}: A Reversible Temperature Dependant Phase Transition."

- Research Day in Dublin City University, 23^{rd} March 2003.
  Oral presentation: "Study of Adsorption at Surfaces by Scanning Tunnelling Microscopy and Low Energy Electron Diffraction."

- ESEAC 2004, National University of Ireland, Galway, 6^{th} – 10^{th} June 2004.
  Poster presentation: "Copper Microelectrodes: Metal Deposition and Electroanalysis".

- 56^{th} Irish Universities Chemistry Research Colloquium, University of Limerick, 23^{rd} – 25^{th} June 2004.
  Oral presentation: "Copper Microelectrodes: Fabrication, Characterisation and Metal Deposition"

Acknowledgements

Mister Thomas F. McEvoy would like to thank,
My inspirational folks, Pamela and Frank,
Parents who supported me day and night,
Even paid my rent when things were tight,
My 4 brothers who remained strong and true,
Each a rock, i salute you,
Paddy, Petes, Ants and Frank,
Without whose presence I would have sank.

Professionally, I wouldn't be here,
If it wasn't for a certain peer,
Dr. Colin Barnes was a mentor and a friend,
Enthusiastic and inspiring, he found the blend,
No problem ever came as a surprise,
Just an opportunity for learning in disguise,
Colin has tragically passed from here,
But I hope up there he's enjoying a beer.

It was my great privilege and relief,
To be given Prof. Forster as my chief,
In times of darkness he provided light,
Insight and solutions when i met plight,
Great craic and excellent banter
He's kinda like a beardless Santa,
What makes this all so hard to take,
He comes from Meath for gods sake!

Prof. Smyth and the other DCU staff,
All distinguished genii but up for a laugh,
Thank you so much for all your help,
And for putting up with a cheeky whelp,
Veronica and Mick, you're both a star,
Thanks for helping me get this far
Thanks to the 'begrudging' technicians too,
Team McEvoy's victory is dedicated to you.

My final thanks go to all of the smoking crew,
Things would've been unbearable if it not for you,
Shane O'Malley, 'the surfer' dude,
Or cranky pants depending on his mood,
Without you mate I'dve left by now,
We'll keep in touch and that's a vow,
Leon Barron, see you in the future,
Hope that's alright, OK computer?

Aoife Morrin, spookily she's always right,
Though surely no-one could be that bright,
Always seemed to make me laugh,
But what'll happen now she's staff,
Darragh Lucey, a man without malice,
If it wasn't for him I'd still be in Paris,
Well that's about it for me, thanks guys,
See you in 5 years with my Nobel Prize.

On a more serious note Thomas F. McEvoy would like to sincerely thank those mentioned above for all their help, encouragement and good company over the course of my study. Thomas F. McEvoy would also like to thank the following: Susan, Lynn, Jonny, John, Ian, Ray, Tony K, Adriano, Padraic, Maire, Blainead, Gill, Orla, Nigel, Ben, Martina, Eadaoin, Claire, Karl, Ehab, Hamid, Johan, Javed, Elena, Fabio and of course Jesus.

Abstract

Vapour and Electro-deposited Metal Films on Copper: Structure and Reactivity.

The systems studied involve deposition of metals of a larger atomic diameter on a Cu{100} single crystal surface under vacuum and determining the structures formed along with the effect on the Cu{100} substrate. Cu microelectrodes were fabricated and characterised with Indium electrodeposited on the electrode surface. The In on Cu{100} growth mode is compared with the growth mode of electrodeposited Indium on Cu microelectrodes.

The Cu{100}/In system has been studied for the In coverage range 0.1-0.65 monolayer using Auger electron spectroscopy (AES), low energy electron diffraction (LEED) and scanning tunnelling microscopy (STM). The Auger signal versus deposition time plot for the deposition of In on Cu{100} is characteristic of the Stranski-Krastanov growth mode. In this deposition mechanism the first atomic layer grows in a layer by layer fashion but when monolayer point is reached, subsequent growth occurs in the form of 3D crystallites. At a concentration of 0.4±0.05 monolayer In forms a $(9\sqrt{2}x2\sqrt{2})R45°$ on the Cu{100} surface which on heating above a temperature of 373K undergoes a reproducible phase transition to form a c(2x2) phase. Increasing the In deposited to a surface concentration of 0.6±0.05 monolayer results in a Cu{100}-c(4x4)-In overlayer structure which remains uniform with heating. A Tensor LEED analysis was conducted on this structure in conjunction with K. Pussi et al., from which it was found that the In overlayer consisted of two layers. The In layer closest to bulk comprises a c(2x2) structure with In atoms occupying 4 fold hollow sites with respect to substrate. The top layer is a c(4x4) In layer in which the atoms lie at four fold hollow sites with respect to the c(2x2) layer.

The deposition of 0.25ML Sb on clean Cu{100} at room temperature results in a p(2x2) LEED pattern which is confirmed by STM. Using Tensor LEED calculations, the structure of the Cu{100}-p(2x2)-Sb phase has been determined. The results show that despite the large size mismatch between Sb (atomic radius = 1.450Å) and Cu (atomic radius = 1.278Å), a surface alloy is formed in which Sb atoms substitute Cu atoms in the outermost layer. Sb is found to ripple outward from the surface by 0.56±0.05 Å. The second and deeper Cu layers are found to be close to their bulk values. As the Sb coverage is increased to a concentration of 0.33ML, the surface exhibits a p(6x6) LEED pattern. The atomic resolution STM images for this surface display alternating double and single rows of atoms implying a reconstruction in the selvedge. Based on the STM and LEED results possible models for the Cu{100}-p(6x6)-Sb structure have been proposed. The favoured structures are based on a slight deformation from the simple c(2x2) surface.

Cu microelectrodes were fabricated and characterized using cyclic voltammetry and chronoamperometry. The Cu microelectrodes were found to have a potential window of –0.08 to –0.6V in $HClO_4$, although this can be improved with pH adjustment, with the potential window found to be at a maximum of +0.1 to –1.0V at a pH of 4. Chronoamperometric data was taken in differing concentrations of $HClO_4$ giving

resistance, capacitance and RC time constant values for the Cu microelectrode in an $HClO_4$ electrolyte system.

Indium was electrochemically deposited on the Cu microelectrode at a potential of –0.6V. Cyclic voltammograms are taken at different scan rates to determine the dynamics of In deposition. At low scan rates there was an increase in the amount of In deposited as witnessed by hysteresis on the cyclic voltammograms. This hysteresis is thought to be caused by In on In deposition. At scan rates of $1.0Vs^{-1}$ and above it is thought that little or no In deposition occurs as peaks corresponding to indium reduction or subsequent oxidation are no longer observed. SEM and EDX were used to confirm the deposition of In on the Cu microelectrodes. Chronoamperometric measurements were taken to determine the growth mode and nucleation type of the deposited In. From these measurements, a plot of I/I_{max} versus t for the In deposition is compared with nucleation and growth models for 2D progressive, 2D instantaneous, 3D progressive and 3D instantaneous. After comparison it was found that the electrodeposition of In on Cu microelectrodes obeys a progressive nucleation mode with further In growth found to be 3D. This result compares favourably with the growth mode for In deposition on a Cu{100} substrate under vacuum, with the growth mode for both being 3D. It was found that the nucleation types for both were remarkably similar with vacuum deposited In and electrodeposited indium both undergoing progressive nucleation.

Table of Contents

Chapter 1

Theoretical Framework and Literature Survey

1.1 Introduction

Surface science tries to understand the relationship between the physical and chemical properties of surfaces. Catalytic performance strongly depends on the surface properties of heterogenous catalysts and several qualitative and quantitative techniques have been applied to study the structure and composition of surfaces. In the course of this work, low energy electron diffraction (LEED), Auger electron spectroscopy (AES) and scanning tunnelling microscopy (STM) were used for structural studies. These techniques will be elaborated upon and discussed in more detail in a later section.

Cu{100} surface alloys and overlayers

The importance of copper as a heterogeous catalyst is demonstrated by its use in large-scale industrial processes including the synthesis of methanol [1], higher alcohols, ethers and in phenol oxidation [2].

The single crystal Cu{100} is usually chosen as a model substrate due to its highly well-defined and stable surface structure and its relatively low cost. Model systems like the Cu{100} single crystal and well-characterised Cu-based surface alloys and overlayers are studied to establish a link between the microscopic level of understanding the bonding and reactivity of adsorbates and the macroscopic measurement of kinetics rate and thermodynamic properties of the reacting system [3]. This knowledge is then exploited to create surfaces with the required microscopic structure to produce the desired catalytic properties. Two different elements were deposited during the course of this work, namely indium (In) and antimony (Sb).

The Cu-In alloy is of most technological importance as a precursor for the formation of economic, efficient solar cells. The precursor is exposed to either selenium [4,5], gallium [6]or sulphur [6,7] to form very photoactive compounds which are economic to create. The Cu-In alloy has also been used as a solder for interconnections in the electronics industry [5].

The Cu-Sb alloy has been used most extensively as a Sn-Au-Cu-Sb alloy which has replaced the Sn-Pb alloy as an environmentally friendly solder in the electronics industry [8].

The objective of this study is to monitor the vacuum deposition of indium and antimony at coverages up to monolayer point and elucidate and characterise any surface structures formed by the deposits prior to this coverage. AES, LEED and STM were used to provide a detailed overview of each of the systems studied. AES was used primarily to quantify the amount of material being deposited on the sample substrate. LEED and STM were used in tandem to determine if deposited material had formed a surface structure on the sample substrate and to characterise each surface structure which was formed. LEED I(V)s were taken for a number of surface structures in each of these systems and from these a Tensor LEED study was conducted by our colleagues at Tampere University in Finland. These Tensor LEED studies provide exact atomic locations for both the deposited material and the atoms comprising the Cu{100} substrate.

Comparison of vapour deposition and electrodeposition

Both methods of metal on metal deposition have their respective advantages and disadvantages over one another. In vapour deposition it is necessary to work under UHV but the quality of the deposit is higher and easier to control. The rate of deposition can be controlled by varying the flux of the deposited material towards the substrate surface with the amount of deposited material dependant on the sticking probability of the deposited material. This process is easier to control than potential but is expensive to set up and transfer of the deposited sample is awkward with the sample suffering a high level of contamination with a loss of UHV.

In electrodeposition the quality of the deposit is less easily controlled with any control over the shape and structure of the deposit relying on the addition of additives, such as cyanide, to the electrochemical system. However, electrodeposition has a number of advantages over vapour deposition, namely electrodeposition allows for the avoidance of a vacuum system, it is also a highly flexible process and the overall cost of the process is much less than that of vapour deposition.

It is impossible to view one method as superior to the other as both processes meet different requirements. If the purpose of the experiment was a quantitative study of the amount of deposited material on a sample substrate and the shape and structure of the deposited material in relation to the sample substrate was of utmost importance then vapour deposition would be the method of choice. However, if the shape and structure of the deposit was a secondary issue and the purpose of the study was on the effect of the deposit on the physical properties of the sample substrate, then electrodeposition would be preferential. There are many other situations where one technique would be preferred to the other and this is just one example of why one technique would be chosen over the other.

In electrodeposition, the effect of mass transport of the deposited material to the electrode surface is comparable with the flux of evaporated metal to the sample substrate. By using microelectrodes as opposed to macroelectrodes the control of mass transport from solution to electrode surface is much more stringently controlled. With microelectrodes having more control over the amount of mass transport to the electrode surface, it allows for more control over deposited material on the electrode substrate. The aim of our studies was to determine and characterise the dynamics of indium deposition in an effort to exact more control over the quantity and quality of the indium deposit and the subsequent effect on the electrochemical properties of the copper microelectrodes.

1.2 Surface Theory

How is a surface defined?

The top layer of surface atoms are those which are the immediate interface with the other phases (gas, liquid or solid) in contact with it, this is commonly thought of as being the surface. The problem with this definition is that the structure and chemistry of this top layer of atoms will be significantly determined by the atoms immediately below. In a very real sense therefore, the surface could be said to be the top 2-10 atomic layers (e.g. 0.5-3nm). However, many technologies apply surface films in the range 10-100nm, to devices and components in an effort to protect, lubricate, change the surface optical properties etc. Beyond 100nm it is more appropriate to describe such an applied film in terms of bulk solid state properties.

With these points in mind, the surface can be considered in terms of three regimes: the top surface monolayer; the first ten or so atomic layers; and the surface film, no greater than 100nm. To understand fully the surface of a solid material, we need techniques which not only distinguish the surface from the bulk solid, but also ones that distinguish the properties of these three regimes [9].

Single Crystal Surfaces

A single crystal surface is formed when a solid is cut parallel to a selected plane of atoms. Surface atoms' properties are expected to be different from the bulk of the solid due to the loss of neighbouring atoms. At the vacuum interface, rearrangement of atomic positions at the solid single crystal surface may take place such as atomic relaxation or reconstruction. Surface relaxation takes place in order for the surface to compensate for the loss of 'bonding' in the form of an oscillatory change in the interlayer spacing. Surface reconstruction happens when simple truncation of the bulk crystal does not lead to the 'expected' surface periodicity. Surface relaxation and reconstruction are discussed in a lot more detail with examples provided in many of the reviews on surface science [10-14]. The region over which atoms relax or reconstruct is commonly known as the selvedge region.

Unit Cell

The atomic order in crystalline solids indicate that small groups of atoms form a repetitive pattern. Thus, in describing crystal structures, it is often convenient to subdivide the structure into small repeat entities called unit cells. Unit cells for most crystal structures are parallelpipeds or prisms having three sets of parallel faces; one is drawn within the aggregate of spheres [15]. A unit cell is chosen to represent the symmetry of the crystal structure, wherein all the atom positions in the crystal may be generated by translations of the unit cell integral distances along each of its edges. Thus, the unit cell is the basic structural unit or building block of the crystal structures by virtue of its geometry and the atom positions within. More than a single unit cell may be chosen for a particular crystal structure, however, the unit cell having the highest level of geometrical symmetry is generally used.

Lattices, directions and planes

Crystal structures in three dimensions are defined in terms of their Bravais lattices. A Bravais lattice is an infinite regular array of points that fills all space. This lattice is made up from a basic building called the unit cell, which is usually specified in terms of three unit cell vectors (a, b, c), whose lengths and directions define the size, shape and orientation of the unit cell. This notation is illustrated below for the case of the simple cubic unit cell. The volume of the unit cell is

$$V = [a.(bxc)] \qquad \text{(Eqn 1.1)}$$

Each unit cell can be translated to the position of any other cell in the lattice by the operation of a translation vector

$$T(hkl) = ha + kb + lc \qquad \text{(Eqn 1.2)}$$

where (h,k,l) are integers.

Crystal lattices often have several other symmetry properties to translational symmetry. The symmetry operations that occur in both two and three dimensional

crystallography are rotation, reflection and glide plane. Operating on the lattice with any of these, or with combinations of them, always leaves the lattice unchanged [8].

A specific direction in a lattice is specified by the vector

$$R(uvw) = ua + vb + wc \qquad \text{(Eqn 1.3)}$$

which is often written in shorthand using the square bracket notation $[uvw]$. As examples, $[001]$ is parallel to c and $[111]$ is parallel to the unit cell diagonal R(111) = a+b+c as shown in Figure 1.1. A line drawn over a character indicates negative values; i.e., $\left[\bar{u}\,vw\right] = [-u, v, w]$. In most lattices, several directions are equivalent since at least one of the symmetry properties of the lattice transforms them into each other. A group of such symmetry related directions is called directions of a form and is denoted by angle brackets; e.g. <uvw>. For example, the simplest cubic lattice whose unit cell is shown in Figure 1.1, is left unchanged when rotated about the a, b or c axes by integral multiples of $\pi/2$. Thus, the specific directions $[001]$, $\left[00\bar{1}\right]$, $[010]$, $\left[0\bar{1}0\right]$, $[100]$ and $\left[\bar{1}00\right]$ are all members of the form <001>. Once the coordinate system is specified, the direction [uvw] is unambiguous. However, because the form <uvw> represents more than one direction, its correct interpretation requires that both the unit cell vectors and the symmetry operations of the lattice have also been specified. These two types of notation are not interchangeable [16].

A lattice plane is any plane that contains three or more non-collinear, lattice points. Families of equally spaced parallel lattice planes can be constructed so that together they contain all points of the Bavais lattice. Each such family of lattice planes is denoted by the notation (hkl), where the indices h, k and l are the Miller indices.

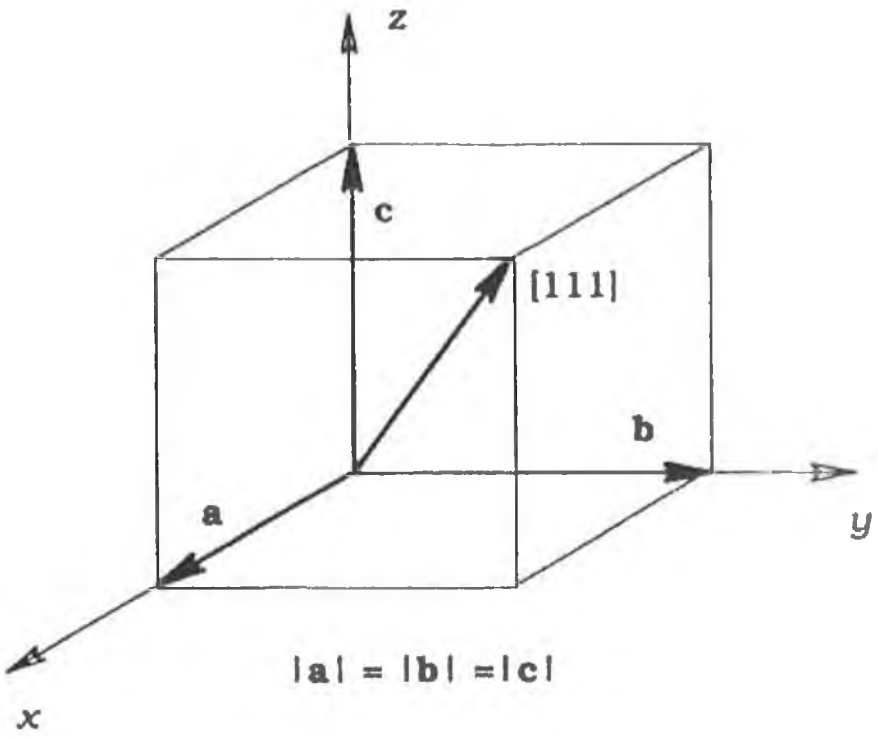

Figure 1.1 Schematic diagram of a simple cubic lattice [11].

Main crystal types

The Face-Centred Cubic Crystal Structure

The Face-Centred Cubic (FCC) crystal structure has a unit cell of cubic geomentry, with atoms located at each of the corners and the centres of all the cube faces. Examples of FCC crystal structures are copper, aluminium, silver and gold' During the course of this study Cu{100} acted as substrate, meaning all work done was on the FCC crystal structure.

For the FCC crystal structure, each corner atom is shared among eight unit cells, whereas a face-centred atom belongs to only two. Therefore, one eighth of each of the eight corner atoms and one half of each of the six face atoms, or a total of four whole atoms, may be assigned to a given unit cell. Corner and face positions are really equivalent; that is, translation of the cube corner from an original corner atom to the centre of a face atom will not alter the cell structure.

Two other important characteristics of a crystal structure are the coordination number and the atomic packing factor (APF). For metals, each atom has the same number of nearest-neighbour or touching atoms, which is the coordination number. For FCC crystals, the coordination number is 12 [15].

The APF is the fraction of solid sphere volume in a unit cell, assuming that

$$\text{APF} = \text{Volume of atoms in a unit cell/ total unit cell volume} \qquad \text{(Eqn 1.4)}$$

For the FCC structure, the atomic packing factor is 0.74, which is the maximum packing possible for spheres all having the same diameter. Metals typically have relatively large atomic packing factors to maximise the shielding provided by the free electron cloud [15].

The Body-Centred Cubic Crystal Structure

The Body-Centred Cubic (BCC) is another common metallic crystal structure, similar to the FCC crystal structure in that it also has a cubic unit cell with atoms located at

all eight corners and a single atom at the cube centre. Some typical examples of BCC unit cells are chromium, iron and tungsten.

Two atoms are associated with each BCC unit cell; the equivalence of one atom from the eight corners, each of which is shared amongst eight unit cells, and the single atom positions are equivalent. The coordination number for BCC crystal structures is 8; each centre atom has as nearest neighbours its eight corner atoms. Since the coordination number is less for BCC than FCC, so also is its APF at 0.68 [15].

The Hexagonal Close-Packed Crystal Structure

Not all metals have unit cells of cubic symmetry, the final common metallic crystal structure has a unit cell that is hexagonal. For Hexagonal close-packed (HCP) the top and bottom faces of the unit cell consist of six atoms that form regular hexagons and surround a single atom in the centre. Another plane that provides three additional atoms to the unit cell is situated between the top and bottom planes. The atoms in this midplane have as nearest neighbours atoms in both of the adjacent two planes. The equivalence of six atoms is contained in each unit cell; one-sixth of each of the 12 top and bottom face corner atoms, one-half of each of the 2 centre face atoms, and all 3 midplane interior atoms.

Examples of some HCP metals include cadmium, magnesium, titanium and zinc. The coordination number and the APF for the HCP crystal structure are the same as for FCC: 12 and 0.74, respectively.

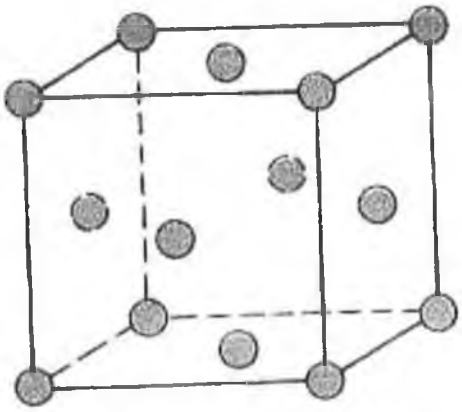

(A)

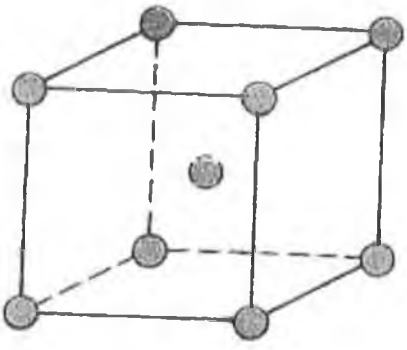

(B)

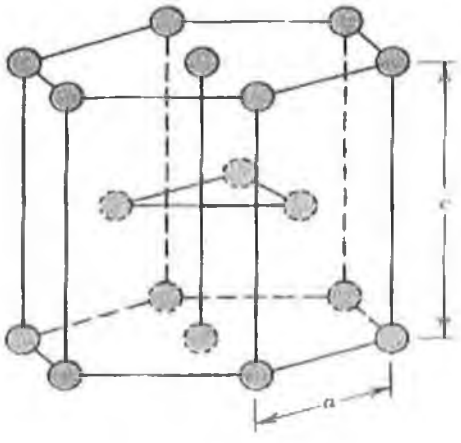

(C)

Figure 1.2 Unit cells for each of the simplest metal unit cells. (A) Face centred cubic, (B) Body centred cubic and (C) Hexagonal close packed [11].

1.3 Ultra High Vacuum

History of UHV

Ultra High Vacuum began in 1950 with the invention of the Bayard-Alpert gauge [17] which allowed measurements below pressures of 10^{-8} Torr for the first time [18]. Prior to this the production of pressures as low as possibly 10^{-12} Torr had been possible since the 1920's, however, there was no gauge capable of making direct measurements below 10^{-8} Torr because of a lower limit to hot-cathode ionisation gauges, the existence of this limit being unknown. The accepted wisdom of the time was that the pumping speed of diffusion pumps went to zero at about 10^{-6} Torr. By the late 1930s several visionaries [19, 20] had evidence that the pressure in their systems was less than that indicated by their ionisation gauges. The existence of an x-ray limit to pressure measurement by electron-impact ionisation was clearly shown in 1938 by the work of Bell [21], but it was not until 1947 that attention was drawn to the possibility of an x-ray limit in ionisation gauges by a comment by Nottingham at the 1947 Physical Electronics Conference. Several pioneers built hot-cathode ionisation gauges between 1947 and 1950 designed to reduce the x-ray effect. The design of Bayard and Alpert reduced the x-ray limit by a factor of more than 200 allowing pressure measurements to less than 10^{-10} Torr and became the principal gauge for UHV measurements [18].

Developments in the measurements of total pressure in the UHV range since 1950 have pursued the following major directions:

(i) the development of ionisation gauges, both hot and cold cathode, designed to reduce the limit set by the x-ray effect,

(ii) the study of electron stimulated desorption (ESD) effects in hot-cathode gauges and the design of gauges to reduce errors caused by ESD,

(iii) the study of the interaction of gauges with the vacuum system (outgassing, pumping, chemical effects at hot filaments)

The Need for UHV

For a clean surface, the rate of contamination depends on the rate of collision of gas molecules with the surface as the less contact with contaminants the cleaner the surface will be. From the kinetic theory of gases, the rate of surface bombardment (Z) by molecules is given by the following equation:

$$Z = p/(2\pi mkT)^{1/2}\, m^{-2}s^{-1} \qquad \text{(Eqn 1.5)}$$

where p is the ambient pressure in Nm^{-2}, m is the molecular mass in kg $molecule^{-1}$, T is the temperature in K and k is the Boltzmann constant in JK^{-1} [22].

Assuming a sticking probability of unity (every molecule sticks that hits the surface) and applying the previous equation, a monolayer (full surface coverage) of CO gas will adsorb on a surface in approximately 2 seconds at a pressure of 10^{-6} Torr at room temperature. In comparison, at a pressure of 10^{-10} Torr, such a contamination requires longer than 7 hours to take place. For most solid-gas interface studies, and since sticking probabilities are usually lower than unity and decrease as a function of coverage, it is found that at a base pressure of $1x10^{-10}$ Torr is sufficient.

1.4 Auger Electron Spectroscopy (AES)

Theory of operation of AES

In 1925 Pierre Auger discovered the effect which now bears his name while observing tracks produced by cosmic rays in a Wilson cloud chamber.
If an atom is ionised by the removal of an inner shell electron, it will rearrange with an electron from a higher shell falling into the initial hole. This is accompanied by the release of energy E(K)-E(L1) which may appear in the form of a photon, in the case of X-ray fluorescence or may be transferred to another electron in a higher electron shell which, if it has sufficient energy, may escape from the atom. Such an electron is known as an Auger electron and has an energy given by:

$$E(Z) = E_K(Z) - E_{L1}(Z) - E_{L2}(Z + \Delta) - \phi \qquad \text{(Eqn 1.6)}$$

where Z is the atomic number of the atom and ϕ is the work function of the surface. The third term on the right hand side of this equation has an extra component Δ included to take account of the fact that the atom is in a charged state when the final electron is ejected. Experimentally Δ is found to have a value between 1/2 and 3/2. An Auger electron is described by the transitions which take part in its production. For example, an ABC electron is one which results from the ionisation of the A electron shell, with an electron from shell B falling into the hole created and an electron from orbital C being ejected. The energies of the Auger electron transitions are plotted as a function of atomic number. The most intense Auger peaks are observed for transitions ABC where B=C=A+1, e.g. KLL, LMM, MNN etc, which reflects the fact that electron interactions are strongest between electrons whose orbits are close together [23].
Auger electrons can be produced in any atom that has been ionised by the removal of an inner shell electron (i.e., any element other than H or He). This ionisation may be caused by bombarding the atom with electrons, photons or ions provided that the energy is greater than the binding energy of the electron which must be removed in the initial ionisation. It therefore follows that Auger peaks will be observed in XPS in which the surface is exposed to X-rays. These peaks are often regarded as a nuisance

by operators of XPS instruments but they can in fact provide much useful information. It is common practice in Auger electron spectrometers to use an electron beam to produce the initial ionisation in the surface atoms. This has the advantage that the incident beam may be focused thus giving good spatial resolution. In addition, the electron beam energy does not have to be known accurately, as is the case in XPS where considerable effort is put into obtaining incident photons of accurately known energy and small energy spread. It is simply sufficient for the incident electron energy to be four times greater than the energy of the Auger electron. This comes from the fact that the ionisation cross-section is greatest when the ratio of the primary electron energy to the Auger electron energy is ~3 and falls slowly as this increases [23]. A schematic diagram of the Auger process is illustrated in Figure 1.3.

Auger Spectra

Figure 1.4 shows a typical survey spectrum as a result of a point analysis indicating the number of detected electrons N(E)/E as a function of kinetic energy. This spectrum contains a large number of secondary electrons on which the Auger electrons are superimposed. Transitions of oxygen and tantalum have been labelled. Carbon is found as a surface contamination and is often observed on samples introduced into the UHV [23].

Peaks are generally represented in their differentiated form after background subtraction, i.e. dN(E)/dE, which can be seen in Figure 1.4, where different forms of titanium are shown. This mode of representation is often applied to point out subtle differences and fine structure of the spectrum.

Detection Limits

Identification of Auger peaks is often easier for light elements as, with heavier elements, there is a greater amount of interference because of a larger number of transitions. Peaks with higher kinetic energy have a larger width and thus peak overlap is more likely. The sensitivity of elements varies only by one order of magnitude, where silver is the most sensitive and yttrium one of the least sensitive elements. The detection limits are set by the signal/noise ratio [23].

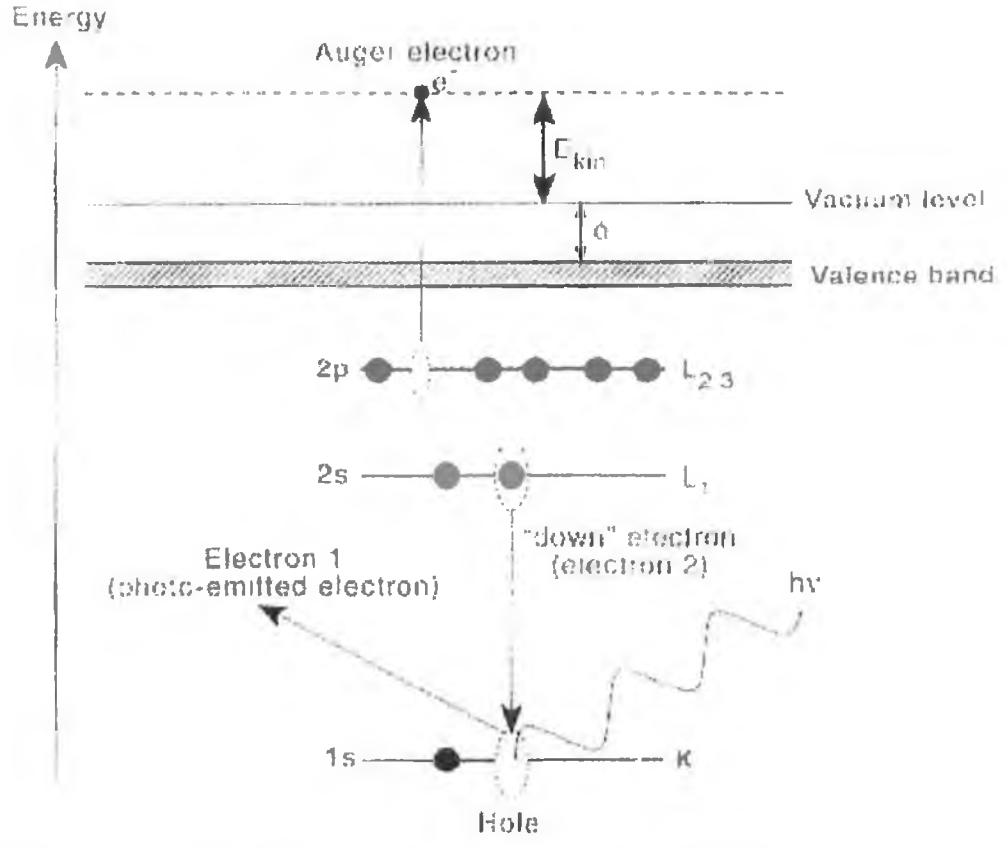

Figure 1.3 Overview of the Auger Electron Spectroscopy process [36].

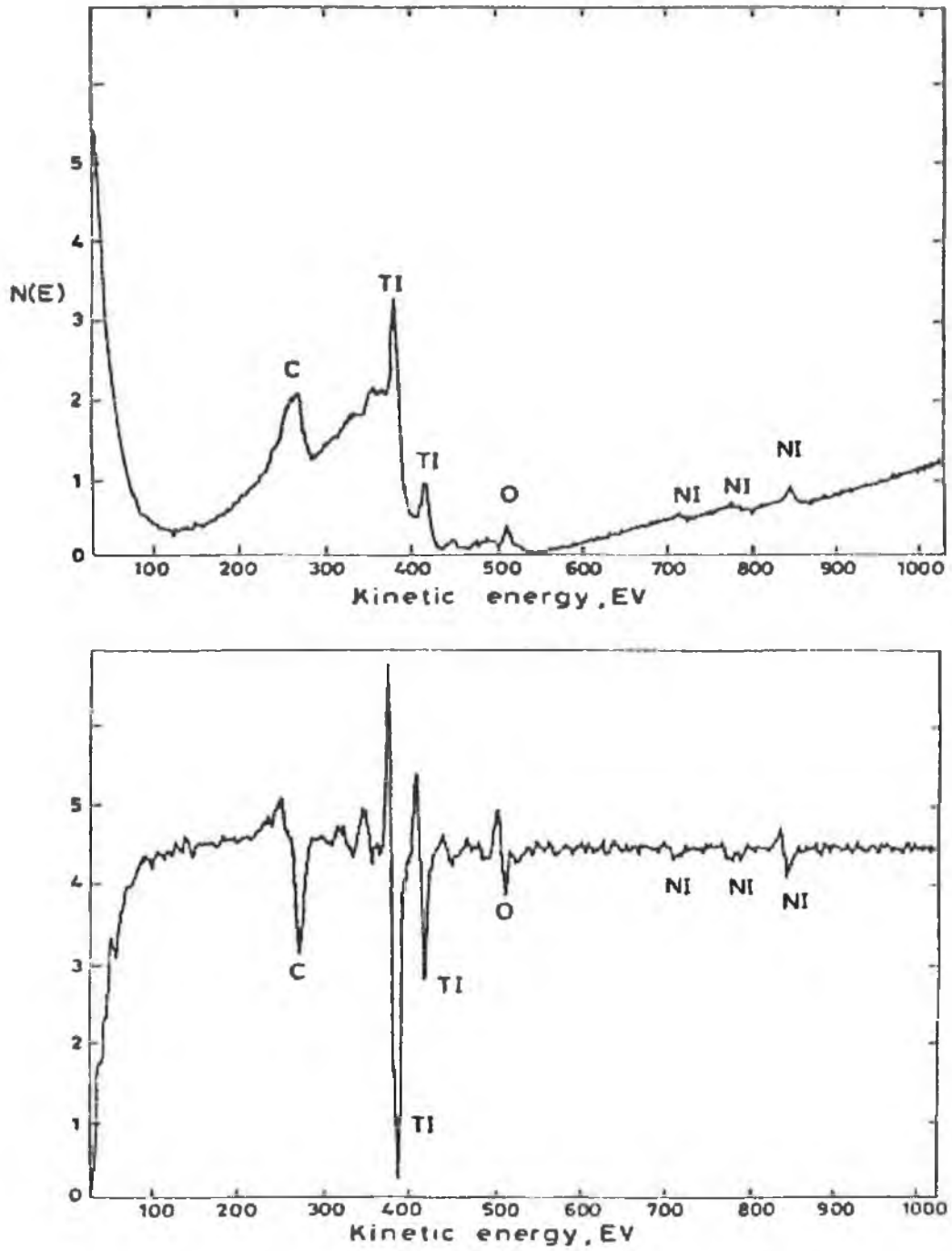

Figure 1.4 Shows (a) shows a typical survey spectrum as a result of a point analysis and (b) the same spectrum in differentiated form [23].

1.5 Low Energy Electron Diffraction (LEED)

History of LEED

The theoretical possibility of the occurrence of electron diffraction was a direct consequence of the wave mechanics proposed by de Broglie in 1924 [24].This theory extended to all particles the coexistence of waves and particles discovered by Einstein in 1908 for light and photons. De Broglie postulated that the wavelength of a particle which has a linear momentum p is given by h/p, where h is Planck's constant. For electrons with a kinetic energy of 100eV, this corresponds to a wavelength of approximately 1Å.

The experimental observation of LEED was made by Davisson and Germer as a consequence of a laboratory accident at Bell laboratories [25]. The experimental observations caused Davisson and Germer to realise that the angular dependence of the elastic electron scattering is due to crystal effects rather than intra-atomic effects as they had believed previously. Davisson and Germer focussed their efforts on the search for well-defined electron-diffraction effects that could be related to de Broglie's wavelength-momentum relationship. It took until 1927 to achieve this whereby they witnessed a clear observation of an off-specular intensity peak for a Ni(111) single-crystal surface and of three-fold azimuthal symmetry corresponding to the structural symmetry of the crystal [26]. This paper established the wave-particle duality of electrons on a firm experimental basis.

Davisson and Germer's article in Nature [27] preceded by one month another article in Nature by Thompson and Reid [28], which also revealed the wave nature of electrons. Thompson had realised that a positive-ray scattering apparatus could easily be adapted to search for electron diffraction. Thompson's experiment exhibited higher kinetic energies (tens of keV rather than tens of eV), which meant the experimental apparatus required a less stringent vacuum. Later experiments used the better-known lattices of metal samples in the form of films and produced further justification the de Broglie postulate. In 1937, Davisson and Thompson shared the Nobel Prize for

Physics for their pioneering work in electron diffraction. It took over 40 years from its discovery until LEED could be used to determine atomic positions.
Rather little experimental LEED work was carried out from this period until the mid 1960s. This is presumed to be due to both the technological complexity of the measurement and the lack of adequate theory [25].

During the 1960s there was a huge upturn in the amount of experimental LEED work. This upturn was made possible by commercialisation: the commercial availability of ion-pumped UHV systems, the commercial availability of LEED optics compatible with the UHV hardware and finally the commercial availability of Auger spectrometers which could monitor the chemical composition of a surface and ensure its cleanliness. At this point in time a quantitative theory of LEED had not been developed, meaning a detailed determination of surface structures was not possible. Instead at this time, LEED was used as a tool to monitor the surface condition of a sample and establish its reproducibility.

From the beginning of the 1970s a streamlining of the number of LEED formalisms took place, as calculations began to be applied to actual structural determinations of surfaces. The first reliable structural determinations came in 1971 as by-products of the above-mentioned comparisons between theory and experiments. These initial surface structural determinations concerned simple clean metal surfaces [25].
From this point onwards, the theoretical developments were aimed at reducing the computational effort needed in the structural determination. Van Hove [29] systematically applied symmetries and other efficiency features to overlayer systems with superlattices from 1974.

A large number of surface structures were solved during the 1970s and 1980s with all these methods, initiating the 'era of structural determination by LEED'. It was hereby shown that LEED can be applied not only to clean metal surfaces but also to atomic overlayers on these metals, to semiconductors, to ionic compounds and even adsorbed molecules. R-factors were also introduced in this period to help in performing structural determinations.

Increasingly complex structures have been tackled recently, including some semiconductors which require the optimisation of over a dozen structural parameters. On the experimental side, much has been learned about maintaining reproducible surface conditions. Moreover, improved intensity measurement techniques have been introduced, in particular photography and use of video camera and position sensitive detectors [25].

Theory of operation of LEED

A typical experimental arrangement used in a LEED experiment is shown in Figure 1.6. An electron beam of variable energy is produced by an electron gun and is incident on the sample. The electrons are then backscattered from the sample surface onto a system of grids surrounding the electron gun. The backscattered electrons are of two types; elastically scattered electrons forming a set of diffracted beams which create the LEED pattern, and inelastically scattered electrons, which may make up 99% of the total flux, but which do not contribute to the measured signal. After reaching the first grid, G1, which is earthed, the elastically scattered electrons are accelerated towards the fluorescent screen, S, which carries a high positive potential (~5kV). This provides the electrons in the diffracted beams with enough energy to excite fluorescence in the screen, so that a pattern of bright LEED spots is seen. The grids G2 and G3 are held at an adjustable negative potential, and are used to reject the inelastically scattered electrons which would otherwise contribute to a bright diffuse background across the whole of the LEED screen. The potential on these grids is adjusted to minimise the diffuse background to the LEED pattern. The LEED pattern which is observed may be recorded using a still or video camera mounted onto a chamber window placed directly opposite the LEED screen. This arrangement is known as 'front view LEED', and has remained very popular as the screen and grid arrangement is essentially a retarding field analyser (RFA) and may also be used for Auger spectroscopy [25].

Use of LEED

The simple production of a LEED image, without an analysis of the intensities of the individual spots is by far the most widespread use of LEED. In most surface science

experiments LEED is commonly used to check the cleanliness and order of surfaces being prepared. This is mainly due to the sensitivity of LEED to surface contamination and surface roughness, with the appearance of a LEED pattern with bright, sharp spots widely regarded as evidence of a completely clean, ordered surface.

In addition to its routine use in sample preparation in UHV, the pattern of LEED spots may also be used to obtain information about surface symmetry or surface reconstruction. It can also be used to determine whether any molecules on the surface are adsorbed in an ordered or random way. If an overlayer is ordered, its surface unit mesh size can be determined and if the layer is adsorbed commensurately with the substrate, its orientation relative to the underlying substrate may be determined.
It is also possible to determine the positions of atoms within a unit mesh. This is done by measuring the intensities of particular LEED spots versus beam energy and is referred to as an I(V) curve. Pendry [30] has developed an iterative procedure for determining the geometrical arrangements of surface atoms within the surface unit mesh from these I(V) curves. The starting point for the calculation is an initial guess at the arrangement of atoms on the surface, chosen to be consistent with the symmetry of the LEED pattern. The intensity of a number of the diffracted beams expected for this arrangement is then calculated as a function of beam energy. This is done by solving the Schrodinger equation for the electron wavefunction in the first few atomic layers of the solid. The resulting calculated I(V) curves are compared to the experimental results and the guessed atomic arrangement is adjusted to tie in with the experimental results. The process is repeated until satisfactory agreement is obtained.

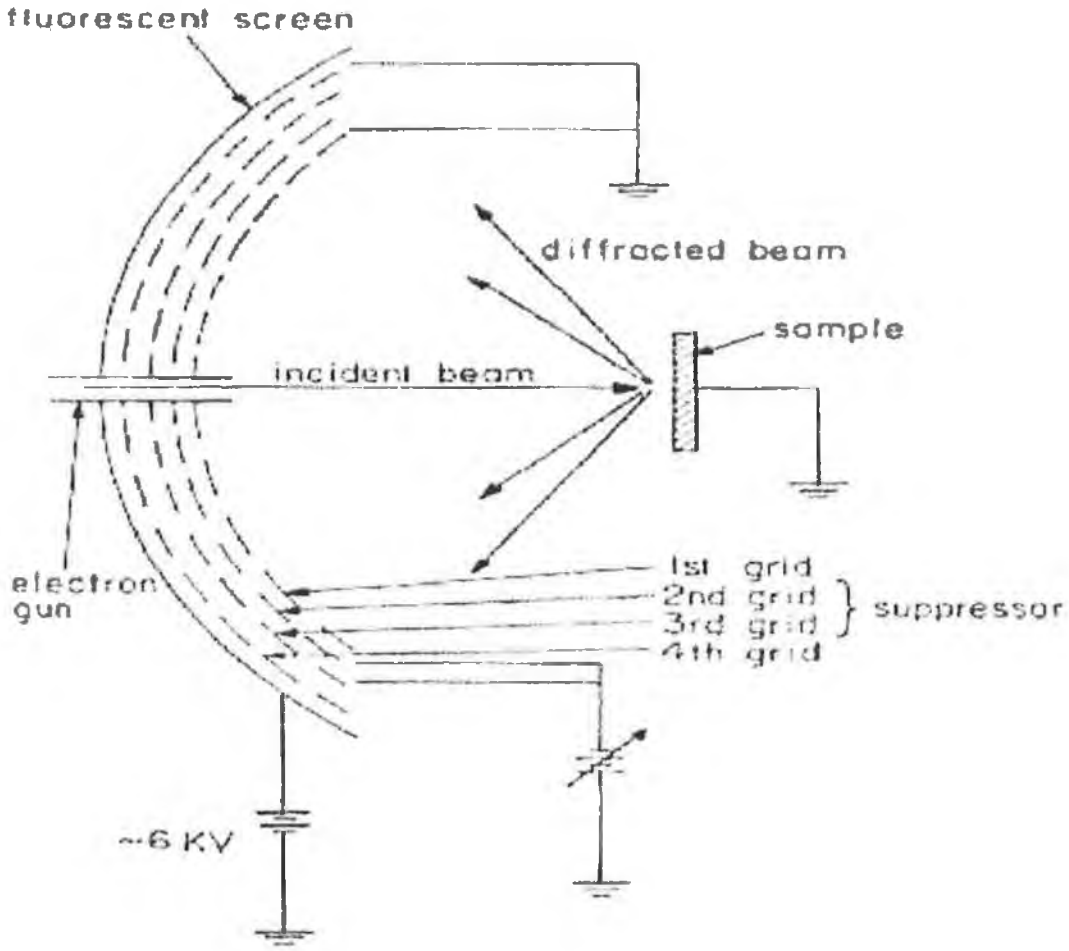

Figure 1.6 Schematic diagram of the LEED process [36].

1.6 Scanning Tunnelling Microscopy (STM)

History of STM

The scanning tunnelling microscope was first created in 1982 by Binnig and Rohrer [31] and capped many years of previous work not least by the National Bureau of Standards. The NBS wanted to create a surface imaging technique, which involved a non-contacting tip. This tip would be able to scan a surface under feedback control of a field emission current between sample and tip. This led to the creation of the Topografiner. The final design of the Topografiner bore a remarkable resemblance to the STM which was created over 10 years later.

The Topografiner managed to overcome three problems which until then had meant that this type of instrument just would not have worked. The first of these problems was that although physics theory explained quantum tunnelling through a vacuum, making it possible to ensure that a gap of a few Angstroms remained constant, the actual process had not been accomplished. The second problem encountered was that even though the technology to position and scan the surface using a probe was already in place, modifications were needed to the piezoelectric transducers to make this feat possible. Finally, it was necessary to create a way of bringing the tip of the probe to within 5 Angstrom of the surface for scanning, without crashing the tip into the sample surface.

Although the Topografiner overcame these problems it suffered badly from problems with stability as it had difficulty coping with vibrations leading to instabilities in the tip-sample separation.

In 1982 Binnig and Rohrer had a paper published in Applied Physics Letters reporting the first case of electron tunnelling across a stable vacuum gap for several different tip-sample biases [32]. The problems with stability encountered by the NBS's Topografiner were removed by mounting the STM on a magnetically levitated platform, which operated by decoupling high frequencies, thus leaving the vacuum system resting on a bench supported by air cushions. A tungsten tip mounted on a piezoelectric transducer was used to approach a platinum surface. This gave the

exponential dependence of current versus gap separation over four orders of magnitude. The data produced from this experiment proved that vacuum tunnelling had at last been achieved. Shortly afterwards, Binnig and Rohrer demonstrated the STM as an atomic-resolution microscope, which provided even more proof of the immense value of the instrument to the scientific community.

Before the introduction of the STM, only specialised techniques, e.g. field ion spectroscopy, could be used for direct atomic resolution images of surfaces. However, these were severely limited by sample preparation as to their range of application. The invention of the STM made it possible to examine surfaces on the nanometre scale, a vast improvement on previous instruments. The STM makes this feat possible as it can relate geometry and electronic structure to surfaces in an atom-by-atom process.

Since this revolutionary instrument has emerged, new additions have been developed for use in conjunction with the original system to allow it to: (a) apply STM technology to atomic force measurements at a level of sensitivity of $<10^{-12}$N and (b) the ability to fabricate a microscope probe and control it with nanometre precision. (a) can be achieved using the Atomic Force Microscope (AFM), invented by Binnig and Rohrer in 1986 [33] and (b) was made possible by using Allied Scanning Microprobe techniques, created by Wickramasinghe in 1990 [34].

Theory of operation for STM

The basic concept that allows STM to work is quantum mechanical tunnelling. This is the transfer of electrons from one atom to another, through a vacuum, in the case of STM from tip to sample or vice-versa.

In classical physics terms, the transfer of electrons between metals not touching is impossible due to the fact that the metal work function prevents electron transfer over the barrier. The kinetic energies of the electrons are smaller than the potential energy of the barrier, so technically this should keep the electrons in their respective orbitals and rule out transfer of electrons. However, the theory of quantum mechanics states that electrons can take two forms, a particle or a waveform. Following this theory, the electron can behave like a cloud or wave. When the cloud/wave collides with the

barrier, part of the cloud may penetrate the barrier, depending on the barrier thickness- the closer one metal is to the other constitutes the thickness of the potential barrier, and appears on the other side. This process is known as quantum tunnelling because the electron does not have enough kinetic energy to travel through the barrier but is still able to exist on the other side. In this case quantum mechanics and classical physics have contradictory views.

In STM the opposing atoms are located in the probe and the surface, so if the probe is positioned ~10Å or less from the sample, then quantum mechanical tunnelling will take place. The tunnelling creates an electrical current which can be measured and analysed. As the probe is scanned over the surface, the electron density will change, thus affecting the amount of current created. So, if a comprehensive scan is done of the sample surface along the x, y and z-axes, an image can be produced detailing exactly what the surface topography looks like.

The sample is moved to approximately 10Å from the STM tip using one of a variety of methods, typically by mechanical or electro-mechanical methods.
The scanning of the x, y and z directions is made possible by using a piezoelectric tripod, on which the probe is mounted. The piezoelectric tripod allows the probe to be controlled with sub-atomic scale accuracy, allowing the tip of the probe, which actually interacts with the surface atoms, to be brought to within the desired range of less than 10Å. The tripod is made up of three piezoelectric transducers whose movement can be controlled at all times. They operate by applying a voltage across them causing them to distort and thus moving the tip in one of three dimensions. The degree of distortion with voltage is in the order of ~1mV applied causing an expansion/contraction of 1Å.

Atomic resolution can now be obtained almost routinely using STM. This is due to the fact that (i) the tips can be prepared with only a single atom at the apex and (ii) tunnelling probability decays rapidly with separation. Thus, for STM to obtain atomic resolution, the tip must be sharp and the tip must lie within Angstroms of the samples surface.

The direction of flow of electrons from tip to sample or vice-versa can be controlled by applying either a positive or negative bias to the tip. If the tip has a positive bias, an energetic pull is provided for electrons from the sample to the tip, where their potential energy decreases, with the opposite true for applying a negative bias. The transfer of electrons produces a small current which is measured, with the magnitude of the current exponentially dependant on the tip-surface separation [35].

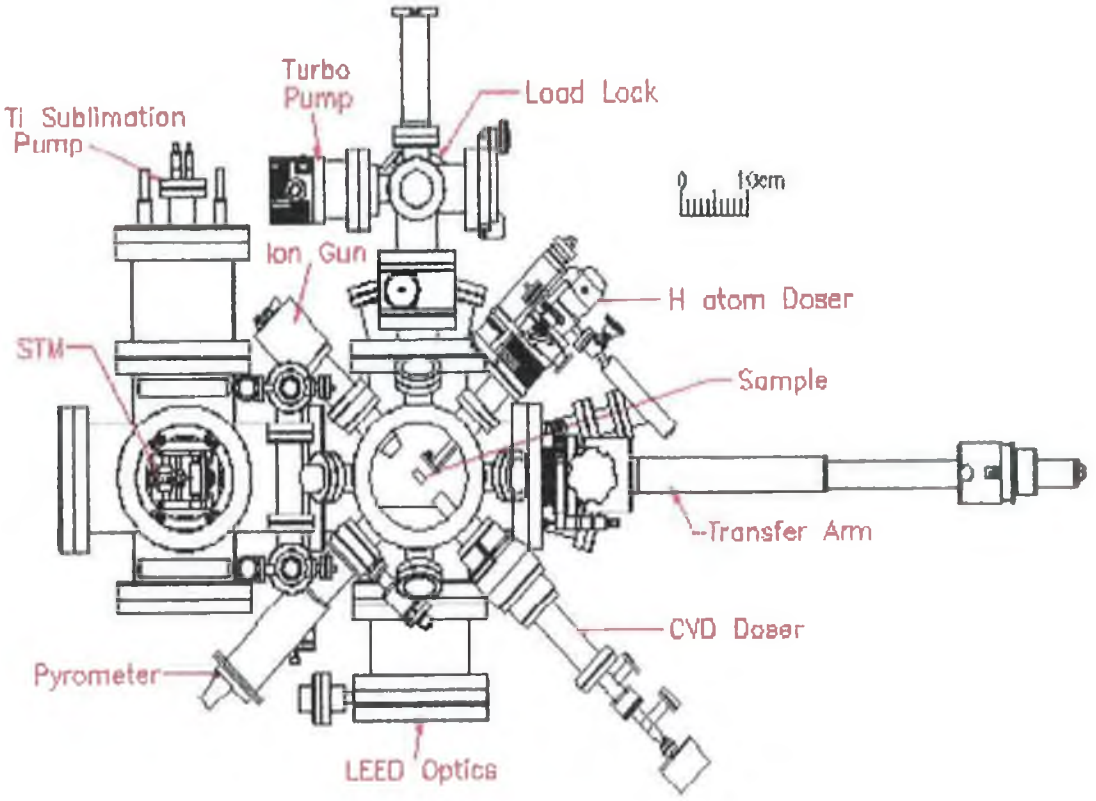

Figure 1.7 Schematic diagram of the STM chamber used [37].

Isolation of the STM from vibration and shock caused by the external environment is critical to the operation of the instrument, with even the slightest effect likely to cause the tip to crash into the sample surface. The most common methods for vibration isolation in STM are (i) Spring suspension/Elastomer support and (ii) Coil springs with an eddy-current damping system. The spring suspension/elastomer support uses multiple suspension stages with the entire apparatus mounted on pneumatic support. The coil springs with an eddy-current damping system explains itself, with the STM chamber suspended from coiled springs and an eddy current is used as a damping system.

Modes of operation of STM

The STM has three modes of operation, these being (i) constant height mode, (ii) constant current mode and (iii) spectroscopic mode.

The constant height mode operates as follows: The tip is positioned a set distance away from the surface of the sample. Before scanning the current between tip and sample is measured, but as the tip moves across the sample the current will vary as the topography of the sample varies, i.e. the current will increase as the tip is closer to the sample and decreases as the tip is further away from the sample. As the tip is at a set height, differences in current must be due to the shape of the sample surface, thus the microcomputer acquires tunnelling current as a function of position giving a detailed view of the sample surface. This mode is only possible on samples which have a reasonably smooth or uniform surface otherwise the tip could be damaged by hitting off a protrusion from the sample surface.

The constant current mode operates by using a set current between tip and surface and as the tip scans across the sample surface, the height of the tip from the sample surface changes to ensure that the current remains constant. This is done by passing the signal through a feedback circuit which produces an error signal. This error signal is fed through both a proportional amplifier and an integrating amplifier. The resulting signal is passed through a high-voltage amplifier which converts the tip position to obtain the desired tunnelling current. A readout of tip position versus tip height is given by the microcomputer which results in a comprehensive picture of the sample

surface. The constant current mode is used for samples with many protrusions and indents. This mode of operation is much slower than the constant height mode as the tip must move up and down to maintain the constant current and avoid damage from collision with the sample surface.

The final mode of operation is the spectroscopic mode. The spectroscopic mode operates with the height set at a desired tip-sample bias and tunnelling current. Once the desired height is obtained and held in a fixed position, the bias is scanned and the current versus bias is recorded through the current ADC. From this point by point measurement an image and spectrum are obtained at various positions across the sample surface.

Applications of the scanning tunnelling microscope

Another great advantage of the scanning tunnelling microscope is its wide field of applications. It can be used in a vacuum, in the natural environment in air and even in liquids. This characteristic has led to a variety of applications in different fields such as metallurgy, electrochemistry and molecular biology. It allows engineers to obtain an insight into the miniaturisation of electronic components, biologists to investigate the basic components of life under almost natural conditions, and it also allows chemists to gain a better understanding of batteries, by directly observing chemical surface reactions in an electrolytic solution at a molecular level.

However, the area of nanotechnology is where STM really excels, with it possible to position individual atoms on a sample surface using STM in a similar way to a pair of tweezers. In 1989 scientists succeeded in doing this for the first time at the IBM Research Centre Almaden, California. At temperatures near absolute zero (-273°C), scientists wrote the name IBM on a surface, using 35 xenon atoms. This was but a first step towards the development of the nanotechnology - the construction and application of minute machines such as pumps, and the development of new fabrication methods at the molecular scale. But this is still a long way off [37].

1.8 Electrochemistry theory

Electrodeposition

Electrodeposition is an electrochemical liquid phase thin film or powder preparation method where the reactions, either reduction or oxidation, are accomplished using an external current source. The deposition is carried out in an electrochemical cell consisting of a reaction vessel and either two or three electrodes. In the two electrode cell, the reactions are controlled by the current applied between a working electrode (substrate) and a counter electrode. In the three electrode cell, a reference electrode is used to control or measure the potential of the working electrode and deposition is carried out by controlling either current or potential and the corresponding potential or current, respectively may be measured [38]. During the course of this study, a three electrode cell was used for all electrochemical experiments.

Electrodeposition of metals is commonly carried out galvanostatically, i.e. with constant current applied. No reference electrode is needed which makes the galvanostatic system very practical but it can be used only if the chemical composition of the deposit does not have to be controlled by the applied potential. The potentiostatic electrodeposition, i.e. deposition at a controlled, constant potential is the most often used mode in a compound deposition where the stoichiometry of the product needs to be directly controlled. In addition to the constant current and potential techniques, deposition may also occur using a pulse mode, where the potential or current is pulsed between two different values or between a constant value and an open circuit. Pulsed deposition offers better adhesion and morphology of the deposit [38].

Compound electrodeposition can be carried out either cathodically or anodically, i.e. the working electrode is a cathode or an anode, respectively and the deposition reactions are accordingly reductions and oxidations. In the anodic system, the substrate or anode is made of a metal which is a constituent of the product compound, for example lead in the preparation of PbS [38]. In cathodic deposition, the choice of substrate material is not limited, the cathode can be comprised of any conducting material.

In addition to the one step deposition process mentioned above, compounds may be grown by depositing first elemental layers which are then suitably annealed, The annealing may be carried out under various atmospheres, reactive or inert depending if the composition of the product needs to be altered. The initially deposited layers may also consist of different compounds, for example in the case of CuInSe solar cells, the CuInSe consists of $CuSe_x$ and $InSe_y$ [38].

The potential where a reduction reaction occurs can be estimated from the Nernst equation, given below

$$E = E^{\circ} - \frac{RT}{zF} \ln\left[\frac{a(M)}{a(M^{z+})}\right] \qquad \text{(Eqn 1.7)}$$

for the following reaction

$$M^{z+}(aq) + ze \rightarrow M(s) \qquad \text{(Eqn 1.8)}$$

where E is the reduction potential, E^0 is the standard potential for the reaction, R is the gas constant, T is temperature in Kelvin, F is Faraday's constant, z is the number of electrons transferred and a(M) and $a(M^{z+})$ are the activities of M and M^{z+}. Activities of the ions are usually approximated to be the same as the concentrations and the activity of a pure element is 1. The calculated potential is valid only under the equilibrium conditions, which are rarely met in practice. For example, the reduction often needs a certain overvoltage to be applied, which is the irreversible excess potential required for a reaction to occur.

Therefore, it is more useful to measure the actual reduction potential under the experimental conditions for example by cyclic voltammetry, which is discussed in a subsequent section.

History of Metal Electrodeposition

The basic theory of electrodeposition was developed following the work of Kossel [39], Stranski [40], Becker and Doring [41], Volmer [42], and Burton, Cabrera and Frank [43]. Their results offered the generally accepted mechanism of electrocrystallisation, with the lattice growth occurring by charge transfer resulting in the deposition of the metals on the electrode surface. This original deposition is followed by surface diffusion of the low coordination number atom to a growth point [44].

An important series of papers were produced by Fleischmann, Rangarajan and Thirsk [45] which consider a formal mathematical treatment for the diffusion of an ion in solution, charge transfer and subsequent diffusion of adatoms onto the electrode surface. These equations have been applied to diverse systems including polyaniline films by Hwang et al. [46] to compare experimental results with theoretical current transients for each of the four nucleation types and growth modes.

Theory of Metal Electrodeposition

The process of electrodeposition or electrocrystallisation has many important industrial uses including solar cell manufacture [47] and corrosion protection [48] among others. Due to their industrial importance there have been many laboratory investigations into the electrodeposition mechanism.

The mechanism of metal electrodeposition or electrocrystallisation [49, 50] involves, as a first step, the reduction of a cation with the aid of an applied potential or current. This reduced cation forms an adatom and migrates over the substrate surface to an energetically favourable site. Similar atoms of the electrodeposit aggregate with the first deposited atoms forming the nucleus of a new phase. From this original nucleus, the deposit grows parallel and/or perpendicular to the substrate surface. A number of growth centres can grow onto one another to either form a continuous deposit or form islands of deposited material on the substrate. If the electrodeposited material forms a monolayer on the substrate surface, further deposition occurs on the electrodeposited

material. The formation of the first layer of the electrodeposited material determines the structure and adhesion of the overall electrodeposit.

Qualitatively the process is very similar to the formation of a precipitate in homogenous solution [51]. The difference is in the structure of the precipitate [52] as well as its formation. With the precipitate in an homogenous solution being controlled by the degree of supersaturation whereas the precipitate in electrodeposition is controlled by the overpotential.

Nucleation of growth centres on a foreign substrate normally follows a first order reaction with the first order rate law as follows:

$$N = N_0(1 - \exp(-A_t)) \qquad \text{(Eqn 1.9)}$$

where N_0 is the number of nucleation sites and A the nucleation constant.

As in any electrode process, the potential applied to the electrode determines the reaction rate. In electrodeposition, it is expected that the potential applied affects the rate of deposition and hence the structure of the deposit, with a low overpotential meaning more time is available to form an electrodeposit of perfectly crystalline structure. This can be observed in Figure 1.8.

Another factor thought to influence the quality of electrodeposit arises from differences in current density between different parts of the electrode owing to electrode shape. The shape of the electrode affects mass transport and thus accessibility to the cations to be deposited. It is generally accepted that it is best to apply a potential corresponding to the formation of crystalline deposits. It is clear that a more perfect crystalline structure would be desirable, however the low rate of electrodeposition does not compensate for using such low overpotentials.

In an industrial electrodeposition bath additives are added to improve the quality of the deposit along with the cation for electrodeposition and an inert electrolyte for good conduction. Organic compounds and surfactants are used to make the deposit

smoother, brighter and to modify its structure, thought to occur in the initial nucleation step [51]. Complexing agents can also be added to the electrochemical system to alter the deposition potential and avoid spontaneous chemical reactions.

Our experiments were concerned with the quantification of the electrodeposition procedure for metallic indium on a copper microelectrode substrate, so the quality of the crystal structure was of minimal interest. With this in mind, the electrochemical cell used over the course of our experiments consisted of a dissolved salt of the cations required for electrodeposition of metallic indium ($InCl_3$) and an inert electrolyte (Boric acid).

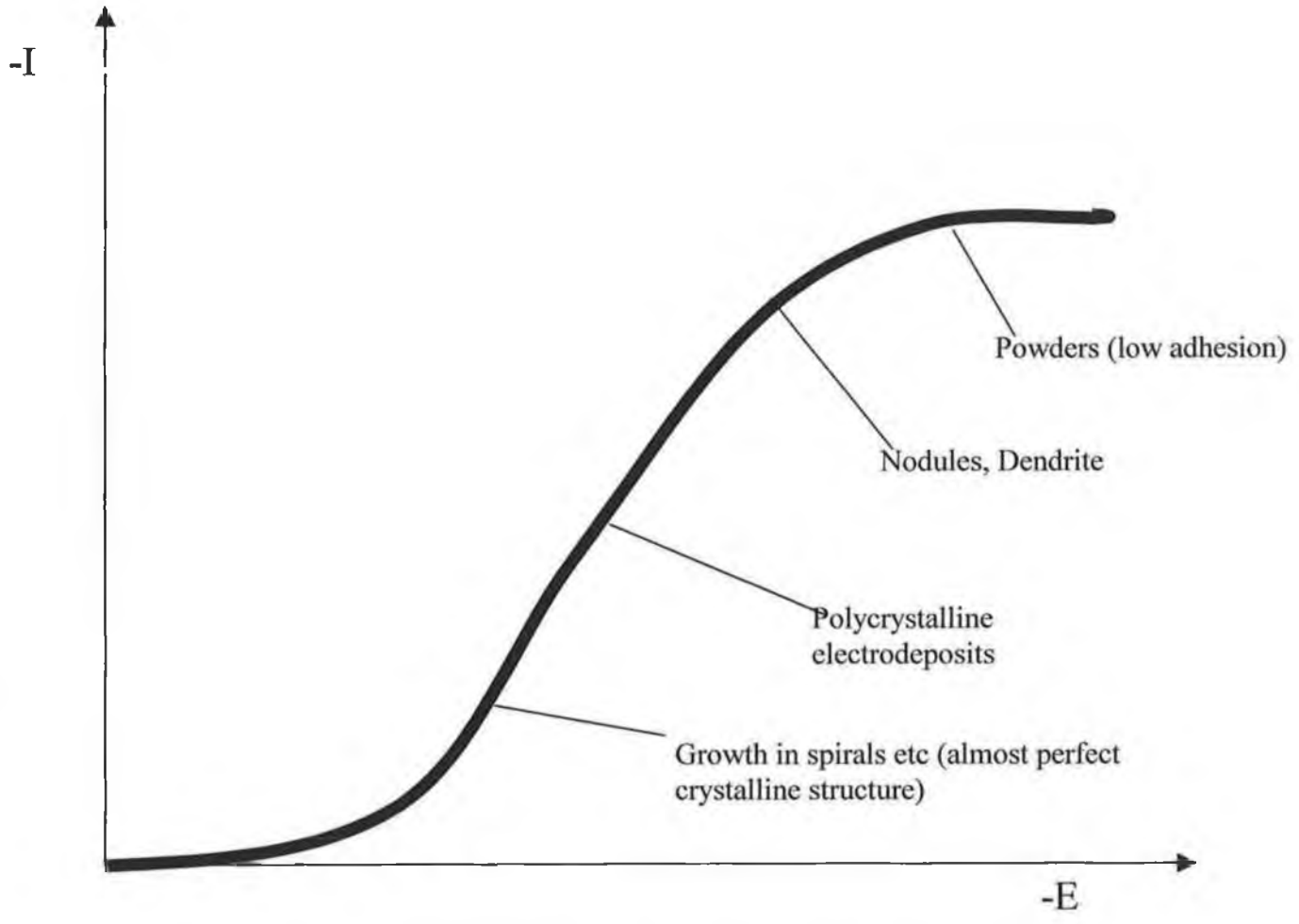

Figure 1.8 Theoretical plot of current versus potential for an electrodeposition process.

1.8 Cyclic Voltammetry

Theory of operation

Cyclic Voltammetry is one of the most widely used electrochemical techniques. It is classed as a potential sweep technique, which means it consists of the application of a continuously time-varying potential to a working electrode. This results in the occurrence of oxidation or reduction reactions of electroactive species in solution (faradaic reactions), possibly adsorption of species according to potential and a capacitive current due to double layer charging. The principal uses of potential sweep techniques have been to diagnose mechanisms of electrochemical reactions, for the identification of species present in solution and for the semi-quantitative analysis of reaction rates [53-55].

In cyclic voltammetry, the potential is scanned from a potential E_i and stopped at a chosen value E_f and on reaching a time equal to t_l, the sweep direction is inverted and swept until E_{min}, then inverted and swept to E_{max}. This triangular waveform is illustrated in Figure 1.9. The important parameters to note in a cyclic voltammogram are as follows (i) E_i, the initial potential, (ii) the initial sweep direction, (iii) v, the scan rate, (iv) E_{max}, the maximum potential (v) E_{min}, the minimum potential and (vi) E_f, the final potential [50].

A faradaic current, I_f, due to the electrode reaction, is registered in the relevant zone of applied potential where electrode reaction occurs. There is also a capacitive contribution, i.e. on sweeping the potential the double layer charge changes and this contribution increases with increasing scan rate. The total current is given by:

$$I = I_c + I_f = C_d \frac{dE}{dt} + I_f = \nu C_d + I_f \qquad \text{(Eqn 1.10)}$$

From this we see that I_c is proportional to v and also I_f is proportional to $v^{1/2}$. This means that for very high scan rates, the capacitive current must be subtracted in order to obtain accurate values of rate constants. On increasing the scan rate there is less time to reach equilibrium at the electrode surface, thus reactions which appear as reversible at slow scan rates may be quasi-reversible at high scan rates.

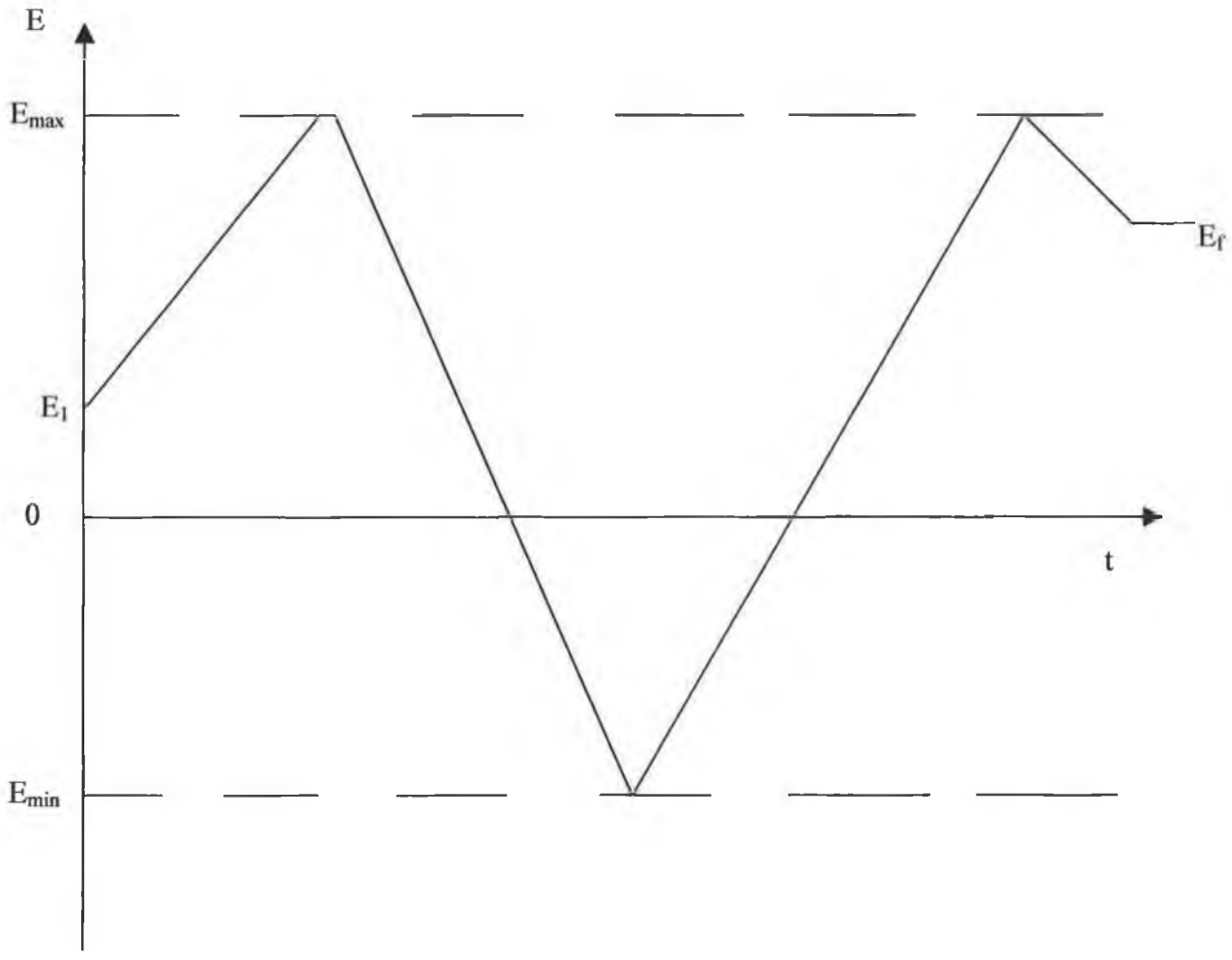

Figure 1.9 Triangular waveform used in Cyclic Voltammetry [50].

Cyclic Voltammetry at microelectrodes

The current density at a microelectrode is larger than that at a spherical or planar electrode of larger dimensions owing to radial diffusion. In cyclic voltammetry the current due to perpendicular diffusion is superimposed on the contribution from radial diffusion. Radial diffusion is independent of scan rate. For small scan rates ($0.1Vs^{-1}$) a steady-state cyclic voltammogram is obtained which is independent of scan rate. For large scan rates ($>10Vs^{-1}$) a more conventional cyclic voltammogram is obtained. The shorter response times of microelectrodes mean that higher rate constants for electron transfer or coupled homogenous reactions can be determined [51].

1.9 Chronoamperometry

Theory of operation

A step in applied potential or current represents an instantaneous alteration to the electrochemical system. Analysis of the evolution of the system after this disturbance allows electrode reactions and reaction rates to be determined [54,56]. A change in current is used to charge the double layer of the electrochemical system for a length of time corresponding to the RC time constant for the system. The study of the variation of the current response with time under potentiostatic control is referred to as chronoamperometry.

For the following reaction, where only O is present in solution

$$O + ne^- \xleftrightarrow{k} R \qquad \text{(Eqn 1.11)}$$

A potential-time profile shown in Figure 1.10 is applied to the working electrode. E_1 is chosen such that no reduction of O, or indeed any other electrode reaction, occurs. At a time t=0, the potential is stepped to a new value E_2, where the reduction of O takes place at a diffusion controlled rate. Ficks 2nd law can then be solved with the appropriate boundary conditions, for planar electrodes this is given by the Cottrell equation

$$|I| = \frac{nFD^{\frac{1}{2}}c_o^{\infty}}{\pi^{\frac{1}{2}}t^{\frac{1}{2}}} \qquad \text{(Eqn 1.12)}$$

This means that as time increases the current decreases. A plot of I vs. $t^{-1/2}$ should be linear and should pass through the origin. This plot is frequently used to determine the diffusion coefficient of species O (typically $10^{-5}cm^2s^{-1}$ [56]) from the slope of the straight line. The shortest time is determined by the charging time of the cell, typically a few hundred microseconds. The longest time is determined by the effects of natural convection but typically a value of a few seconds should suffice.

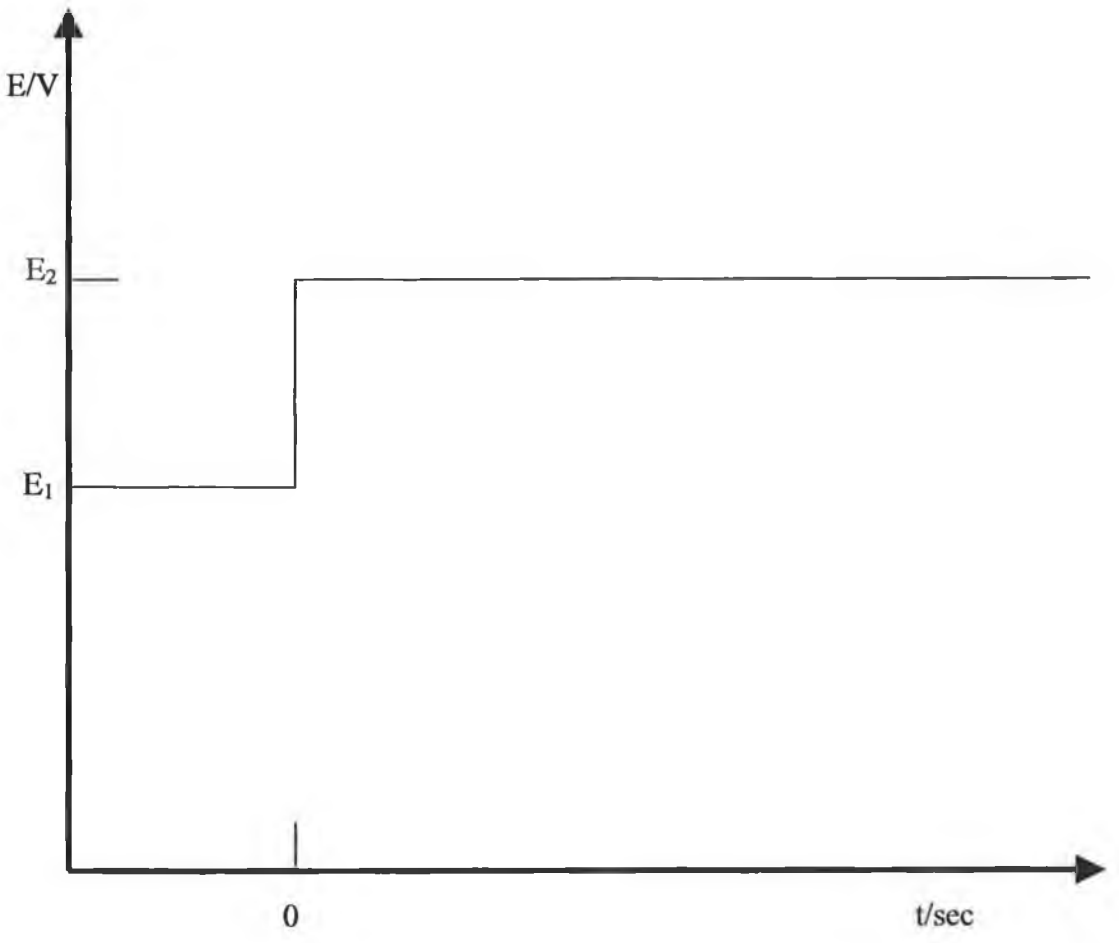

Figure 1.10 A potential-time profile for a typical chronoamperometric experiment [57].

1.10 References

1. Nerlov, J., Sckerl, S., Wambach, J., Chorkendorff, I., App. Catal. A 191(2000) 97.
2. Herman, R.G., Catal. Today, 55(2000) 233.
3. Al Shamaileh, E., Ph.D in Surface Science, Dublin City University, Dublin, 2002.
4. Albin, D.S., Moonet, G.D., Carapella, J., Duda, A., Noufi, R., Solar Cells 30(1990)41.
5. Orbey, N., Hichri, H., Birkmore, R.W., Russell, T.W.F., Progress in Photovoltaics 5(1997)237.
6. Contreras, M.A., Egaas, B., Ramanathan, K., Hiltner, J.Ul., Swartzlander, A. Hasoon, F. Noufi, R., Prog. in Photovoltaics Jul-Aug (1999)
7. Dzionk, C., Metzner, H., Hessler, S., Mahnke, H.-E., Thin Solid Films 299 (1997) 38-44.
8. http://www.alphametals.com/products/lead_free/PDF/thewayforward.pdf
9. Vickerman, J.C., "Surface Analysis: The Principal Techniques", Wiley, New York, 1997.
10. Van Beijeren, H., Nolden, I., "Structures and Dynamics of Surfaces", Springer, Berlin, 1987.
11. Clarke, L.J., "Surface Crystallography", Wiley, New York, 1985.
12. Prutton, M., "Surface Physics", Oxford University Press, Oxford, 1985.
13. Bohnen, K.P., Ho, K.M., Surf. Sci. Rep. 19 (1993) 99.
14. Nijs, M., "The Chemical Physics of Solid Surfaces and Heterogenous Catalysis", Vol. 7, Chapter 4, Elsevier, Amsterdam, 1994.
15. Callister, W.D., "Journal of Materials Science and Engineering" 6th edition, Wiley, New York, 2003.
16. Unertl, W.N., "Physical Structure: Volume 1 of the Handbook of Surface Science", Elsevier, Amsterdam, 1996.
17. Bayard, R.T., Alpert, D., Rev. Sci. Instrum., 21 (1950) 571.
18. Redhead, P.A., J. Vac. Sci. Tech. A, 12(1994)4.
19. Anderson, P.A., Phys. Rev. 47 (1935) 958.
20. Nottingham, W.B., J. Appl. Phys. 8 (1937) 762.

21. Bell, J., Davies, J.W., Gosling, B.S., J.I.E.E. 83 (1938) 176.
22. Atkins, P.W., "Physical Chemistry", Oxford University Press, Oxford, 1982.
23. Wild, R.K., Vacuum 31 (1980) 183.
24. de Broglie, L., "Recherches sur la théorie des quanta", Thesis, Paris, 1924.
25. Van Hove, M.A., Weinberg, W.H., Chan, C.-M., "Low Energy Electron Diffraction", Springer, Berlin, 1986.
26. Pendry, J.B., J. Phys. C. 13 (1980) 937.
27. Davisson, C., Germer, L.H., Phys. Rev. 30 (1927) 30.
28. Davisson, C., Germer, L.H., Nature 119 (1927) 558.
29. Thomson G.P., Reid, A., Nature 120 (1927) 801.
30. Van Hove, M.A., Ph.D in Theoretical Solid State Physics, Cambridge University, Cambridge, 1974.
31. Binnig, G., Rohrer, H., Helv. Phys. Acta. 55 (1982) 726.
32. Binnig, G., Rohrer, H., Phys. Lett. 40 (1982) 178.
33. Binnig, G., Rohrer, H., Phys. Rev. Lett. 56 (1986) 930.
34. Nonnenmacher, M., O'Boyle, M.P., Wickramasinghe, Appl. Phys. Lett. 58 (1991) 25.
35. DiNardo, N. John, "Characterization of Surfaces and Interfaces", Wiley, Canada, 1994.
36. Attard, G., Barnes, C.J., "Surfaces", Oxford university Press Inc., New York, 1998.
37. http://www.deutsches-museum.de/ausstell/meister/e_rtm.htm.
38. Saloniemi, H., Ph.D in Physical Chemistry, University of Helsinki, Helsinki, 2000.
39. Kossel, W., Ges. Wiss. Gottingen, math-physik, K1 (1927) 135.
40. Stranski, J.N., Z. phys. Chem., 136 (1928) 239.
41. Becker, R., Doring, W., Ann Physik, 24 (1935) 719.
42. Volmer, M., "Kinetic der Phasenbildung", Steinkopf, Dresden, 1939.
43. Burton, W.K., Cabrera, N., Frank, F.C., Nature, 163 (1949) 398.
44. Conway, B.E., Bockris, J.O'M, Proc. Roy. Soc., A248 (1958) 394.
45. Fleischmann, M., Rangarajan, S.K., Thirsk, H.R., Trans. Faraday Soc., 63 (1967) 1240.
46. Hwang, B-J., Santhanam, R., Chung-Ru, W., Yin-When, T., Electroanalysis, 13 (2001) 37.

47. Orbey, N., Hichri, H., Birkmore, R.W., Russell, T.W.F., Progress in Photovoltaics 5(1997)237.
48. Kuhn, A.T., "Techniques in electrochemistry, corrosion and metal finishing- a handbook", Wiley, London, 1987.
49. Budevski, E.D., "Comprehensive treatise of electrochemistry", Plenum, New York, Vol. 7, 1983.
50. Sluyters-Rehbach, M., Wigenberg, J.H.O.G., Bosco, E., Sluyters, J.H., J. Electroanal. Chem., 236 (1987) 1.
51. Brett, C.M.A., Brett, M.O.B., Oxford University Press, Oxford, 1993.
52. Despic A.R., "Comprehensive Treatise of Electrochemistry", Plenum, New York, Vol. 7, 1983.
53. McDonald, D.D., "Transient Techniques in Electrochemistry", Plenum, New York, 1977.
54. Parker, V.D., "Comprehensive chemical kinetics", Elsevier, Amsterdam, 1986.
55. Kissinger, P.T., Heinemann, W.R., J. Chem. Ed., 60 (1983) 702.
56. Naggy, Z., "Modern aspects of electrochemistry", Plenum, New York, 1990.
57. Southampton Electrochemistry Group, "Instrumental Methods in Electrochemistry", Horwood, Chichester, 2001.

Chapter 2

Vapour Deposition of In on a Cu{100} substrate

2.1 Introduction

In-Cu alloys have an established technological importance in thin film solar cell manufacturing and as solders for interconnections in the electronics industry [1]. Despite their importance in these fields very few structural studies have been conducted on these systems.

In 1992 Breeman and Boerma conducted the first study on this system at a coverage of 0.013ML In on a Cu{100} surface [2]. They monitored the system using low energy ion scattering and varied the deposition temperature from 63-300K. They found that with increasing temperatures In adatoms first migrate to step edges and form one- and two-dimensional clusters and then are incorporated into the terraces at near-substitutional sites.

In 1995 van der Vegt et al. investigated the effect of In on the homoepitaxial growth of Cu{100} by surface x-ray diffraction [3]. They found that indium enhances the interlayer transport by lowering the barrier for interlayer diffusion (Schwoebel barrier) at step edges. The effect is most pronounced for growth at low temperatures or when In is annealed on the surface before copper deposition occurs.

In 2001 Nakagawa et al. [4] conducted a study on Fermi surface nesting and structural transition on a metal surface for In on Cu{001}. The 'Fermi level' is the term used to describe the most energetic of electron energy at absolute zero temperature. Electrons are fermions and by the Pauli exclusion principle cannot exist in identical energy states. So at absolute zero they pack into the lowest available energy states and build up a 'Fermi Sea' of electron energy states [5]. Nakagawa's study briefly looked at the structures formed by indium at concentrations below the monolayer point on a Cu{001} substrate.
They found that at a coverage of 1ML, indium undergoes a phase transition between a high temperature (HT) c(2x2) and low temperature (LT) $(9\sqrt{2}x2\sqrt{2})R45°$ phase at a temperature of ~350K. Scanning Tunneling Microscopy (STM) of the LT phase shows a local atomic arrangement similar to the HT phase but with a strong periodic lattice disorder (PLD). They found

that the Auger Electron Spectroscopy (AES) intensities of copper and indium show a series of simultaneous breaks as a function of deposition time. The $(9\sqrt{2}x2\sqrt{2})R45^{\circ}$ phase formed at the first break point. A c(4x4) and $(\sqrt{10}x\sqrt{10})R18.4^{\circ}$ + (2x2) formed at longer deposition times. The c(4x4) phase formed at a concentration of ~1.3ML, with the $(\sqrt{10}x\sqrt{10})R18.4^{\circ}$ + (2x2) phase forming at 2.0ML. Their experiments were conducted using AES, LEED, STM and ARPES (Angle-resolved photoelectron spectroscopy).

In 2003 R. van Gastel et al. conducted a study on very low concentrations of In on a Cu{001} surface [6]. They found that In 'tracer' atoms embedded themselves in the copper substrate but rather than remain in their substituted positions they tended to jump over several lattice spacings around the surface. It is thought the embedded indium jumps from its original position to vacancies in the substrate.

A number of other studies have been conducted on the use of In/Cu alloys, but they deal with Cu/In alloys as precursors for solar cells [1, 7-10]. The Cu-In precursors are reacted with Se_2 [8,11], Ga [12], S [12, 13] etc. and are more interested in electrochemical deposition on a variety of substrates than in UHV structural studies of the deposited indium on copper system.

2.2 Experimental

The experiments conducted during the course of this study were performed in two separate systems. The first system was used for all STM and Auger work with preliminary LEED also involved; the second system was used for more detailed LEED measurements including LEED (I)V and line profiles at different concentrations and different temperatures.

The first system consisted of a stainless steel chamber attached to a variable temperature SPM (Omicron, UK) with a range of 40 to 1500K. The chamber has facilities for Auger and LEED analysis through interchangeable connections. All LEED and Auger results were analysed using the Spectraview video LEED package. The chamber was maintained at UHV using ion and titanium sublimation pumps. The STM was used in constant current mode to avoid crashing the tip as the surface had a varied topography. The tips used were made from etched tungsten.

The second system consisted of a stainless steel chamber with reverse view four-grid LEED optics (VG Microtech, UK). A base pressure of $1x10^{-10}$ was achieved using ion and titanium sublimation pumps. All LEED (I)Vs and line profiles were taken using a computer interfaced, high-sensitivity, CCD camera (Fuji Photo optical co., Japan) with the data acquisition software supplied by Data-Quire Corporation (Stony Brook, New York). The temperature range for these experiments was between room temperature and 378K and controlled via a Farnell regulated power supply. The sample was mounted on a high precision LEED goniometer, suspended between 2 stainless steel blocks by tantalum wires. Sample temperature was measured using a chromel-alumel thermocouple, which was placed in a 0.25mm hole in the middle of the sample.

In each case the copper sample (Metal Crystals and Oxides Ltd., UK) used had dimensions of 15x12x1.5mm and was mechanically and electronically polished to expose the {100} face within ±0.5°.

The sample was cleaned by argon plasma (Ar^+) bombardment for 30 minutes at 4KeV followed by annealing the sample to ~ 573K for 10 minutes. The Ar^+ bombard removes contamination with the anneal restoring the surface order of the sample. Prior to bombardment the argon stream was analysed using a mass spectrometer to ensure there was no contamination of the gas. The Cu{100} surface was checked using LEED to ensure a p(1x1) pattern with low background was attained prior to dosing and this pattern was checked against recorded literature reports for clean Cu{100} [14].

Indium was deposited using a Knudsen cell evaporator with the evaporation rate being calibrated by Auger Spectroscopy. This allowed the establishment of a relationship between the indium exposure and the indium and copper Auger intensities.

2.3 Results and Discussion

2.3a AES results

Auger Electron Spectroscopy (AES) represents the one of the most important chemical surface analysis tools today for conducting samples. Today's AES is based on the use of primary electrons with typical energies between 3 and 30keV and the possibility to focus and scan the primary electron beam in the nanometre and micrometre range analysing the top-most atomic layers of matter. The emitted Auger electrons are part of the secondary electron spectrum obtained under electron bombardment with a characteristic energy allowing one to identify the emitting elements. AES is useful for not only qualitative but also quantitative analysis along with elemental identification, AES determines the concentration of specific elements in the first 1-10 surface layers [15]. There are some difficulties associated with quantitative AES, the most important being the high background caused by the vast number of secondary electrons generated by a multitude of inelastic scattering processes. Secondary electrons are electrons which have undergone multiple energy losses, so they will not be recorded at the required energy, e.g. in the case of copper the Auger electron is emitted with 60eV and anything else will not be recorded as the copper signal. To overcome this problem the Auger spectra are often differentiated using a locking technique. Differentiation allows for the spectra to be measured directly and also gives a better sensitivity of detection.

AES measurements were taken as increasing concentrations of indium were deposited on an atomically clean Cu{100} substrate. Auger peaks were observed at 59/61, 105 and 404 eV, which are specific to copper, copper and indium respectively.

All elements apart from H and He exhibit characteristic transitions from the core hole electron, the 'down' electron and the Auger electron. The elemental transition is calculated using the following formula.

$$E_{kin} = E_K - E_{L1} - E_{L2,3} - \phi \qquad \text{(Eqn 2.1)}$$

$E_K - E_{L1}$ is an expression for the energy available to the Auger electron from the 'down' electron, with $E_{L2,3} - \phi$ being an expression for the energy required to overcome the barrier to emission from within the atom. These values were obtained from Auger tables contained in Appendix 1. This calculation is for a KLL transition.

From these values, it was calculated that in this experiment copper undergoes a M_IVV transition, with indium giving a $L_IL_{III}V$ transition. All Auger data was recorded at 300K.

Figure 2.2 is a plot of Auger signal versus deposition time for indium on Cu{100}. Both the In 404eV and Cu 105eV peaks have been multiplied by a factor of 5.7 to allow comparison with the Cu 59/61eV peak, which is of a much higher intensity. As the In signal increases, the Cu signal decreases proportionally. This is to be expected, as when the amount of indium deposited on the surface increases, the amount of copper on the surface must decrease. AES measures the top-most atomic layers, so even when monolayer point is reached for deposited indium, there will still be a large copper peak due to the layers below the surface. As the number of monolayers of indium increases the copper peaks will diminish towards zero.

A plot of theoretical layer-by-layer growth has also been added for indium on Cu{100} using a mean free path of 5Å. The inclusion of this theoretical growth is to highlight the difference in growth modes between the calculated and experimental Auger signal versus time (As-t) curves.

The As-t plot may be approximated to a series of linear segments of differing gradients, with each 'break point' between linear segments representing the completion of one monolayer. This type of growth mode is known as the Stranski-Krastanov growth mode. The Stranski-Krastanov growth mode involves the indium initially growing to become a two-dimensional layer or

monolayer, with the additional indium growing as three-dimensional clusters above the indium monolayer [16].

In the As-t plot in Figure 2.2 the first 'break point' is formed at an exposure of 9×10^5 nA/sec In, thus according to the Stranski-Krastanov growth mode, it is thought that this is where the first physical monolayer is formed. The indium is deposited from a faradaic cup, with the flux of indium dependant on its ionisation energy. As the indium wire is heated, a proportion of the indium atoms are ionised and they pass through a cylinder on their way to the sample surface. This cylinder has an electrical current flowing from it to a detector, as the ions come in contact with the cylinder the current changes according to the amount of ions that come in contact with the cylinder surface. From this change in current it is possible to calculate the exposure of indium ions to the sample surface.

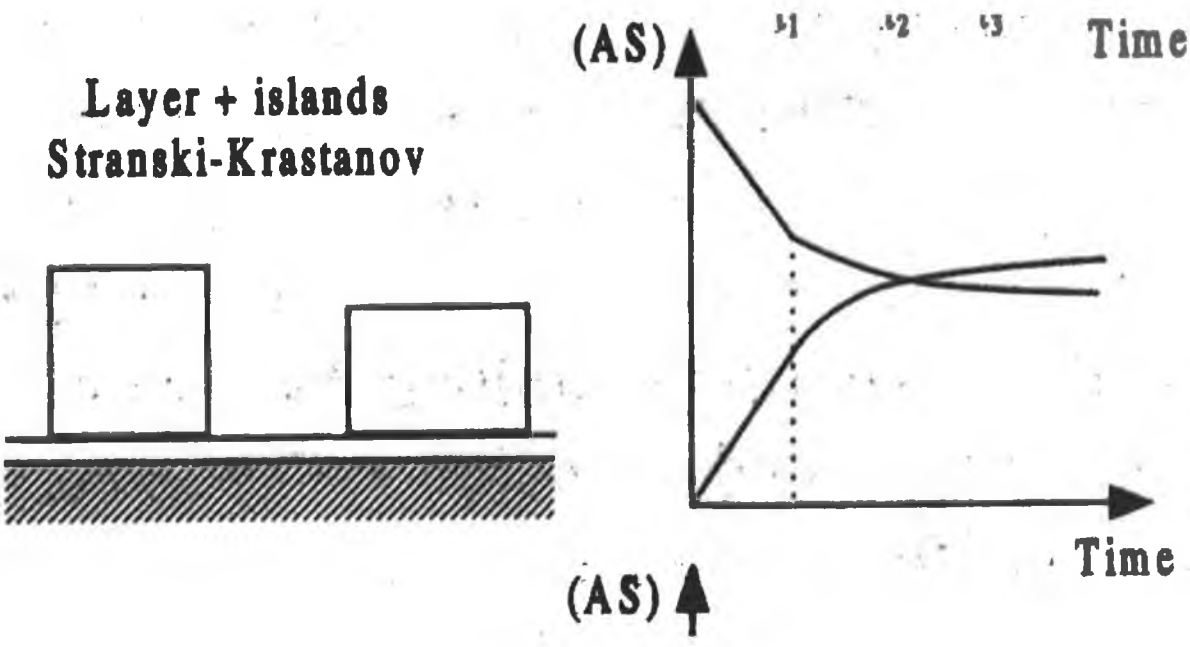

Figure 2.1 Theoretical view of Stranski-Krastanov growth mode with an example of a perfect Auger signal versus time plot to illustrate behaviour. [16].

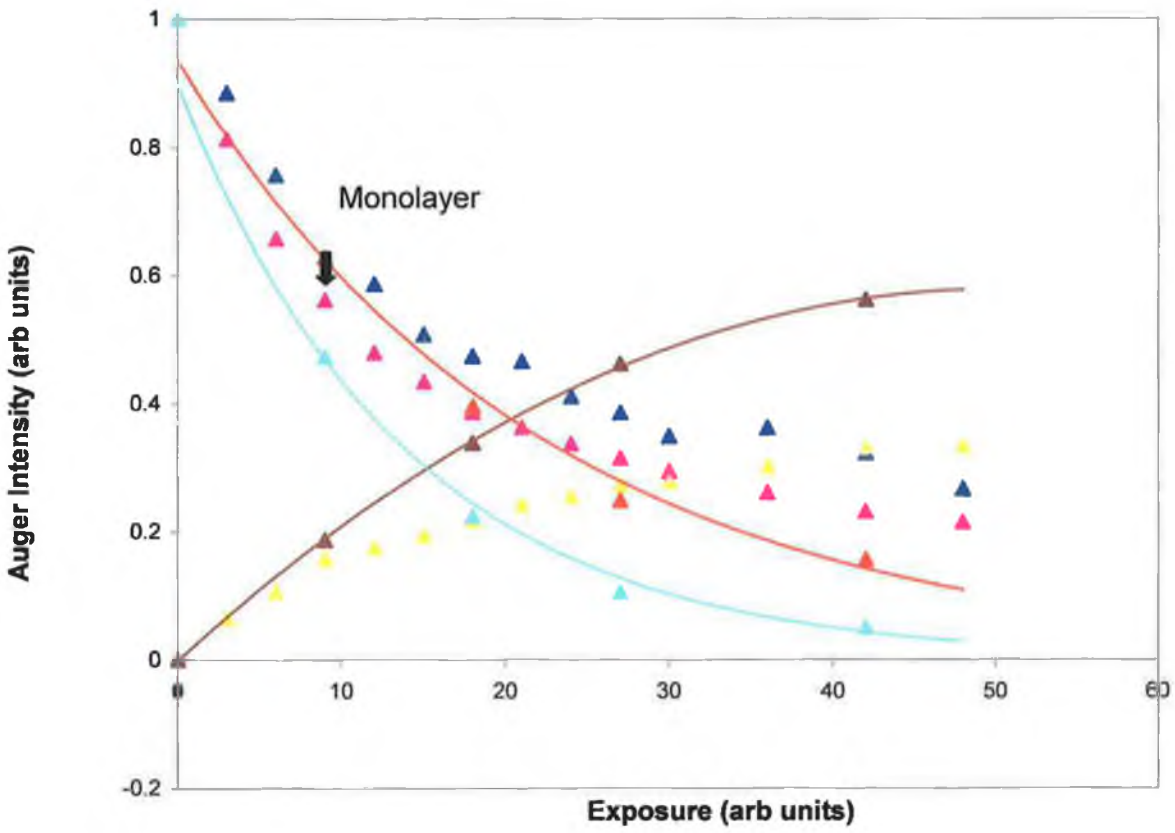

Figure 2.2 An Auger signal versus time plot for In on Cu{100} at room temperature. I_e=12mA, V=650V, I_{fil}=1.4A, Time=60min, Flux=900 - 2600nA/sec, Total Exposure=5.0×10^6. Legend ▲Cu105eV(x5.7), ▲Cu59/61eV, ▲In404eV, ▲ Theoretical layer-by-layer growth for Cu105eV ▲ Theoretical layer-by-layer growth for Cu59/61eV ▲ Theoretical layer-by-layer growth for In404eV.

The data points in the theoretical As-t plot were calculated using two formulae, the first is an empirical relationship suggested by Seah and Dench [17]:

$$\lambda/\text{nm} = 538a/E^2 + 0.41a^{3/2}(E_{kin})^{1/2} \qquad \text{(Eqn 2.2)}$$

where λ is the inelastic mean free path, E is the kinetic energy of the electrons, in eV and a is the mean atomic diameter of the element in nm (e.g. for Cu 105, E=105eV with a= 2.556Å).

This calculation gives a value for the inelastic mean free path (λ), which is the average distance (in nanometres) that an electron with a given energy travels between successive inelastic collisions. A small λ indicates a high probability of energy loss and the ability to travel only a short distance before being inelastically scattered. Therefore, electrons with a small inelastic mean free path are highly surface sensitive. The inelastic mean free path is only slightly material dependant, but is heavily dependant on the electron kinetic energy. It was necessary to calculate the inelastic mean free path prior to using the second formula. The IMFP values for Cu 59/61eV, Cu 105eV and In 404eV are 18.14, 23.53 and 65.95Å respectively.

The second formula used is based on the Beer-Lambert law for the absorbance of electromagnetic radiation, though this calculation deals with electrons rather than photons.

$$I(d) = I_0 \exp(-d/\lambda(E)) \qquad \text{(Eqn 2.3)}$$

where I(d) is the intensity after the primary electron beam has travelled a distance, d, through the solid and I_0 is the initial beam intensity before interaction with the solid. $\lambda(E)$ as mentioned previously is the inelastic mean free path. This formula calculates the intensity decay and follows an exponential first-order decay law for the travel of electrons through matter. The I(d) value is plotted versus In exposure to give the As-t plot (Figure 2.2)

2.3b LEED Results

The most widespread use of Low Energy Electron Diffraction is to check the cleanliness and order of surfaces being prepared for other experiments, because of the sensitivity of LEED to surface contamination and surface roughness, the appearance of a LEED pattern with bright, sharp spots is widely regarded as evidence of a completely clean, ordered surface. Added to its routine use in sample preparation in UHV, the pattern of LEED spots can be used to obtain information about imperfections in the surface such as steps or islands. It can also be used to determine whether any molecules on the surface are adsorbed in an ordered or random way. If an overlayer is ordered, its surface unit mesh size can be determined, and if the layer is adsorbed commensurately with the substrate, its orientation relative to the underlying substrate may be determined. Analysis of the intensities of the diffracted beams as a function of beam energy ((I)V curves) allows the determination of positions of atoms within each unit cell to allow an exact overlayer structure to be established [15]. LEED is a useful tool for understanding both long range and short range ordering of a metal on metal system.

During the deposition of indium on Cu{100} five different LEED patterns were observed. These were (a) Clean Cu{100}; (b) (9√2x2√2)R45°; (c) c(2x2); (d) c(4x4) and (e) a 'complex' phase. From Figure 2.3, it can be seen that the (9√2x2√2)R45° phase begins at approximately 17 minutes In deposition time at a flux of 390nA/sec. This gives a total exposure of 3.978×10^5nA, corresponding to a coverage of 0.4+/-0.05ML. The c(4x4) phase was found to begin at 23 minutes which is thought to be a coverage of 0.6+/-0.05ML In at a total exposure of 5.382×10^5nA. Above 25 minutes (total exposure of 5.85×10^5nA) the 'complex' phase is formed and remains until monolayer point is reached. At a deposition time of 25 minutes, the complex phase exhibits sharp spots with a low background but as the deposited In is increased beyond this point, the LEED pattern deteriorates with the spots becoming increasingly more diffuse and the background increasing substantially.

These patterns are shown in Figure 2.4. Each LEED pattern exhibits high background indicating the presence of disorder on the sample surface.

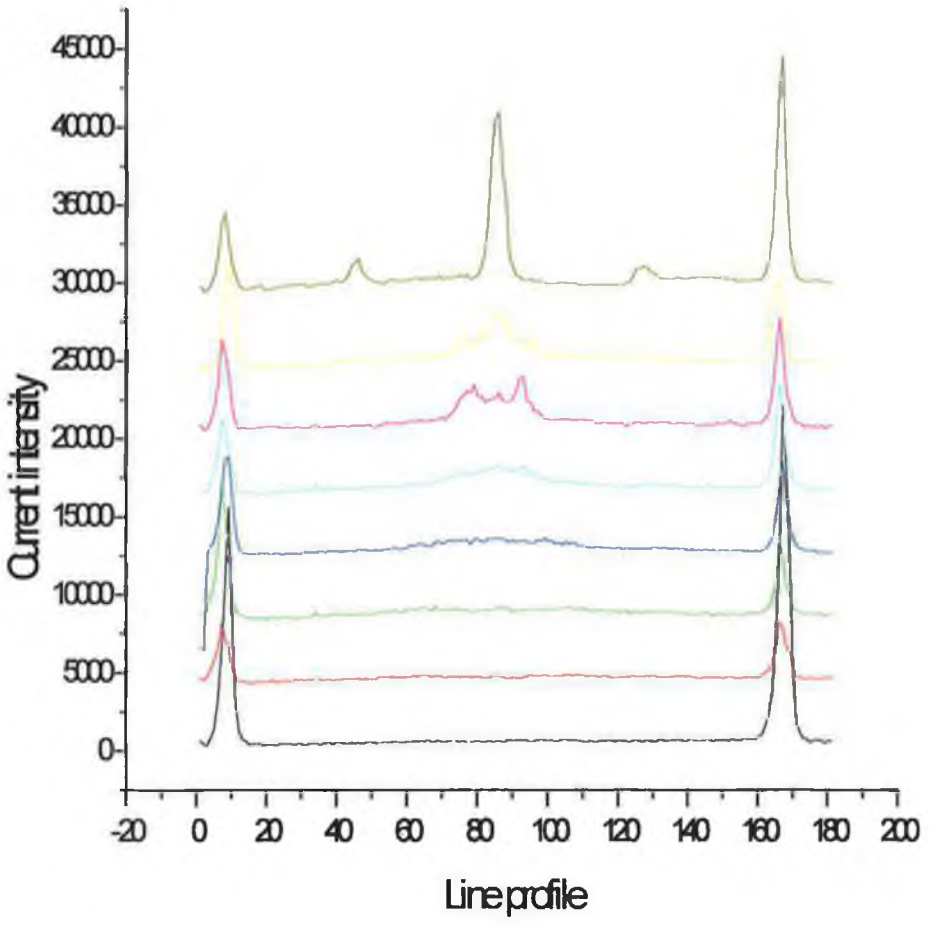

Figure 2.3 LEED line profiles through the (1/2, 1/2) spots and neighbouring integral order beams at increasing deposition times through the range 0 to 25 mins. Indium was deposited at a flux of 300nA/sec. Legend – Clean, - 4mins, -12mins, -17mins, - 19mins, -21mins, 24mins and - 25mins.

(a)

(b)

(c)

(d)

(e)

Figure 2.4 LEED images of In on Cu{100}, (a) clean Cu{100}, (b) LT ($9\sqrt{2}x2\sqrt{2}$) R45° phase, (c) HT c(2x2) phase, (d) c(4x4) phase and (e) complex phase.

The clean copper LEED pattern (a) was observed at room temperature. It exhibits a sharp low background intensity p(1x1) LEED pattern and was in excellent agreement with reported literature for clean Cu{100} [14]. The LEED image (a) was taken at a beam energy of 108eV, this energy was chosen as it was important to take all LEED images at approximately the same energy to allow easy comparison.

The $(9\sqrt{2}x2\sqrt{2})R45°$ overlayer structure (b) was formed by depositing 0.4+/-.05ML In on Cu{100}, at a flux of $8.0x10^5$ nA/sec and was taken at room temperature. The LEED image was taken at a beam energy of 102eV.

This LT $(9\sqrt{2}x2\sqrt{2})R45°$ phase is heated above a temperature of 373K, resulting in this phase undergoing a reversible phase transition to become a HT c(2x2) structure (c). This LEED image was taken at a beam energy of 107eV.

Figure 2.5 illustrates line profiles taken throughout this phase transition. This phase transition is reversible, and shows the gradual process the surface undergoes in changing from the LT phase to the HT phase.

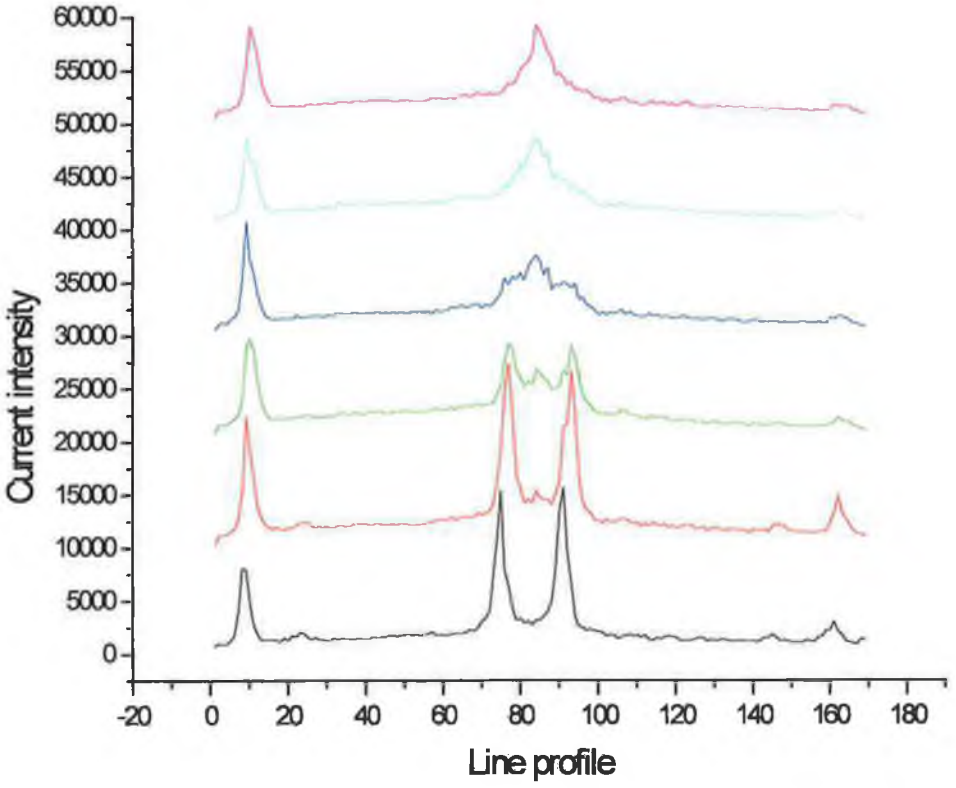

Figure 2.5 Line profiles taken through the (1/2, 1/2) and neighbouring integral order beams at a coverage of 0.4+/-0.05ML In on Cu{100} through a temperature range of 318K to 373K. Legend – 318K, - 328K, -338K, - 348K, - 358K and – 373K.

If the LEED images are compared (Figure 2.4), it can be seen that in the $(9\sqrt{2}x2\sqrt{2})R45°$ phase there are a 'box of four' spots located in each of the (½ , ½) locations, but as the surface is heated above 373k they gradually combine to form (½, ½) beams which are much more intense in energy compared with each of the previous spots. As the heat is applied the copper lattice becomes more relaxed, allowing the indium to move more freely across the surface. As the indium becoming more mobile, it is thought that due to the extra energy provided by the addition of heat, the indium lying in the adsorption sites represented by the 'box of four' spots in the LEED pattern, move to occupy the adsorption sites that are represented by the ½, ½ spots in the c(2x2) structure. The resulting spot is thought to be 4 times as bright as the singular spots in the 'box of four' spots pattern. Indium is reported to have a low surface energy [21]. In the $(9\sqrt{2}x2\sqrt{2})R45°$ structure it is thought that the indium occupies the sites of lowest energy but as heat is applied the indium is given more energy, mobilizing the adsorbed metal and allowing them occupy sites of higher energy, as seen in the c(2x2) structure. This reaction is reversible, so, as the surface cools, the ½, ½ beams move from their adsorption sites again to reform the 'box of four' spots in the LEED pattern and thus the $(9\sqrt{2}x2\sqrt{2})R45°$ structure. This is thought to be due to the copper lattice becoming more rigid and forcing the indium atoms into returning to adsorption sites of lower energy.

The c(4x4) structure (Figure 2.4(d)) is formed at room temperature, at a concentration of 0.6 +/-0.05ML. As can be seen from the LEED image, the c(4x4) LEED pattern contains both the ½, ½ fractional beams as with the c(2x2) but also spots in the ¼, ¼ positions. The LEED image (d) was taken at an energy of 110eV.

Above this concentration of indium on Cu{100} a 'complex' pattern (e) is formed. This corresponds to 0.65ML point, and this 'complex' formation is present to monolayer coverage and above. Nakagawa et al [4] found this to be a $Cu\{100\}-(\sqrt{10}x\sqrt{10})R18.4°+(2x2)$-In, but it is felt that this diagnosis is

inaccurate as all spots in the LEED pattern are not accounted for. Image (e) was taken at 120.3eV.

Figure 2.5 charts the change in line profile through the (½, ½), (-½, ½) and neighbouring integral order beams with increasing temperature, the line profile taken is seen in Figure 2.4. It can be seen that as the temperature increases, the 2 peaks from the 'box of four' spots decrease until at a temperature of 363K, both peaks are no longer present. As the peaks from the 'box of four' spots decrease in intensity, the ½, ½ beam peak from the c(2x2) structure increases in intensity. This beam first appears at a temperature of 323K, indicating that at temperatures from 323K to 363K there is a mixed indium phase on the Cu{100} substrate. This is witnessed in the LEED results with a high background present and the spots in the ½, ½ positions proving to be diffuse. At a temperature of 373K the background, although higher than normal becomes much lower than during the transition temperatures and the ½, ½ beams for the c(2x2) are sharp. This suggests that the high background and diffuse spots witnessed during the transition are a result of surface disorder rather than simply a temperature effect.

Figures 2.6 and 2.7 show the LEED I(V)'s of the (1,0) and (½, ½) beams (respectively) for each of the ordered phases for In on Cu, i.e. ($9\sqrt{2}$ x $2\sqrt{2}$)R45°, c(2x2) and c(4x4). Each beam has been individually background subtracted by empirical fitting a monotomically rising function to user defined minima in the spectra. Symmetrically equivalent beams for each overlayer structure were averaged to reduce the effect of residual sample misalignment and stray fields and more importantly to improve the signal-to-noise ratio. After averaging, each beam was normalised to constant incoming primary beam current and smoothed by 5-point adjacent averaging. Unfortunately, to acquire the Cu{100}-c(2x2)-In (½, ½) spots it was necessary to heat the sample above 373K, giving a high background, meaning the intensity for these beams were much weaker than the other (½, ½) beams, thus to allow comparison they were plotted on a separate graph.

The (1,0) and (½, ½) beams for each of the structured overlayers are similar in shape, indicating that all structures share similar In adsorption sites. The c(4x4) and c(2x2) patterns are almost identical, so it is thought that the c(4x4) pattern is a variation on the c(2x2) pattern but exact determination is only possible through a Tensor LEED analysis of the spot profiles.

A Tensor LEED study of the Cu{100}-c(4x4)-In structure was conducted by K. Pussi et al. [21] to determine the exact location of the indium atoms on the Cu{100} surface, see Figure 2.8. It was found that the indium overlayer consisted of two layers. The indium layer closest to bulk comprised a c(2x2) periodicity, with the indium atoms lying at four fold hollow sites with respect to substrate. This c(2x2) In layer is overlayed by a c(4x4) In layer in which the indium atoms lie at four fold hollow sites with respect to the c(2x2) layer. It was calculated that the atoms in the c(2x2) In layer are laterally shifted by 0.28+/-0.09A from the four fold hollow sites towards bridge sites.

The perpendicular distance between the c(2x2) In layer and the c(4x4) In layer is 1.30+/-0.08Å, with the effective radius of indium in this structure being 1.56 – 1.61A with a nearest neighbour Cu-In separation of 2.86Å.

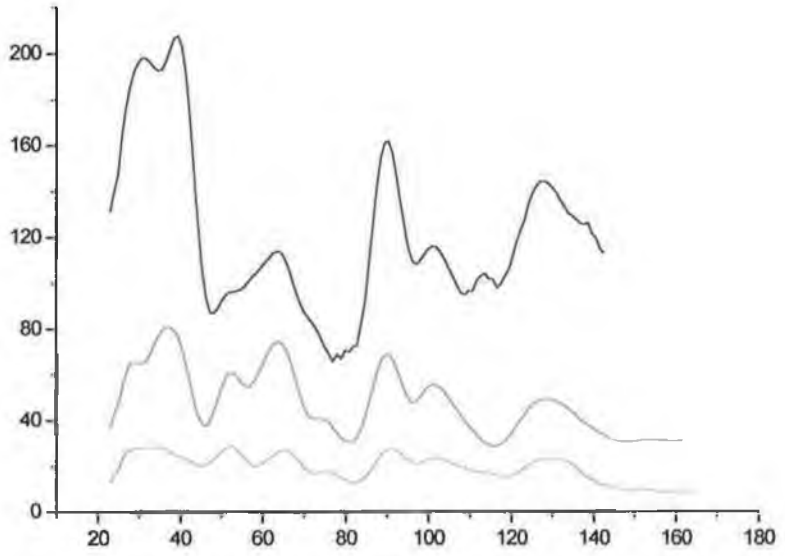

Figure 2.6 Symmetry averaged normal incidence I-V spectrum of the (1,0) beams for Cu{100}-(9√2x2√2)R45°-In, Cu{100}-c(2x2)-In and Cu{100}-c(4x4)-In overlayer. Legend – Cu{100}-(9√2x2√2)R45°-In, - Cu{100}-c(2x2)-In and - Cu{100}-c(4x4)-In.

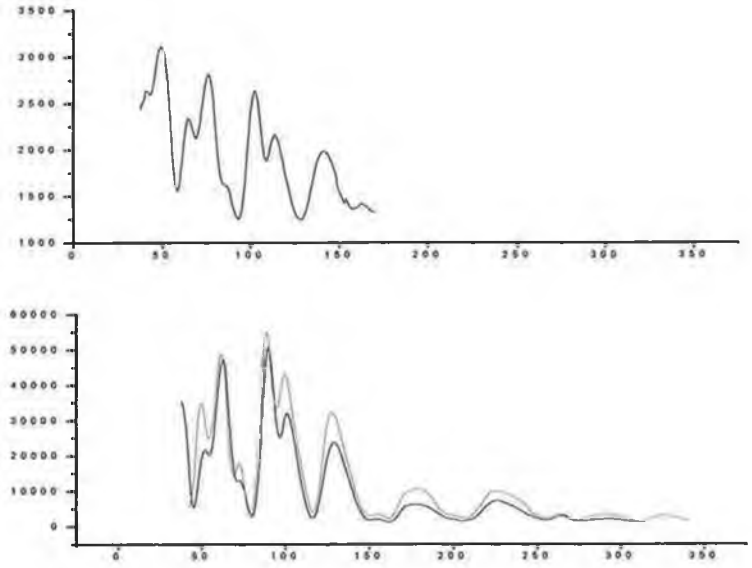

Figure 2.7 Symmetry averaged normal incidence I-V spectrum of the (½, ½) beams for Cu{100}-c(2x2)-In, Cu{100}-(9√2x2√2)R45°-In and Cu{100}-c(4x4)-In overlayer. Legend - Cu{100}-c(2x2)-In, (bottom image) - Cu{100}-(9√2x2√2)R45°-In and - Cu{100}-c(4x4)-In overlayer.

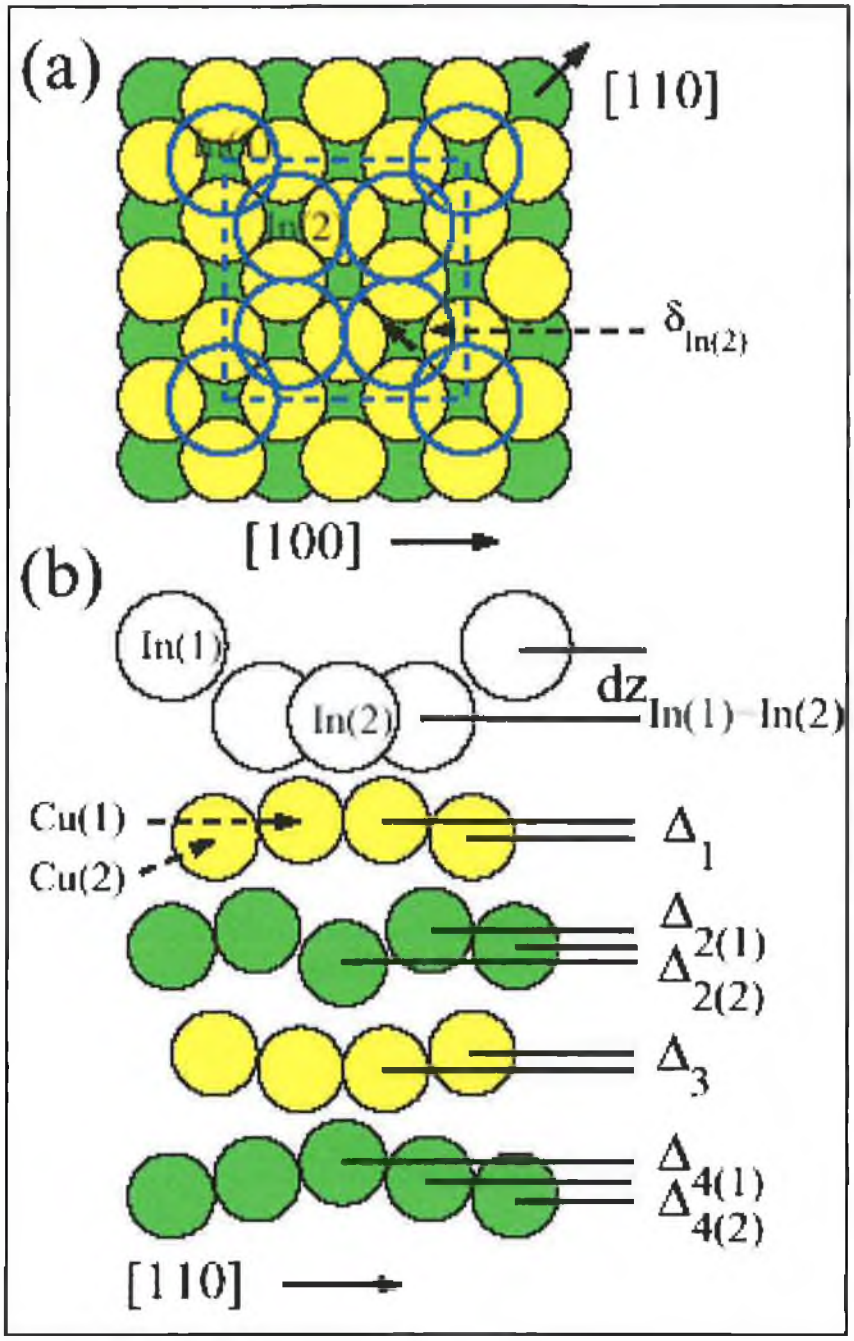

Figure 2.8(a) The top view of the favoured model of the Cu{100}-c(4x4)-In surface as calculated using Tensor LEED by K. Pussi et al. [21], with the c(4x4) unit cell shown using dashed lines. The main crystallographic directions are shown using arrows.

Figure 2.8(b) A side view of the favoured model of the Cu{100}-c(4x4)-In surface, along the [110] direction layer spacing and bucklings are overestimated for clarity.

2.3c STM Results

A Scanning Tunnelling Microscope (STM) is a stylus-type instrument in which a sharp probe is scanned raster-like across a sample. STM is employed primarily to detect changes in surface structure on the atomic scale, by measuring changes in the surface electron density. For surfaces that have relatively uniform electronic properties (and in the limits of dimensions >10 Å), the STM image effectively represents the surface topography. For electronically inhomogenous surfaces, the electronic structure becomes more important in determining the nature of the image [18].

Several techniques do exist by which the surface crystal structure may be studied, the main one being LEED (as mentioned earlier). However, the possibility of being able to visualise directly the arrangement of atoms at a surface, atomic-scale topographic information and atomic-scale electronic structure information sets the STM apart from other analytical surface techniques [15] (It is thought that STM, LEED and AES results will give a detailed understanding of the In-Cu system.)

A low resolution image of the clean Cu{100} surface is shown in Figure 2.9(a). As can be seen from the image, the Cu{100} surface has long terraces, making it perfect for analysis by STM, as these are flat and allow for high resolution study. The corresponding LEED image for this structure is a sharp p(1x1) pattern with low background. This would indicate that the Cu{100} surface is close to atomically flat but as can be seen from the STM image this is not always true as the Cu{100} surface in this case contains many surface features (e.g. terraces, steps etc.). A line profile was taken across this image to give an idea of each of the step heights, this is seen in Figure 2.9(b). From this line profile each step height is thought to be in the region of 2Å.

Figure 2.9(c) reveals one of the terraces in Figure 2.9(a) magnified to atomic resolution.

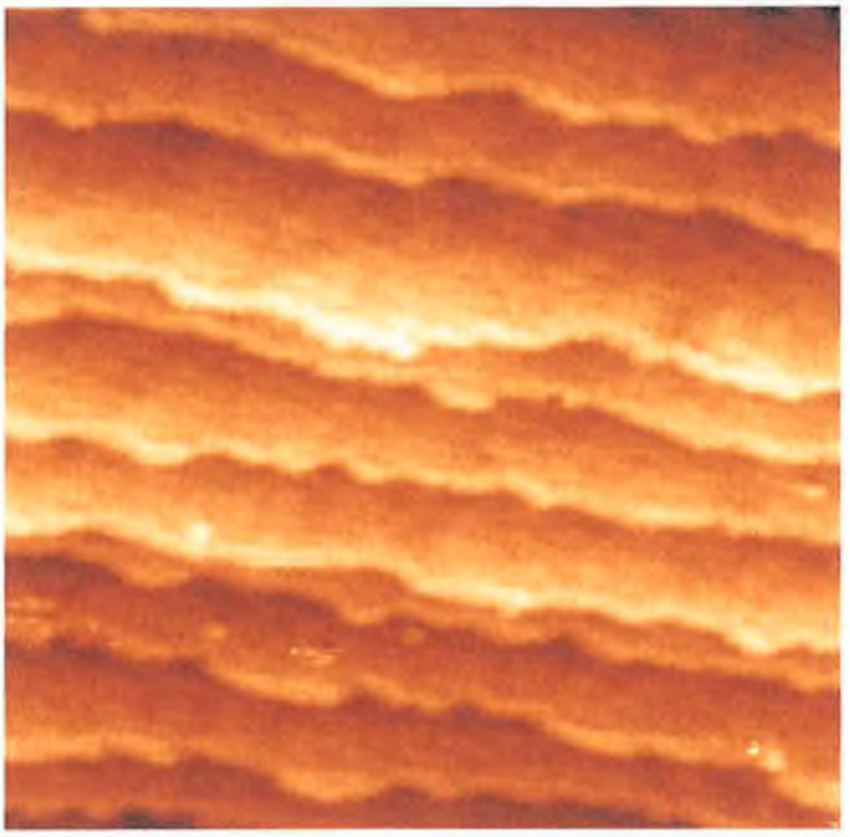

Figure 2.9(a) Low resolution image of clean Cu{100}, with a sample bias, $V_s = 0.05V$ and a tunnelling current $I_t = 2nA$.

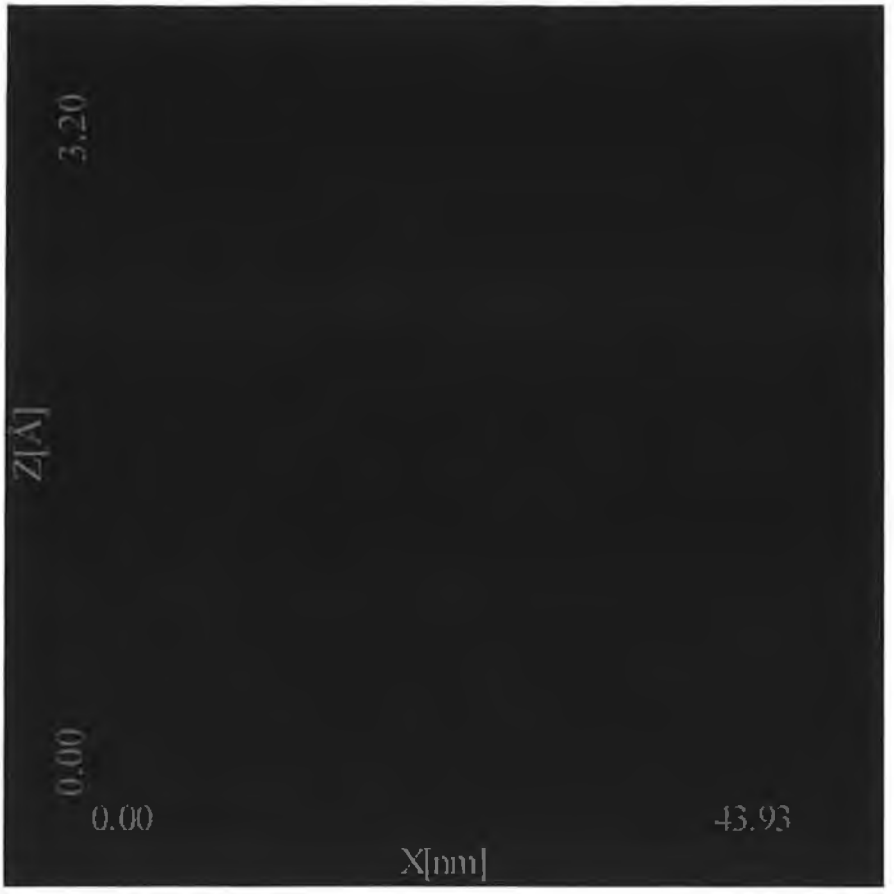

Figure 2.9(b) Line profile taken across the steps of the clean copper image from Figure 2.9(a)

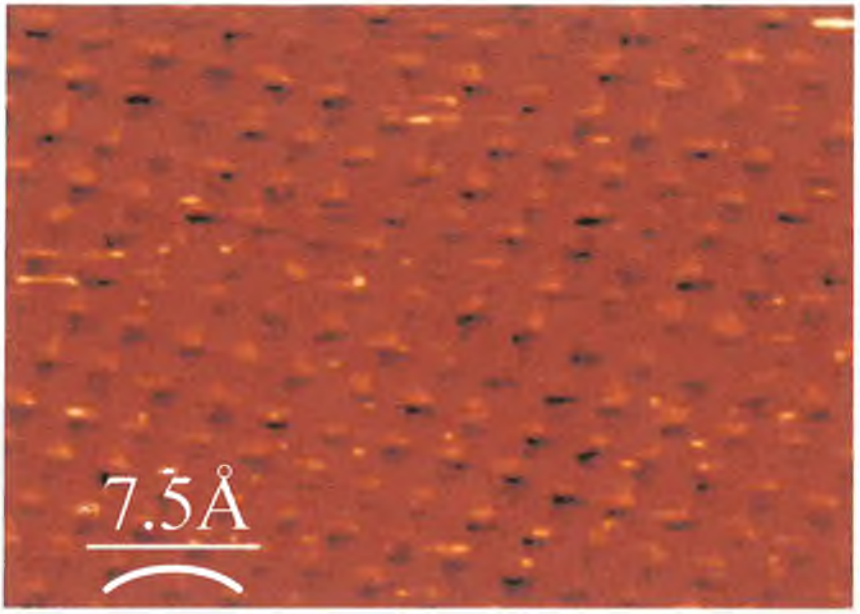

Figure 2.9(c) A high resolution image of the same clean Cu{100} surface in Figure 2.9(a), with a sample bias, $V_s = 0.005V$ and a tunnelling current $I_t = 5nA$.

2.3d Surface Alloy Formation

At a concentration of 0.2ML In deposited on the Cu{100} substrate, a weak p(1x1) LEED pattern is exhibited with very high background. This indicates that an ordered indium structure is not formed on the Cu{100} surface although the high background is thought to be caused by indium atoms disrupting the (1x1) periodicity of the substrate.

At low coverages of In on Cu{100} it is thought that a Cu{100}-p(1x1)-In surface alloy is formed as evidenced by previous studies by Nagl and Aufray on metals of a similar radius to In on a Cu{100} surface [19, 20]. The STM image taken at this concentration of deposited indium (Figure 2.10) is consistent with this theory, with indium atoms seemingly substituting into the uppermost copper layer. It is thought that these indium atoms cause the original copper atoms to be pushed out onto the surface, these atoms then rearrange to form islands, which can be clearly seen on the low resolution Cu{100}-p(1x1)-In surface. A selection of these islands were cross-sectioned, Figure 3.10(a), to reveal the average height of these islands to be ~1.8A, which is equivalent to the Cu{100} interlayer spacing value of 1.81Å [16]. This observation reinforces the hypothesis that each island is formed by ejected copper atoms.

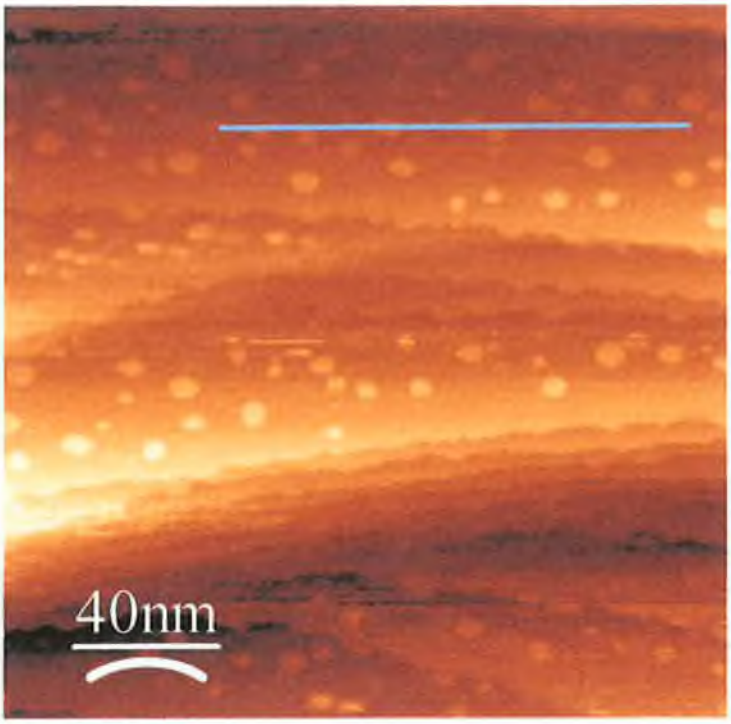

Figure 2.10 An STM image of ~0.2+/-0.05ML In coverage on Cu{100}, with a sample bias, V_s = +0.5V and a tunnelling current I_t = 0.2nA

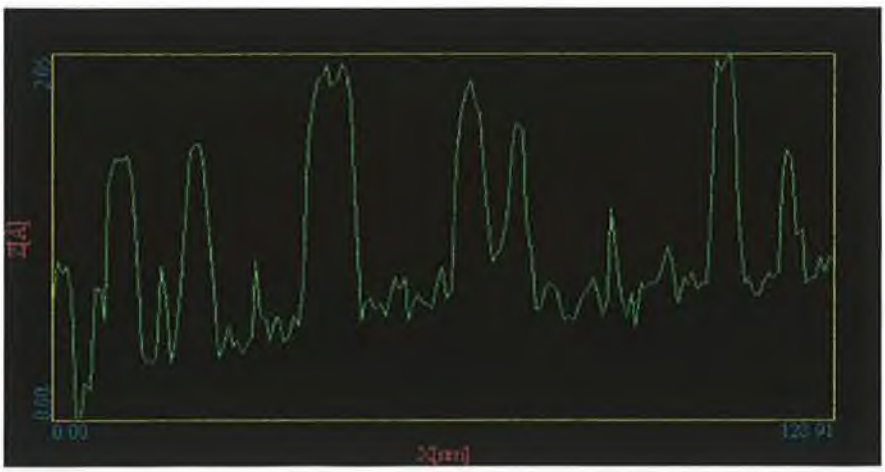

Figure 2.10(a) A line profile through a series of ejected copper islands.

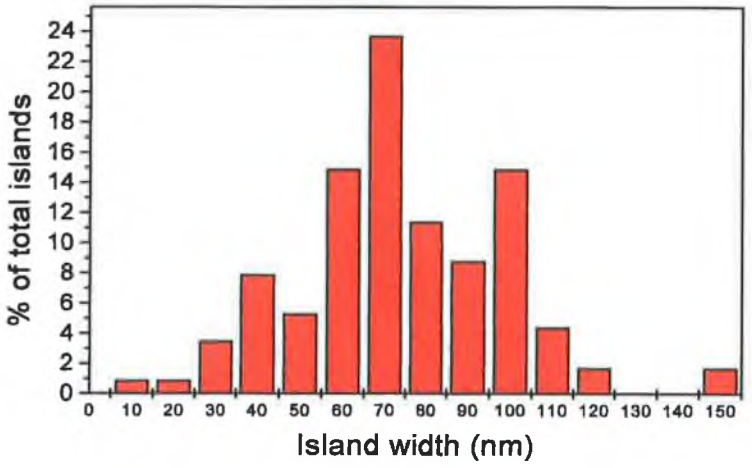

Figure 2.11 Features a bar chart of % total islands versus island width to give the average island width of ~70nm.

Figure 2.11 shows a bar chart of island width (nm) versus % of total islands. This implies that the average width of these islands is ~70nm, but there is a huge variation in sizes of these copper islands, ranging from 10nm to 150nm revealing that there is little uniformity in island width.

The location of each island shows very little consistency, as there are islands located at step edges, kinks and on terraces in equal measure with little or no preference.

2.3e *High In coverages: overlayer formation*

As mentioned previously, at 0.4+/-0.05ML In on Cu{100} forms a ($9\sqrt{2}$ x $2\sqrt{2}$)R45° LEED pattern. However in Figure 2.12, an STM image of the Cu{100}-($9\sqrt{2}$ x $2\sqrt{2}$)R45°-In LEED pattern reveals that the overlayer structure is more complex than the LEED image indicates. The STM data suggest the presence of two separate patterns. The first structure is as indicated by the LEED pattern, a ($9\sqrt{2}$ x $2\sqrt{2}$)R45° structure, with each unit cell separated by a trench measuring ~4.4A wide and with varying length, as can be seen in the line profile in Figure 2.12 (a). This would indicate that each trench is made up of two copper atoms side by side, as copper has a radius of 1.57A and a bond length in Cu-Cu of 2.55A.

However, along with the ($9\sqrt{2}$ x $2\sqrt{2}$)R45° overlayer structure there are a number of c(2x2) arrangements, (which Nakagawa et al. [4], believed to be in anti-phase relation to the ($9\sqrt{2}$ x $2\sqrt{2}$)R45° structure). These structures are more evident in the LEED analysis on heating above a temperature of 373K. As there was no heating option available on the STM chamber it was impossible to view an STM image of this structure higher temperatures.

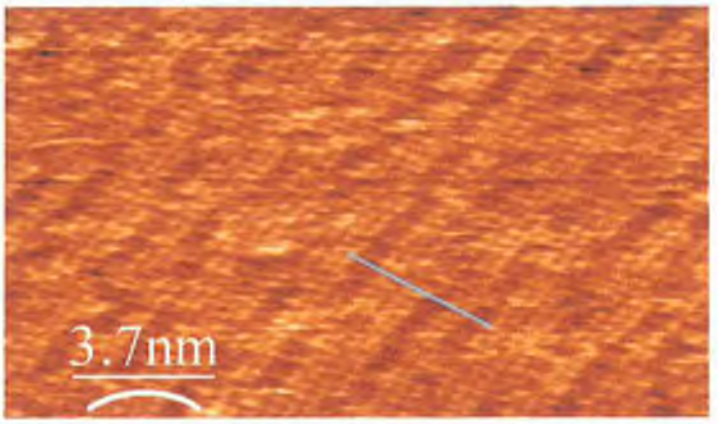

Figure 2.12 High resolution STM image of Cu{100}-(9√2 x 2√2)R45°-In surface, with a sample bias, V_s = -0.02V and a tunnelling current I_t = 2.0nA

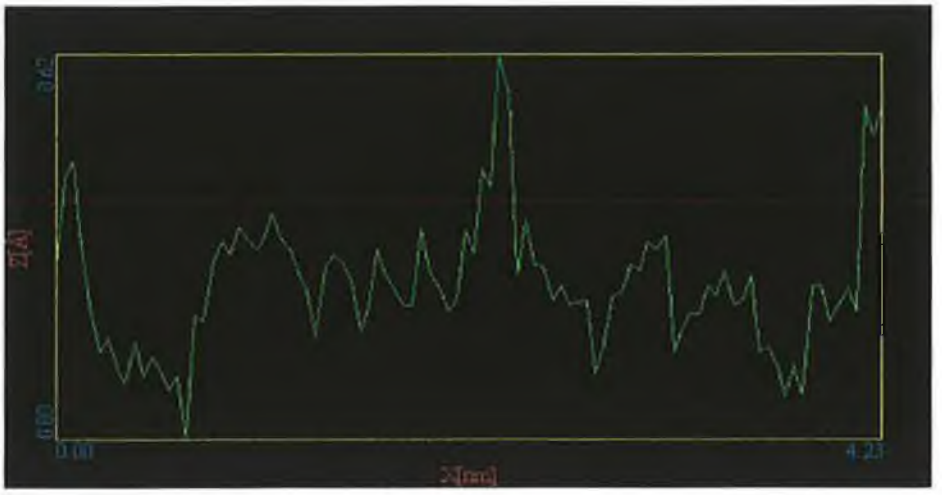

Figure 2.12(a) Line profile of (9√2 x 2√2)R45° overlayer.

Figure 2.13 shows an example of a possible structure for the Cu{100}-(9√2 x 2√2)R45°-In phase. Although there are a number of differences between the structures, the unit cell of this structure is uniform over the surface, but inside this unit cell there is a great deal of variation.

At 373K and above the Indium becomes more mobile and re-orders itself to form a strained c(2x2) structure, which is uniform across the Cu{100} substrate. Figure 2.14 features an example of a possible structure for the Cu{100}-c(2x2)-In phase. It is clear that, as with the Cu{100}-(9√2 x 2√2)R45°-In overlayer, there is some disorder inside the unit cell, to such an extent that the substrate atoms shift their position to accommodate the extra indium atoms rather than altering the unit cell shape.

From the results obtained it is impossible to determine whether the Cu{100}-(9√2 x 2√2)R45°-In structure is an overlayer or surface alloy.

Due to the complexity of the LEED pattern, a Tensor LEED study would prove too difficult, however one surface science method which would clear up any ambiguity is ion scattering spectroscopy (ISS). ISS operates by bombarding the surface with a beam of ions, a certain number of which will be elastically reflected. The intensity of the scattered ions as a function of angle of emission provides information regarding the surface crystallographic structure. The variation in the intensity of the scattered beam is partly due to shadowing of substrate atoms by adsorbed atoms. By use of scattering theory, knowledge of the sites that the surface atoms occupy can be derived.

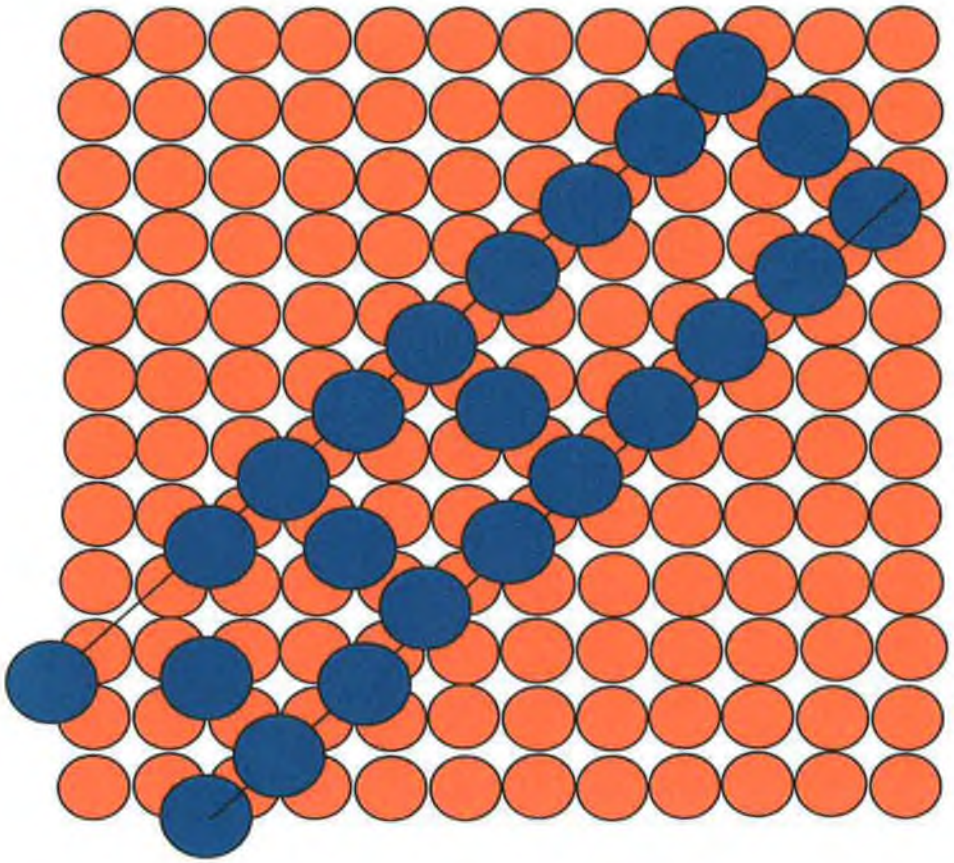

Figure 2.13 Possible structure for the Cu{100}-(9√2 x 2√2)R45°-In phase unit cell.

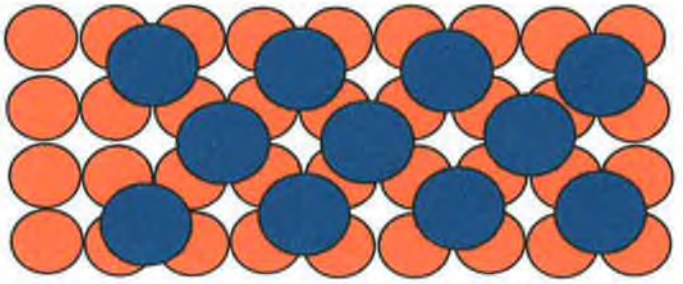

Figure 2.14 Possible structure for the Cu{100}-c(2x2)-In unit cell.

Figure 2.15 is a high resolution STM image of Indium on Cu{100} at a concentration of 0.6+/-0.05ML. At this coverage a Cu{100}-c(4x4)-In overlayer structure is formed. Though it is difficult to differentiate between a surface alloy and overlayer structure from the STM image. Figure 2.15 reveals that the Cu{100}-c(4x4)-In has long and short range ordering throughout the surface, as opposed to the Cu{100}-(9√2 x 2√2)R45°-In, which contains much disorder, particularly inside each unit cell. In Figure 2.15 (a) a line profile taken across four unit cells show that each unit cell is close in appearance to the adjacent unit cells.

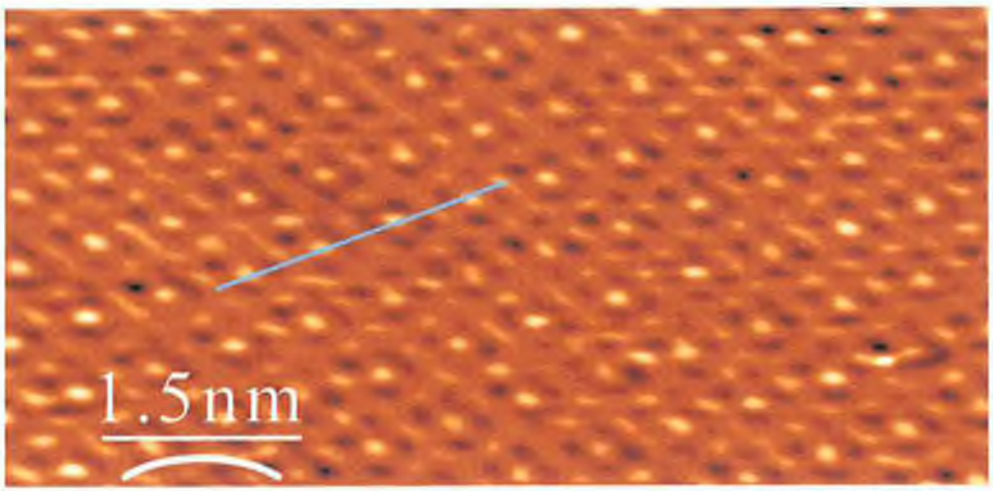

Figure 2.15 A high resolution STM image of the Cu{100}-c(4x4)-In phase, with a sample bias, V_s = -0.2V and a tunnelling current I_t = 4.0nA.

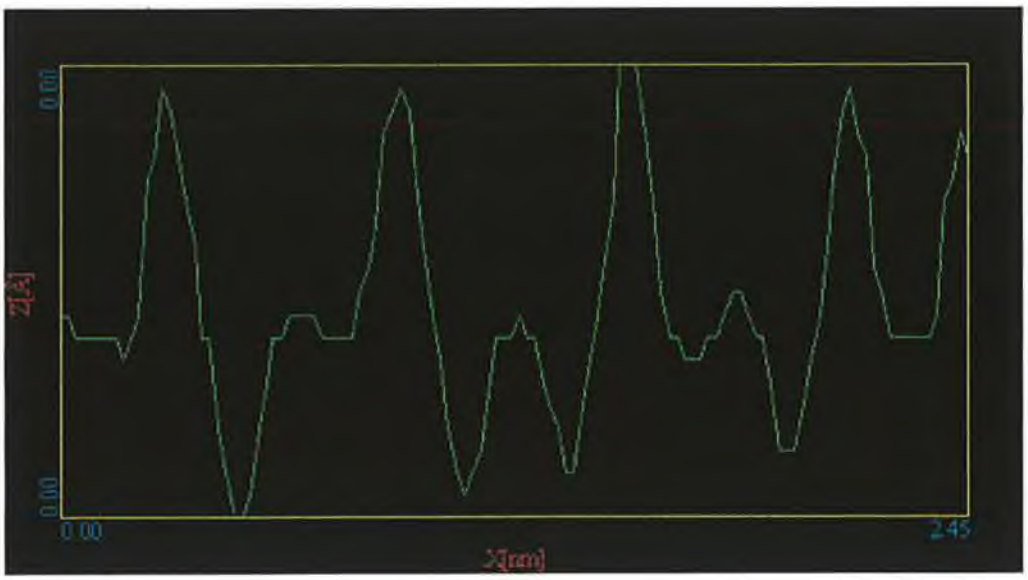

Figure 2.15(a) A line profile of the Cu{100}-c(4x4)-In phase.

Above the concentration of 0.65ML the 'complex' phase is formed, unfortunately it was impossible to image this phase on the STM as with so much excess indium on the surface, every scan resulted in a number of indium atoms sticking to the tip giving very poor images with little or no resolution. This phase continues to monolayer coverage. At a concentration of 0.65ML the 'complex' phase is well ordered according to the LEED results but as the concentration increases beyond this point the LEED image exhibits an increasingly higher background with the spots becoming progressively more diffuse.

2.4 Conclusion

According to the Auger electron spectroscopy results, the M_IVV is the transition used to monitor the amount of copper present in the top 10 surface layers of the sample while the concentration of deposited In is measured using the $L_IL_{II}V$ transition. Other transitions were also undergone by both elements but it was felt these transitions gave the most accurate results.

The Auger signal versus deposition time plot is characteristic of the Stranski-Krastanov growth mode for the deposition of indium on Cu{100}, where the first atomic layer grows in a layer by layer fashion, but when critical film thickness is reached (monolayer point), subsequent growth occurs in the form of 3-D crystallites. The key to the diagnosis of Stranski-Krastanov growth mode being the characteristic 'break points' at each monolayer coverage.

Increasing amounts of indium deposited on the Cu{100} surface gave rise to 4 different LEED patterns, indicating the presence of 4 different overlayer or alloy structures prior to monolayer point. These structures being a Cu{100}-$(9\sqrt{2}x2\sqrt{2})R45°$-In, Cu{100}-c(2x2)-In, Cu{100}-c(4x4)-In and a 'complex' phase.

The Cu{100}-$(9\sqrt{2}x2\sqrt{2})R45°$-In and Cu{100}-c(2x2)-In are both formed at a concentration of 0.4+/-0.05ML In, however at room temperature the LEED pattern reveals only the $(9\sqrt{2}x2\sqrt{2})R45°$ phase to be present. As this structure is heated above a temperature of 373K the $(9\sqrt{2}x2\sqrt{2})R45°$ phase undergoes a reproducible phase transition to form the c(2x2) phase, with the $(9\sqrt{2}x2\sqrt{2})R45°$ phase disappearing altogether from the LEED image. As the surface cools it reverts to solely the $(9\sqrt{2}x2\sqrt{2})R45°$ phase. According to Nakagawa et al. [4], both structures are present at room temperature with the $(9\sqrt{2}x2\sqrt{2})R45°$ phase being predominant and the c(2x2) structure lying in anti-phase relation, with the c(2x2) phase becoming predominant after heating the sample to a temperature of 373K. Unfortunately it is not clear if these phases are overlayers or surface alloys. ISS techniques would allow

determination of the type of ordered structures formed in each of the two phases. These techniques, however, were not available to me during the course of this study.

LEED I(V) curves were taken of the (1,0) and (1/2, 1/2) beams for the $(9\sqrt{2}x2\sqrt{2})R45°$, c(2x2) and c(4x4) structures. Although the I(V) spectra appeared similar, i.e. peaks and hollows at similar energies, the height of these peaks varied. This would suggest that although they share similar adsorption sites, there are slight differences in the amount of indium spread across these sites.

On analysis of the STM results it is suggested that at concentrations of 0.35ML and below the indium and copper form a Cu{100}-p(1x1)-In surface alloy, with the indium atoms substituting into the top layer of copper and pushing the excess copper atoms out onto the surface. These ejected copper atoms then group together to form islands on the surface.

At a concentration of 0.4+/-0.05ML In the STM results appear to reinforce Nakagawa et al.'s theory, with structures $(9\sqrt{2}x2\sqrt{2})R45°$ plainly visible on the surface, with small clusters of c(2x2) structures scattered amongst them. This structure would have been less ambiguous if it had been possible to image the HT phase, unfortunately though there is no heater on the STM chamber. Both the $(9\sqrt{2}x2\sqrt{2})R45°$ and c(2x2) are strained structures as at a coverage of 0.4ML each structure has more atoms than can be contained in the unit cell resulting in the Cu{100} substrate distorting to accommodate the extra atoms.

At 0.6+/-0.05ML In concentration a Cu{100}-c(4x4)-In overlayer is formed, with STM indicating more uniformity across the surface than in earlier phases.

A Tensor LEED study was conducted on this phase by K. Pussi et al. [21] in which they found that the In overlayer consisted of two layers. The In layer closest to bulk comprising a c(2x2) structure, with indium atoms occupying four fold hollow sites with respect to substrate. On top of this layer is a c(4x4)

In layer in which the atoms lie at four fold hollow with respect to the c(2x2) layer.

Above a concentration of 0.65ML it was impossible to image the 'complex' structure as it was found that there was too much mobile indium. Thus 'clumps' of indium attached themselves to the tip making a clean tip impossible to achieve.

2.5 References

1. Nese, Orbey, Jones, Glover A., Birkmire, Robert W., Fraser Russell, T.W., Journal of Phase Equilibria 21(6)(2000)509.
2. Breeman, M., Boerma, D.O., Phys. Rev. B 46(3)(1992)1703.
3. van der Vegt, H.A., Breeman, M., Ferrer, S., Phys. Rev. B 51(1995)14806.
4. Nakagawa, T., Boishin, G.I., Fujioka, H., et al. Phys. Rev. Lett. 86(5)(2001)854.
5. http://hyperphysics.phy-astr.gsu.edu/hbase/solids/fermi.html.
6. Van Gastel, R., Somfai, E., van Albada, S.B., van Sarloos, W., Frenken, J. W. M., Phys. Rev. Lett. 86(2001)1562.
7. Subramanian, P.R., Laughlin D.E., Bulletin of Alloy Phase Diagrams 10(1989) 554.
8. Albin, D.S., Moonet, G.D., Carapella, J., Duda, A., Noufi, R., Solar Cells 30(1990)41.
9. Bolcovage, A., Chen, S.W., Kao, C.R., Chang, Y.A., Romig, A.D., Journal of Phase Equilibria, 14(1993)14.
10. Chen, J.S., Kolowa, E., Nicolet, M.-A., Solar Cells 30(1991)451.
11. Orbey, N., Hichri, H., Birkmore, R.W., Russell, T.W.F., Progress in Photovoltaics 5(1997)237.
12. Contreras, M.A., Egaas, B., Ramanathan, K., Hiltner, J.Ul., Swartzlander, A. Hasoon, F. Noufi, R., Prog. in Photovoltaics Jul-Aug (1999).
13. Dzionk, C., Metzner, H., Hessler, S., Mahnke, H.-E., Thin Solid Films 299 (1997) 38-44.
14. Jona, F., Surf.Sci. 192(1987)398.
15. Vickerman. John C., 1997, Surface Analysis – The Principal Techniques.
16. Attard, G., Barnes, C.J., "Surfaces", Oxford university Press Inc., New York, 1998.
17. Seah, M.P., Dench, W.A., Surf. Interface Anal.1(1979)10.

18. DiNardo, N. John, "Characterization of Surfaces and Interfaces", Wiley, Canada, 1994.
19. Nagl, C., Surf. Sci. 321(1994)237-248.
20. Aufray, B., Surf. Sci. 442(1999)55-64.
21. Pussi, K., Lindroos, M., McEvoy, T., Barnes, C.J., AlShamaileh, E., Surf. Sci. 526(2003)141-148.
22. Prutton, M., "Surface Physics", Oxford University Press, Oxford, 1985.
23. Clarke, L.J., "Surface Crystallography", Wiley, New York, 1985.
24. Van Hove, M.A., Weinberg, W.H., Chan, C.-M., "Low Energy Electron Diffraction", Springer, Berlin, 1986.
25. Al Shamaileh, E., Ph.D in Surface Science, Dublin City University, Dublin, 2002.

Chapter 3

Vapour Deposition of Sb on a Cu{100} Substrate

3.1 Introduction

Although Antimony has been shown to have a surfactant effect on epitaxial growth of both thin semiconductor and metal films [1-4], giving it a strong tendency for surface segregation, very little research has been done on its interaction with Cu in comparison to elements of similar atomic radii. Pd, Sn and In have all received a lot more attention in recent years, with each being the subject of Scanning Tunnelling Microscopy (STM), Low Energy Electron Diffraction (LEED) and Auger Electron Spectroscopy (AES) structural studies[5-15]. In each case at low concentrations despite a large atomic radii mismatch (~15%), a surface alloy is formed. With increasing concentration of deposited metal, a number of overlayer structures are formed on the copper substrate. Indium forms a $(9\sqrt{2}x2\sqrt{2})R45°$, a c(4x4) and a 'complex' phase on a Cu{100} surface, as the concentration of deposited indium is increased to monolayer point [14]. Tin forms a p(2x6) and a $p(3\sqrt{2}x\sqrt{2})R45°$ phase on Cu{100} as the deposited tin concentration is increased [8]. This would indicate that Sb would be expected to firstly form a surface alloy with Cu{100}at low concentrations and an overlayer structure as the concentration approaches monolayer point. However, it was also discovered that Pd forms surface alloys with Cu from a concentration of 0.1ML (monolayer) to 6ML [15], which leaves the expected results for Sb on Cu{100} difficult to predict.

Similar results were obtained for a recent study by Aufray et al [16], who found that at low concentrations of Sb, a surface alloy was formed on Cu(111). Aufray et al. found that at a concentration of 0.45ML, Sb forms a $p(\sqrt{3} \times \sqrt{3})\ R30°$ surface alloy on a Cu(111) substrate. The symmetry of the STM images taken clearly demonstrates that surface segregation leads to Sb atoms occupying substitutionally rather than as adatoms, which was found to be a consistent fit with previously obtained experimental kinetics and theoretical simulations employing the kinetic tight-binding Ising model [17, 18]. The $p(\sqrt{3} \times \sqrt{3})R30°$ surface alloy of Sb and Cu(111) results confirm previous results by Giordano et al [18] and Göthelid et al [19] who studied the same system using SXRD and XPS respectively. The STM images taken by Aufray et al. clearly show that the Sb segregation induces a modification of at least the topmost Cu layer causing a

symmetry breaking of the (111) surface. This broken symmetry was not detected by LEED, since the LEED pattern represents an average of the contributions of all domains existing on a surface. According to Aufray et al., this symmetry breaking could be due to temperature effects, a difference in atomic radii between Sb and Cu or possibly electronic effects from STM rather than actual atomic rearrangements.

This study attempts to determine the surface structures formed by Sb on the Cu{100} substrate at both lower coverages of Sb up to a concentration of 0.45ML. The surface techniques used during the course of this study were LEED and STM in conjunction with Symmetrised Automated Tensor LEED (SATLEED) calculations. The SATLEED calculations were conducted in conjunction with our colleagues K. Pussi and M. Lindroos at the Institute of Physics in Tampere University of Technology, Finland.

The LEED results were used to determine the long range ordering of the surface structures formed by the deposition of Sb on the Cu{100} substrate. LEED I(V)'s were taken from the Cu{100}-p(2x2)-Sb structure to allow SATLEED analysis of the structure. The SATLEED calculations were used to determine the short range order of the Cu{100}-p(2x2)-Sb structure and allowed us differentiate between a surface alloy and overlayer structure. The STM results provided some information on the short range order and topographic information on each structure formed along with confirming the LEED results. A combination of the three techniques provided detailed information on each of the surface structures formed.

3.2 Experimental

All experiments were performed in an ion and titanium sublimation pumped ultra-high-vacuum chamber of base pressure $1x10^{-10}$ Torr. The chamber was equipped with Low energy electron diffraction (LEED), Auger electron spectroscopy (AES) and Mass Spectrometry facilities. The Cu{100} sample was heated by the resistive heating and monitored by a chromel-alumel thermocouple. The sample was cleaned *in situ* by repeated cycles of argon ion bombardment and annealing. The clean Cu{100} sample exhibited a sharp well contrasted p(1x1) LEED pattern with normal incidence I(V) spectra from the (1,0) beam in excellent agreement with previous literature reports [20].

The Cu sample (Metal Crystals and Oxides Ltd., UK) used had dimensions of 15x12x1.5mm and was mechanically and electronically polished to expose a {100} face within 0.5°.

The LEED images were recorded at room temperature (RT) from well ordered Cu{100}-p(2x2)-Sb and Cu{100}-p(6x6)-Sb under conditions of normal incidence using a CCD video camera and collecting data by automatic spot tracking. All LEED results were analysed using the Spectaview video LEED package.

Another attached chamber to the previously mentioned one has a Scanning tunnelling microscope (STM)(Omicron, UK) attached, with the sample being transferred under vacuum between chambers. The STM was used in constant current mode with tips made from electronically etched polycrystalline tungsten. The clean Cu{100} surface was checked using STM before deposition.

Antimony was deposited onto the Cu substrate from a homemade Knudsen cell evaporator at room temperature (RT). The Sb evaporation was performed in a preparation chamber isolated from the STM chamber. The Sb evaporator was degassed at close to evaporation temperature for 10 minutes prior to each evaporation in order to ensure a constant deposition rate. The rate of evaporation

was estimated to be approximately 0.035ML/min. However, the calculations for the amount of deposited antimony come from a previous calibration of the antimony source. Since that calibration, the source was baked to ensure cleanliness, thus, some of the concentration values for the deposited antimony may contain slight error.

3.3 Results and Discussion

Cu{100}-p2x2-Sb surface alloy

3.3a LEED results

According to a study by Aufray et al. on Sb on Cu(111), a p($\sqrt{3}$x$\sqrt{3}$) R30° surface alloy at a concentration of 0.45ML Sb on Cu. To find this level of coverage for Sb on Cu(100), increasing amounts of Sb were deposited on the clean Cu surface until the p(1x1) LEED pattern changes. At deposition times of 2, 3, 5, 6 and 7 minutes, the LEED pattern was checked to see if there were any changes to the Cu surface. As the concentration of Sb increases, the clean p(1x1) pattern changes, firstly to exhibit high background at 2 and 3 minutes, indication of weak diffuse (1/2, 0) spots at 5 minutes, weak diffuse (1,1/2) spots at 6 minutes, until at a deposition time of 7 minutes a good p(2x2) LEED pattern is formed. This is thought to be a coverage of 0.245ML Sb. This is calculated from a previous calibration of the Sb source, however, prior to this study the source was baked to ensure cleanliness, so there may be slight errors in the actual amount of deposited antimony.

This p(2x2) LEED pattern can be seen in Figure 3.1 at different energies. The p(2x2) LEED pattern is characterised by the presence of fractional order spots in the (1/2,0), (1/2,1/2), (1,1/2) and (3/2,0) positions which are not present in the clean Cu LEED pattern. The clean Cu surface forms a p(1x1) pattern with only integral spots present. The extra spots in the p(2x2) LEED pattern are due to the larger unit cell, as distances which are larger in real space become smaller in reciprocal space i.e., the LEED pattern, so a larger unit cell will produce more spots with less distance between them than the p(1x1) pattern.

This structure was evident over the whole surface of the sample indicating that this was the exact coverage to form the p(2x2) Sb structure on Cu (100). All LEED measurements were taken at room temperature.

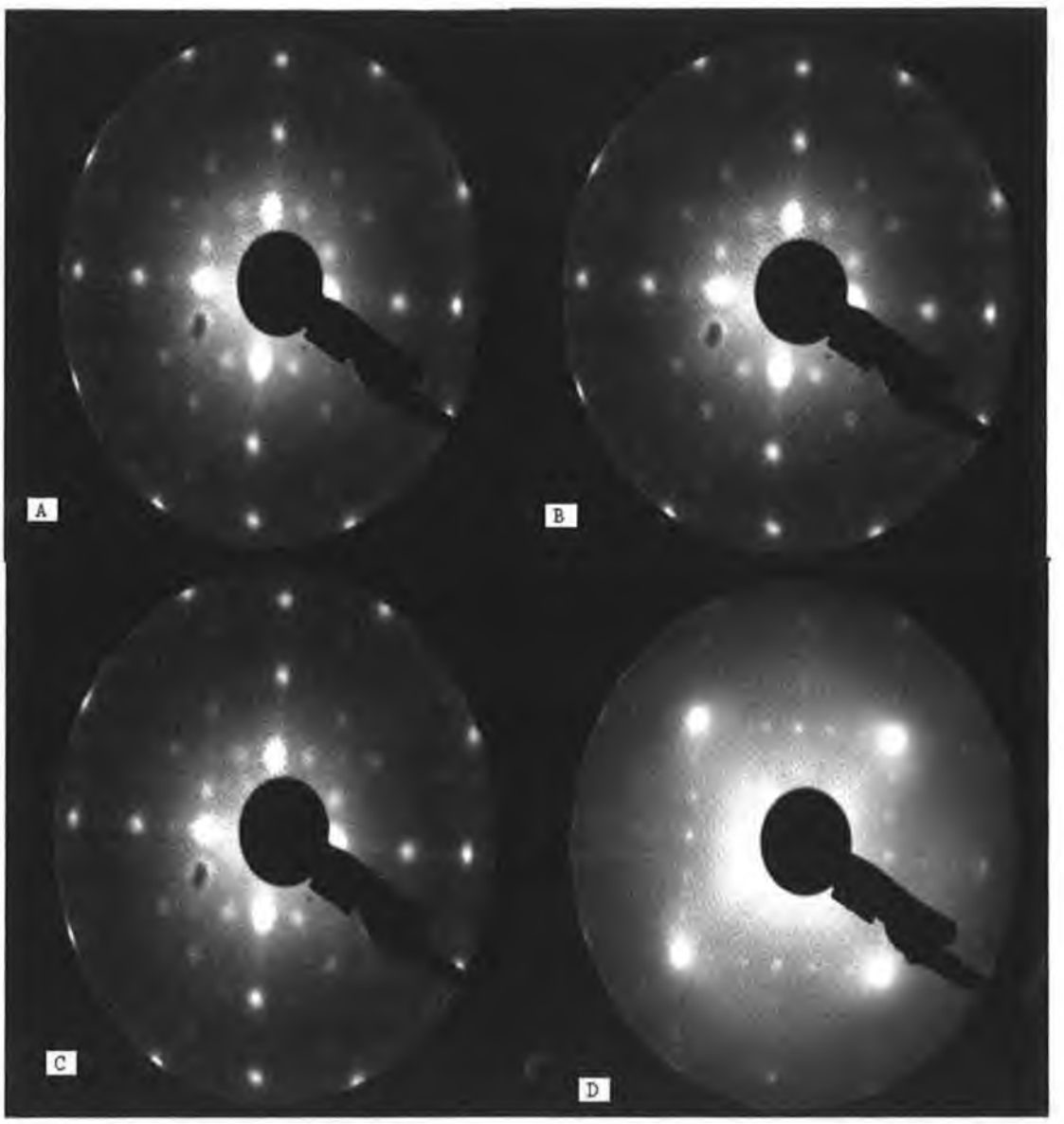

Figure 3.1 LEED images of Cu{100}-p2x2-Sb structure, at a coverage of 0.25ML, taken at energies of (A) 60eV, (B) 90eV, (C) 120eV and (D) 198eV.

Normal incidence was attained by variation of the sample alignment until the four (1,0) beams had identical spectral structure and highly similar relative intensities over the energy range 50 – 350eV, this ensures any change in beam energy is due to changes on the sample surface rather than misalignment problems.

The Cu{100}-p(2x2)-Sb structure provided a simple LEED pattern, making it possible to conduct a SATLEED analysis. The SATLEED calculations rely on the LEED I(V) results of the Cu{100}-p(2x2)-Sb LEED pattern to determine the exact positions of each atom involved the unit cell. The LEED I(V)s were taken for all integral order spots, namely (1,0), (1,1), (2,0), (2,1) and (2,2) and the most important fractional order beams, (1/2,0), (1/2,1/2), (1,1/2) and (3/2,0). Symmetry equivalent beams were co-added to reduce the effects of residual sample misalignment. Prior to symmetry addition, each beam was individually background subtracted by fitting an exponential background for chosen minima in the I(V) curves. The data was then normalised to constant incoming beam current. The total energy range in this analysis was 1540eV out of which 400eV was from fractional order beams.

The theoretical LEED calculations were performed using the Symmetrised Automated Tensor LEED program (SATLEED) [21]. Up to 12 phase shifts were used to describe the scattering properties for copper and antimony and were calculated using the Barbieri/Van Hove Phase Shift Package [22]. In the initial stages of the analysis the structural parameters including the interlayer spacings and the bucklings in the five outermost surface layers were allowed to vary. Non-structural parameters were kept fixed including the imaginary part of the inner potential (V1), which was set to –5eV, the Debye temperatures for bulk Cu: θ_D (Cu_{bulk}), for surface Cu: θ_D – ($Cu_{surface}$) and for Sb: θ_D (Sb), which were set to 343K, 343K and 211K, respectively. The energy independent real part of the inner potential was allowed to vary via a rigid shift in the LEED calculations with theory-experiment agreement being tested with the Pendry R-factor [23]. Error bars were calculated based on the variance of the Pendry R-factor using the standard prescription [23]. The observed LEED pattern possessed the high

symmetry of four mirror planes (p4mm). For the trial structures that have lower symmetry than p4mm, proper domain averaging has been taken into account.

The analysis started with the calculation of LEED I(V)s for four different models: three overlayer structures where Sb atoms occupy (I) four-fold hollow sites (Figure 3.2 (a)), (II) atop sites (Figure 3.2 (b)), (III) bridge sites (Figure 3.2 (c)) and the fourth model is a surface alloy, where Sb substitutes 25% of the top layer of Cu atoms (Figure 3.2 (d)).

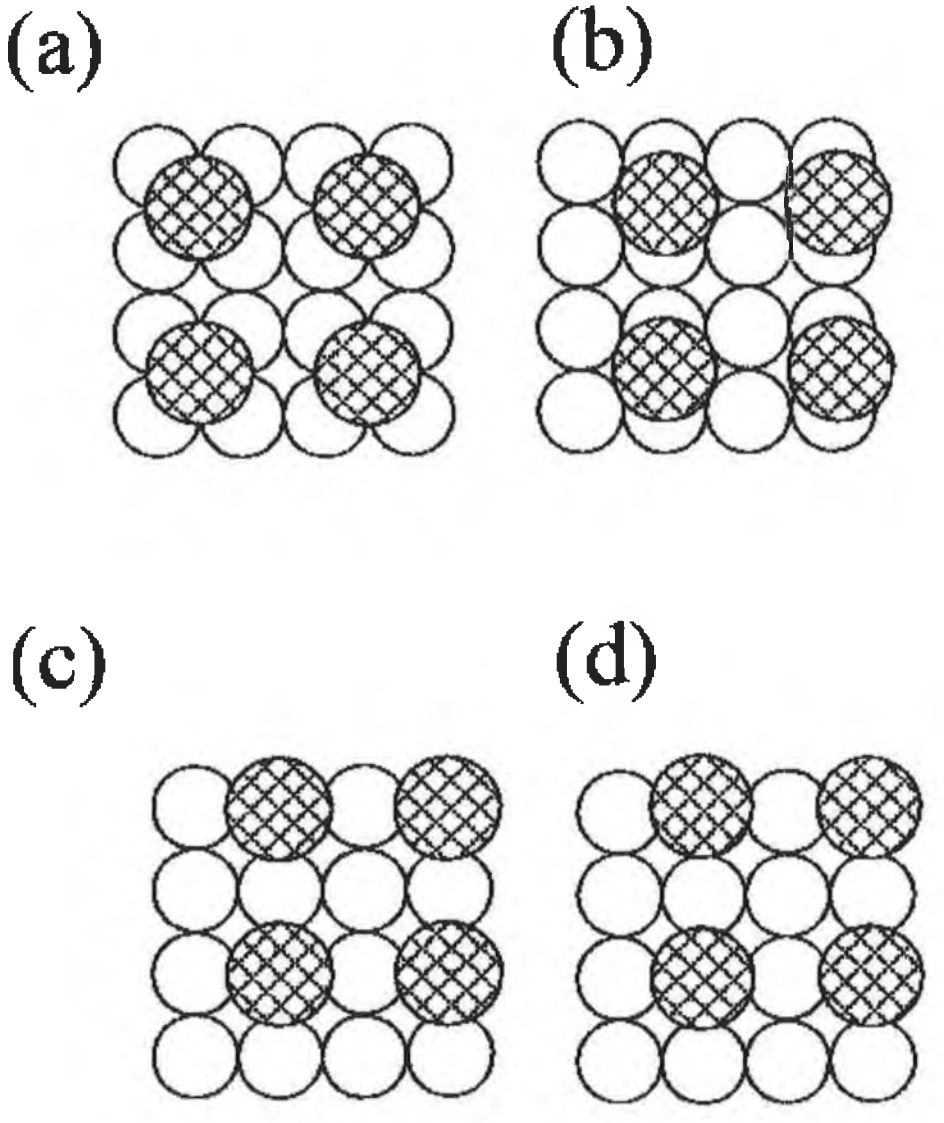

Figure 3.2 Schematic diagram of four models for Cu{100}-p(2x2)-Sb structure including: (a) four-fold hollow overlayer; (b) bridge overlayer; (c) atop overlayer and (d) four-fold substitutional surface alloy. Cross hatched circles represent Sb atoms.

Table 3.1 shows the results of the screening (preliminary) stage of the analysis, where only the first interlayer spacing was allowed to vary. For the overlayer models, the Sb-Cu bond length was allowed to have values of r(Cu)+r(Sb)+/- 20% (Cu and Sb radii were calculated from bulk Cu and Sb, respectively). For the alloy model, the Cu-Sb bond length was allowed to have values in the range r(Cu)+r(Cu) to r(Cu)+r(Sb). The calculations were done in steps of 0.05 Å followed by steps of 0.01 Å for the optimum model.

From Table 3.1 and according to the Pendry RR-method [23], all overlayer models can be excluded and therefore only the p(2x2) surface alloy was considered for further analysis. The optimum geometry was found by optimising the top 5 interlayer spacings and non-structural parameters, these results are outlined in Table 3.2. A comparison between experimental and theoretical LEED I(V)s for the best optimised and final surface alloy model is illustrated in Figure 3.3.

Adsorption site	Range of dz_{Sb-Cu} Å	Optimum dz_{Sb-Cu} Å	R_p
Atop	2.15-3.30	3.19	0.54
Bridge	1.60-2.40	2.26	0.53
Four-fold hollow (overlayer)	1.90-2.85	2.55	0.51
Four-fold substitutional (surface alloy)	**0.00-1.00**	**0.51**	**0.39**

Table 3.1 Minimum Pendry R-factors for the models tested in the initial screening stage of the analysis

Structural		Non-structural	
Parameter	Value(Å)	Parameter	Value
d(Cu-Sb)	2.61±0.05	V_I	-5eV
Δ_{Sb-Cu}	0.56±0.05	$\theta_D(Cu_{bulk})$	343K
dz_{12}	1.84±0.05	$\theta D(Cu_{surface})$	260K
dz_{23}	1.80±0.05	θD(Sb)	200K
dz_{34}	1.79±0.05		
dz_{45}	1.83±0.05		
dz_{56}	1.78±0.05		
Δ_1	0.05±0.06		
Δ_3	0.02±0.06		
Δ_5	0.05±0.10		

Table 3.2 Best fit parameters for the final structure of Cu{100}-p(2x2)-Sb four-fold hollow surface alloy.

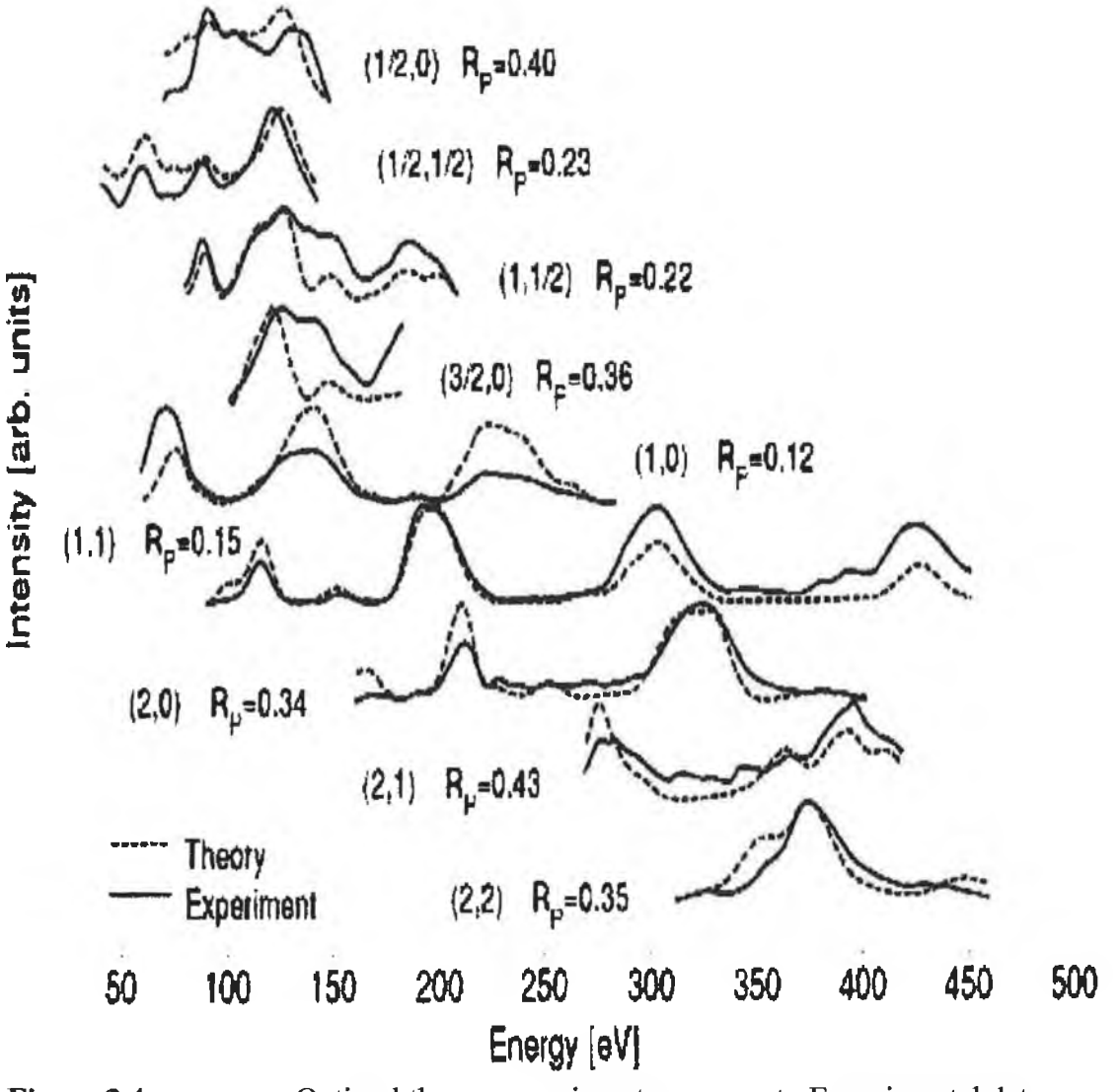

Figure 3.4 Optimal theory-experiment agreement. Experimental data is shown as full lines and theory as dotted lines.

The total Pendry R-factor is 0.26. This comparison produced the best model in terms of structural and non-structural parameters. The final values for the structural and non-structural parameters are summarised in Table 3.2. The optimum structure of the surface alloy Cu{100}-p(2x2)-Sb obtained from this study is shown in Figure 3.4. In spite of the fact that only one model stands out as the best fit structure, we notice that the level of agreement between theory and experiment is moderate (R_p= 0.26). This result might indicate the presence of structural imperfections in the surface alloy formation process.

The best fit structure has a relatively corrugated CuSb surface alloy with Sb atoms being at 0.56 Å above the centre of mass of surface Cu atoms. Despite the alloying of Sb with the outermost Cu atoms, the addition of Sb atoms on the Cu{100} substrate has not produced a significant perturbation in the deeper Cu layers. The maximum determined buckling was less than 3% (0.05 Å) relative to the Cu bulk interlayer spacing (1.81 Å). Another observation is that the Cu outermost interlayer spacing is significantly expanded (less than 2%).

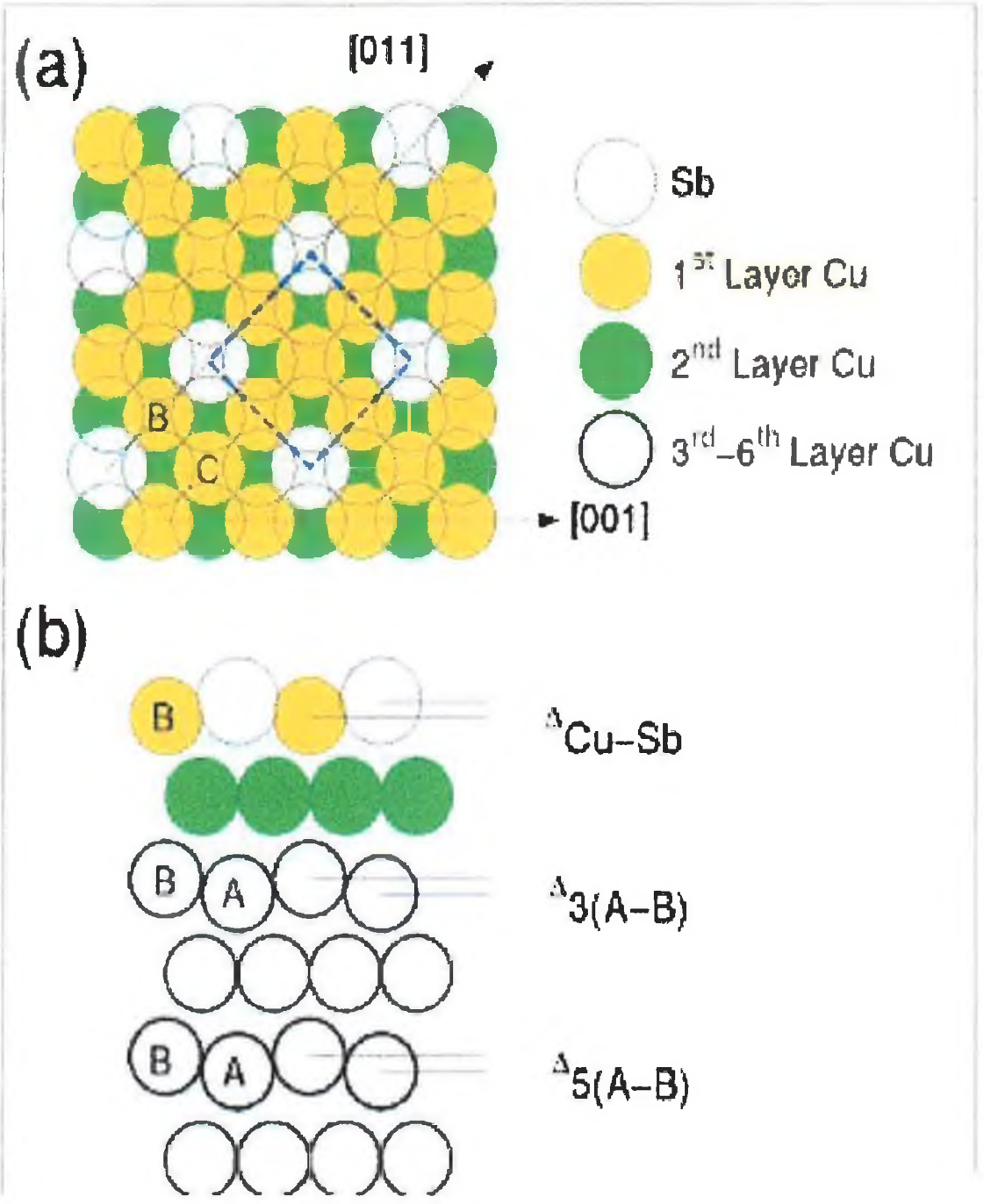

Figure 3.4 Model of the favoured geometry for the Cu{100}-p(2x2)-Sb surface alloy: (a) top view (outermost two layers only shown); (b) side view along the [011] azimuth defining the major geometric parameters varied within the analysis (the bucklings in layers 3 and 5 is over-emphasised for clarity as is the z-spacing between adjacent layers).

3.3b STM results

Although the LEED pattern and subsequent SATLEED calculations have determined the structure of Sb on Cu (100) at a coverage of 0.25ML to be a p(2x2) surface alloy, it is important that the STM results are in agreement with these results, as the LEED technique represents an average of the contributions of all domains on a surface, so there could be small areas of disorder or remote domains of different phases on the surface which could be missed. An STM study would remove any ambiguity from the LEED results.

Figure 3.5 is an STM image of the Cu{100}/Sb surface recorded at room temperature. Figure 3.5(a) displays a $14nm^2$ area of the Cu{100} surface, recorded at a sample bias of –0.075mV and a tunnelling current of 1nA. Figure 3.5(b) and (c) show line profiles taken across the (100) and (010) directions respectively. Figure 3.5(d) is a zoomed image of Figure 3.5(a) with a lattice of vectors v_1= 0.59nm and v_2= 0.556nm fitted to it to show the considered unit cell, which in agreement with the LEED and SATLEED results, is a p(2x2) structure.

Although it is impossible to tell the type of structure formed using STM, the STM results suggest that at this coverage Sb forms a p(2x2) structure, particularly when the lattice has been fitted. The figures for the vectors of the lattice represent the sum of the atomic diameters of one Sb and one Cu atom (3.18Å(Sb) and 2.556Å(Cu) giving a value of (5.7736Å), with slight discrepancies taken into account for drift.

Both profiles indicate that the p(2x2) surface alloy is a well-ordered uniform structure with little or no disorder between unit cells. This is witnessed by sharp peaks and troughs in the line profiles. The peaks are representative of atoms, while the troughs are indicative of atomic spacings, the height of each peak is approximately 15Å with the troughs approximately 3Å apart. This corresponds well with values of 1.45Å and 2.9Å for the atomic radius and Sb-Sb interatomic spacing respectively.

There are slight problems with the STM image of the p(2x2) surface alloy for antimony on Cu{100}. If the structure is indeed p(2x2), it would be expected that the rows which are evident in the vertical direction would also be present in the horizontal direction about the p(2x2) unit cell. The presence of these troughs in only one direction are indication that the unit cell may be a mixed domain of two sets of p(2x1) unit cells. This theorem was not tested in the SATLEED analysis, which would also explain the high Pendry R-factors found for the p(2x2) surface alloy.

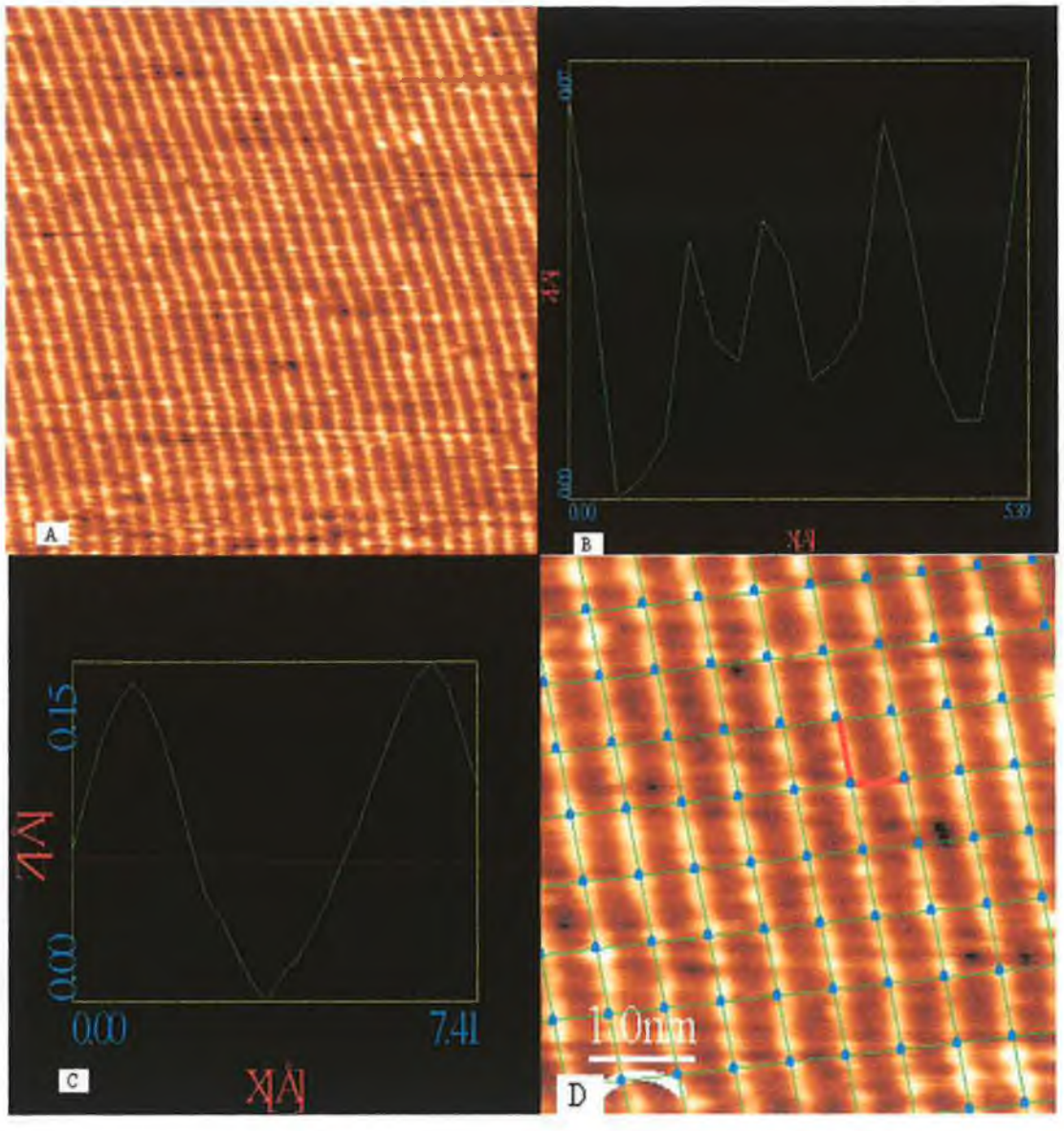

Figure 3.5 (a) STM image (14nm x 14nm; V_s = -0.075V; I_t = 1.0nA) showing chains of p(2x2) Sb on the Cu{100} surface at a coverage of = 0.25ML (b) horizontal cross-section profile along the line AC (c) Vertical cross-section profile along the line AB (d) Zoomed STM image of (a) (4.9nm x 2.45nm) with a p2x2 lattice fitted to it, V_1 =0.59nm, V_2 = 0.556nm.

p(6x6) Sb structure on Cu(100)

3.3c LEED results

The Sb coverage needed to the produce the Cu{100}-p(2x2)-Sb surface alloy (0.25ML) is increased by 2 minutes in 1-minute increments, to give firstly a weak mixed complex followed after the second minute by a good p(6x6) LEED pattern. This coverage was calculated to be 0.32ML, as depositing for 7 minutes gave a coverage of 0.25ML, thus, depositing at the same flux with the same sample alignment for a further 2 minutes gives a coverage of 0.32ML Sb.

This p(6x6) LEED pattern can be seen in Figure 3.6 at different energies. The p(6x6) LEED pattern is characterised by 5 spots between the (0,0) spot and each of the integral beams, namely the four (1,0) and (1,1) beams, giving a 'grid' of 36 spots in each direction. The small distance between each spot as compared with the p(2x2) LEED pattern is due to the larger unit cell of the p(6x6) structure, as discussed previously, the larger the distance between atoms in real space, the smaller the distance between their corresponding spots in the LEED pattern. This p(6x6) structure can be seen over the whole surface of the sample confirming that this coverage of Sb forms a good p(6x6) structure.

Unfortunately, due to the complexity and number of spots contained in the LEED pattern it proved too difficult to acquire a reasonable set of LEED I(V) data, so a SATLEED study was impossible.

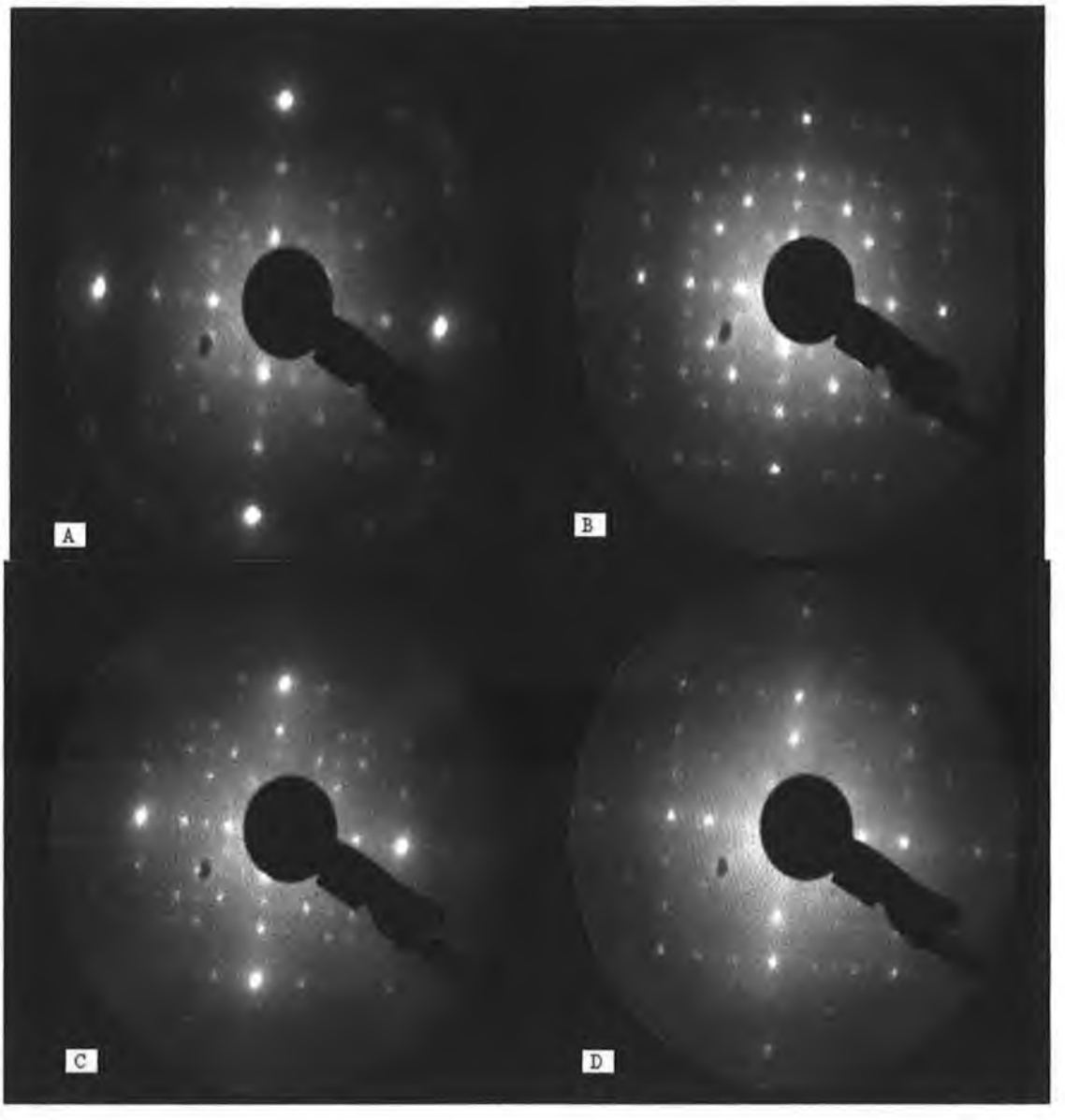

Figure 3.7 LEED image of p(6x6) Sb-Cu surface alloy, with a coverage of θ = 0.33ML, taken at energies of (A) 70eV, (B) 90eV, (C) 127eV and (D) 153eV.

3.3d STM results

An STM study of the Cu{100}-p(6x6)-Sb system is conducted in conjunction with the LEED study to determine the exact arrangement of the Sb atoms on the Cu(100) surface. This determines whether the unit cell of Sb at a concentration of 0.32ML is indeed p(6x6) in accordance with the LEED results or if the LEED pattern is the result of a number of domains of Sb on the sample surface.

Figure 3.7 shows an STM image of the Cu{100}/Sb surface recorded at room temperature. Figure 3.7(a) displays a 7.5nm^2 area of the Cu{100} surface, recorded at a sample bias of –0.01mV and a tunnelling current of 2nA. A lattice of vectors v_1=1.53nm and v_2=1.56nm has been fitted to this image to show the considered unit cell, which in agreement with the LEED pattern, is a p(6x6) structure as the distance of 6 Cu atoms laid side by side is 1.534nm It would be expected that the unit cell for a p(6x6) unit cell would be square rather than oblique but this is thought to be the result of drift during the capture of the STM image. Figure 3.8(b) and (c) show line profiles taken across the (100) and (010) directions respectively, these images show the peaks for the respective atoms to be clean and crisp indicating that the Cu{100}-p(6x6)-Sb structure is uniform and well-formed.

The apparent height of the step edges is measured to be 0.178 +/- 0.015nm. This is in good agreement with the value of 0.180nm expected for bulk copper and is consistent with a slight relaxation of the topmost layer. Care must be taken when assigning the bright features in the STM images to atoms as they only reflect variations in the electronic charge density, but for metals it is generally accepted that the maxima observed in an image correspond effectively to the lateral positions of the atoms [24]. If these conditions are accepted, then the p(6x6) arrangement of the Sb atoms can be readily seen in these images.

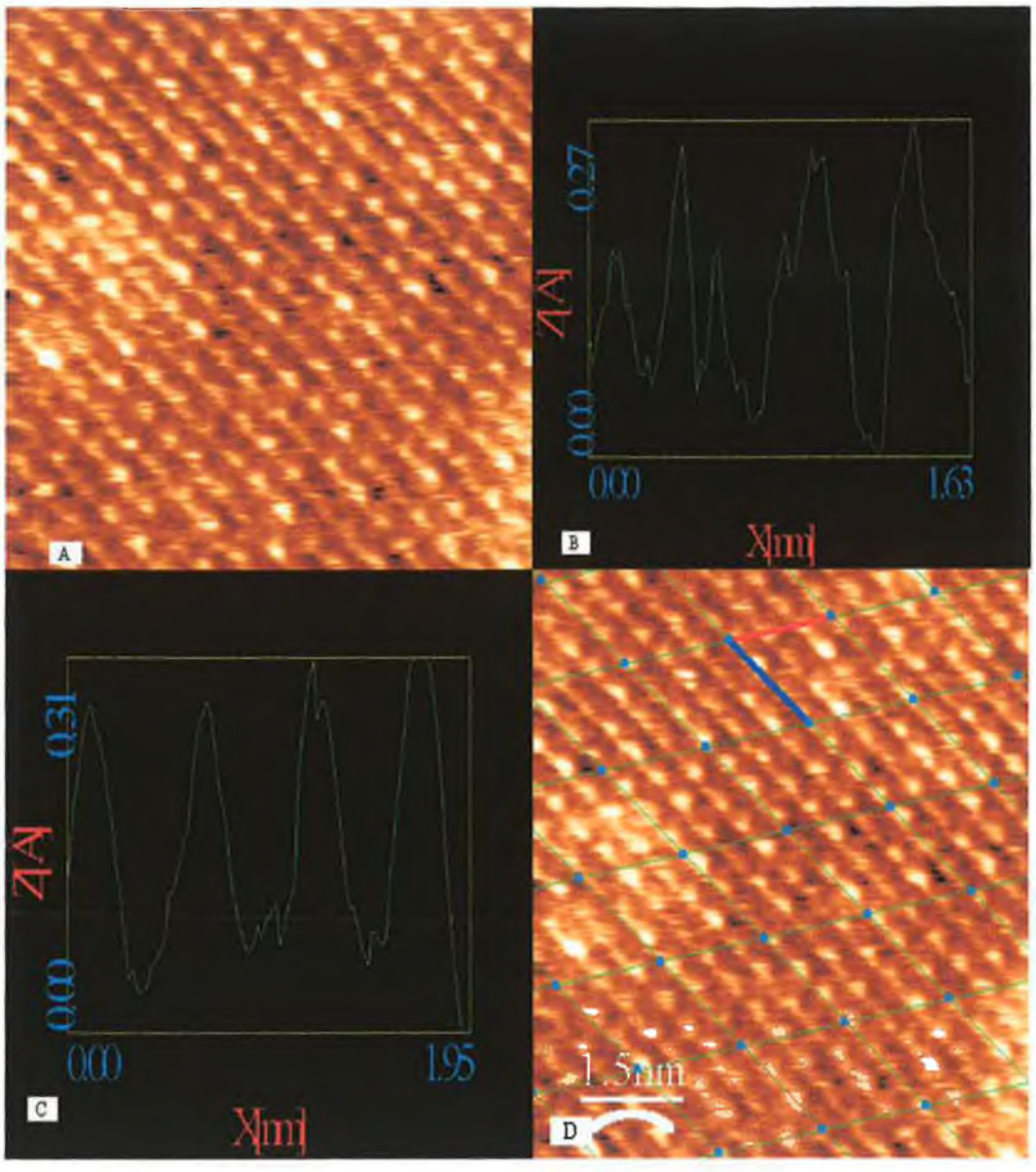

Figure 3.7 (a) STM image (7.5nm x 7.5nm; Vs = -0.01V; It = 2.0nA) showing clusters of p(6x6) Sb on Cu{100} at a coverage of = 0.3ML (b) Horizontal cross-section profile along the line AC (c) Vertical cross-section profile along the line AB (d) p(6x6) lattice fit on image (a) V1 = 1.53nm, V2 = 1.56nm.

The atomic resolution STM images for the Cu{100}-p(6x6)-Sb surface display both double and single rows of atoms which implies that the deposited Sb causes a reconstruction in the selvedge as the topmost surface layers of the Cu{100} substrate have been modified from their original single row structure.

The STM and LEED studies will only give information on the shape and structure of the unit cell for Sb on the Cu{100} sample, which makes it impossible to determine if the Cu{100}-p(6x6)-Sb is an overlayer structure or surface alloy. Based on the available data, Figure 3.9 shows possible models for the Cu{100}-p(6x6)-Sb structure. The favoured structures are based on a slight deformation from the simple p(2x2) surface. Figures 3.8 (A) and (B) illustrate a Cu{100}-p(6x6)-Sb overlayer structure and a Cu{100}-p(6x6)-Sb surface alloy, respectively.

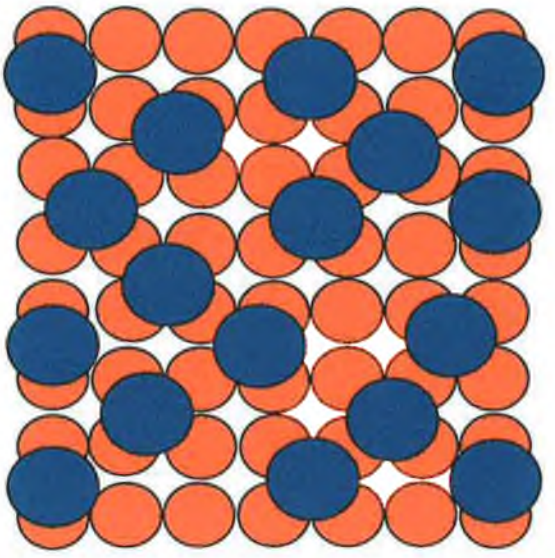

(A)

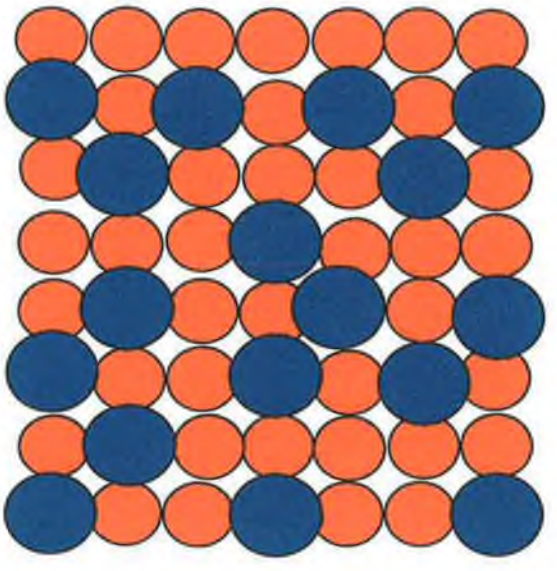

(B)

Figure 3.8 Possible structures for the Cu{100}-p(6x6)-Sb system. (A) is a p(6x6) overlayer structure at a concentration of 0.32ML Sb. (B) is a p(6x6) surface alloy with the Cu{100} substrate at a coverage of 0.32ML Sb .

3.4 Conclusion

Aufray et al. found that at a concentration of 0.45ML, Sb forms a p($\sqrt{3}$x$\sqrt{3}$) R30° surface alloy with Cu{111}. The STM images taken by Aufray et al. clearly show that the Sb segregation induces a modification of at least the topmost Cu layer causing a symmetry breaking of the Cu {111} surface.

This study was conducted at concentrations below those studied by Aufray et al., to determine if Sb forms any ordered structures on the Cu {100} substrate.

At a concentration of ~0.25ML, Sb forms a p(2x2) surface alloy with the Cu{100} substrate. The p(2x2) LEED pattern is characterised by the presence of fractional order spots in the (1/2,0), (1/2,1/2), (1,1/2) and (3/2,0) positions which are not present in the clean Cu LEED pattern. LEED I(V)s were taken for all integral order spots, namely (1,0), (1,1), (2,0), (2,1) and (2,2) and the most important fractional order beams, (1/2,0), (1/2,1/2), (1,1/2) and (3/2,0). The total energy range in this analysis was 1540eV out of which 400eV was from fractional order beams. The theoretical LEED calculations were performed using the Symmetrised Automated Tensor LEED program (SATLEED). The observed LEED pattern possessed the high symmetry of four mirror planes (p4mm).

The analysis started with the calculation of LEED I(V)s for four different models: three overlayer structures and a surface alloy. According to the pendry RR-method, all overlayer models can be excluded and therefore only the p(2x2) surface alloy was considered for further analysis. The optimum geometry was found by optimising the top 5 interlayer spacings and non-structural parameters. The total Pendry R-factor is 0.26. This comparison produced the best model's structural and non-structural parameters. The best fit structure has a relatively corrugated CuSb surface alloy with Sb atoms being at 0.56 Å above the centre of mass of surface Cu atoms. Despite the alloying of Sb with the outermost Cu atoms, the addition of Sb atoms on the Cu{100} substrate has not produced a significant perturbation in the deeper Cu layers. The maximum determined buckling was less than 3% (0.05 Å) relative to the Cu bulk interlayer spacing

(1.81 Å). Another observation is that the Cu outermost interlayer spacing is significantly expanded (less than 2%).

STM results confirm those of LEED and SATLEED with the unit cell clearly a p(2x2) structure, particularly once the lattice fit operation is conducted on the images. The figures for the vectors of the lattice represent the sum of the atomic diameters of one Sb and one Cu atom (3.18Å(Sb) and 2.556Å(Cu) giving a value of 5.7736Å, with slight discrepancies taken into account for drift. Both profiles indicate that the p(2x2) surface alloy is a well-ordered uniform structure with little or no disorder between unit cells.

At a concentration of ~0.32ML Sb on the Cu{100} surface, Sb forms a p(6x6) structure. The p(6x6) LEED pattern is characterised by 5 spots between the (0,0) spot and each of the integral beams, namely the four (1,0) and (1,1) beams, giving a 'grid' of 36 spots in each direction. Unfortunately due to the complexity and number of spots contained in the LEED pattern it proved too difficult to acquire a reasonable set of LEED IV data, so a Tensor LEED study was not possible. This makes it incredibly difficult to determine whether the Cu{100}-p(6x6)-Sb system is an overlayer structure or surface alloy.

An STM study of the Cu{100}-p(6x6)-Sb system was conducted in conjunction with the LEED study to determine the exact arrangement of the Sb atoms on the Cu(100) surface. A lattice of vectors v_1=1.53nm and v_2=1.56nm was fitted to this image to show the considered unit cell, which in agreement with the LEED pattern, is a p(6x6) structure as the distance of 6 Cu atoms laid side by side is 1.534nm, with slight differences expected due to drift. The apparent height of the step edges is measured to be 0.178 +/- 0.015nm. This is in good agreement with the value of 0.180nm expected for bulk copper and is consistent with a slight relaxation of the topmost layer. The atomic resolution STM images for the Cu{100}-p(6x6)-Sb surface display both double and single rows of atoms which implies that the deposited Sb causes a reconstruction in the selvedge.

It is thought that the Cu{100}-p(6x6)-Sb system is a surface alloy as at both lower and higher concentrations of deposited Sb, p(2x2) and p($\sqrt{3}$ x $\sqrt{3}$) R30° surface alloys are formed respectively.

3.5 References

1. Eaglesham, D.J., Unterwald, F.C., Jacobson, D.C., Phys. Rev. Lett. 70(1993)966.
2. Snyder, C.W., Orr, B.G., Phys. Rev. Lett. 70(1993)1030.
3. van der Vegt, H.A., Pinxteren, H.M., Lohmeier, M., Vlieg, E., Thornton, J.M.C., Phys. Rev. Lett. 68(1992)3335.
4. Meyer, J.A., van der Vegt, H. A., Vrimoeth J., Vlieg, E., Surf. Sci. Lett. 335(1996)L375.
5. Barnes, C.J., AlShamaileh, E., Pitkanen, T., Lindroos, M., Surf. Sci. 482(2001)1425.
6. Barnes, C.J., AlShamaileh, E., Pitkanen, T., Kaukasoina, P., Lindroos, M., Surf. Sci. 492(2001)55.
7. Pussi, K., Lindroos, M., AlShamaileh, E., Barnes, C.J., Surf. Sci. 513(2002)555.
8. McLoughlin, E., Cafolla A.A., AlShamaileh, E., Barnes, C.J., Surf. Sci. 482(2001)1431.
9. Pussi, K., AlShamaileh, E., McLoughlin, E., Cafolla, A.A., Lindroos, M., Surf. Sci. 549(2004)24.
10. Cafolla, A.A., McLoughlin, E., AlShamaileh, E., Guaino, Ph., Sheerin, G., Carty, D., McEvoy, T.F., Barnes, C.J., Dhanak, V., Santoni, A., Surf. Sci. 544(2003)121.
11. Pussi, K., McEvoy, T.F., Barnes, C.J., Cafolla, A.A., AlShamaileh, E., Lindroos, M., Surf. Sci. 526(2003)141.
12. Nakagawa, T., Boishin, G.I., Fujioka, H., et al. Phys. Rev. Lett. 86(5)(2001)854.
13. Breeman, M., Boerma, D.O., Phys. Rev. B 46(3)(1992)170.
14. McEvoy, T., AlShamaileh, E., Barnes, C.J., (to be submitted).
15. Abel, M., Robach, Y., Porte, L., Surf. Sci. 498(2002)244.
16. Aufray, B., Giordano, H., Seidman, D.N., Surf. Sci. 447(200)180.
17. Saenhaji, A., Treglia, G., Legrand, B., Barett, N.T., Guillot, C., Villette, B., Surf. Sci. 274(1992)297.
18. Giordano, H., Aufray, B., Surf. Sci. 280(1996)352.

19. Gothelid, M., Aufray, B., Giordano, H., Gay, J.M., Le Lay, G., Bellchou, R., Marsot, N., Guillet, C., Surf. Rev. Lett. 4(1997)1205.
20. Jona, F., Surf. Sci. 192(1987)398.
21. Van Hove, M.A., Moritz, W., Over, H., Rous, P.T., Wander, A., Barbieri, A., Materer, N., Starke, U., Somorjai, G.A., Surf. Sci. Rep. 19(1993)191.
22. Van Hove Website (Phase Shifts Package).
23. Pendry, J.B., J. Phys. C: Solid State Phys. 13(1980)937.
24. Besenbacher, F., Rep. Prog. Phys. 59(1996)1737.

Chapter 4

Fabrication and Characterisation of Copper Microelectrodes

4.1 Introduction

Copper represents an important electrode material for applications ranging from metal electrodeposition to the self-assembly of biologically important monolayers [1]. Despite this importance, there have been relatively few reports focussing on the fabrication and properties of copper microelectrodes. This chapter details the fabrication of copper microelectrodes and their characterisation in a background electrolyte and acts as a reference for the next chapter dealing with the electrodeposition of indium on the copper microelectrodes.

For the electrodeposition of a metal on a copper microelectrode, it is imperative to know the potential window for copper microelectrodes in background electrolyte and ensure the deposition potential for the metal in question lies within that window. Determining the RC time constant, resistance and capacitance for the copper microelectrodes in background electrolyte allows comparison with other types of microelectrode and allows the effects of the deposited metal on the overall cell performance be determined.

4.1a Microelectrodes

Microelectrodes may be defined as electrodes whose critical dimension is in the micrometre range[2]. Their introduction has greatly extended the range of sample environments and experimental timescales that are useful in electrochemistry. Micro-disk electrodes predominate because of their ease of construction and because the sensing surface of the electrode can be mechanically polished. Microelectrodes in this form are commonly fabricated by sealing a fine wire or foil into a non-conducting electrode body such as glass and sanding the end to form a disc at the tip [3].

Microelectrodes have several typical attributes including small currents, steady state responses and short response times. The currents observed at microelectrodes typically lie in the pA to nA range, which is several orders of

magnitude smaller than those observed at conventional macroelectrodes where the radius is usually several millimeters.

The small electrolysis currents observed at microelectrodes often completely eliminate problems associated with resistive effects that larger electrodes suffer from. For example, the immunity of microelectrodes to 'ohmic drop' allows one to perform amperometric experiments in previously inaccessible samples such as non-polar solvents, supercritical fluids and solids. [3]

The small size of microelectrodes makes diffusional mass transport extremely efficient, to such an extent that mass transport rates to a microelectrode are comparable to those of a conventional macroelectrode rotated at several thousand r.p.m.. The flux of the electroactive species to the electrode is substantially higher than for the pure planar diffusion case that is typical of a macroelectrode [4].

The efficiency of this mass transport makes it possible to observe steady state responses when the applied potential is slowly scanned in cyclic voltammetry (1-10mVs^{-1}). Kinetic data can be obtained directly from steady-state-voltage measurements analysed on the basis of the Tafel equations. It is also observed that the steady state limiting current is directly proportional to the analyte concentration, making it useful for analysis [5].

Another feature associated with microelectrodes is their ability to respond rapidly to changes in the applied potential. Microelectrodes can accurately monitor electrochemical processes on a low microsecond or even nanosecond timescale, compared with the milliseconds needed for conventional macroelectrodes. This ability of microelectrodes to respond rapidly to change in applied potential makes them particularly useful in dynamic studies of short timescale homogenous and heterogeneous electron transfer processes, a feature of particular importance in

studies on metal deposition as in the case of electrochemical phase formation, equilibrium is established by electron transfer [6].

4.1b Properties of Microelectrodes

(I) Reduced capacitance

When an electrode comes into contact with an electrolytic solution, a double layer is formed at the interface, in which the charge present on the metal electrode is compensated for by a layer of oppositely charged ions in solution [3]. In many respects the electrochemical double layer behaves like a capacitor.

The current required to charge the double layer of capacitance, C, must flow through a resistance, R, corresponding to the total cell time resistance. The product RC represents the cell time constant and it is only at times longer than 5 to 10 times RC that useful analytical information is obtained in an electrochemical experiment. For example, in a potential step experiment of amplitude ΔE, the charging current $i_c(t)$ decreases exponentially in time at a rate dictated by the RC time constant [7]:

$$\mathbf{i_c(t) = \frac{\Delta E}{R} exp(\frac{-t}{RC})} \qquad \text{(Eqn 4.1)}$$

In an electrochemical cell, the resistance depends on the specific conductance of the medium, κ and the radius of the disc electrode, r. This formula assumes the electrode tip is a disc shape.

$$R = \frac{1}{4\pi\kappa r} \qquad \text{(Eqn 4.2)}$$

This equation shows that R increases as the electrode radius decreases, so making the electrode smaller does not reduce the product RC by decreasing the resistance. However, the electrode capacitance is an extensive property and is proportional to the electrode area (r^2).

$$RC \approx \frac{1}{r} r^2 (= r) \qquad \text{(Eqn 4.3)}$$

The r^2 dependance causes the product RC to decrease as the electrode radius decreases. The smaller RC cell time constants of microelectrodes means that they respond more rapidly to changes in the applied potential than macroscopic electrodes. This property makes microelectrodes very attractive for investigating the mechanism of metal/adatom deposition. After short timescales, in the region of 100ms, the current from the RC time constant decays to zero and any changes in current are due to metal deposition.

(II) Ohmic effects

When faradaic and charging currents flow through a solution, they generate a potential that acts to weaken the applied potential by an amount iR, where i is the total current and R is the cell resistance.

Microelectrodes significantly reduce these ohmic effects because the faradaic currents observed are typically six orders of magnitude smaller than those at macroelectrodes. These small currents often completely eliminate iR problems. The resistance increases with decreasing electrode radius rather than electrode area. This causes the product iR to decrease with increasing electrode radius in short timescale experiments [3]. Therefore, apart from reduced iR drop because of low currents, decreasing the electrode radius from 1mm to 10μm also decreases the ohmic iR drop observed at short times by a factor of 100, unless under radical diffusion conditions.

The major focus of this experiment is on adsorbed reactants on microelectrodes, meaning that the interference from iR is negligible as the data does not depend on shifts in peak potential nor do the experiments involve large currents.

4.1c Mass transport to microelectrodes

The most important factor determining the behavior of an electrode is the mass transport in solution in the vicinity of the electrode [8]. When considering an uncomplicated charge-transfer reaction, then the voltammetric current signal is proportional to the flux of the electroactive substance toward the solution–electrode interface described by Fick's first law. Ficks first law states that the flux of any species, I, through a plane parallel to the electrode surface is given by

$$\text{Flux} = -D_i \frac{dc_i}{dx} \qquad \text{(Eqn 4.4)}$$

where D_i is the diffusion coefficient and typically has the value $10^{-5}cm^2s^{-1}$ [9]. Ficks second law describes the change in concentration of i with time due to diffusion. At a point at the centre of an element of solution bounded by two planes parallel to the electrode the concentration will change because diffusion is occurring both into and out of the element. This leads to the equation:

$$\frac{\partial c_i}{\partial t} = D_i \frac{\partial^2 c_i}{\partial x^2} \qquad \text{(Eqn. 4.5)}$$

When the electrode potential is switched from a value at which no electrode reaction occurs to that corresponding to the limiting current of the electrode reaction, then the concentration of the electroactive substance at the electrode surface decreases to zero and a concentration gradient develops over a certain distance from the electrode surface into the bulk of the solution; this distance increases with increasing electrolysis time. The solution volume within which the diffusional flux of the substance occurs is termed the diffusion layer. The flux of the substance toward the electrode is then described by the product of the diffusion coefficient of the substance, D, and its bulk concentration divided by the diffusion layer thickness, δ. This quantity is defined, for planar semi-infinite diffusion, by the relationship

$$\delta = \sqrt{\pi D t} \qquad \text{(Eqn. 4.6)}$$

The diffusion layer thickness can be rigorously calculated for a spherical electrode and for a planar disk electrode placed in a plane of an insulator [10].

If the electrode geometry is approximated by the model of an infinitely large planar electrode with the substance flux perpendicular to the electrode plane, then the flux is uniform over the entire electrode surface and the substance concentration attains the bulk value at a distance of a few diffusion layer thickness values. However, the flux is not uniform over the electrode surface

(edge effect) for other geometries. For example, if an electrode is embedded in a planar insulator, then the size of the electrode can be described by twice the linear dimension of the electrode (e.g., 2r, where r is the radius of a disk or hemispherical electrode). Two limiting cases can then be distinguished, namely, δ is much smaller than r and δ is much larger than r.

For $\delta << r$, the perturbation of the linear diffusion flux caused by the hemispherical diffusion at the electrode edges extends to a short distance of several δ from the edge. Thus, only a small part of the electrode surface is affected, and the behavior of the electrode can be approximated by the infinite electrode model.

For $\delta >> r$, the edge effect plays a predominant role, and the diffusional flux toward the electrode is constant with time but inhomogeneous over the electrode surface; it increases with decreasing distance from the electrode edge. Concentration of the electroactive substance attains the limiting value described by the equation for steady-state transport, which corresponds to the time derivative being zero in Fick's second law.

An extremely important conclusion follows from the effects described above, namely, that the diffusion layer thickness depends on time. Therefore, the differentiation between the two cases considered above also depends on time. At a sufficiently short time, any planar electrode, no matter how small (with the obvious limitations of the diffusion model), behaves as an infinitely large planar electrode. With increasing time, the electrode behavior gradually changes toward the second case. In fact, a single dimensionless parameter, δ/r, is sufficient for describing the electrode behavior. After sufficiently long time, a steady state is established for electrodes of certain geometries (e.g., planar and spherical). However, a true steady state cannot be attained for an infinitely long cylindrical electrode [10].

4.2 Experimental

4.2a Fabrication of the Cu microelectrodes

A length of soft glass tubing approximately 15cm long was cut and cleaned to remove all dust and grease from the inner surface. The cleaning process involved leaving the glass tubing to soak overnight in a beaker of dilute HNO_3. The glass tubing was subsequently washed with acetone and Milli-Q water and left in an oven to dry.

On drying the glass tubing was heated in the middle using a Bunsen flame, and drawn outwards to leave a tapered end of 4cm on both pieces of the glass tubing. Each glass tube should now be approximately 5-8 cm in length.

A wire assembly was prepared for insertion into each glass tube. Each wire assembly consisted of a 5cm length of tin coated copper wire which was stripped of tin at one end and connected to a 'hook up' wire by wrapping the 'hook up' wire around the tin-stripped region of copper wire and then soldering. The hook up wire was zig-zagged a number of times to prevent the assembly from moving around in the glass tubing, which reduced the chances of a breakage occurring. The other end of the hook up wire was attached to a 2cm length of 25μm radius copper wire using solder.

The wire assembly was inserted in each of the glass tubes. The open end of the glass tube was attached to a vacuum during sealing in order to avoid oxide formation on the copper wire. The tapered end was then sealed around the copper wire by rotating it around the flame from the Bunsen burner. At this point the glass was allowed to cool.

Finally the open end of the glass was sealed with a plastic cap using araldite epoxy resin. The electrode was left overnight to allow the araldite epoxy resin to cure. Figure 4.1 illustrates a cross section of the structure of a 25μm radius

copper microelectrode. Figure 4.2 is an SEM image of the tip of a 25μm radius copper microelectrode.

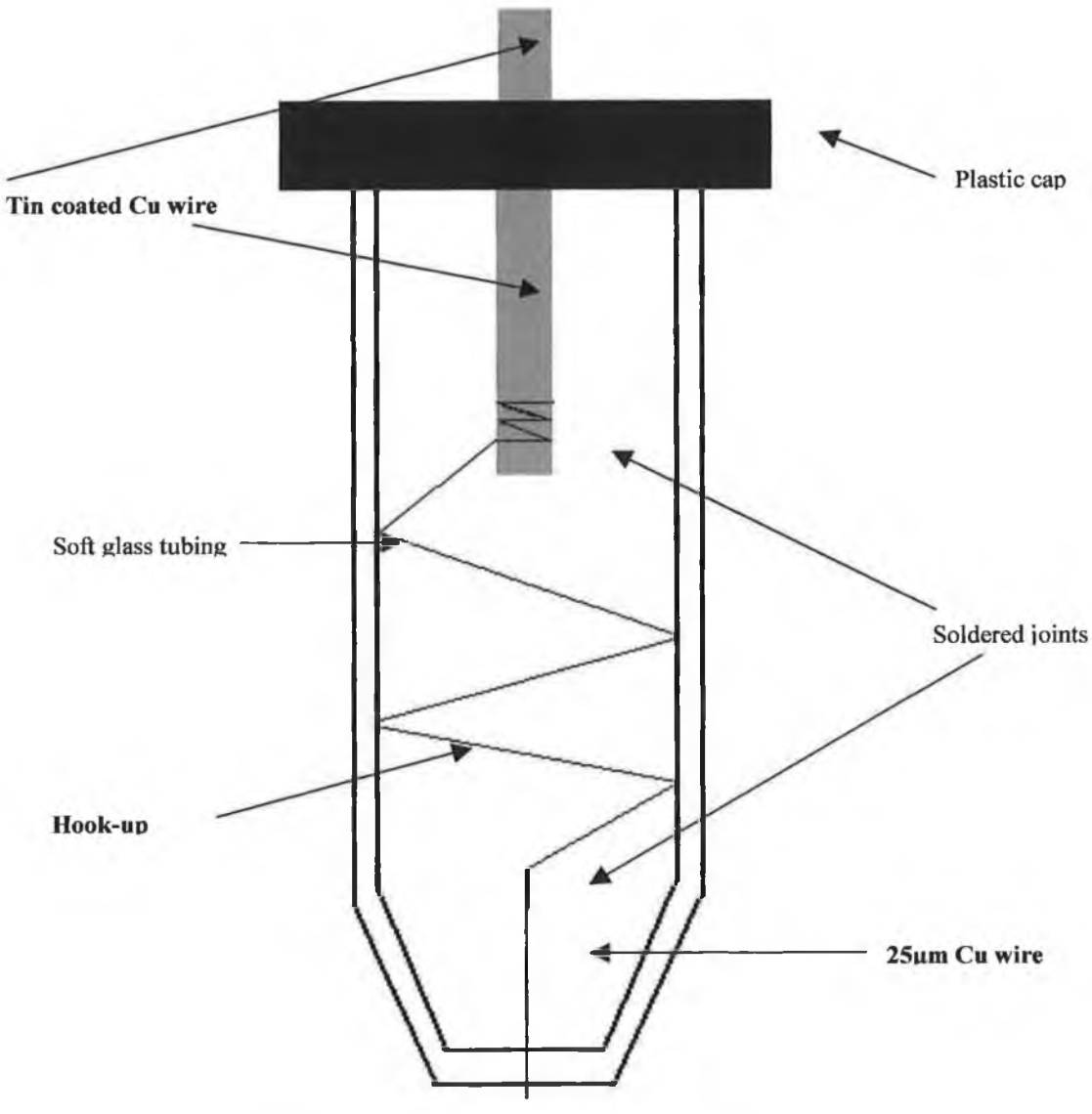

Figure 4.1 Cross section of the structure of a 25µm radius copper microelectrode

Figure 4.2 SEM image of a 25μm radius copper microelectrode. The image was taken at a working distance of 23.9mm, beam energy of 20kV and a magnification of 30.

Once the epoxy had cured, excess glass at the tapered end was removed using fine sandpaper to expose the copper wire. The procedure used was to slightly wet the fine sandpaper with Milli-Q water and with the electrode held perpendicular to the sandpaper, it was rotated in a figure of 8 motion across the sandpaper surface until the copper wire was exposed.

The electrode was examined using a 25x magnifying glass in order to check the wire assembly for loose connections and to ensure the copper wire was exposed.

4.2 Characterisation of the Cu microelectrodes

Polishing the electrode surface

A number of polishing pads were made by placing a piece of polishing cloth (Buehler) on a petri dish and sprinkling alumina on the cloth surface, followed by a small quantity of Milli-Q water.

Each pad had a different alumina size and were used in order of decreasing particle size, from 12.5 to 0.05μm. The electrode tip was rotated in a figure of 8 motion over the polishing pad surface for a period of 10min. Once finished polishing on a pad, the electrode was rinsed with Milli-Q water and placed in a sonicator for approximately 30sec. Once sonication was completed a cyclic voltammogram was run in 0.1M $LiClO_4$.

Determination of potential window

To determine the potential window, a number of cyclic voltammograms were taken at increasing potential ranges until the exact potential window was found (the requirement for acceptable results is that the CV is less than $10\mu Acm^{-2}$). An Ag/AgCl electrode was used as reference and a platinum wire was used as the auxiliary electrode. A suitable background electrolyte was used, in this case $HClO_4$.

pH dependence

The pH of $HClO_4$ was measured as 1.05 and scans were conducted at this pH. A solution of 0.1M NaOH was used to increase the pH and each solution was tested with a pH meter (ThermoOrion model 420) prior to analysis. Cyclic voltammograms were taken at the following pHs 2.25, 3.10, 4.45, 5.89, 6.92 and 7.68 in the potential ranges tested previously to determine whether the system had any reliance on pH. Due to the pH being adjusted with a solution of 0.1M NaOH, the ionic strength of the electrolyte solution increases as the pH increases due to there being increasingly more ions in solution.

Measurement of resistance, capacitance and RC time constants

The measurement of cell resistance, interfacial capacitance and RC time constant were conducted using a custom built programmable function generator-potentiostat. The experimental set-up was similar to the previous experiments, with an Ag/AgCl electrode acting as reference, platinum wire as auxiliary and $HClO_4$ as electrolyte. The concentration range for the $HClO_4$ was from 0.1 to 1M. However, in this set of experiments the experimental technique was changed from cyclic voltammetry to high speed chronoamperometry. The programmable function generator-potentiostat had a rise time of less than 10ns and was used to apply potential steps of the magnitude of 200mV pulse width, for a potential range of –0.1 to –0.6V. This was the experimentally determined potential window for copper microelectrodes in $HClO_4$. The current to voltage converter was based on a Comlinear CLC203 AI operational amplifier with a 1500 Ω feedback resistance and a response time of less than 10ns. The chronoamperograms were recorded using a HP54201A digital oscilloscope in 64x, time average mode.

The chronoamperometric results gave a graph of current versus time for the electrochemical system. The time was corrected to begin when the potential step is applied and the current divided by the internal resistance of the circuit. The

natural log of this value is plotted against corrected time. The slope of this second graph was equal to the RC time constant of the cell.

4.3 Results and Discussion

On fabrication of the copper microelectrode, the electrode is checked for electrical contact using cyclic voltammetry to confirm the appearance of a background charging current. An Ag/AgCl electrode is used as the reference with a platinum wire acting as auxiliary electrode. 0.1M $LiClO_4$ is used as a background electrolyte. Once electrical contact has been confirmed, the electrode is ready for the polishing procedure to begin.

Figure 4.3 features a cyclic voltammogram of the fabricated Cu microelectrode in 0.1M $HClO_4$ over the potential window +0.05 to –1.00V. The figure is intended to confirm electrical contact for the electrode and does not reflect the actual potential window for polished copper microelectrodes in background electrolyte, which is addressed in a later section. In this CV a crossover occurs at a potential of –800mV, this is thought to be due to either the copper electrode oxidizing to form Cu^{2+} as the potential is made more positive, then reducing again as the potential is scanned in the negative direction or contamination on the electrode surface as the CV was taken prior to polishing. Eight microelectrodes were fabricated but it was found that only 50% exhibited electrical contact due to broken connections at the solder joint for the 25μm copper wire during the fabrication procedure.

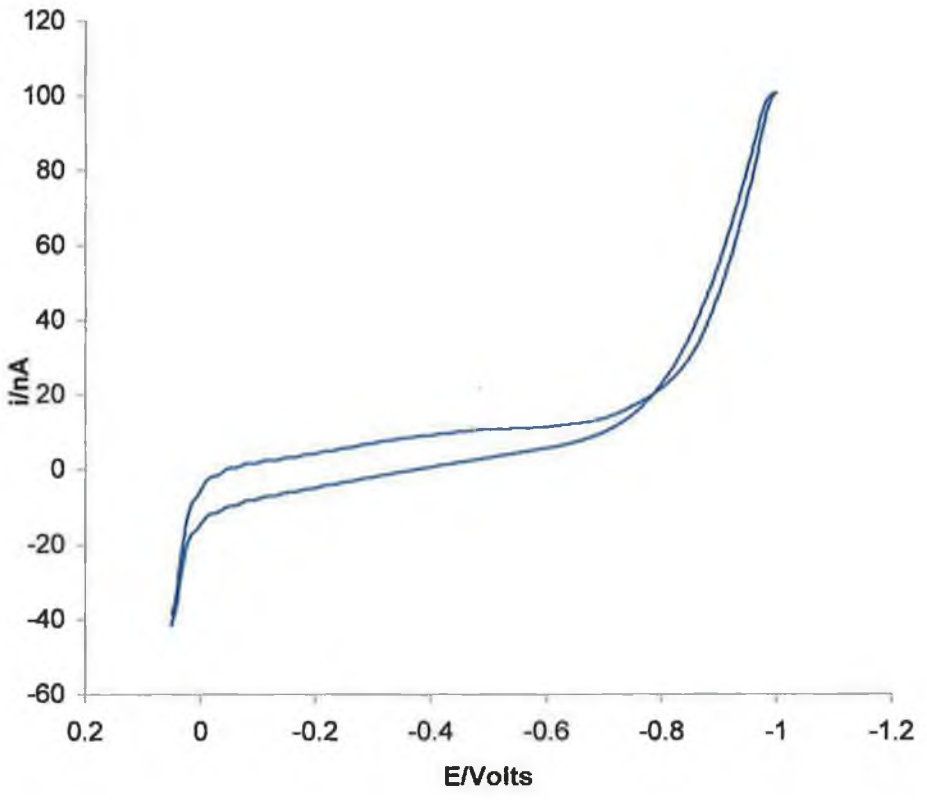

Figure 4.3 Cyclic voltammogram for a 25μm radius copper microelectrode in 0.1M $LiClO_4$. The scan rate is $0.1Vs^{-1}$ with the potential limits between +0.05 and -1.0V.

4.3a Polishing the electrode

The copper electrode is polished to reduce the roughness of the electrode surface, ensuring that the electrode surface is flat and uniform allowing for accurate, reproducible measurements. Beginning with the fine sandpaper and moving through coarse to the fine alumina pads, the cyclic voltammograms should show signs of continuous improvement. This can be seen as a drop in current and a reduction in capacitance (as seen in Figure 4.4). The electrode is considered to be clean and of low resistance when CVs of repeat polishing of the 0.05μm alumina yield an unchanging flat capacitance (less than $10\mu Fcm^{-2}$). If the background has not improved to this point following continued polishing then the only option is to restart the polishing procedure beginning with the 12.5 μm alumina.

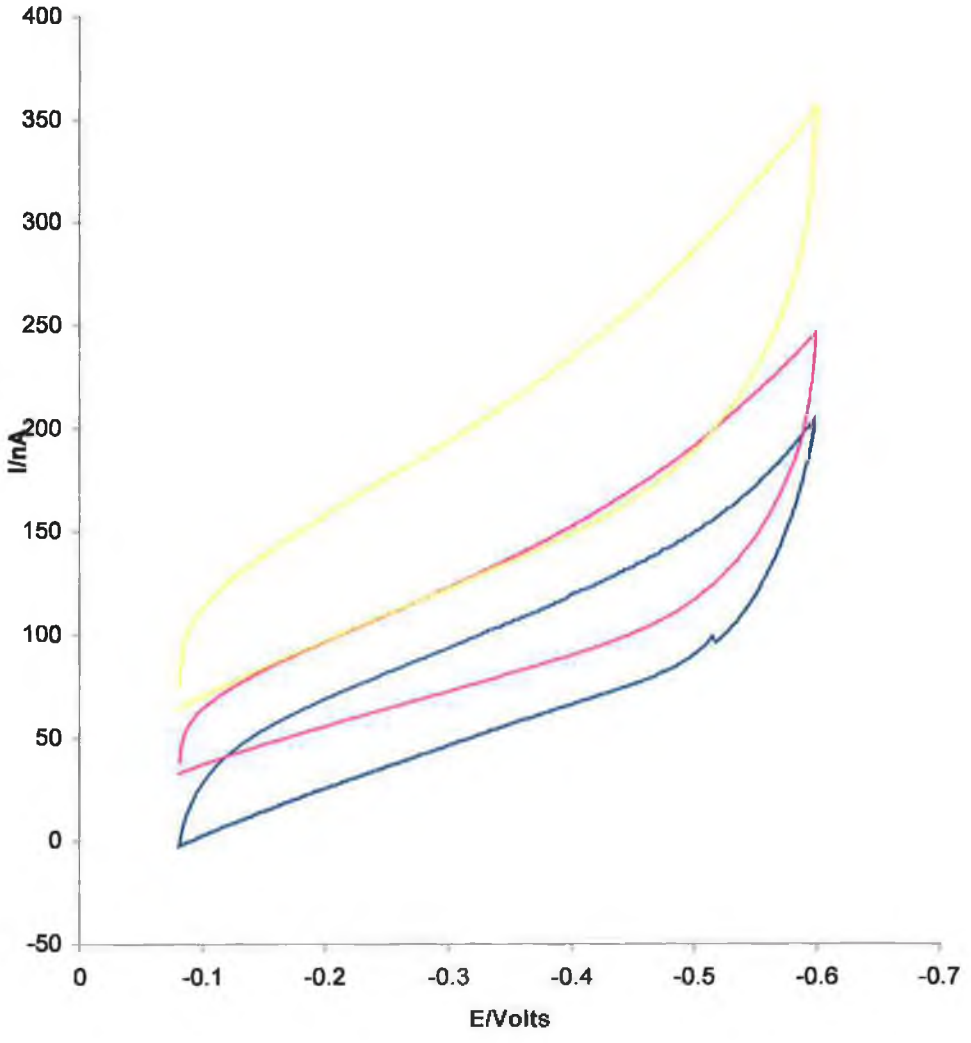

Figure 4.4 Overlay of cyclic voltammograms for a 25μm radius copper microelectrode in 0.1M $HClO_4$, after polishing with 1, 0.3 and 0.5 μm alumina. The scan rate is $0.1Vs^{-1}$. The potential limits are –0.08 and -0.6V. 1 μm alumina, - 0.3 μm alumina and – 0.05 μm alumina.

4.3b Surface Area Measurements

Once the polishing procedure is complete with satisfactory results (repeated polishing at 0.05μm yields unchanging CVs and correlation with theoretical capacitance), the surface area of the electrode is then accurately measured. It is fundamentally important to know the active surface area of the electrode as the loading of the electrode with modifying compounds (both organic and bioorganic) as well as the catalytic reactions of the electrode depends on this factor. For example calculation of the active surface area allows determination of the concentration of electrodeposited indium on the copper microelectrode surface, which is an integral part of the subsequent chapter. Knowing the real surface area of the electrode makes it possible to elucidate when a monolayer of indium has been deposited and quantification of indium concentrations below this value, which allows for comparison with UHV deposition of indium on Cu{100}.

For an adsorbed reactant, e.g. an electrodeposited metal, for a solution phase reaction under semi infinite linear diffusion control, the electrical current of an electrochemical process is proportional to the surface area of the electrode [11].

The theoretical surface area of an electrode can be calculated using the formula:

$$A_{Geom} = \pi r^2 \qquad \text{(Eqn. 4.7)}$$

where r is the radius of the electrode wire, assuming the electrode is circular and atomically smooth. Thus, the theoretical surface area of the 25μm radius Cu microelectrode is $7.85 \times 10^{-7} cm^2$.

However, the surface of the copper microelectrodes is not atomically flat and the real or microscopic area is likely to be larger than A_{Geom}.

For metals which show well defined regions for oxide monolayer formation and reduction, the method of oxide adsorption from solution allows the microscopic surface area to be determined. Prior to oxygen evolution, oxygen is assumed to be chemisorbed in a monoatomic layer on the surface of the electrode. This chemisorption also assumes a one-to-one attachment with surface metal atoms. The charge associated with the formation or reduction of the layer is:

$$Q_{Cu} = 2eN_A\Gamma_O A \qquad \text{(Eqn. 4.8)}$$

where N_A is the Avagadro constant, Γ_O the surface concentration of atomic oxygen assumed to be equal to the surface density of metal atoms.
The microscopic surface area of the electrode can be calculated using the following formula

$$A_{electrode} = \frac{A_p}{Q_{Cu}} \qquad \text{(Eqn. 4.9)}$$

where A_p is the area of the copper oxide peak (Figure 4.7) giving a value of 7.8 x 10^{-8}C, Q_{Cu} is the specific charge on the electrode surface 420μC/cm^2 and $A_{electrode}$ is the real area of the Cu microelectrode in cm^2 (which gives a value of 1.857x10^{-4} cm^2). The oxide formation method for the determination of surface area is the method of choice due to it being rapid and less destructive to the metal substrate than other methods [9]. Formation of a monolayer of oxide on the Cu substrate can result in place exchange of oxygen atoms with copper atoms under the surface layer resulting in deterioration of the electrode.

The ratio of actual surface area to theoretical surface area is a measure of the roughness of the electrode tip. A perfectly smooth electrode will have a surface roughness value of 1. The higher the roughness value, the rougher the electrode. The formula used to calculate the surface roughness is:

$$Surfaceroughness = \frac{A_{electrode}}{A_{geom}} \qquad \text{(Eqn. 4.10)}$$

For the Cu microelectrodes the surface roughness was calculated to be 2.3. This indicates that despite prolonged polishing, the electrode surface remains rough to some degree. It can also be seen from the SEM image of the electrode surface that the electrode is an elliptical shape rather than the expected spherical shape. The theoretical surface area is calculated on the presumption that the electrode shape is spherical, as the actual shape of the electrode is elliptical the roughness factor value will be inaccurate even if the surface is completely smooth. Thus the calculated roughness factor represents an upper limit on the actual roughness of the electrode.

The determination of the real A_{geom} was attempted by conducting solution phase experiments on bianthrone and a number of other anthraquinones but it was discovered that their redox potential lay outside the potential window for copper microelectrodes in $HClO_4$.

4.3c Potential Window

The potential window for an electrochemical experiment is the potential range in which the electrode can operate in the electrolyte solution to give reliable results (less than $10\mu Acm^{-2}$). In the case of copper electrodes, the reported potential range is between +1 and –1V although this range is pH dependent [13].
A potential range smaller than reported is tested first, this range being from –0.08 to –0.6V, seen in Figure 4.5. Although this range is small, the CV is the desired shape (elliptical shape with a low slope), giving reliable results, with no indication of coupled chemical reactions taking place such as oxidation of Cu or reduction of H_2O.

As this potential window exhibits a voltammogram below $10\mu Acm^{-2}$, the potential window is expanded to a range of +0.05 to –0.8V. The electrode is repolished to ensure that the experimental response is not compromised by the electrode history. Figure 4.6 is of the resulting CV, the results in this range are considered to be less than ideal as the CV exhibits unacceptable levels of rising current, with current amplitude being above $10\mu Acm^{-2}$. The potential window is limited by a large peak forming on the negative side of the potential range, thought to be from the bulk evolution of hydrogen from the acidic background electrolyte and on the positive limit there is an indication of possible oxide formation at a potential of +0.1V. To verify this the potential window is expanded in the positive direction to a range of +0.2 to -0.8V. Again, the electrode was repolished to avoid contamination from previous experiments.

On enlarging the potential window, it is noted that a large irreversible peak is formed at a potential of +0.2V, this is due to the formation of an oxide layer on the surface of the copper microelectrode. The reported E^0 value for Cu/Cu^{2+} in literature is +0.339V [14]. This may suggest that the peak formed at +0.2V is only the beginning of the overall copper oxide reaction with the copper becoming increasingly more oxidised as the potential range is expanded in the positive direction. Theoretically, the peak caused by the oxidation of the copper electrode should grow in size until reaching a maximum at +0.339V. This means that although some oxidation of the copper occurs, overall oxidation of the copper electrode will only occur at a more positive potential.

Due to the limits on the potential range imposed by the presence of peaks caused by copper oxide formation in the positive direction and hydrogen evolution in the negative direction the potential window determined for Cu microelectrodes in a solution using $HClO_4$ as background electrolyte is from –0.08 to –0.6V. This agrees with Robinson et al [15] who found the potential window for a copper electrode in $HClO_4$ to lie between –0.05 and –0.6V.

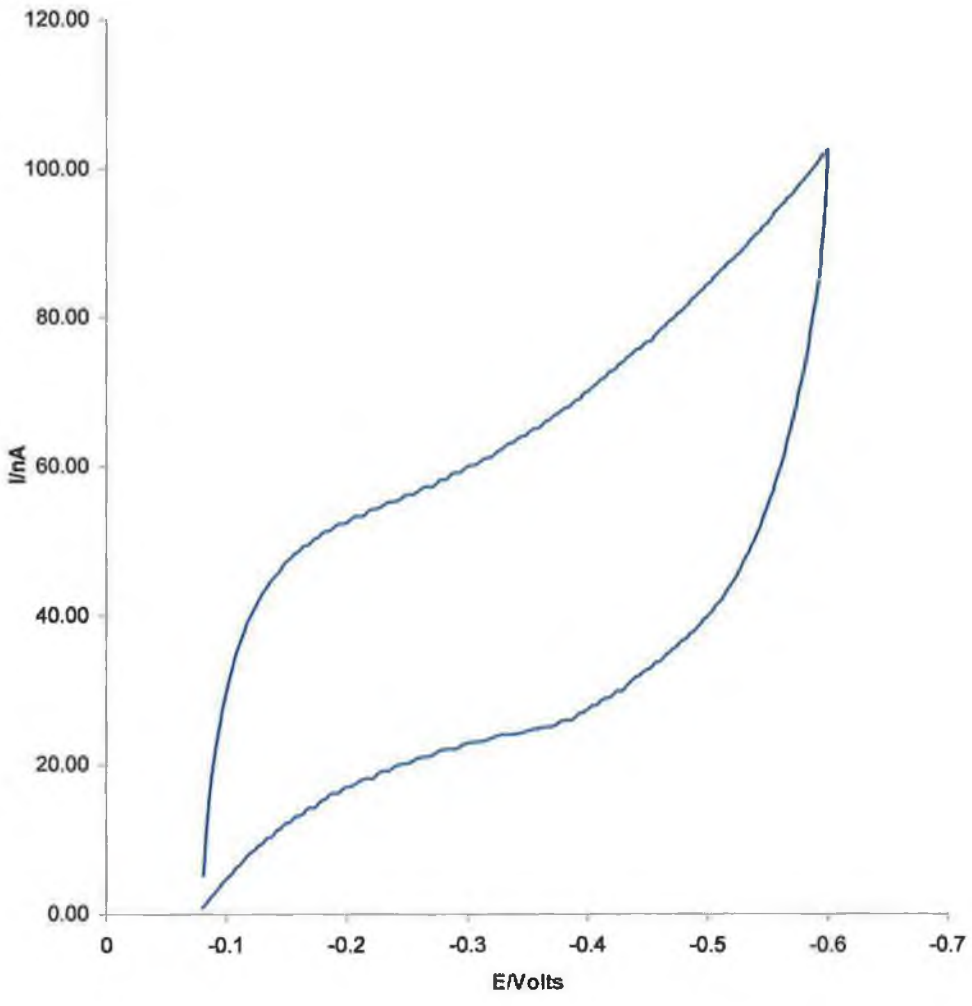

Figure 4.5 Cyclic voltammogram for a 25μm radius copper microelectrode in 0.1M $HClO_4$. The scan rate is $0.1Vs^{-1}$. The potential limits are –0.08 and -0.6V.

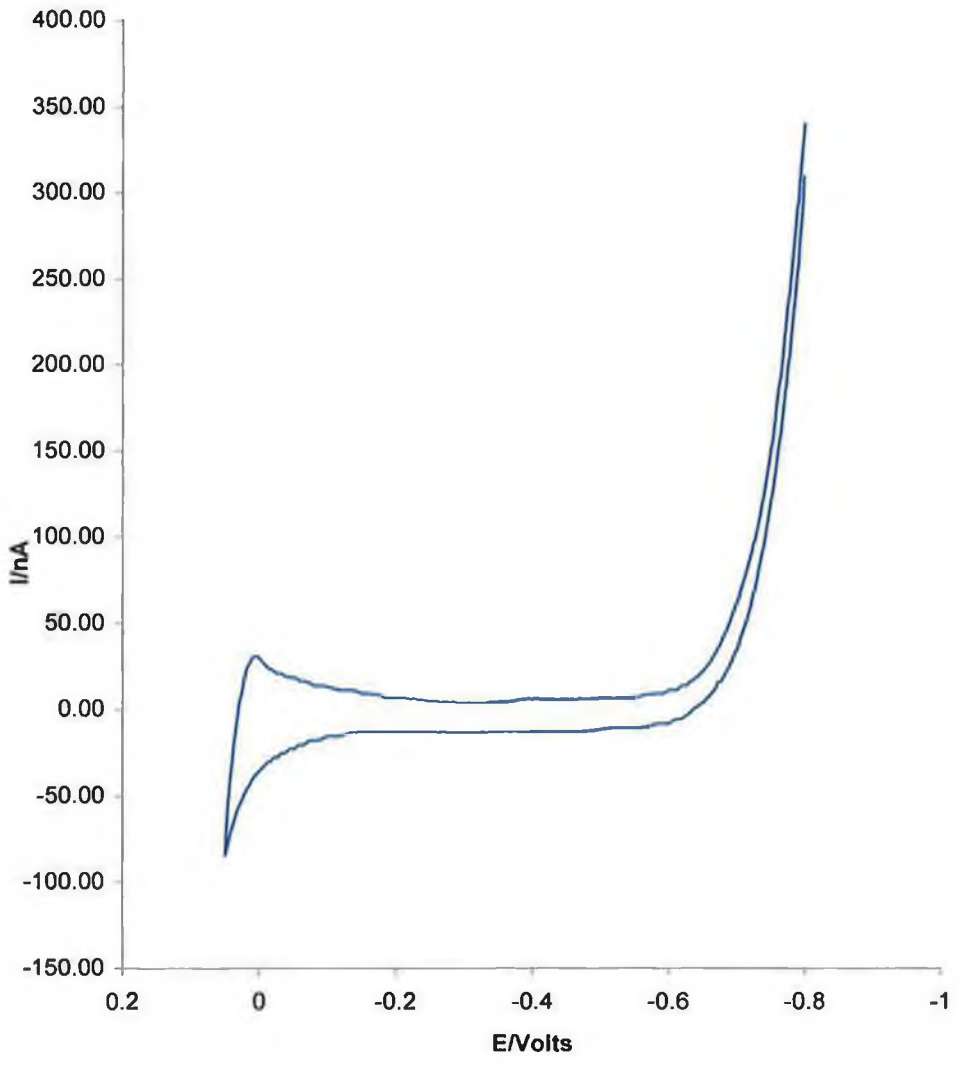

Figure 4.6 Cyclic voltammogram for a 25μm radius copper microelectrode in 0.1M $HClO_4$. The scan rate is 0.1Vs^{-1}. The potential limits are 0.05 and -0.8V.

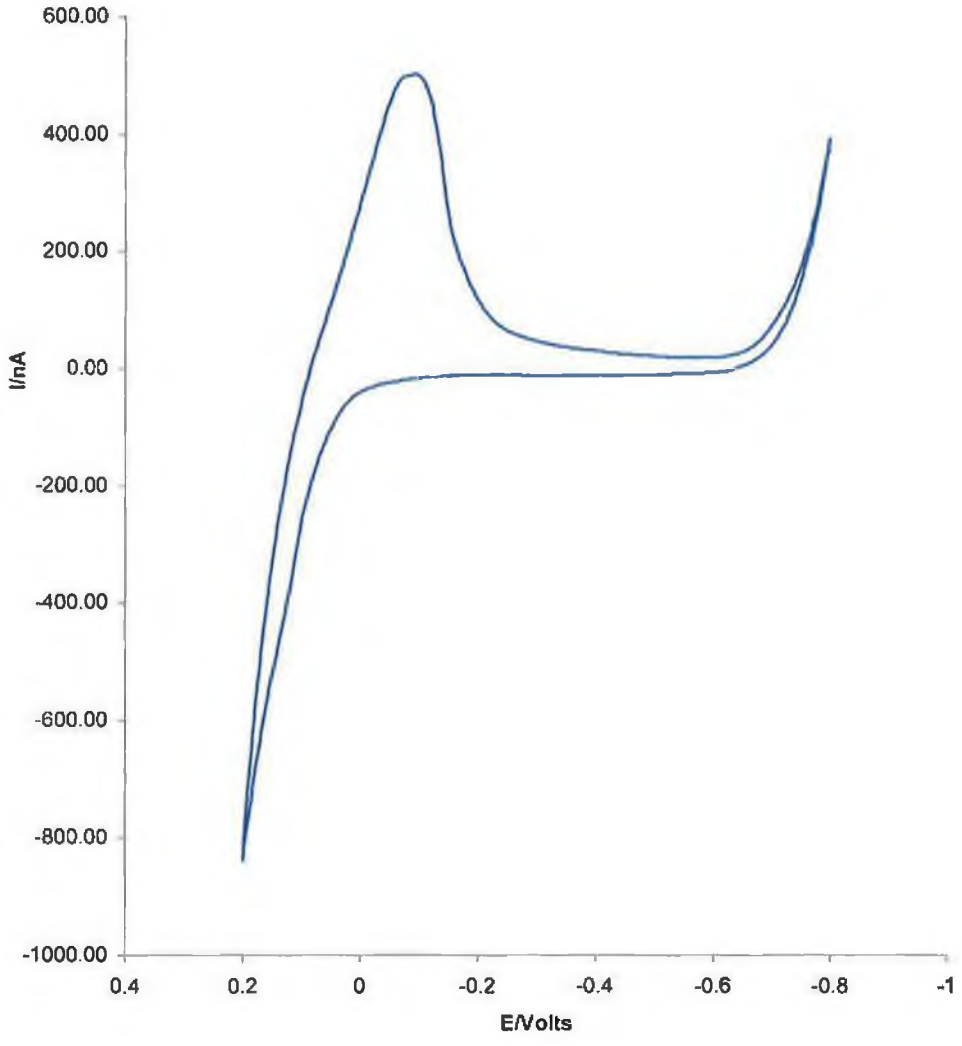

Figure 4.7 Cyclic voltammogram for a 25μm radius copper microelectrode in 0.1M $HClO_4$. The scan rate is $0.1Vs^{-1}$. The potential limits are +0.2 - -0.8V.

4.3d pH dependance

As determined in the previous section, copper electrodes have a relatively small potential window where the supporting electrolyte is 0.1M $HClO_4$ as compared with potential windows for other electrodes in the same electrolyte (e.g. the potential window for Pt microelectrodes in 0.1M $HClO_4$ is from +1.2V to –0.2V [16]), meaning the range of compounds which may be studied using copper electrodes is restricted. The potential window is curtailed on the positive side by the formation of copper oxide and on the negative side by hydrogen evolution from the acidic medium.

The copper oxide reaction is thought to be:

$$2Cu^{2+} + H_2O + 2e^- \rightarrow Cu_2O + 2H^+$$

which occurs at a potential of 0.207 + 0.0591pH [17]. 0.1M $HClO_4$ has a pH of 1.06 which means copper oxide will occur at a potential of approximately +0.25V. Experimentally, it was found that copper oxide formed at a potential of +0.2V, though this was the limit of the widest potential range tested so it is more likely that the peak would have grown to a maximum at +0.25V as calculated above if the potential window was expanded.

The hydrogen evolution reaction occurring in an acidic solution is as follows:

$$2H^+ + 2e^- \rightarrow H_2$$

with this reaction occurring at a potential just above -0.6V [18].

Figure 4.8 illustrates overlaid cyclic voltammograms as the pH is increased from 2 to 7, taken in the range –0.08 to –0.6V. The increase in pH improves the shape of the CV, particularly at a pH of 4, where the CV has a decreased current amplitude (from an I_c value of 1.13×10^{-7}A to 7.1×10^{-8}A) giving a reduced

capacitance (from 1.55 x $10^{-4}\mu F/cm^2$ to 9.73 x $10^{-5}\mu F/cm^2$). As the pH is increased above 4, the CVs become less reliable with both the current and size of the voltammogram increasing and a significant change in the CV slope indicative of an increased level of capacitance in the system.

The electrode is polished between changes in range to ensure any results obtained are not affected by previous scans. Figure 4.9 illustrates a CV where the potential window is expanded to a range of 0 to –0.8V. In this wider potential range changes in pH have a more obvious effect. At a pH of 1.03, a large peak forms just above –0.6V, thought to be caused by hydrogen evolution from the acidic electrolyte. As the pH increases this peak is shifted to a more negative potential, due to the reduction in H^+ concentration in solution. The rate of hydrogen evolution cannot exceed the rate at which H^+ ions can be transported to the surface from the bulk solution. In solutions with a pH >4 this mass transfer controlled limiting current is small [19], so hydrogen evolution is greatly reduced in the potential window being studied. The best results were at a pH of 4 with the CV exhibiting low current and a flat thin shape, above this pH there is a large increase in current and distortion in CV shape.

In Figure 4.10, the window is increased in both directions to a range of 0.1 to –1V. As the pH increases, the copper oxide peak disappears from the potential window due to the formation potential becoming more positive [9], and although there is some evidence of the hydrogen evolution peak, it is minimal, particularly at a pH of 4 and above. Again the optimum CV is obtained at a pH of 4 with a flat CV with low current obtained, above this pH the capacitance increases, indicated by an increase in CV current.

From these results it was found that for the system of Cu microelectrodes in a background electrolyte of 0.1M $HClO_4$, the optimum pH is 4, which allows for a potential window of +0.1 to –1V.

It is noticeable from each of the overlaid sets of CVs that above a pH of 4 the capacitance increases dramatically, with the shape of the CV deteriorating as the pH increases. This is due to an increase in the ionic strength of the system. The pH is increased by adding increments of 0.1M NaOH until the desired pH is achieved. This means that as the pH increases the concentration of NaOH in the solution increases linearly. The capacitance value is a measure of an objects ability to retain an electrical charge [20]. In this case the electrical double layer acts as a capacitor. According to the Guoy-Chapman-Stern model for the double layer, the ions in solution arrange themselves in a series of laminae parallel to the electrode and of uniform thickness [9]. The capacitance of this system is related to the distance between the laminae. As the concentration of ions increases, the distance between laminae decreases which causes the capacitance of the electrochemical system to increase. This phenomenon is observed in Figure 4.11, as can be seen, an increase in ionic strength results in an increase in the capacitance of the system.

Figure 4.11 is a plot of ionic strength versus capacitance of the system. The ionic strengths of each solution are calculated from the formula:

$$I = \frac{1}{2}\sum C_i Z_i^{\,2} \qquad \text{(Eqn. 4.11)}$$

where I is the ionic strength, C_i is the concentration in moles and Z_i is the charge of each ion present in solution. The total ionic strength of the electrolyte solution is the sum of ionic strengths for both $HClO_4$ and NaOH in the electrolyte solution.

The capacitance is calculated using the formula:

$$I_c = CA\nu \qquad \text{(Eqn 4.12)}$$

where I_c is the charging current, C is capacitance, A is the geometric area of the electrode and ν is the scan rate. The values for I_c are taken from Figures 4.5 and 4.8, with I_c equal to half the CV width.

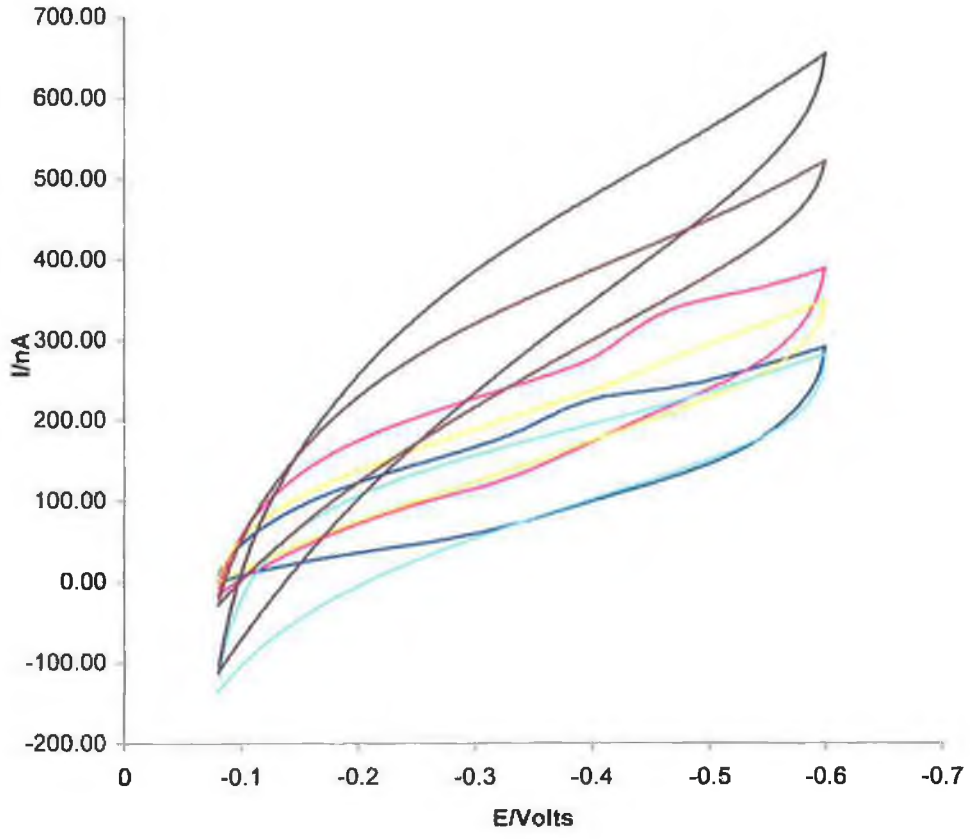

Figure 4.8 Overlay of cyclic voltammograms for a 25μm radius copper microelectrode in 0.1M $HClO_4$, with increasing pH to a pH of 7. The scan rate is $0.1Vs^{-1}$. The potential limits are –0.08 and -0.6V. Legend = - pH2, - pH3, - pH4, - pH5, - pH6, - pH7.

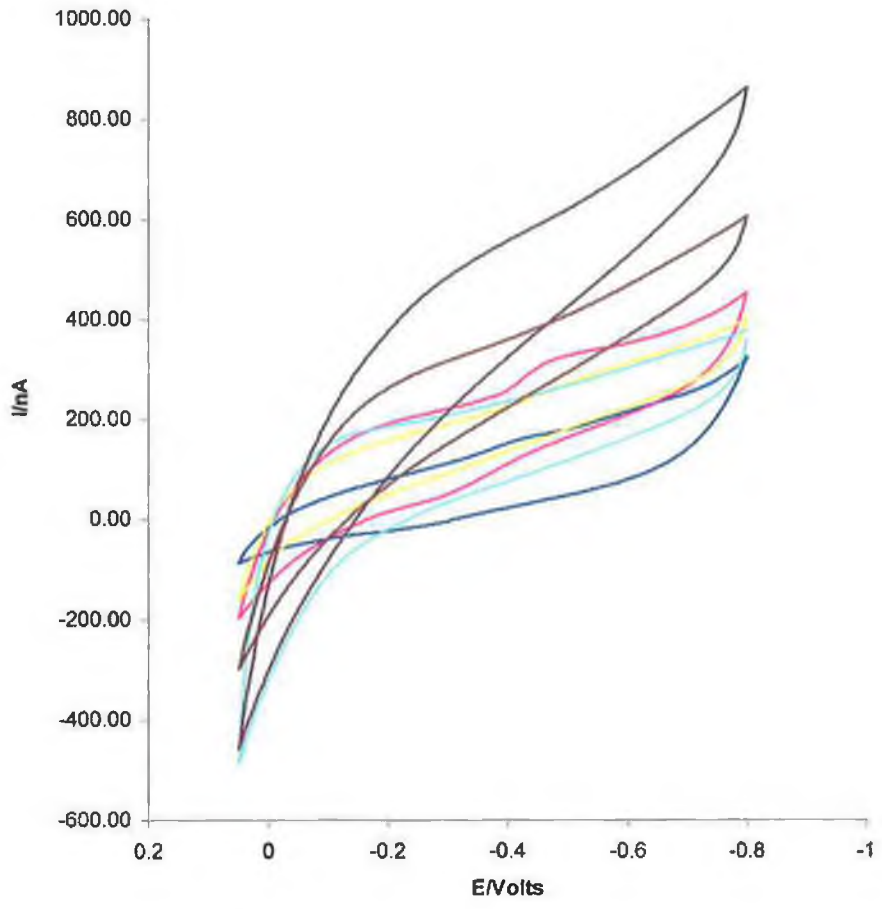

Figure 4.9 Overlay of cyclic voltammograms for a 25μm radius copper microelectrode in 0.1M $HClO_4$, with increasing pH to a pH of 7. The scan rate is $0.1Vs^{-1}$. The potential limits are 0 and -0.8V. Legend = - pH2, - pH3, pH4, - pH5, - pH6, - pH7.

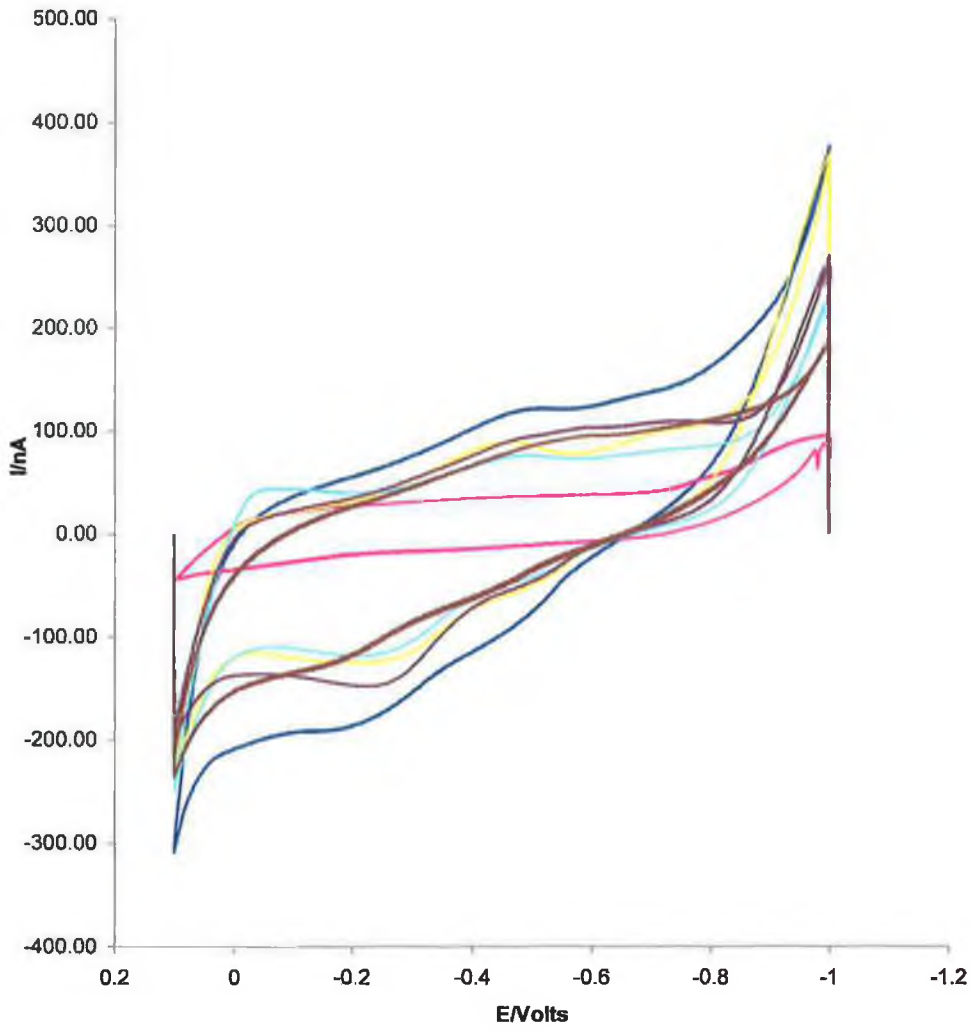

Figure 4.10 Overlay of cyclic voltammograms for a 25μm radius copper microelectrode in 0.1M $HClO_4$, with increasing pH to a pH of 7. The scan rate is $0.1Vs^{-1}$. The potential limits are 0 and -0.8V. Legend = - pH2, - pH3, - pH4, - pH5, - pH6, - pH7.

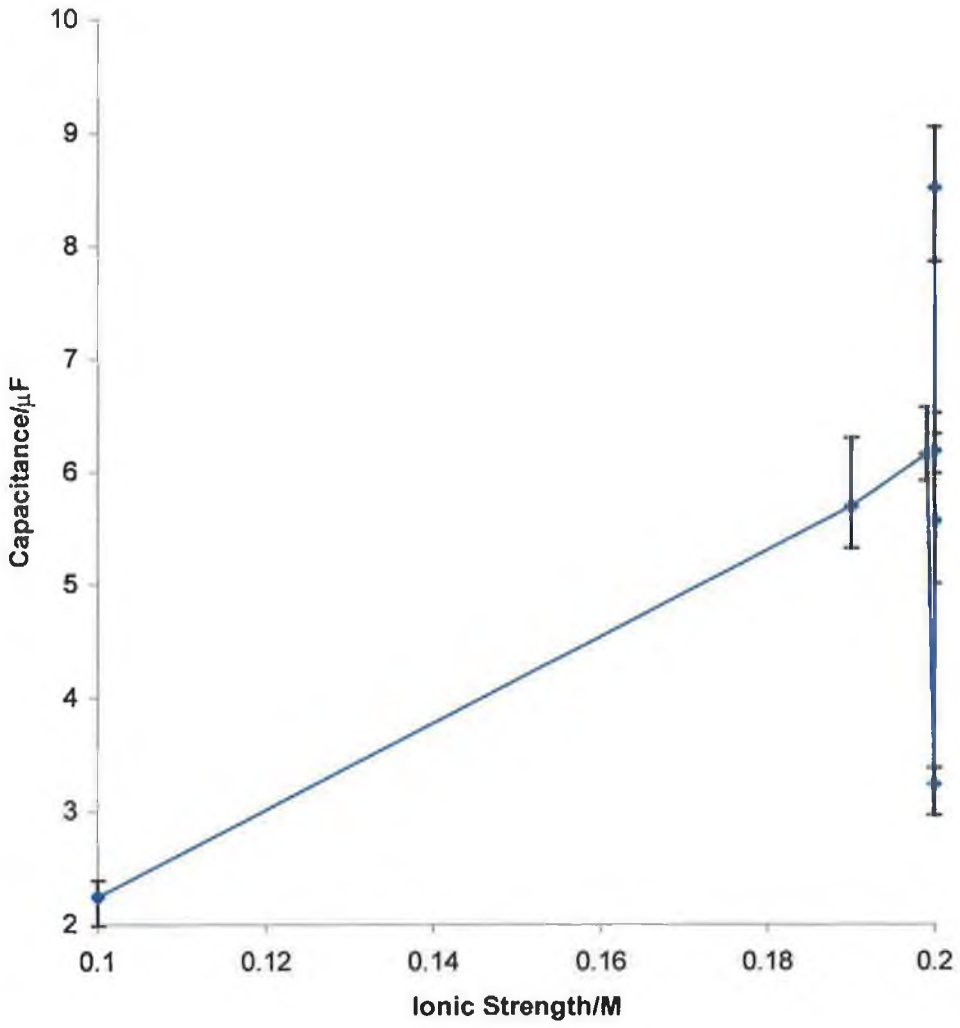

Figure 4.11 A plot of ionic strength of the electrolyte solution versus capacitance.

4.3e Chronoamperometric measurements

The time required to charge a capacitor to 63% of its full charge or to discharge it to 37% of its initial voltage is known as the time constant of the circuit [21]. The value of this time constant in seconds is equal to the product of the resistance, in ohms and the circuit capacitance in farads [9]. Resistance directly affects the time required to charge a capacitor with the time constant increasing with increasing resistance. The resistance in this case is the total resistance of the system, a combination of the resistance of both the copper electrode and the electrolyte solution.

It is imperative to know the resistance, capacitance and RC time constant of the clean copper microelectrodes in background electrolyte so as to evaluate the effects of metal deposition on the system, e.g. increased/decreased capacitance, longer/shorter RC time constants etc. A low RC time constant is necessary for the calculation of the dynamics of metal adsorption, which is one of the major objectives of Chapter 5 for the electrodeposition of indium on copper microelectrodes.

This experiment involves a potential step being applied to the electrochemical cell and measuring the current from the time the potential step is applied to the time it takes for the current to decay to a minimum. From this data, a plot of natural log of current versus time is constructed. The slope of this plot gives the RC time constant for the cell and from this value, the resistance and capacitance for the overall cell can be calculated. The resistance is calculated using the following equation:

$$i_c(t) = \frac{\Delta E}{R}\exp\left(\frac{-t}{RC}\right) \qquad \text{(Eqn. 4.13)}$$

where $i_c(t)$ is the charging current, ΔE is the amplitude of the potential step, R is cell resistance, t is time and RC is the resistive-capacitive time constant for the

system. Once the resistance and the RC time constant is known, it is possible to calculate the capacitance of the system from the RC time constant divided by the resistance.

The chronoamperometric results from this chapter allows for the determination of the double layer charging current for the system of copper microelectrodes in background electrolyte. With this value known, the faradaic current can be calculated leading to the determination of the kinetics for the electrode reaction. Figure 4.12 illustrates a chronoamperometric plot of current versus time for Cu microelectrodes in $HClO_4$.

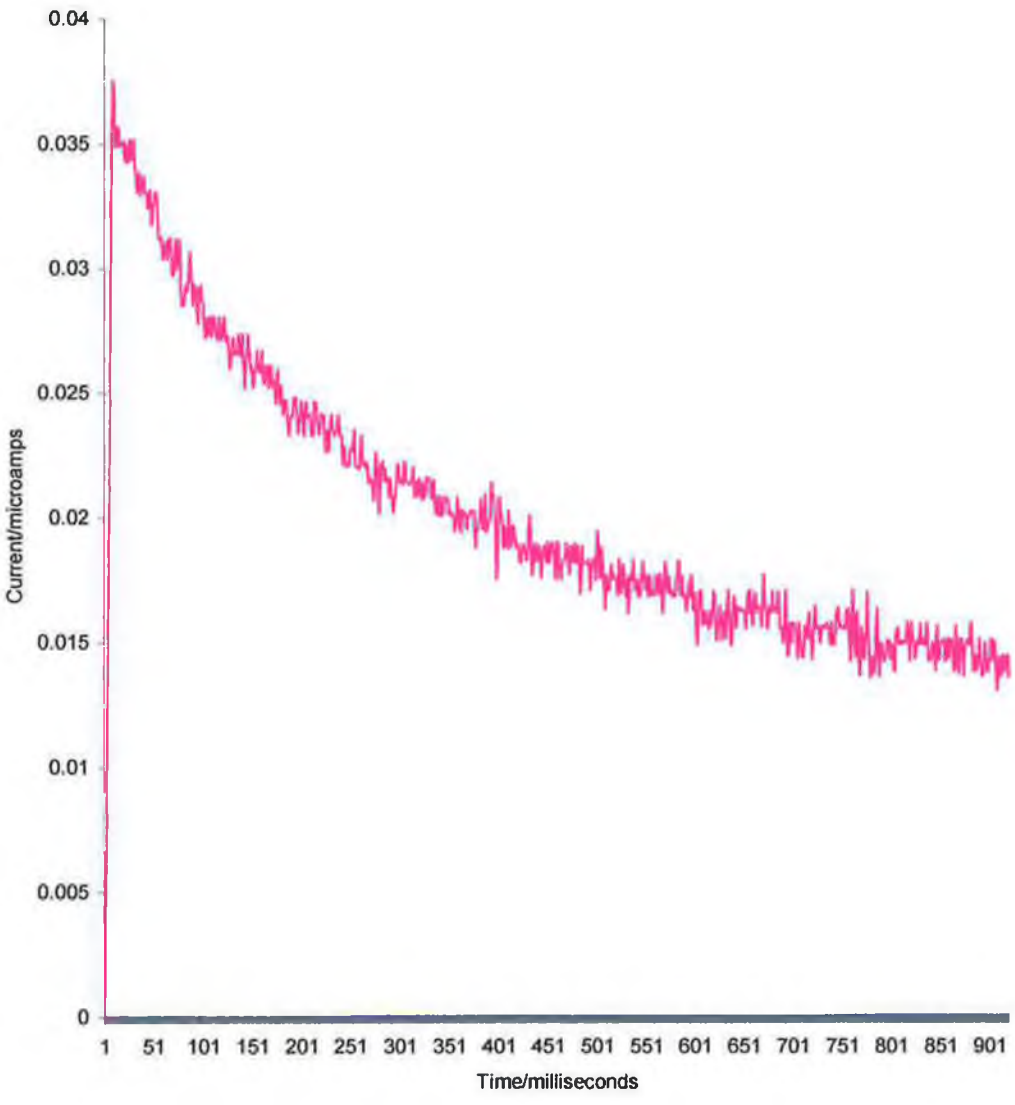

Figure 4.12 Experimental plot of current versus time for a 25μm radius copper microelectrode in 0.1M $HClO_4$. This potential step is from a potential of –77 to –377mV.

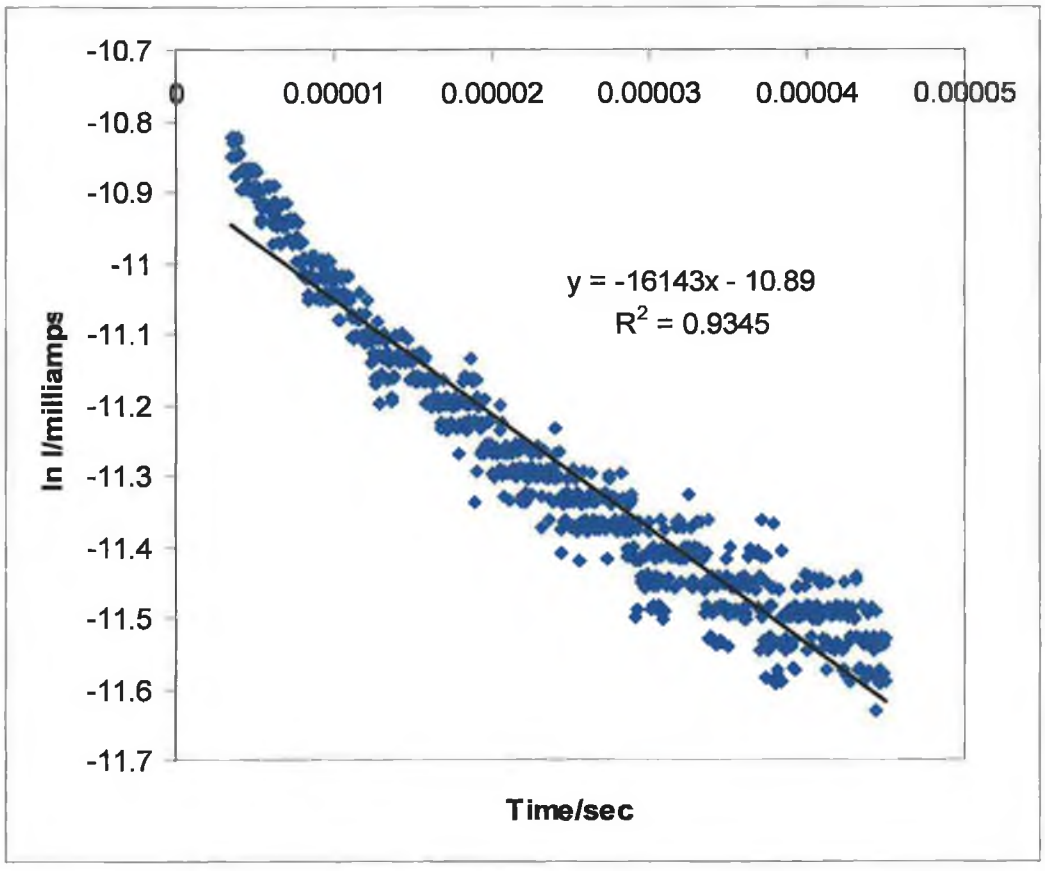

Figure 4.13 Plot of natural log of current versus corrected time of chronoamperometric data for a 25μm radius copper microelectrode in 0.1M $HClO_4$. The potential step for this plot is from –77 to –377mV.

The slope of this line is equal to the product of the resistance and the capacitance to provide the RC time constant for the electrode and the given conditions. Theoretically the semi log plot of Figure 4.14 should be linear if the system was made up of a single capacitor with a single resistance. As can be seen from the graph the system gives a non-linear plot indicating that the capacitor in this system is non-ideal.

Figure 4.14 shows a graph of RC time constant versus potential for each concentration of $HClO_4$. From this graph it would seem that the RC time constant values are not dependent on potential, as only the resistance and capacitance have any bearing on the value of the RC time constant [12]. This is not completely true as capacitance is dependent on potential (discussed later), so a change in capacitance will affect the RC time constant. However, in this experiment the capacitance is several orders of magnitude lower than the resistance of the system, so the effect of potential on the RC values is minimal.

The chronoamperometric experiments were conducted for three different copper microelectrodes to ensure reproducibility with the error bars indicating the range of results about the average of all three results.

From Figure 4.14 it can be seen that there is a relationship between concentration of electrolyte solution and RC time constant as the more concentrated the electrolyte solution, the lower the RC time constant. This is consistent with the fact that as the concentration of electrolyte in solution increases, the resistance decreases because there is an increased number of electrolyte ions to carry the charge.

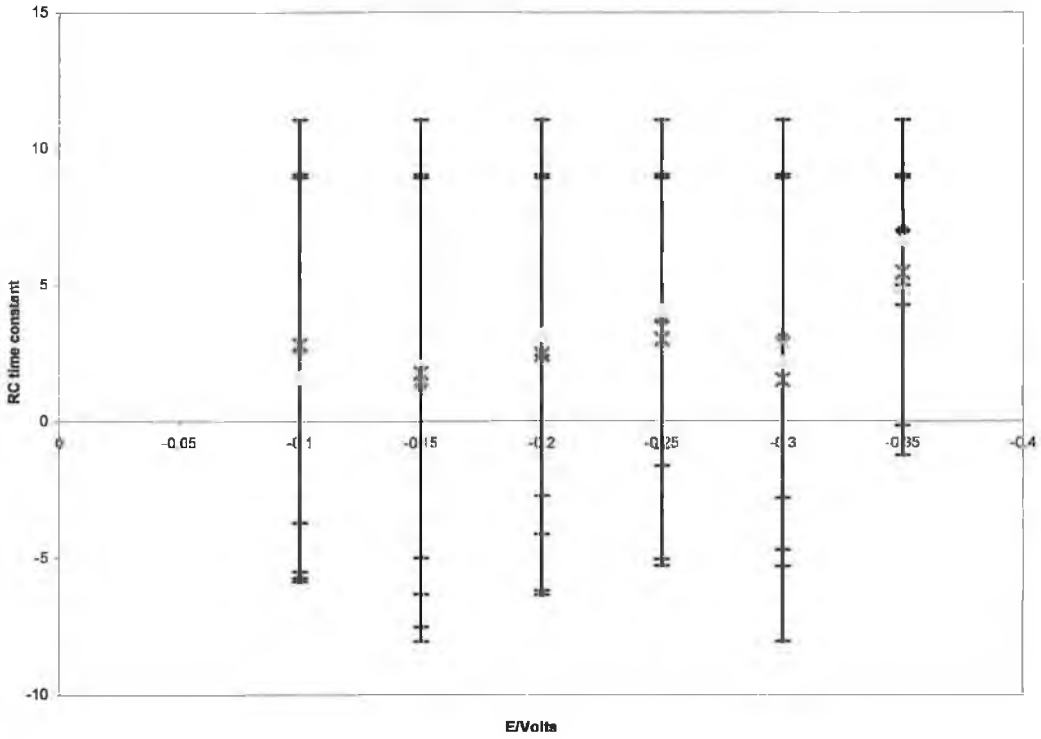

Figure 4.14 Plot of RC time constant versus potential using a 25 μm radius copper microelectrode in $HClO_4$ for electrolyte concentrations in the range 0.1M to 1.0M. Legend ◆0.1M, 0.5M, ×0.75M and ✱1.0M.

The resistance of the copper microelectrodes in solutions of increasing concentrations of $HClO_4$ is calculated from the graph of natural log of current versus corrected time. Figure 4.15 illustrates a plot of resistance of each concentration of $HClO_4$ versus potential. Experimental results indicate that the total resistance of the system is independent of potential, with resistance values remaining constant over the potential range. Resistance found within the electrode-electrolyte solution is however dependant on ion sizes, as this variable determines the ease with which ions are able to diffuse through to the electrode [22].

As expected, the resistance did change with concentration of electrolyte, with the 0.1M $HClO_4$ solution exhibiting the highest level of resistance with resistance decreasing as the concentration of electrolyte increases above this concentration. From this and in accordance with theory [23], the resistance of an electrolyte (also known as conductance) is equal to 1/concentration of electrolyte.

A solution of 0.25M $HClO_4$ was also part of the experimental series of solutions but unfortunately there were problems with the results. The experimentally determined resistance of the 0.25M solution was compared to the theoretical value of resistance for a solution of 0.25M $HClO_4$ using the formula [24]:

$$R = \frac{1}{4\kappa r}$$

Where R is resistance, κ is the equivalent conductivity of the electrolyte [25] and r is the radius of the electrode. On comparison it was found that both values differed by approximately an order of magnitude, with the experimental resistance calculated to be 2.3×10^4 compared to a theoretical resistance of 2.5×10^3. The experimental resistance of the 0.1M $HClO_4$ was calculated to be 1.62×10^3, with the theoretical resistance calculated to be approximately 1×10^3. A Q-test was conducted on the resistance values for the 0.25M $HClO_4$ solution to determine

whether the result should be accepted as an outlier or rejected as unreliable data. The result of the Q-test was to reject the set of results as it gave a value of 4.58 when the accepted value was 0.64.

Using both the resistance and the RC time constant, the capacitance for each concentration of $HClO_4$ can be calculated from the slope of the semi-log plot. As illustrated in Figure 4.16, the capacitance is then divided by the area of the electrode to give values for capacitance per cm^2 and plotted against potential for each concentration of $HClO_4$ It can be seen that as the concentration of electrolyte increases, the capacitance increases accordingly, with the 1.0M $HClO_4$ solution exhibiting the highest level of capacitance. This is explained by the Guoy-Chapman model for the electrical double layer, who proposed that the electrolyte solution is subdivided into laminae, parallel to the electrode and of uniform thickness [9]. All of these laminae are in thermal equilibrium with each other but are not at the same energy due to variation in the electrostatic potential. These laminae can be regarded as energy states with equivalent degeneracies, hence the number concentrations of species in two laminae have a ratio determined by a Boltzmann Factor. This model therefore involves a diffuse layer of charge in solution. The greatest concentration of excess charge would be adjacent to the electrode, where electrostatic forces are most able to overcome the thermal processes, while progressively lesser concentrations would be found at greater distances as those forces become significantly weaker. We can also expect the average distance of charge separation to show dependence on potential and electrolyte concentration. As the electrode becomes more highly charged, the diffuse layer should become more compact and the differential capacitance (C_d) should rise. As the electrolyte concentration rises, there should be a similar compression of the diffuse layer and a consequent rise in capacitance. The main problem with this model is that ions are not restricted with respect to location in the solution phase, they are considered as point charges that can approach the surface arbitrarily closely. This doesn't take into account that ions have a finite size and cannot approach the surface any closer than the ionic radius. Also if they

remain solvated, the thickness of the primary solution sheath plus a layer of solvent on the electrode surface, must be added to the ionic radius. Thus we can envisage a plane of closest approach for the centers of the ions at a distance x. Stern modified the Guoy-Chapman model to consider these additional considerations. He proposed that the capacitance of the double layer consists of the capacitance of the compact layer in series with that of the diffuse layer, i.e.

$$\frac{1}{C_d} = \frac{1}{C_H} + \frac{1}{C_D} \qquad \text{(Eqn. 4.14)}$$

where C_H and C_D represent the capacitance of the charges held at the Outer Helmholtz (compact) layer and diffuse layer, respectively. The value of C_H is independent of potential, but C_D varies in a V-shaped fashion around the point of zero charge (PZC). The composite capacitance C_d shows a complex behaviour and is governed by the smaller of the two components. Near the PZC in systems with low electrolyte concentration, we expect to see the V-shaped function characteristic of C_D. At larger electrolyte concentrations C_D becomes so large it no longer contributes to C_d and one sees only the constant capacitance of C_H. The experimental results for this system as seen in Figure 4.16 agree with the theory suggested by the GCS model. From this figure, there is clearly a relationship between capacitance and applied potential, with the capacitance increasing as the potential is made more negative.

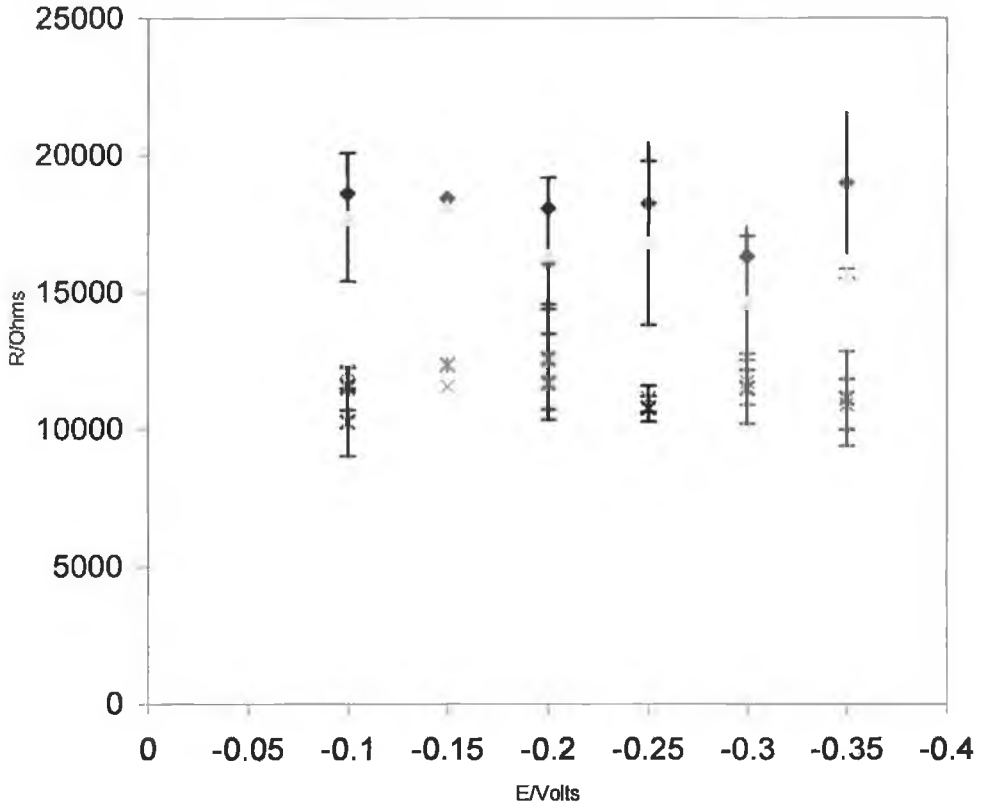

Figure 4.15 Plot of resistance versus potential using a 25 μm radius copper microelectrode in $HClO_4$ for electrolyte concentrations in the range 0.1M to 1.0M. Legend ◆0.1M, 0.5M, ×0.75M and ∗1.0M.

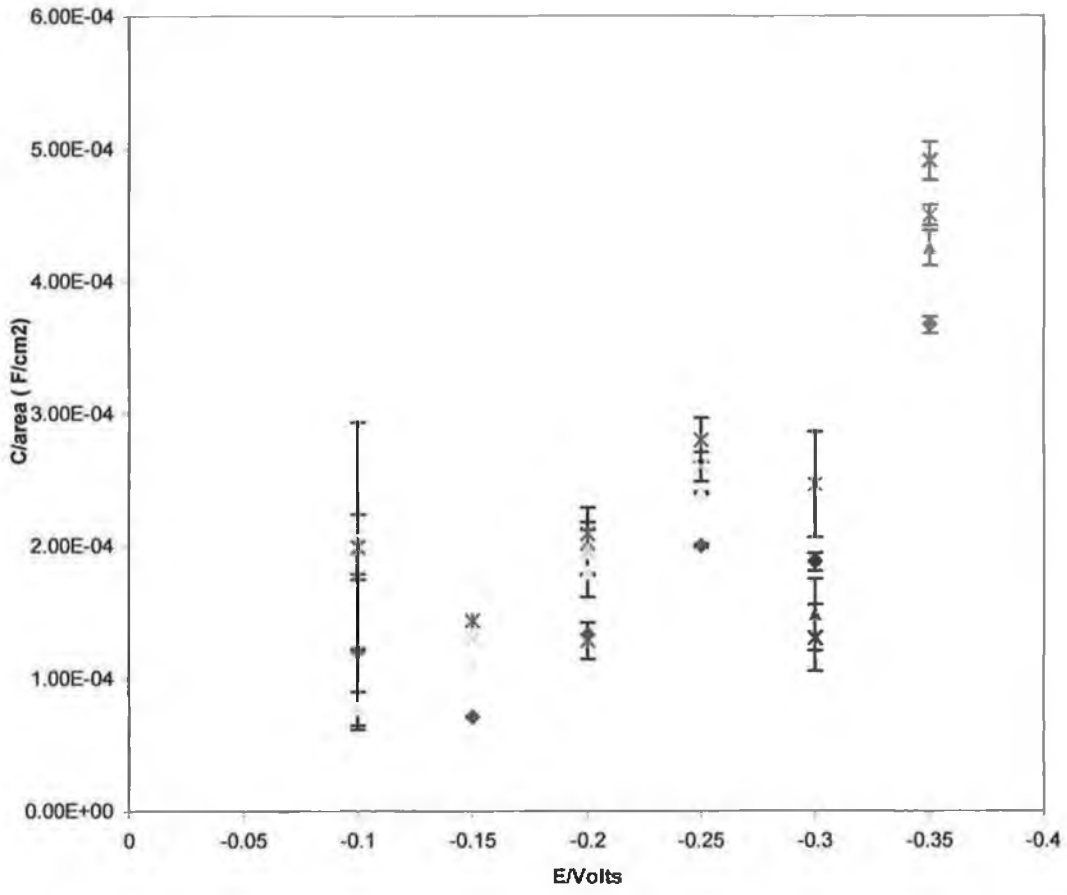

Figure 4.16 Plot of capacitance per unit area versus potential using a 25 μm copper microelectrode in $HClO_4$ for electrolyte concentrations in the range 0.1M to 1.0M. Legend ◆0.1M, 0.5M, 0.75M and ∗1.0M.

4.4 Conclusion

Very little information has been published on the fabrication or properties of copper microelectrodes [26]. The fabrication process developed here, is fairly reproducible but there is a tendency to form Cu_2O during the heat-sealing of the glass tubing. This tendency was minimized by applying a vacuum to the untapered end of the glass tube, though this does not fully remove the possibility of Cu_2O formation. The formation of Cu_2O is only noticeable once the tapered end has been sealed and only through the use of a strong magnifying glass, as Cu_2O manifests itself as a dull greenish colour on the bright copper wire. If Cu_2O is indeed formed, it renders the electrode useless as the resistance is increased by several orders of magnitude and the electrode must be abandoned.

The real surface area of a 25μm copper microelectrode is 1.85×10^{-4} with a surface roughness value of 2.3, indicating that the surface of the electrode is relatively smooth.

A wide potential window for Cu microelectrodes in 0.1M $HClO_4$ is desirable for electroanalysis. However, it was discovered that at potentials positive of –0.08V a large peak is formed due to the formation of Cu_2O at the electrode surface. In the negative direction, the potential window is curtailed by the formation of a large peak below –0.6V, thought to be due to the bulk evolution of hydrogen from the acidic electrolyte, 0.1M $HClO_4$.

The problems of oxide formation on the electrode and bulk evolution of hydrogen from the electrolyte were greatly reduced by an increase in pH of the background electrolyte. At a pH of 4.45 the interference from both reactions is at a minimum giving a potential window of +0.1 to –1.0V. Increasing the pH above 4.45 causes a large increase in capacitance, so it becomes a trade-off between keeping the pH low enough to achieve a good cyclic voltammogram and high enough to avoid the

limitations caused by the oxide formation and hydrogen evolution reactions. This is best achieved at a pH of approx. 4.5.

The chronoamperometric results are in accordance with theoretical propositions. Capacitance was found to be dependent on potential, as the potential is increased from the PZC, the capacitance increases linearly in accordance with the GCS model. The relationship between the two is also evidenced by the formation of a dip in the straight line between –0.25 and –0.3V, this is thought to be caused by contact adsorption from ions in the electrolyte and solvent reorganization around the electrode. It can also be seen that the capacitance increases with higher concentrations of electrolyte, this agrees with the Gouy-Chapman-Stern model for the double layer. In the GCS model, as the concentration of electrolyte increases, the capacitance increases as the diffuse layer becomes more compact, meaning less distance between ions and enabling easier retention of charge.

Experimentally, it was found that both the RC time constant and resistance are independent of potential. In theory, the RC time constant should vary with potential as it is the product of the resistance and capacitance, however in this system the resistance is orders of magnitude larger than the capacitance so the effect of capacitance on the RC time constant value is minimal.

It is noticeable that there is a relationship between the concentration of electrolyte and the RC time constant as the more concentrated the electrolyte solution the lower the RC time constant. This is because as the concentration of solution increases the resistance of the solution decreases due to an increased number of ions available to carry the charge. This view is also borne out by the graph of resistance versus potential whereby the relationship between resistance and concentration of electrolyte is similar to that of the RC time constant, with an increase in concentration of electrolyte corresponding to a reduction in cell resistance.

The results from this study offer much significant information on the fabrication of copper microelectrodes, their use in electroanalysis and in particular their importance in conducting a consequent study on the electrochemical deposition of indium on copper microelectrodes in background electrolyte. The size of the potential window is small in respect to other metals (e.g. the potential range for platinum in background electrolyte is from +1.2V to –0.2V [4]), due to peaks formed by oxide formation in the positive direction and hydrogen evolution from the acidic medium in the negative direction. This limits the potential window from –0.08 to –0.6V at a pH of 1.03. Although this range is useful to a degree in electroanalysis as there are some compounds whose potentials lie within this limit, the number of compounds available for analysis is restricted. Changing the pH from 1.03 (original pH of $HClO_4$) to a pH of approx. 4.5, expands the potential window to a range of +0.1 to –1.0V, allowing for a much wider variety of compounds to be analysed. An example of this is seen in the next study as the deposition of In on copper microelectrodes in background electrolyte occurs at a potential of –0.6V. If the system was limited to the original potential window then electrodeposition of In would be impossible to measure as it would be masked by the hydrogen evolution peak. As it is possible to widen the potential window with increased pH the In deposition potential lies well within this improved potential window making the study of electrochemically deposited indium on copper microelectrodes possible. The system is at its peak at a pH of 4.5, below this pH the potential window has limitations imposed by both the copper oxide and the hydrogen evolution reactions. The pH is altered using NaOH, so above a pH of 4.5 the capacitance increases to a level where the results become unreliable, the increase in capacitance is due to an increase in ionic strength from the presence of large amounts of NaOH in the system.

Calculation of the microscopic surface area of the electrode gives the value of active surface sites on the electrode. The loading of the electrode with deposited materials rely on this value for accurate determination of the concentration of deposited material. This value is necessary for the establishment of the amount of

deposited indium needed to deposit concentrations of up to 1ML on the electrode surface in the subsequent chapter.

The chronoamperometric results from this chapter enable the kinetics of the electrode reaction for deposited materials to be calculated. As discussed earlier, once the double layer charging current in the system is ascertained, the faradaic current for a deposition reaction can be calculated and from this value it is possible to resolve the kinetics of the electrode reaction. The RC time constant, resistance and capacitance results for the copper microelectrodes in background electrolyte can act as a reference for results obtained from deposition reaction. Any differences in behaviour of the system after deposition occurs must be due to the deposited material.

4.5 References

1. S. Bloxham, O. Eicher-Lorka, R. Jakubenas, Spectroscopy Lett., 36(2003)3.
2. J. Newman, J. Electrochem. Soc., 1970, 117, 198.
3. Robert J. Forster, Chem. Soc. Rev. (1994)
4. Shin Lin Chou, Tankang Tse-Chuan, Journal of Science and Engineering 6(2003)195.
5. Robert J. Forster, The Electrochemical Society Interface, (2000)24
6. Matthew Scott, Karan V.I.S. Kaler, Reginald Paul, Journal of Colloid and Interfacial Science, 238(2001)449.
7. R.M. Wightman and D.O. Wipf, Electroanal. Chem., 1989.
8. Adrian W. Bott, Current Separations, 14(1996)3/4.
9. Southampton Electrochemistry Group, 'Instrumental Methods in Electrochemistry', Horwood, Chichester, 2001.
10. Karel Stulik, Christian Amatore, Karel Holub, Vladimir Marecek, Wlodzimierz Kutner, Pure Appl. Chemistry, 72(2000)1483.
11. Donald T. Sawyer and Julian L. Roberts JR., 'Experimental Electrochemistry for Chemists', 118 , Wiley, New York, 1974.
12. http://chem.ch.huji.ac.il/~eugeniik/electrochemical_tutorials.htm
13. S. Pons and M. Fleischmann, Anal. Chem., 1987, 59, 1391A.
14. www.chem.unc.edu/undergrads/2001summer/sum1/chem_wallen/pptfiles/week04/62201.ppt
15. L. K. Robinson, Y. S. Chu and A. A. Gewirth, 'Water-interface structures on Cu(111) electrodes', University of Illinois, Urbana IL 61801, USA.
16. A.J. Bard and L.R. Faulkner, 'Electrochemical Methods', 15, 267, Wiley, New York, 1980.
17. William J. Clarke and Richard L. McCreery, Journal of the Electrochem. Soc., 149, B379-B386, 2002.
18. Serdar Aksu and Fiona M. Doyle, University of California at Berkeley, 2003.

19. Srdjan Nesic, and Miran Vrhovac, Journal of Corrosion Science and Engineering, Vol. 1, 1997.
20. http://www.qprox.com/background/capacitance.php
21. http://www.tpub.com/neets/book2/3d.htm
22. A. Burke, Journal of Power Sources, 2000, 91, 3750.
23. www.chemistry.nmsu.edu/studntres/chem435/Lab4/intro.html
24. http://www.eng.hawaii.edu/~ssi11/SSI-11Papers/A59.pdf
25. C. Xu, PhD Thesis, University of Illinois at Urbana-Champaign, 1992.
26. Dominic P. O'Hanlon, PhD Thesis, Dublin City University, 1999.
27. Darren Walsh, PhD Thesis, Dublin City University, 2002.
28. Y. Sato, Journal of Electroanalytical Chemistry, 409 (1996) 145-154.

Chapter 5
Electrodeposition of Indium on Copper Microelectrodes

5.1 Introduction

During the last two decades, great interest has developed among electrochemists in the preparation of modified electrodes by deposition on the electrode surface [1]. The properties of deposited heavy metals and conducting polymers have been extensively studied. However, there have been only a few investigations considering the nucleation and growth processes using microelectrodes. Potentiodynamic conditions are mainly used to perform the electrochemical work at which the growth cannot be easily subjected to theoretical analysis [2]. Potentiostatic experiments can be conveniently used to monitor and elucidate the kinetic and mechanistic details of the deposition itself. As a result of extensive work, various theories and models have been developed and some mechanistic details have been revealed for the electrochemical deposition of metal [3]

Many important electrode reactions involve the formation of a solid phase, either as the result of the reduction of ions in solution, as in the case of metal deposition, or by oxidation of the electrode and subsequent reaction with anions to form a film. The term electrocrystallisation is used to describe electrode processes of this kind.

Electrocrystallisation involves a number of distinct steps, these being

(I) diffusion of ions in solution to the electrode surface,
(II) electron transfer,
(III) partial or complete loss of the solvation sheath, resulting in the formation of ad-atoms,
(IV) surface diffusion of ad-atoms,
(V) clustering of ad-atoms to form critical nuclei on a perfectly smooth surface or on a foreign substrate,
(VI) incorporation of ad-atoms at lattice sites,
(VII) development of crystallographic and morphological characteristics of the deposit.

Although, in practical terms, the last of these steps is of most interest, it is also necessary to look more closely at the earlier stages of the electrocrystallisation

process in order to gain a fundamental understanding of the thermodynamics and kinetics of electrocrystallisation [4].

This chapter attempts to investigate the process of electrodepositing indium on a copper electrode surface, in particular the nucleation type and growth mode of the electrodeposited material.

Although no information has been published on the electrodeposition of indium on copper electrodes, a number of previous studies have been conducted on the co-deposition of indium and copper on other metal substrates as precursors for the formation of $CuInSe_2$ used as an economically viable solar cell. In 1996, Prosini et al. conducted a study on thin films of copper-indium alloys on a molybdenum electrode substrate [5]. They used solutions of 4mM copper chloride and 4mM indium chloride with 0.1M Boric acid acting as background electrolyte. The copper-indium alloys were plated potentiostatically at –0.825V versus Ag/AgCl. At this potential they encountered problems with double-layer charging and the reduction of other electroactive species which gave rise to a superimposed current that totally hid the signal related to the nucleation phenomena. The nucleation kinetics was investigated by potentiometric current-time transients. They found the deposition process involved instantaneous nucleation on an untreated molybdenum electrode and progressive nucleation for deposition on an ammonia treated molybdenum electrode with diffusional-controlled growth of the three-dimensional nuclei. This study was a follow on from a previous study by the same group earlier on in 1996 [6], which looked at electrodepositing Cu and In on sputtered molybdenum on glass as a working electrode under diffusion-limiting current. A set of Cu-In alloys were deposited from solutions with different compositions at –0.825Vin a three-electrode cell, and the diffusion limiting currents were measured. They felt that owing to the simple correlation between [Cu]/[In] ratio in solution and [Cu]/[In] ratio in the deposited film, the potentiostatic electrodeposition technique can be considered an effective method for obtaining Cu-In alloys with fine control of the composition.

Another study in 1996 by Calixta et al. looked at electro and electroless deposition and characterisation of Cu-In alloys as precursors for $CuInSe_2$ [7]. The electrodeposition method involved the sequential deposition of Cu/In and In/Cu on

Mo/glass, SnO_2/glass and Cu foils. The Cu-In precursors were characterised using X-Ray Diffraction (XRD), Scanning Electron Microscopy (SEM) and Electron Probe Microanalysis (EPMA). The electrodeposited films were characterised with respect to their morphological and compositional nature. They found the major phases in the precursors to be $Cu_{11}In_9$ and elemental indium which may lead to the In-rich CIS phase ($CuIn_2Se_{3.5}$), during sintering in argon at lower temperatures.

Other studies conducted on copper and indium co-deposition involved simultaneous deposition of selenium [8-13] but it is felt these studies stray too far from the subject of this study.

5.2 Experimental

Determination of potential window

To determine the potential window, a number of cyclic voltammograms were taken at increasing potential ranges until a suitable potential window for electrodeposition of indium was found. Potential windows of –0.08 to –0.6V, -0.08 to –0.8V and –0.08 to –1.0V, were examined. The electrochemical cell consisted of a copper microelectrode which acted as the working electrode, an Ag/AgCl electrode as reference and a platinum wire as the auxiliary electrode, in a solution of 4mM $InCl_3$ and 0.1M Boric acid, which acted as supporting electrolyte.

Effect of increasing scan rate versus amount of indium deposited

Cyclic voltammograms were taken of increasing scan rates from 0.01 to 5 Vs^{-1} for the three potential windows tested to determine the effect of scan rate on the electrodeposition of indium.

SEM and EDX results

Indium was electrodeposited on 1.25mm macroelectrodes. Once the cyclic voltammogram was scanned to the negative limit of the potential window, the potential was held while the copper macroelectrode was removed, leaving indium deposited on the electrode surface. This macroelectrode was analysed using SEM and EDX to view the deposited indium.

Nucleation type and growth mode

Chronoamperometry was used to apply two potential steps of equal potential width. The first (+0.1 to –0.4V) was at a potential positive of the $E_{½}$ value for indium electrodeposition, with the second (-0.3 to –0.8V) traversing the $E_{½}$ value and driving metal deposition. The current versus time was measured for each potential step. The current versus time plot for the first potential step, taken prior to indium's $E_{½}$ potential was used as a background, as any change in current is due to the decay of the RC time constant for the system. This background is mathematically subtracted from the current versus time plot for the potential step incorporating the indium's $E_{½}$

potential to leave any change in current due to metal deposition on the copper substrate. From this graph a plot of I/I_{max} and $(I/I_{max})^2$ versus time is constructed and overlaid on a plot of current transients for the four different nucleation types and growth modes. These transients are constructed from formulae derived by Harrison et al. [14].

Kinetics of electrodeposited indium on the copper microelectrodes

Using the plot of current versus time due purely to metal deposition as derived in the last experiment, a plot of Ln of current versus time was constructed. From this graph the reaction order was determined. A plot of current versus $t^{-½}$ was also constructed to elucidate the influence of diffusion on the electrochemical system.

Electrochemical stripping

Using a two-step chronoamperometry experiment, the first potential step deposits indium on the copper substrate and the second potential step electrochemically removes the deposited material from the substrate surface. In this experiment only the second step is of interest, with current versus time plots constructed for the return step for both potential ranges. The current versus time plot for the potential step prior to the $E_{½}$ potential again acted as background and was mathematically subtracted from the current versus time plot for the potential step incorporating the $E_{½}$ value for indium deposition. This gave a current versus time plot for the electrochemical removal of indium from the copper substrate. From this graph the kinetics for the electrochemical removal of indium can be elucidated and an insight into the mechanism of indium removal obtained.

5.3 Results and Discussion

In Chapter 2 of this thesis, the method of UHV deposition of indium on a Cu{100} substrate was studied and the subsequent structures formed by increased concentrations of indium were investigated. This chapter details the electrochemical deposition of indium on copper micro and macro electrodes. It investigates the potential window for indium electrodeposition on copper microelectrodes, determines the effect of the adsorbed indium on the electrochemical properties of the copper microelectrodes, attempts to establish the metal deposition kinetics and endeavours to elucidate the nucleation type and growth mode of the electrodeposited indium.

It is hoped that a comparison of the methods of UHV deposition of indium on Cu{100} and electrodeposition of indium on copper electrodes will provide not only information on the respective techniques and their application but also evaluate the effects of the deposited indium on each substrate.

5.3a Potential Window

In the previous chapter it was established that copper microelectrodes in background electrolyte (0.1M $HClO_4$) have a potential window of –0.08 to –0.6V, however after adjusting the pH to a value of 4.45, the potential window was widened to a range of +0.1 to –1.0V.

The theoretical $E_{½}$ value for indium on Cu electrodes was thought to be in the region of –0.6V, based on the $E_{½}$ values of –0.541V [12] and –0.825V[4] for the electrodeposition of indium on antimony electrodes and the electrodeposition of copper and indium on molybdenum microelectrodes.

It was decided to run a cyclic voltammogram over the original potential window for copper microelectrodes in background electrolyte of –0.08 to –0.6V. Figure 5.1 features this cyclic voltammogram for a system of copper microelectrodes in a solution of 4mM $InCl_3$ and 0.1M Boric acid at a scan rate of $0.1Vs^{-1}$ and a pH of 4.2.

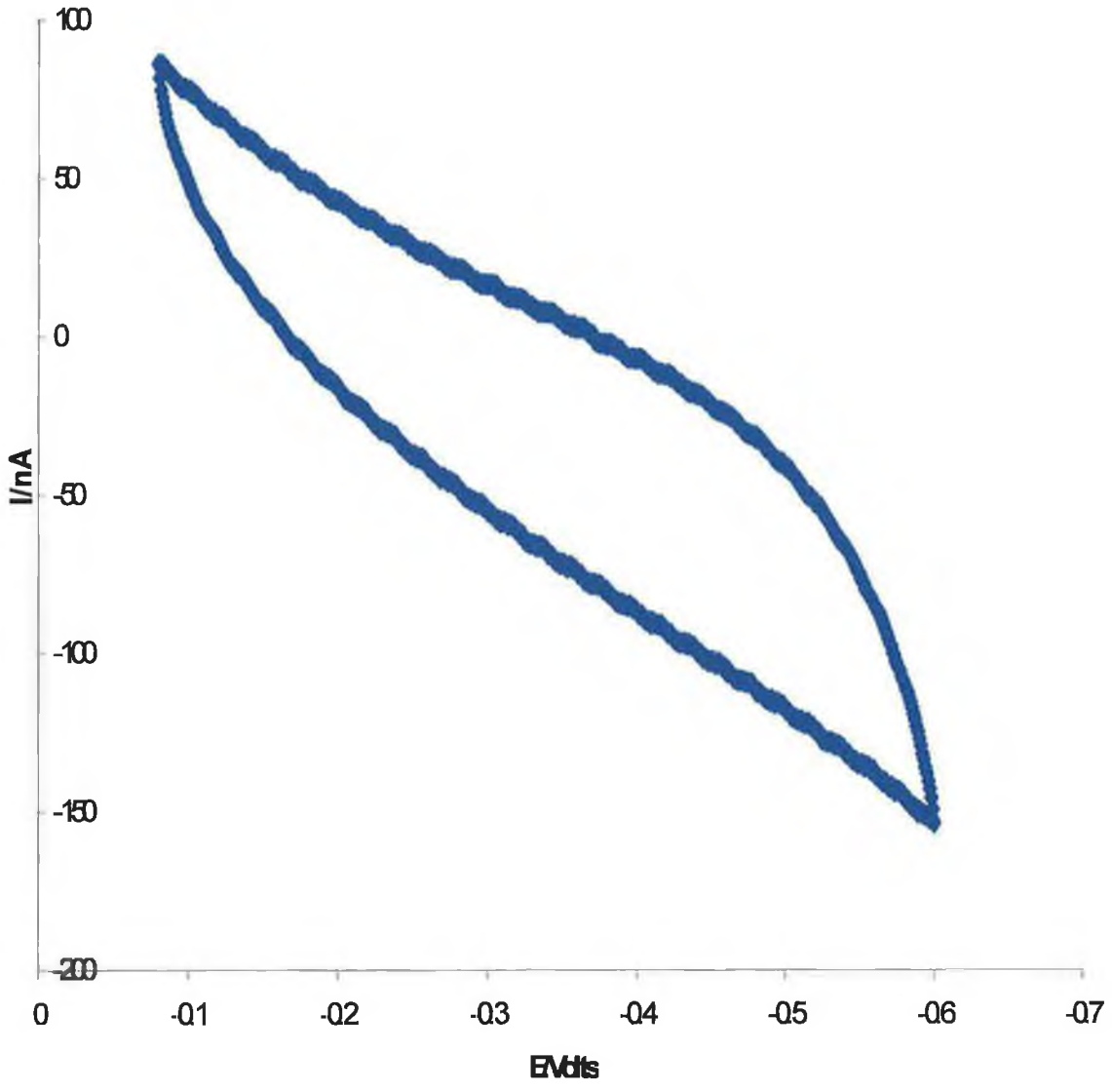

Figure 5.1 Cyclic voltammogram for a 25μm radius copper microelectrode in a solution of 4mM $InCl_3$ and 0.1M boric acid. The scan rate is $0.1Vs^{-1}$. The potential limits are –0.08 and -0.6V.

As expected the CV exhibited no indication of indium reduction or oxidation, as the theoretical value for $E_{½}$ was thought to be in the region of –0.6V. The CV is however of a reliable quality, an elliptical shape with a low slope and a current amplitude of less than $10\mu Acm^{-2}$.

The electrode is polished to ensure that the experimental response is not compromised by the electrode history. The potential window was made more negative in an effort to accommodate the theoretical $E_{½}$ value of indium. The window was expanded to a potential range of –0.08 to –0.8V.

Figure 5.2 illustrates a CV of copper microelectrodes in a solution of 4mM $InCl_3$ and 0.1M Boric acid over the new potential range. Over this potential range indium undergoes both oxidation and reduction. The $E_{½}$ value for indium in this system is found experimentally to be –0.658V, which compares favourably with the expected theoretical value of approximately –0.6V. Indium undergoes reduction from a potential of –0.658V ($E_{½}$ value) to the limit of the potential window at –0.8V. During this potential range, In^{3+} is reduced to In, with the gaining of 3 electrons. As the indium is reduced, a peak-shaped current-potential response is observed.

In the return scan, the current should directly track the forward sweep. However when the sweep is reversed there is a significant concentration of In present near the electrode and In continues to be formed on the reverse sweep until $E_{½}$ is reached again. As $E_{½}$ is approached, In near the electrode starts to be reoxidised back to In^{3+} (in order for the surface concentrations to be those required by the Nernst equation) and a reverse current flows. The surface concentration of In decreases but does not reach zero as the electrodeposition of metals is an irreversible reaction. In line with the explanation for the formation of the reduction peak, it can be shown that the current on the reverse sweep will also exhibit a peaked response though understandably of opposite sign.

The area under the indium oxidation peak was measured to determine the concentration of indium deposited on the copper microelectrode surface, this gave a value of $1.175x10^{-8}C$ at a scan rate of $0.1Vs^{-1}$. This value is divided by the specific

charge on the electrode surface ($420\mu C/cm^2$) to give a concentration of $2.795x10^{-5}$ mols indium on the electrode.

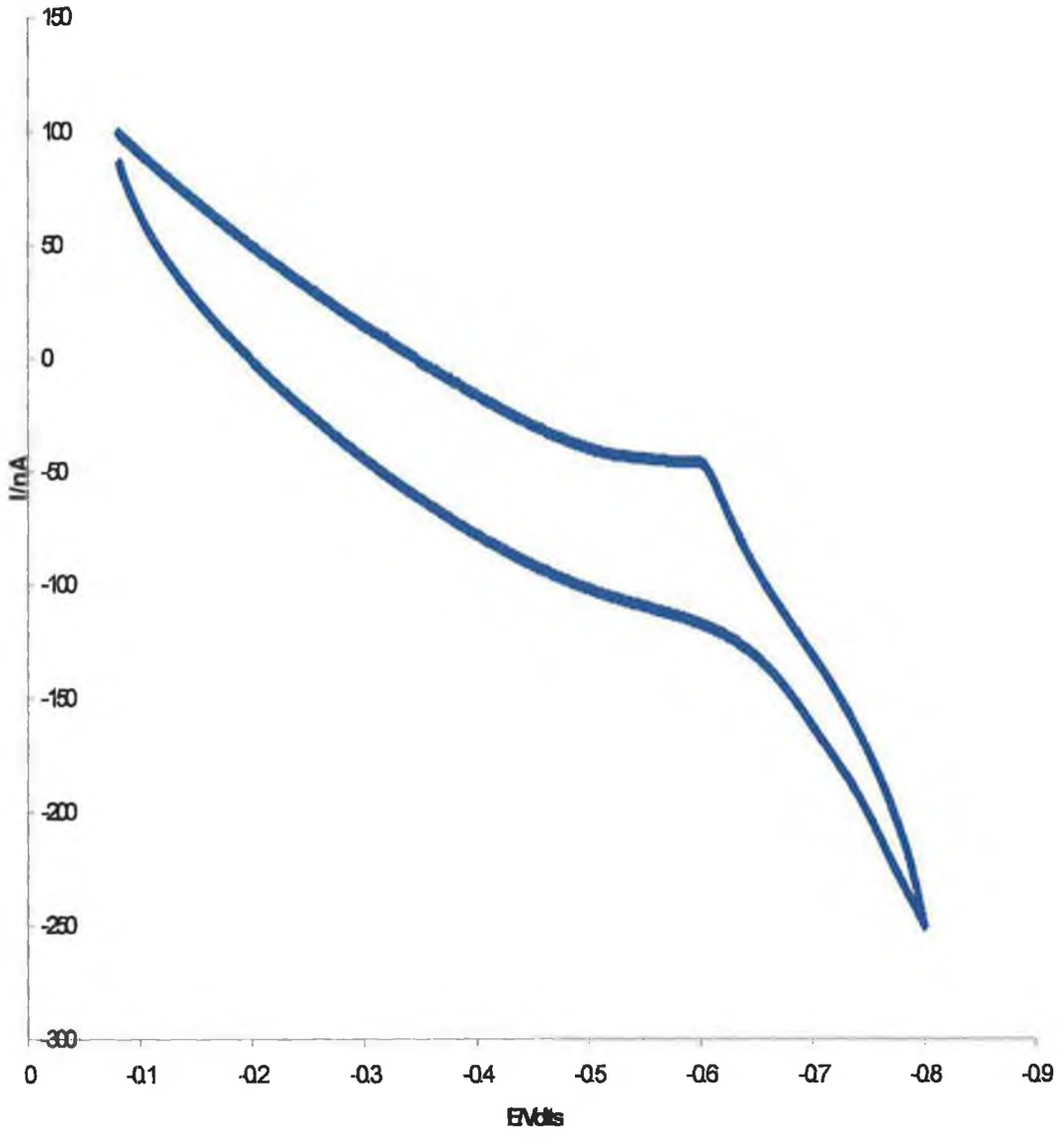

Figure 5.2 Cyclic voltammogram for a 25μm radius copper microelectrode in a solution of 4mM $InCl_3$ and 0.1M boric acid. The scan rate is $0.1Vs^{-1}$. The potential limits are –0.08 and -0.8V.

There is an indication that indium is still undergoing reduction as the potential reaches the limit of the last potential window so it was decided to widen the window again in the negative direction. The microelectrode was repolished and the potential window widened to a potential range of –0.08 to –0.1V. Figure 5.3 illustrates the resulting CV; in this potential range the $E_{½}$ value for indium deposition was found to be –0.638V, which agrees with theoretical propositions and the result from the previous potential window. The area under the indium oxidation peak was again measured to determine the concentration of indium deposited on the surface of the copper microelectrode. The size of the peak was calculated to be 1.324×10^{-8}C, giving a concentration of 3.152×10^{-5} mols of electrodeposited indium.

There is a second oxidation peak formed at a potential of –0.694V, this is thought to be due to under potential deposition (UPD). This peak is thought to be due to indium diffusing from the bulk phase rather than the electrical double layer. The size of this peak is 2.631×10^{-8}C, corresponding to a concentration of 6.264×10^{-5}mols In. To get the overall concentration of indium on the copper microelectrode surface the concentration from both peaks is added, giving an overall surface concentration of 9.416×10^{-5} mols adsorbed indium. In this potential window it can be seen that the indium is fully reduced as the reduction peak tails off before the negative potential limit is reached.

If the dissolved reactant is being consumed or transformed by electron transfer at the electrode, the concentration near the electrode is diminished. A concentration gradient dc/dx will form. Given a reasonably high exchange current density the reaction rate and thus the current may become limited by rate at which the reactant arrives at the electrode by diffusion. This leads to a limiting current for a system. The limiting current is an important design parameter because it represents the maximum rate at which an electrode reaction can proceed.

Moreover, it provides a convenient technique for studies of mass transport rate studies because mass transport coefficients can be readily and accurately calculated from the experimentally obtained current plateau [13]. A comparison of experimental limiting current versus the theoretical value gives information on the diffusion regime for the electrodeposition of indium on the copper electrode substrate and the roughness of the

metal film. The experimental limiting current is calculated by determining the change in current from the UPD $E_{½}$ value to the tip of the bulk deposition reduction peak, giving a value of 1.673×10^{-7} (calculated from Figure 5.3). The theoretical value for the limiting current is calculated using the formula:

$$i_l = 4nFDcr \qquad \text{(Eqn. 5.1)}$$

where i_l is the limiting current, n is the number of electrons transferred in the electrodeposition process (in this case 3, as In^{3+} is reduced to In), F is Faradays constant (9.648×10^{4}), D is the diffusion co-efficient (1×10^{-5} [4]), c is the analyte concentration (4×10^{-3}M) and r is the electrode radius (2.5×10^{-5}m). This gives a value of 1.158×10^{-7} as the theoretical limiting current for this system. Comparing the two values it can be seen that the experimental limiting current is 1.5 times larger than the calculated theoretical value for the limiting current. When the experimental limiting current is greater to the theoretical value it suggests that the electrodeposited indium is somewhat rough causing the modified electrode area to be somewhat larger than the original copper microelectrode.

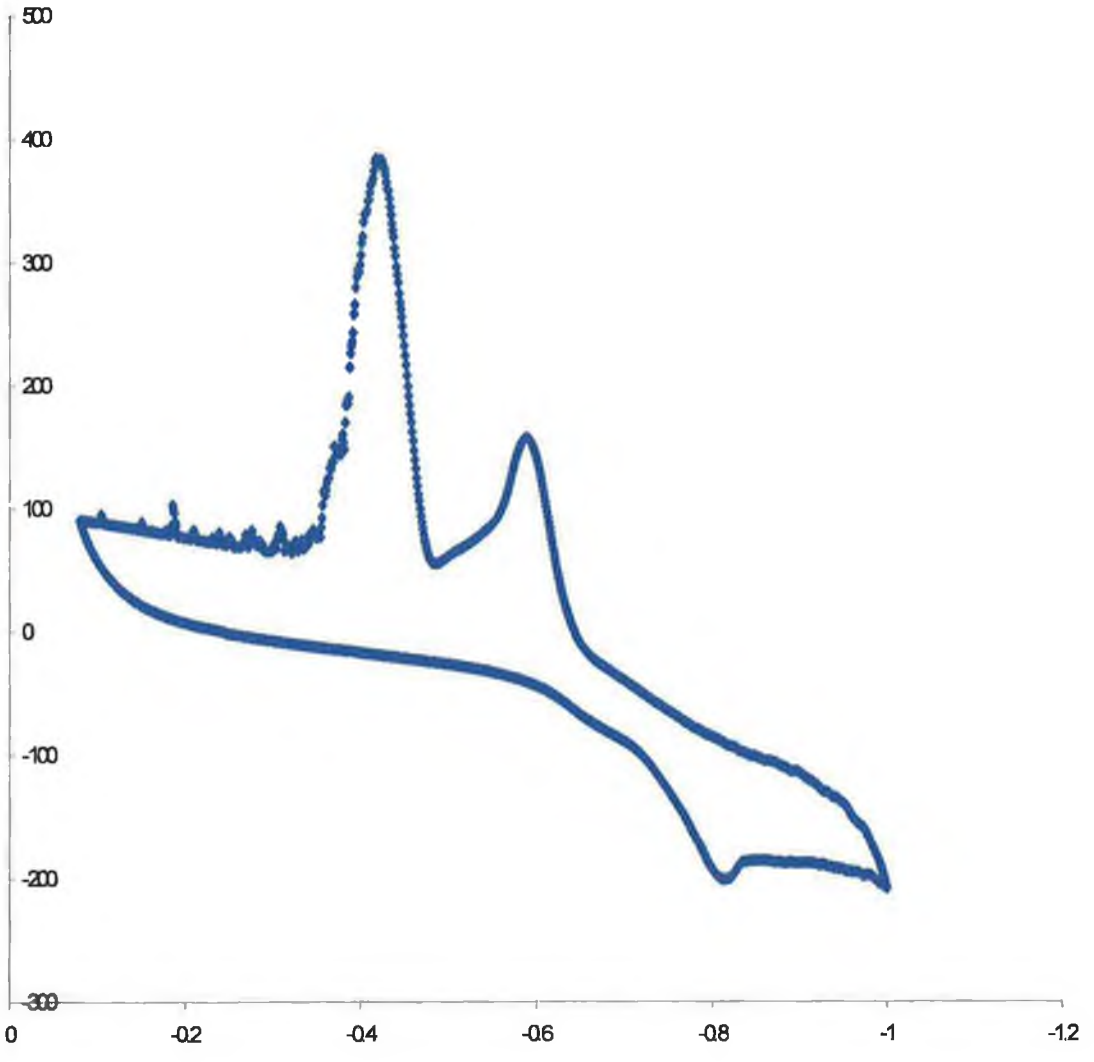

Figure 5.3 Cyclic voltammogram for a 25μm radius copper microelectrode in a solution of 4mM $InCl_3$ and 0.1M boric acid. The scan rate is $0.1Vs^{-1}$. The potential limits are –0.08 and –1.0V.

5.3b Comparison of scan rate versus amount of indium deposition

Figures 5.4, 5.5 and 5.6 are of the three potential ranges tested in the last section with increasing scan rates overlaid. In Figure 5.4, the experimentally determined potential window for copper microelectrodes in background electrolyte as established in Chapter 4 was chosen. Scan rates ranging from 0.01 to 5 Vs^{-1} were investigated. As illustrated by this figure, at a scan rate of 0.01Vs^{-1} and up to a scan rate of 0.5Vs^{-1}, the CV exhibits optimum detail, exhibits a low background current amplitude (below 10μAcm^{-2}), elliptical shape and close to a horizontal slope. As the scan rate is increased the current amplitude increases, the shape of the CV becomes increasingly distorted and the slope of the CV increases, tending towards a vertical angle rather than horizontal. After each scan the electrode is electrochemically cleaned to ensure the experimental results obtained are not affected by the electrode history.

In Figure 5.5, the potential window was expanded as in the previous section to a range of –0.08 to –0.8V; again scan rates from 0.01 to 5 Vs^{-1} are overlaid for ease of comparison. Similar results were obtained to Figure 5.4, with scans at low scan rates proving to be much more detailed and as the scan rate is increased, the resulting CV's decrease in quality with a stark deterioration in significant features. This makes sense as the faster the scan passes through the potential range the less well resolved the CV will be and it is more likely that features which would be clear and sharp could be missed, this is thought to be due to the scan rate being faster than the reaction rate for the electrodeposition of indium on the copper substrate. This is well illustrated by comparing the CVs run at scan rates of 0.01Vs^{-1} and 5Vs^{-1}. In the CV run at a scan rate of 0.01 Vs^{-1}, both the oxidation and reduction peaks are well resolved with a second oxidation peak visible, thought to be due to stripping of the under potential deposited film. There is also indication of metal on metal deposition witnessed by the hysteresis at a potential of –0.673V. In the CV run at a scan rate of 5 Vs^{-1}, there is no indication of any indium electrodeposition, the CV is featureless with a close to vertical slope and an extremely high current amplitude. It is thought from Figure 5.5 that no indium deposition occurs above a scan rate of 0.5Vs^{-1} as there is no evidence of a change in current at the experimental $E_{½}$ potential, so it is thought at this scan rate the CV scan is moving faster than the reaction rate for indium electrodeposition. Above this scan rate the CV's are featureless and deteriorate in shape as the

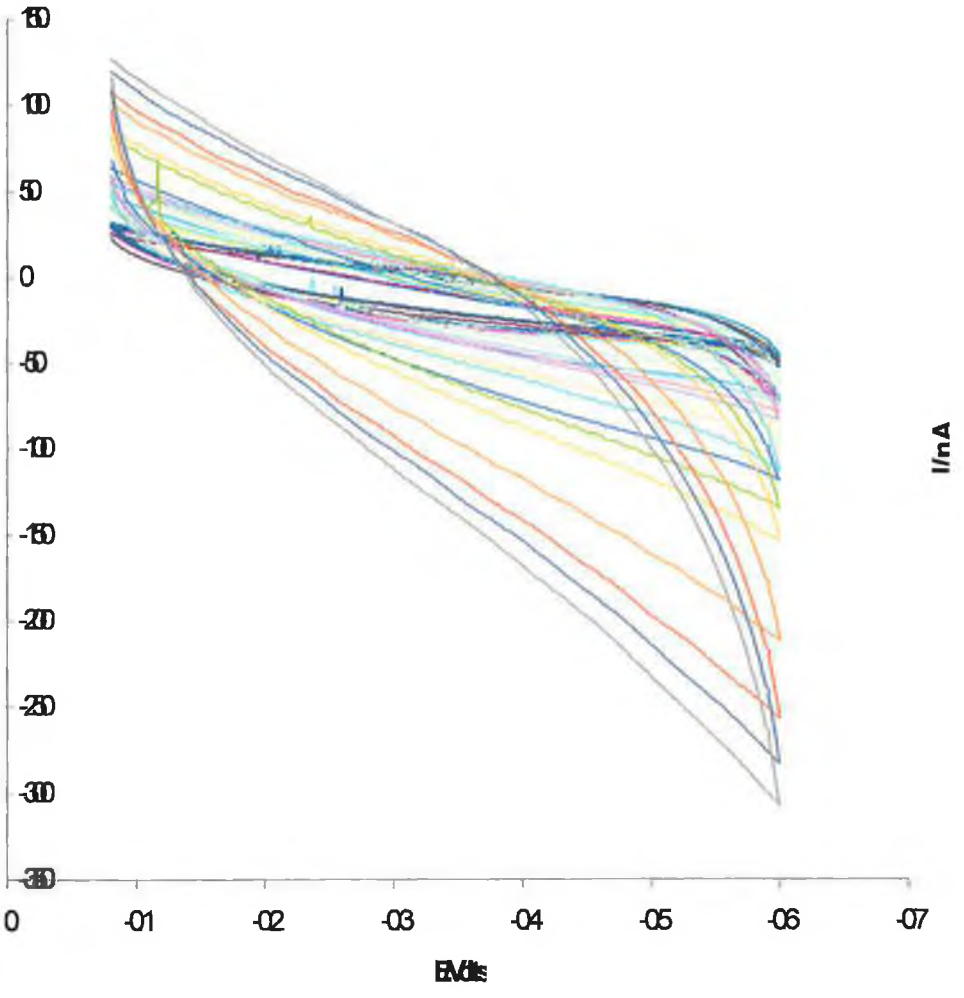

Figure 5.4 Cyclic voltammogram for a 25μm radius copper microelectrode in a solution of 4mM $InCl_3$ and 0.1M Boric acid. The scan rate is increased from $0.01Vs^{-1}$ to $5Vs^{-1}$ and overlaid. The potential limits are –0.08 and -0.6V. Legend $-0.05Vs^{-1}$, $-0.075Vs^{-1}$, $0.08Vs^{-1}$, $-0.085Vs^{-1}$, $-0.09Vs^{-1}$, $-0.095Vs^{-1}$, $-0.1Vs^{-1}$, $-0.15Vs^{-1}$, $-0.2Vs^{-1}$, $0.25Vs^{-1}$, $0.3Vs^{-1}$, $0.35Vs^{-1}$, $0.4Vs^{-1}$, $0.45Vs^{-1}$, $0.5Vs^{-1}$, $0.55Vs^{-1}$, $-0.6Vs^{-1}$, $-0.75Vs^{-1}$, $-1.0Vs^{-1}$, $-2.0Vs^{-1}$, $-3.0Vs^{-1}$, $-4.0Vs^{-1}$ and $-5Vs^{-1}$.

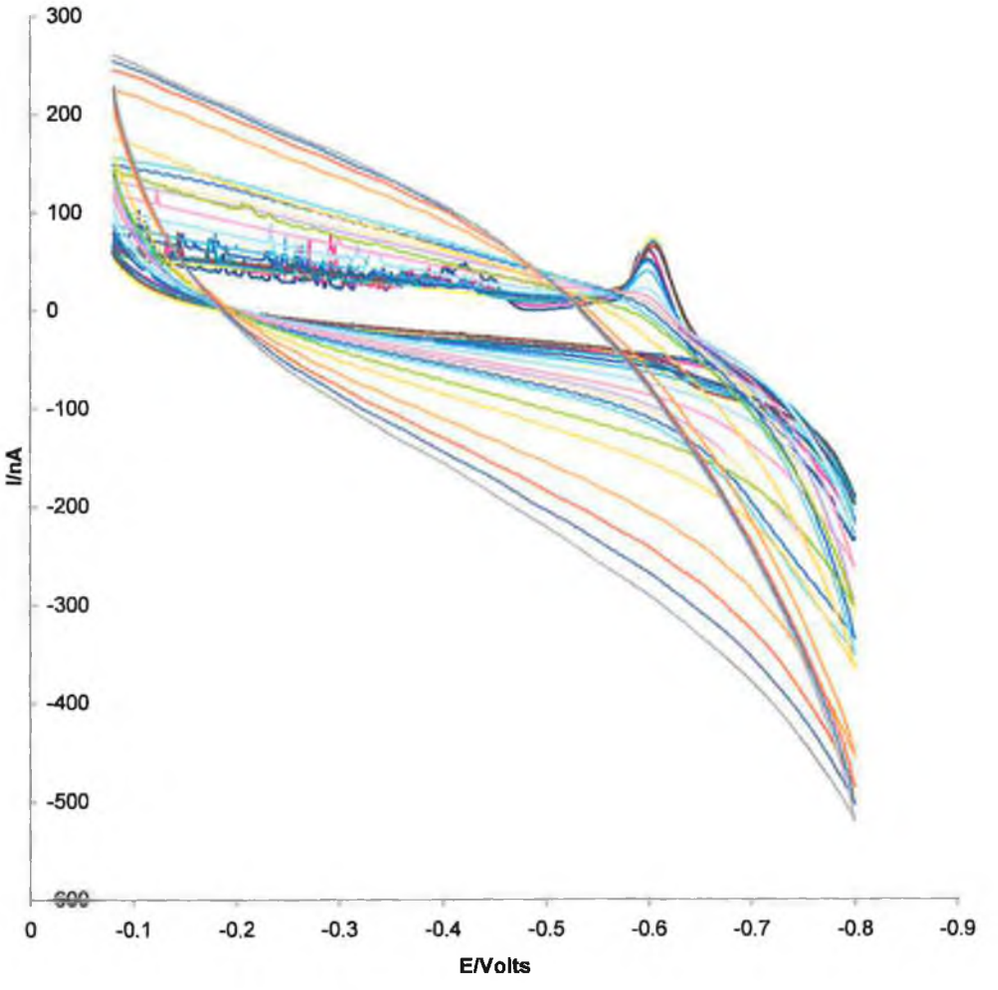

Figure 5.5 Cyclic voltammogram for a 25μm radius copper microelectrode in a solution of 4mM $InCl_3$ and 0.1M Boric acid. The scan rate is increased from $0.01Vs^{-1}$ to $5Vs^{-1}$ and overlaid. The potential limits are –0.08 and -0.8V. Legend –$0.05Vs^{-1}$, -$0.075Vs^{-1}$, $0.08Vs^{-1}$, $0.085Vs^{-1}$, -$0.09Vs^{-1}$, -$0.095Vs^{-1}$, -$0.1Vs^{-1}$, -$0.15Vs^{-1}$, $0.2Vs^{-1}$, $0.25Vs^{-1}$, $0.3Vs^{-1}$, $0.35Vs^{-1}$, $0.4Vs^{-1}$, $0.45Vs^{-1}$, $0.5Vs^{-1}$, $0.55Vs^{-1}$, -$0.6Vs^{-1}$, -$0.75Vs^{-1}$, -$1.0Vs^{-1}$, $2.0Vs^{-1}$, $3.0Vs^{-1}$, -$4.0Vs^{-1}$ and -$5Vs^{-1}$.

scan rate is further increased. It is also clear that as the scan rate is increased from $0.01Vs^{-1}$ to $0.5Vs^{-1}$, less indium is deposited on the electrode surface. This is thought to be due to the fact that at a slower scan rate more time is spent in the potential range where indium is reduced, resulting in a greater amount of In^{3+} being reduced to metallic In. In other words, the dynamics of indium deposition influence the response. At a scan rate of $0.01Vs^{-1}$, a concentration of approximately $1.134x10^{-4}$ mols indium is electrodeposited on the copper microelectrode surface compared to a concentration of $2.451x10^{-5}$ mols indium, which is electrodeposited at a scan rate of $0.5Vs^{-1}$.

The potential window was extended further in the negative direction to a range of –0.08 to –0.1V; Figure 5.6 illustrates a scan rate overlay from 0.01 to $5Vs^{-1}$ for this range. The results in this range are similar to previous potential windows with CVs taken at lower scan rates providing voltammograms of detailed features and low current amplitude but as the scan rate increases the current amplitude increases accordingly and the features of these voltammograms deteriorate to a point at $2.5Vs^{-1}$ where the voltammogram is featureless. In this potential range there are two oxidation peaks for scan rates up to $0.5Vs^{-1}$, as mentioned earlier the second peak is thought to be due to under potential deposition but as the scan rate is increased above $0.5vs^{-1}$ the second peak disappears and the oxidation peak is reduced dramatically. This means that confirms the view that as the scan rate is increased, less indium is electrodeposited on the microelectrode surface.

The difference in the amount of electrodeposited indium with scan rate gives important information regarding the type of growth mode and deposition dynamics for indium on the copper microelectrode surface. It means that the nucleation type must be progressive, as in the case of an instantaneous nucleation type there is no relationship between the amount of electrodeposited indium and scan rate. A progressive nucleation type means that as the In centres nucleate on the copper surface, thought to be at a potential of –0.6558V, the indium clusters grow in size as the potential is scanned further in the negative direction to a potential of –0.84V. The more time the potential is kept between these limits, the more indium is reduced from In^{3+} to In and the more indium that is electrodeposited on the copper electrode surface.

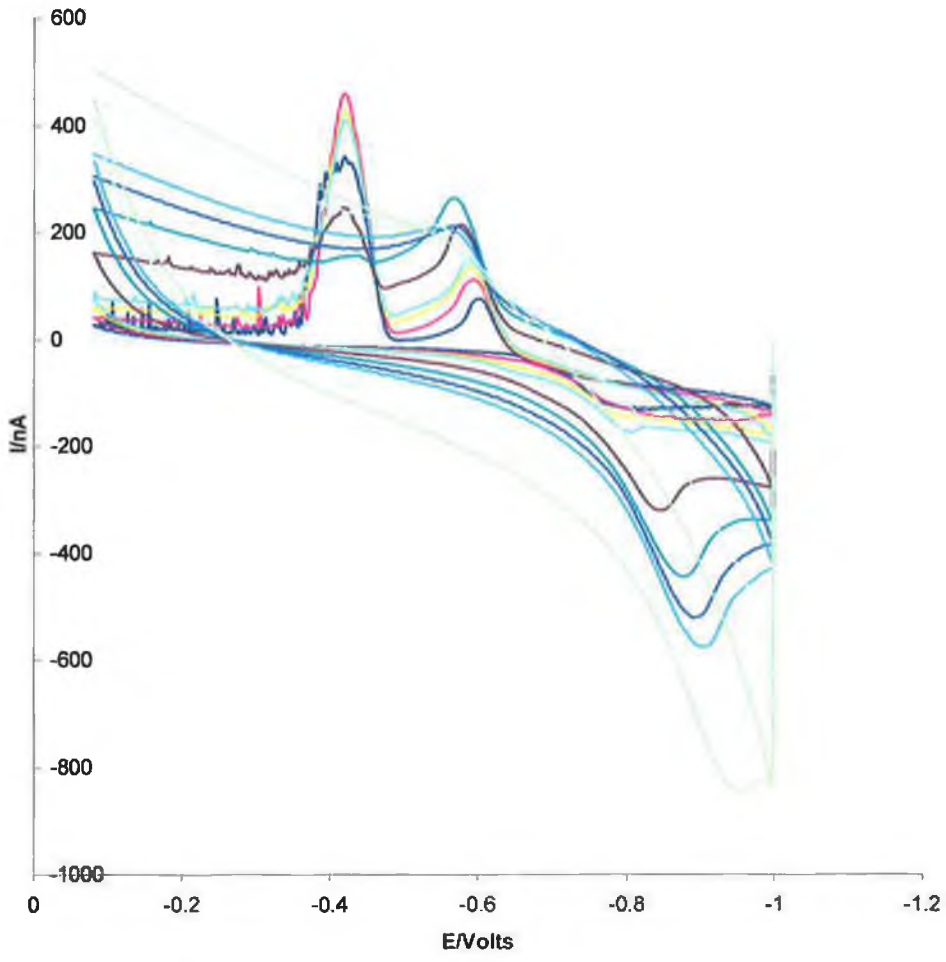

Figure 5.6 Cyclic voltammogram for a 25μm radius copper microelectrode in a solution of 4mM $InCl_3$ and 0.1M boric acid. The scan rate is increased from $0.01Vs^{-1}$ to $5Vs^{-1}$ and overlaid. The potential limits are –0.08 and –1.0V. Legend $-0.01Vs^{-1}$, $-0.025Vs^{-1}$, $0.05Vs^{-1}$, $0.075Vs^{-1}$, $-0.1Vs^{-1}$, $-0.25Vs^{-1}$, $-0.5Vs^{-1}$, $-0.75Vs^{-1}$, $1.0Vs^{-1}$, $2.5Vs^{-1}$ and $5.0Vs^{-1}$.

5.3c Scanning Electron Microscopy (SEM) results

The Scanning Electron Microscope (SEM) is one of the most versatile and widely used tools of modern science as it allows the study of both morphology and composition of biological and physical materials under UHV.

By scanning an electron probe across a specimen, high resolution images of the morphology or topography of a specimen, with great depth of field, at very low or very high magnifications can be obtained. Compositional analysis of a material may also be obtained by monitoring secondary X-rays produced by the electron-specimen interaction. Thus, detailed maps of elemental distribution can be produced from multi-phase materials or complex, bioactive materials. Characterisation of fine particulate matter in terms of size, shape, and distribution as well as statistical analyses of these parameters, may be performed. There are many different types of SEM designed for specific purposes ranging from routine morphological studies, to high-speed compositional analyses or to the study of environment-sensitive materials [15].

Figure 5.7 is of an SEM image of a blank 1.25mm copper macroelectrode. In this image there is no evidence of adsorbed metal on the copper surface, the image is of a clean polished copper macroelectrode. This image of the clean copper surface allows for easy comparison with later images of electrodeposited indium on the copper macroelectrode.

Indium is electrodeposited on this copper macroelectrode using cyclic voltammetry. This modified surface was prepared by holding the potential at –1.0V, that prevents indium from being re-oxidised and dissolving back into solution. The macroelectrode was removed from the cell under potential control and transferred to the SEM chamber.

Figure 5.8 features an SEM image of the same macroelectrode after indium has been electrodeposited on the copper surface. This image is taken at a similar magnification and beam current to allow for easy comparison with the clean copper image. It is clear from this image that indium deposits as clusters on the electrode rather than as a continuous film over the whole surface.

According to Kossel and Stranski [16], electrodeposited material is more likely to occupy sites at the electrode edge rather than surface sites. They proposed that the difference in energy associated with the incorporation (or removal) of atoms from different sites could be related to the effective coordination number of the sites. The cubic coordination number, m for edge sites and surface sites is 2 and 1 respectively. This has been proven to be the case for crystal growth from the vapour phase, as the energy involved in lattice incorporation can be related approximately to the enthalpy of sublimation and it is clear that the most favourable sites for deposition are those with high values of m [17].

In the case of electrochemical nucleation the situation is more complicated, since it is possible that the charge-transfer reaction does not produce a neutral atom, rather a species which has some residual or partial charge and which retains part of the solvation sphere [4]. To address these problems Conway and Bockris [18] attempted to calculate the energy changes involved in the formation of these ad-ions. They concluded that charge transfer reactions are favoured on the plane surfaces, rather than at steps or kinks. Lattice growth at step or kink sites must therefore involve surface diffusion of these surface ad-ions. Lattice incorporation at different sites results in further loss of the hydration sphere until eventually the atom is incorporated into the surface. This view seems to be borne out by the SEM image in Figure 5.9, with indium mainly occupying sites at the edge of the copper macroelectrode with only a very small percentage located at surface sites.

The magnification of the image is increased to allow closer examination of an electrodeposited indium cluster located at a surface site. The magnification is increased from 90 to 200 and finally 1000, these results are illustrated in Figures 5.9 and 5.10 respectively. Figure 5.10 features a group of indium clusters located at surface sites approximately 500μm from the macroelectrode edge. At this magnification the indium clusters appear slightly blurred and are not well resolved. The magnification is increased to 1000 to achieve better resolution of the electrodeposited indium cluster; this image can be seen in Figure 5.10. In this image the indium deposits are of varying sizes, these range in size from 100μm to 300μm.

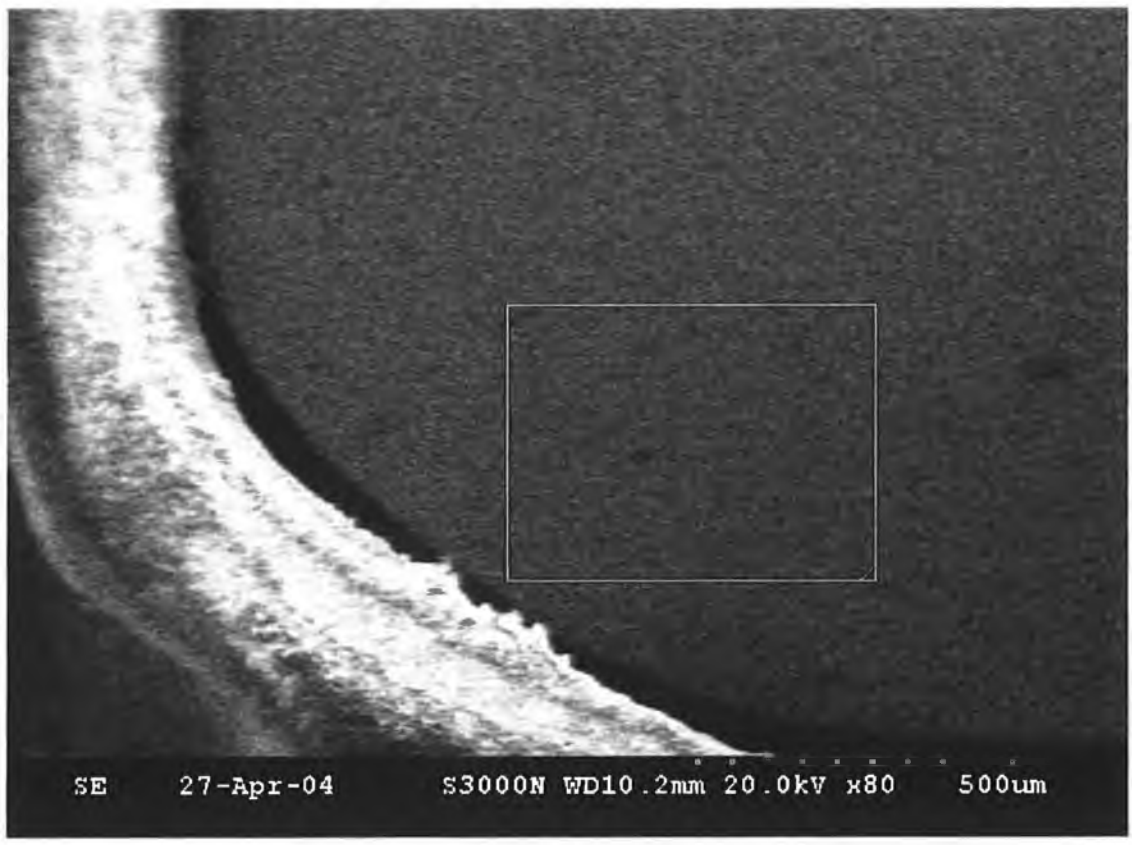

Figure 5.7 SEM image of a 1.25mm radius copper macroelectrode. The image was taken at a working distance of 10.2mm, beam energy of 20kV and a magnification of 80.

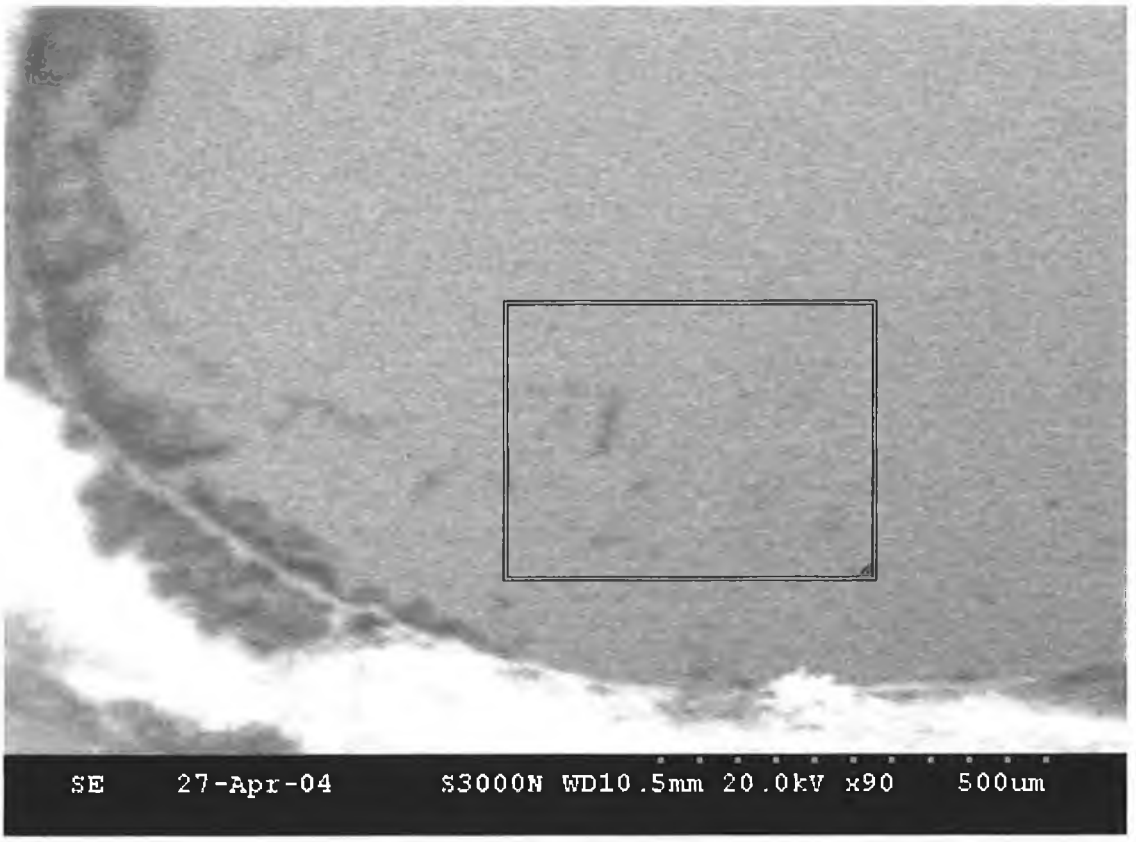

Figure 5.8 SEM image of a 1.25mm radius copper macroelectrode. The image was taken at a working distance of 10.5mm, beam energy of 20kV and a magnification of 90.

Figure 5.9 SEM image of a 1.25mm radius copper macroelectrode. The image was taken at a working distance of 11.4mm, beam energy of 20kV and a magnification of 200.

Figure 5.10 SEM image of a 1.25mm radius copper macroelectrode. The image was taken at a working distance of 10.7mm, beam energy of 20kV and a magnification of 1000.

5.3d Energy Dispersive X-ray analysis (EDX) results

Energy Dispersive X-ray analysis (EDX) is used in conjunction with SEM. An electron beam strikes the surface of a conducting sample. The energy of the beam is typically in the range 10-20keV. This causes X-rays to be emitted from the point of contact on the sample. The energy of the X-rays emitted depend on the material under examination [19]. The X-rays are generated in a region about 2μm in depth, meaning that EDX cannot technically be classed as a surface science technique. By moving the electron beam across the material a map of the elemental composition of the sample can be acquired, in a similar way to Auger Electron Spectroscopy (AES), which was discussed in Chapter 2.

The detector used in EDX is the Lithium drifted Silicon detector. This detector must be operated at liquid nitrogen temperatures. When an X-ray strikes the detector, it will generate a photoelectron within the body of the silicon. As the photoelectron travels through the Si, it generates electron-hole pairs. The electrons and holes are attracted to opposite ends of the detector with the aid of a strong electric field. The size of the current pulse thus generated depends on the number of electron-hole pairs created, which in turn depends on the energy of the incoming X-ray. Thus, an X-ray spectrum can be acquired giving information on the elemental composition of the material under examination [20].

An area of 2400μm^2 is taken from Figure 5.11 and analysed using EDX. The results from this analysis are shown in Figure 5.12. In this analysis only two elements were found, the main peaks as expected were from the copper substrate with a number of small peaks coming from the electrodeposited indium. This experiment was conducted to prove that the STM images were as postulated electrochemically deposited indium and not some form of contamination on the copper macroelectrodes.

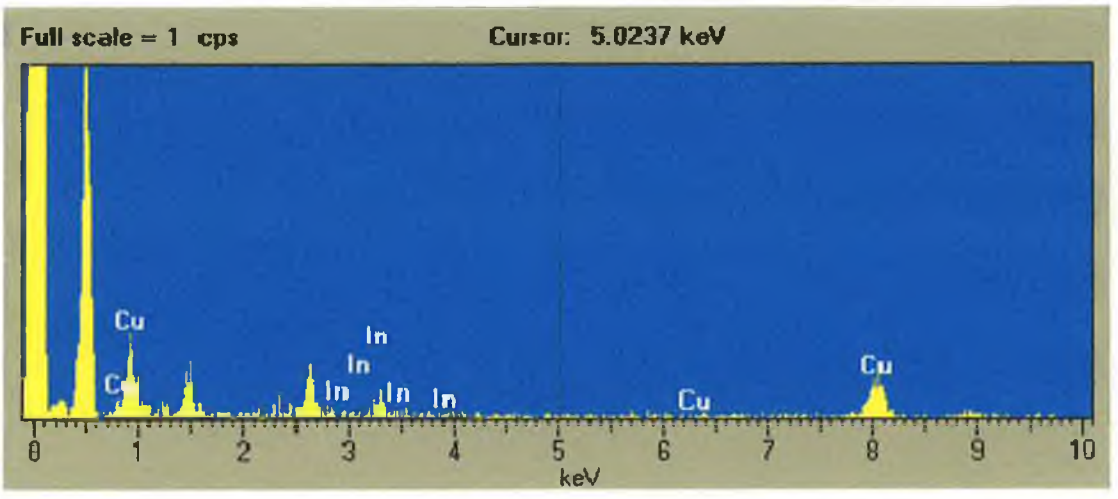

Figure 5.11 EDX image of a 2400μm^2 cross section taken from an indium electrodeposited 1.25mm radius copper macroelectrode.

5.3e Elucidation of nucleation type and growth mode

The electrocrystallisation of a new phase on a foreign substrate involves one of two kinds of nucleation, namely instantaneous or progressive, with the electrodeposited material growing on the substrate according to one of two types of growth mode, either two dimensional (2-D) or three dimensional (3-D), which subsequently overlap to give a continuous deposit.

The number of nuclei in the instantaneous nucleation is constant, and they grow on their former positions on the bare substrate surface without the formation of new nuclei. Hence the radii of nuclei are larger and the surface morphology is rougher. In progressive nucleation, the nuclei not only grow on their former positions on the bare substrate surface but also on new nuclei, which form smaller nuclei particles and generate flatter surface morphology [20].

In the 2-D growth the nuclei grow more quickly in the parallel direction than the perpendicular direction until they meet and overlap. However, in the 3-D growth, the growth rates of nuclei are essentially equal or comparable in the directions parallel or perpendicular to the electrode surface. The geometry of the growth centre is sensitive to the interaction between the deposit and substrate materials, particularly in the case of liquid metal deposits (e.g. mercury) where the contact angle with the substrate determines whether a hemispherical or cap-shaped nucleus is formed. The shape of solid metal growth centres is more complex, but it is instructive to consider simple geometries which lead to analytical expressions for the current transient under potentiostatic conditions. If for example the growth centre is represented as a right circular cone growing on a foreign substrate (3-D growth), growth parallel to the surface takes place with a rate constant k_3, and that perpendicular to the surface with a rate constant k'_3. The units of these rate constants are in $molcm^{-2}s^{-1}$. The total current into the growing cone can be obtained by integration of the contributions of a stack of discs [21]

According to a study by Harrison et al [14], the nucleation type and growth mode can be elucidated from chronoamperometric results conducted on the μs to seconds timescale. If a potential step is applied at a potential below the $E_{½}$ value for the

deposited material to a potential above the $E_{½}$ value, a plot of current versus time gives important information which allows for the elucidation of the growth mode for the deposited material.

If no electrodeposition were taking place, it would be expected that a plot of current versus time would result in an exponential decay curve (see Figure 4.12 from last chapter). However, as can be seen in Figure 5.12, a plot of current versus time for a chronoamperometric step applied from -0.3V to -0.8V in a solution of 4mM $InCl_3$, the resulting curve does not purely exhibit exponential decay but also a current due to the electroreduction of indium. At short timescales, the decay is thought to be due to a combination of both the electrodeposited material and the RC time constant for the system, as the timescale is increased, the RC time constant decays leaving any differences in current from the expected exponential decay due to the electrodeposited metal.

To resolve the current due to metal deposition, it is necessary to remove the current caused by the RC time constant for this particular system, this involves subtracting a background trendline from the Figure 5.12. The exponential decay trendline can be seen in Figure 5.13 and is representative of the RC time constant for the system under investigation, with a large current at short timescales, decaying to a minimum at longer timescales. This exponential decay curve acts as a background and is subtracted from the current versus time plot in Figure 5.12 to give the current due to metal deposition, shown in Figure 5.14.

In Figure 5.15, the current increases to a maximum in a short time and decreases slowly to a steady state. During the course of phase formation, the appearance of a current maximum always indicates processes of nucleation and growth of the new phase up to the formation of full coverage of indium layer. From this figure, the value for I_{max} is determined and a plot of I/I_{max} versus time is constructed. This plot is presented in Figure 5.15, along with a plot of $(I/I_{max})^2$ versus time. From Figure 5.15, the current maximum can be analysed for the nucleation mechanism and growth mode by comparing the experimental data with theoretical plots given for the different nucleation types [14].

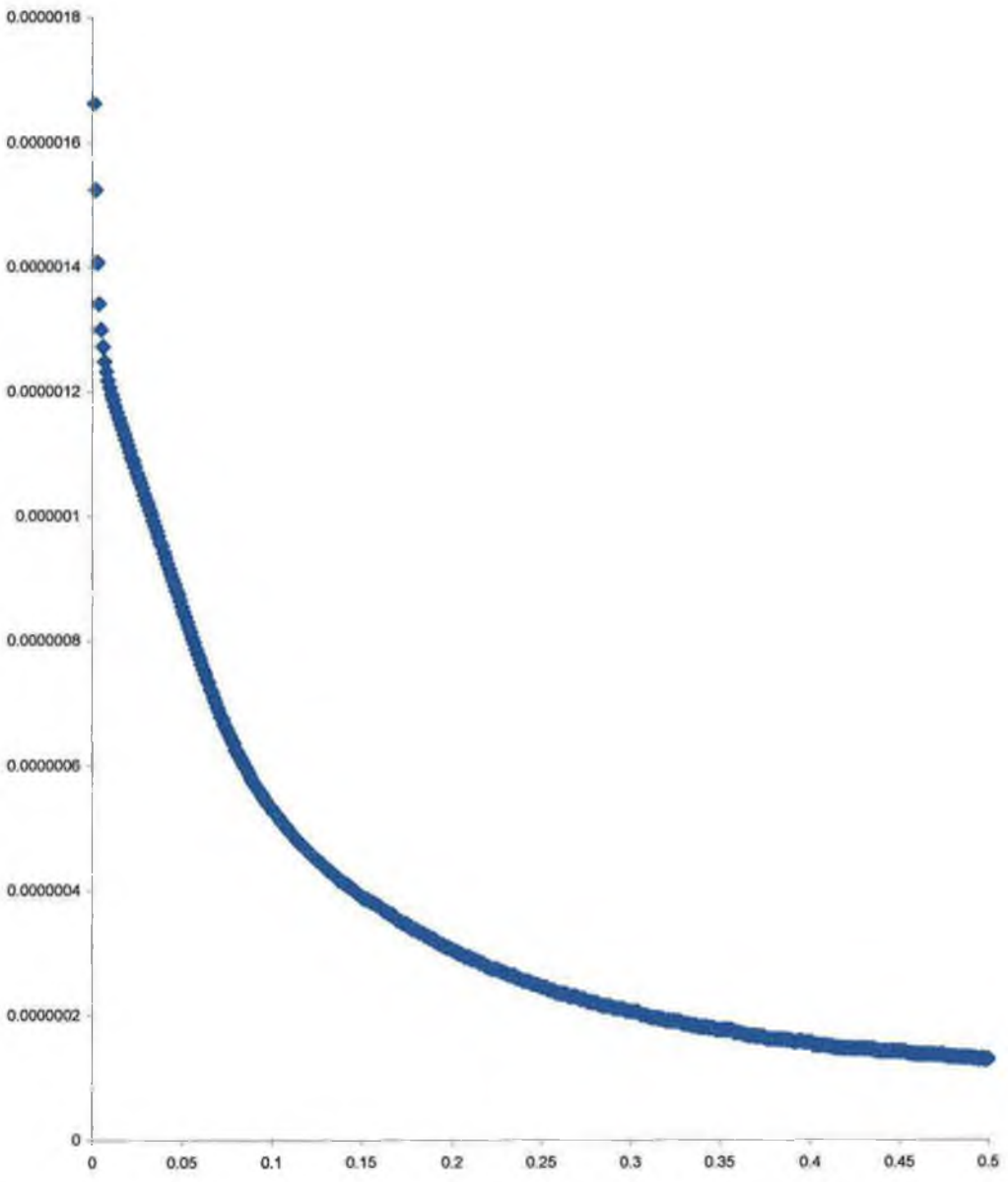

Figure 5.12 Experimental plot of current versus time for a 25μm radius copper microelectrode in a solution of 0.4mM $InCl_3$ and 0.1M Boric acid. This potential step is from a potential of –0.3 to –0.8V.

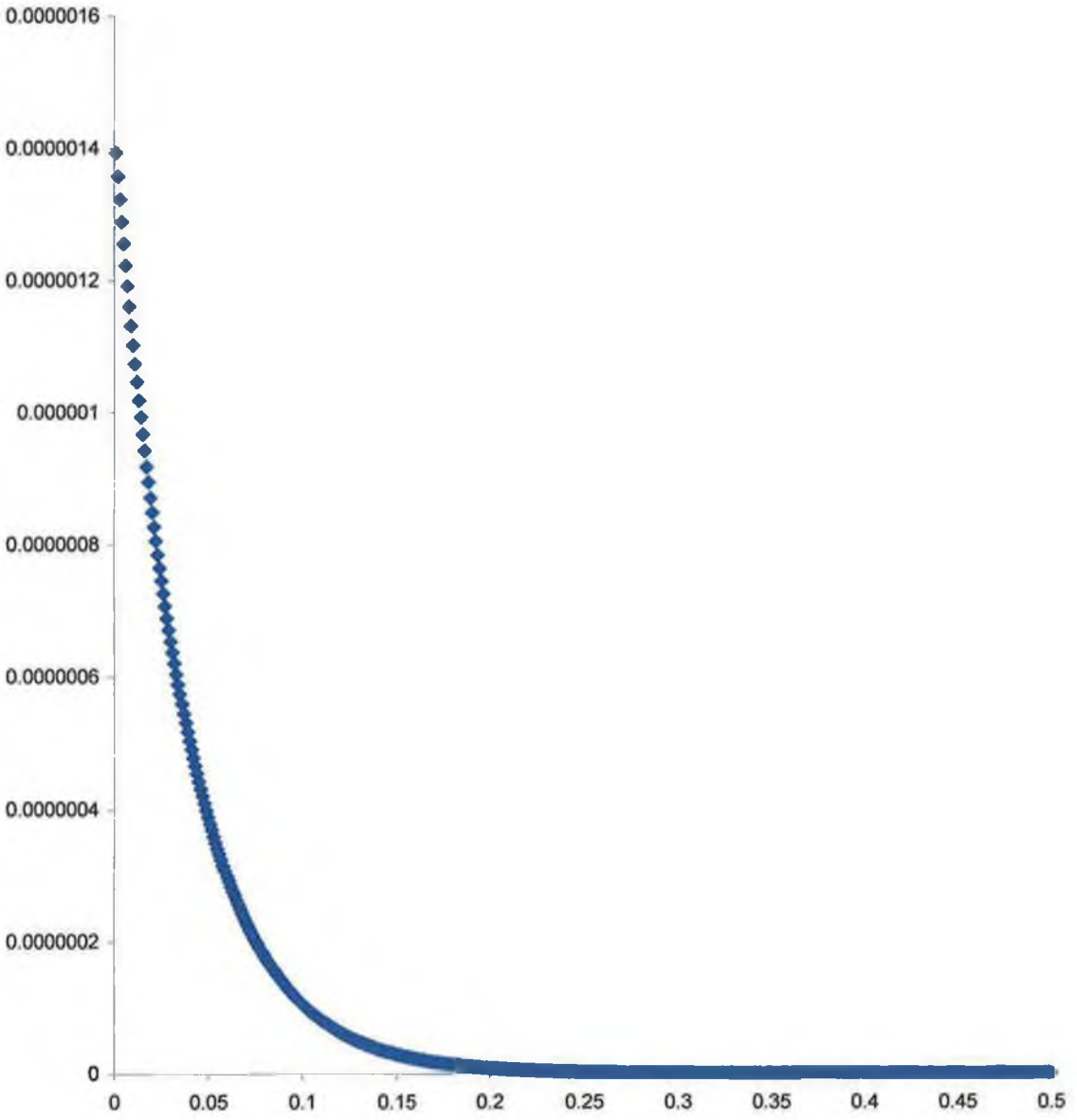

Figure 5.13 Experimental plot of current versus time for a 25μm radius copper microelectrode in a solution of 0.4mM $InCl_3$ and 0.1M Boric acid. This potential step is from a potential of +0.1 to –0.4V, where no faradaic reaction occurs.

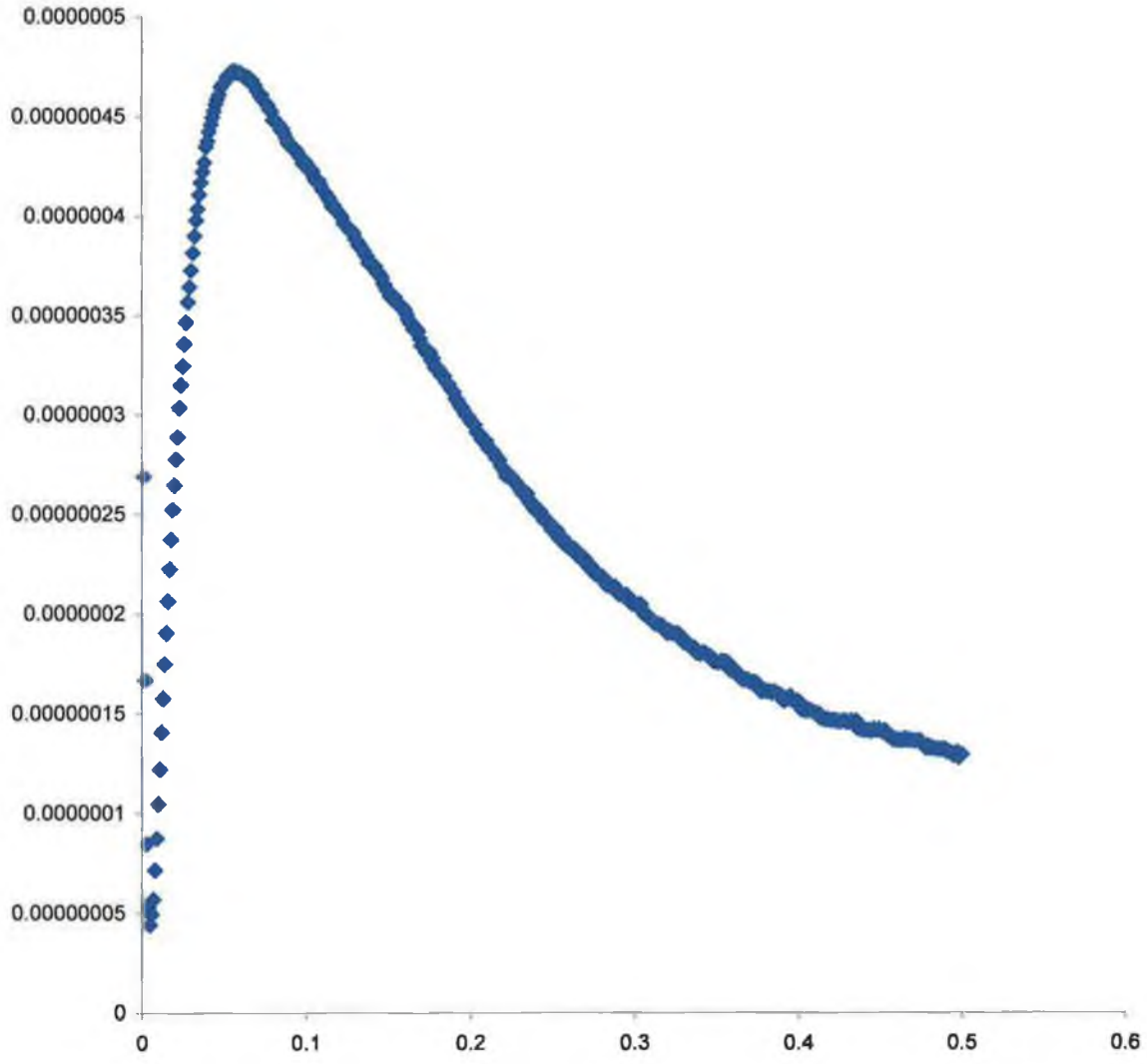

Figure 5.14 Plot of current versus time for a potential step from –0.3 to –0.8V with mathematical background subtraction (Figure 5.12-Figure 5.13).

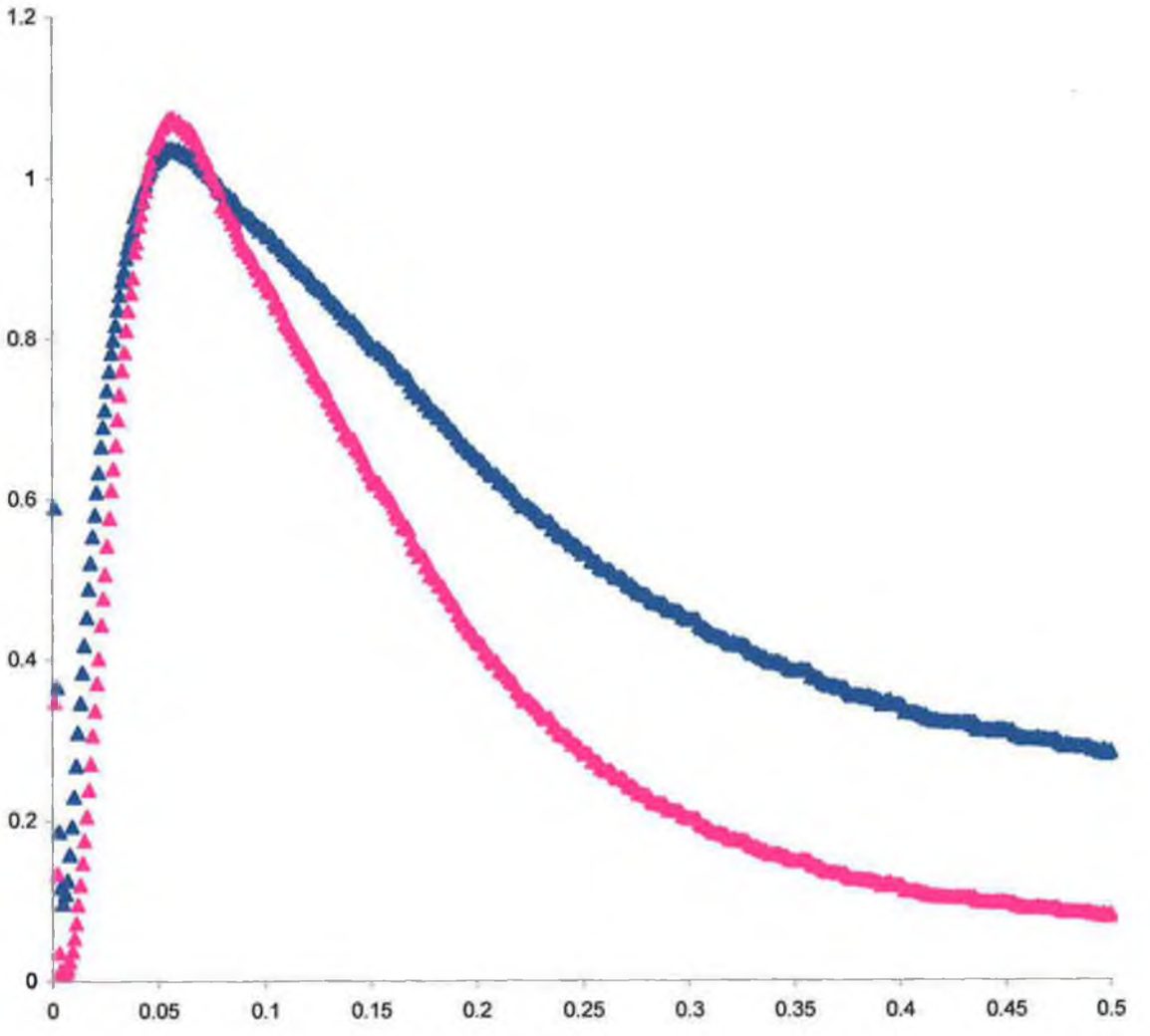

Figure 5.15 Plot of I/I_{max} and $(I/I_{max})^2$ versus time for the data presented in Figure 5.14. Legend ▲I/I_{max} and ▲$(I/I_{max})^2$.

Harrison et al [14] devised formulae to represent current transients representative of each of the four nucleation types and growth modes. The dimensionless forms of 2-D and 3-D growths for instantaneous and progressive nucleation are given by:

2-D progressive

$$I/I_{max} = (t/t_{max})^2 \exp[-2/3\{(t^3 - t^3{}_{max})\}] \qquad \text{(Eqn. 5.2)}$$

2-D instantaneous

$$I/I_{max} = (t/t_{max}) \exp[-1/2\{(t^2 - t^2{}_{max})/t^2{}_{max}\}] \qquad \text{(Eqn. 5.3)}$$

3-D progressive

$$(I/I_{max})^2 = 1.2254/(t/t_{max})\{1 - \exp[-2.3367(t/t_{max})^2]\} \qquad \text{(Eqn. 5.4)}$$

3-D instantaneous

$$(I/I_{max})^2 = 1.9542/(t/t_{max})\{1 - \exp[-1.2564(t/t_{max})]\}^2 \qquad \text{(Eqn. 5.5)}$$

where the parameters t_{max} and i_{max} represents the coordinates of the current maximum. The theoretical curves for nucleation and growth obtained from these equations were fitted with the experimental data of the current maximum for the electrodeposition of indium. These current transients are exhibited in Figure 5.16.

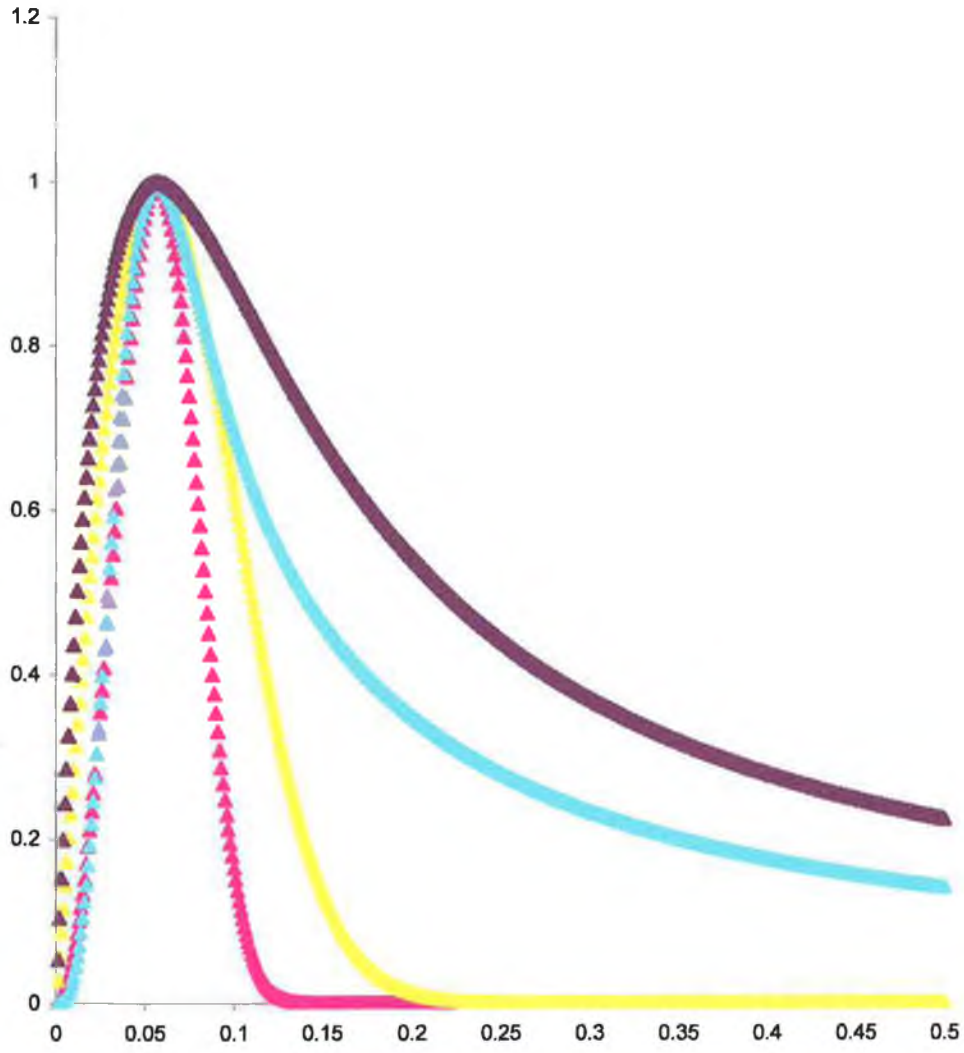

Figure 5.16 Plot of current versus time for four transients representing each of the nucleation types and growth modes. Legend ▲2D instantaneous, ▲2D Progressive, ▲3D instantaneous and ▲3D Progressive.

Figure 5.15 and 5.16 are overlaid to allow for easy comparison, this overlay can be seen in Figure 5.17. When comparing the experimental results to the theoretical transients, according to the formulae derived by Harrison et al. [14], it is important to remember that it is the plot of I/Imax versus time that is compared to the 2-D nucleation models and $(I/I_{max})^2$ versus time which is compared to the 3-D models. With this in mind, it is clear from Figure 5.17 that the nucleation type is 3-D as the I/I_{max} versus time plot bears very little resemblance to the 2-D transients. Thus, it is accepted that the growth mode for electrodeposited indium on a copper electrode substrate is 3-D. As mentioned earlier in this section, for 3-D growth, the growth rates of nuclei are essentially equal or comparable in the directions parallel or perpendicular to the electrode surface.

Although Figure 5.17 indicates clearly that the growth mode is 3-D, the nucleation type is not so obvious. The plot of $(I/I_{max})^2$ versus time is similar in parts to the transients for both 3-D Progressive and 3-D instantaneous. Overall the experimental results resemble the 3-D Progressive nucleation type, although there are some similarities with the 3-D Instantaneous transient. This would indicate that in the main, for the nucleation of indium growth centres on the copper substrate, indium grows progressively. A small percentage of the adsorbed indium may involve instantaneous nucleation, as according to theory there have been cases where both nucleation types occur. For example in the case of the electropolymerisation of aniline on highly orientated pyrolytic graphite (HOPG), Hwang et al. found that there are three types of nucleation and growth exhibited by aniline [22]. However, taking into account the comparison of scan rate versus indium deposition, this result would indicate that the nucleation type is progressive rather than instantaneous as the amount of indium electrodeposited was found to be dependant on scan rate.

This result accompanied by the results from the scan rate overlay indicates that the nucleation type and growth mode for electrodeposited indium on copper microelectrodes is 3-D Progressive.

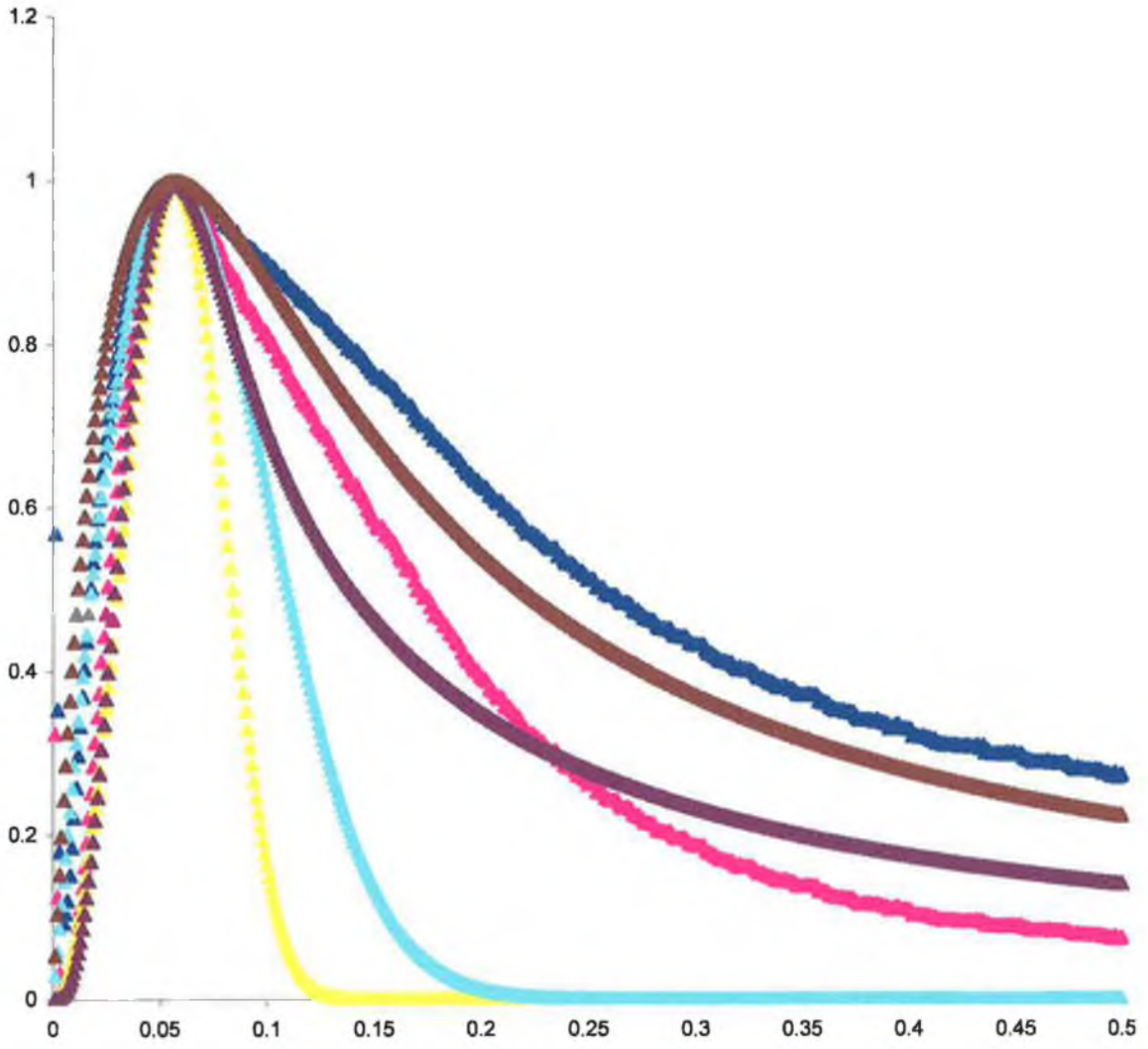

Figure 5.17 Overlay of I/I_{max} and $(I/I_{max})^2$ versus time and the current versus time plot for the four transients representing the four nucleation types and growth modes. Legend ▲ I/I_{max} ▲$(I/I_{max})^2$, ▲2D instantaneous, ▲2D Progressive ▲3D instantaneous and ▲3D Progressive.

5.3f Kinetics for Indium deposition

Metal deposition appears to be a very simple electrochemical process: an ion in solution accepts one or more electrons and becomes a neutral atom, to be incorporated into a metal lattice. However, in reality the situation is significantly more complex. Such an ion is always solvated and it is unlikely that the hydration shell is removed in one step, since this requires a very high energy of activation, which is not consistent with high exchange current densities observed for many metal deposition processes [23]. Another problem with this simplified version of events is encountered when the deposition of the neutral atom onto the metal lattice is investigated. When the neutral atom reaches the electrode surface it is referred to as an adatom. This term is used to indicate that although the ion has landed on the surface and has been discharged, it has not yet reached a position of lowest free energy and in this sense has not been incorporated into the metal lattice. Diffusion of adatoms on the surface, from their initial landing site to edges, kinks or vacancies on the surface, where they can be more highly coordinated and are therefore thermodynamically more stable, is considered to be rate-determining step for many metal deposition reactions.

To derive the kinetics involved in the electrodeposition of indium on the copper electrode, chronoamperometric experiments are conducted for both a potential step below the $E_{½}$ value for indium electrodeposition on a copper electrode (-0.658V) and a potential step which incorporates this $E_{½}$ value. This gives two current versus time plots, the first where no indium electrodeposition takes place as the potential step takes place below the deposition potential and the second which exhibits a change in current due to the electrodeposition of indium on the copper electrode surface as the deposition potential for this process lies within the boundaries of the potential step.

Figure 5.18 illustrates a current versus time plot for copper electrodes in a solution of 4mM $InCl_3$ and 0.1M boric acid, for a potential step of +0.1V to –0.4V. As expected the I-t plot gives no indication of metal deposition but instead any change in current is due to the RC time constant, with the electrical double layer charging to a maximum as the potential step is applied and the current decaying towards zero as the timescale moves from μs to ms.

Figure 5.19 presents a current versus time plot for copper electrodes in a solution of 4mM $InCl_3$ and 0.1M Boric acid, for a potential step of -0.3V to –0.8V. At the μs timescale this plot also illustrates the current due to the RC time constant for the electrochemical system decaying to zero. However, if this figure is compared to Figure 5.18, there is a large difference in current as the timescale is increased from μs to ms.

Comparing both figures, it can be seen that at timescales in the μs range both figures show a sharp decrease in current, thought to be caused by the RC time constant decaying to zero but as the timescale reaches the ms range there is a marked difference. This can be seen by comparing both Figure 5.18 where the current continues decaying to zero and Figure 5.19 where the current seems to level off and the rate of current decay decreases dramatically. This change in current decay is thought to be caused by nucleation of indium growth centres on the copper microelectrode surface and the subsequent growth mode of the indium clusters on the copper substrate.

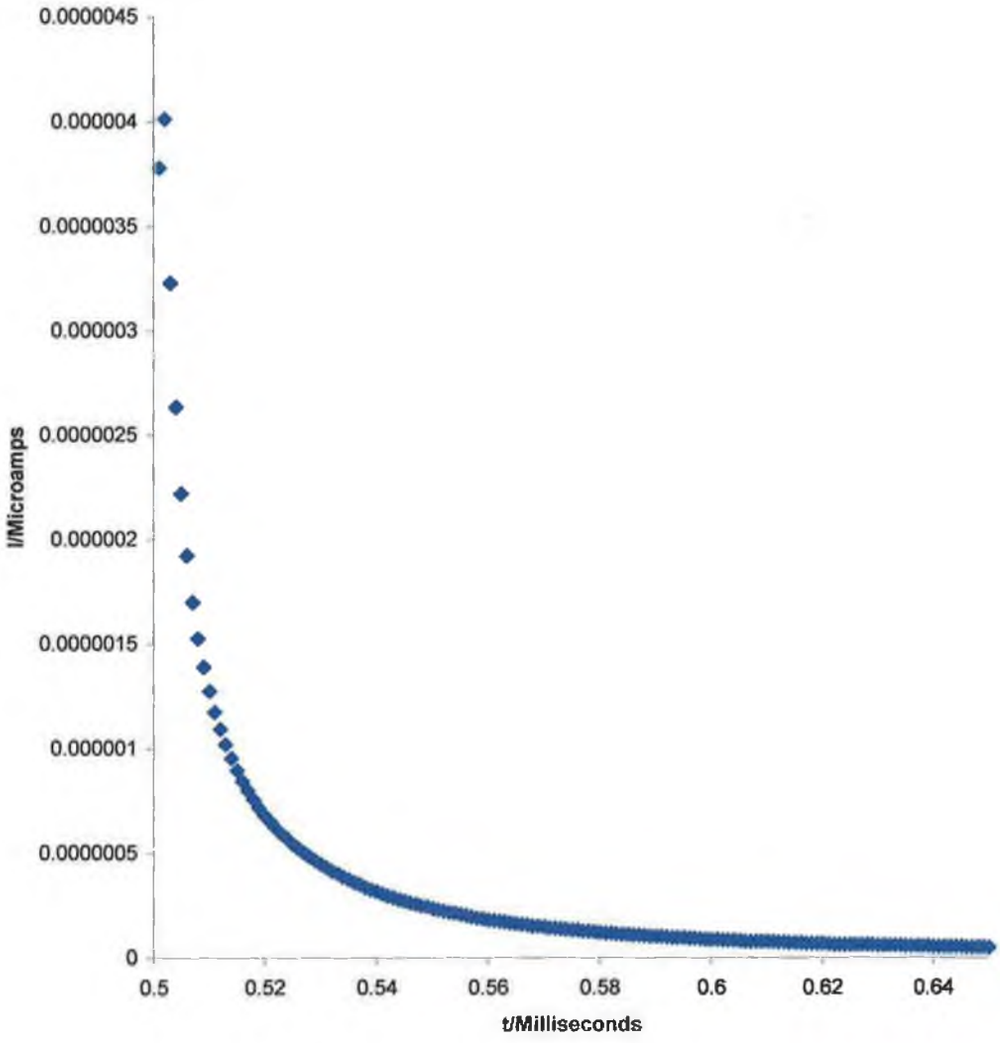

Figure 5.18 Experimental plot of current versus time for a 25μm radius copper microelectrode in a solution of 0.4mM $InCl_3$ and 0.1M Boric acid. This potential step is from a potential of +0.1 to –0.4V.

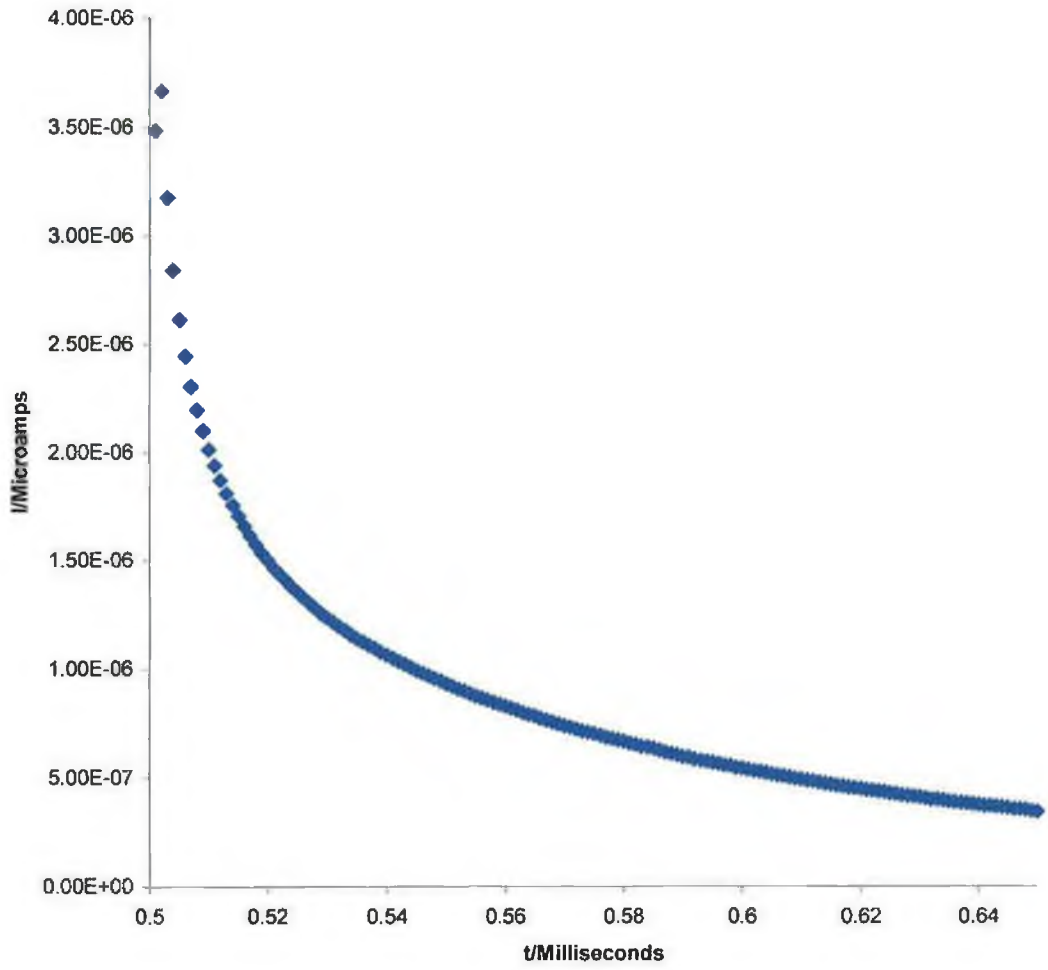

Figure 5.19 Experimental plot of current versus time for a 25μm radius copper microelectrode in a solution of 0.4mM $InCl_3$ and 0.1M Boric acid. This potential step is from a potential of –0.3 to –0.8V.

It is thought that if Figure 5.18 acts as background and is subtracted from Figure 5.19, the result should be a graph of the change in current purely due to the deposition of indium on the copper electrode surface. This graph is shown in Figure 5.20. This figure produces what is close to a straight line graph indicating that the system is first order. The kinetic value for the system can be calculated from this graph, using the formula:

$$Ln(I) = -kt + Ln(I_0) \qquad \text{(Eqn. 5.6)}$$

where I is current, k is the kinetic value, t is time and I_0 is the current when t=0. This formula corresponds to the equation of a straight line for a graph of log of current versus time. In this graph, the formula y=mx+c can be used if ln(I) corresponds to y, m to –k, x to t and c to $\ln(A_0)$. This gives a value of 20.755 s^{-1} for the rate constant for indium electrodeposition on copper.

The graph of log of current versus time must be linear over a number of lifetimes for the result to be accepted as first order. To determine the length of 1 lifetime, the formula 1/k is used. This means that 1 lifetime is equal to 1/20.755, or 0.048s. Figure 5.20 illustrates that this graph of log of current versus time is linear for at least 4 lifetimes, so it is accepted that the system operates according to first order kinetics. This result is given extra credence with a plot of current versus $t^{-½}$, shown in Figure 5.21. If the system were under diffusion control, this graph would be expected to be linear.

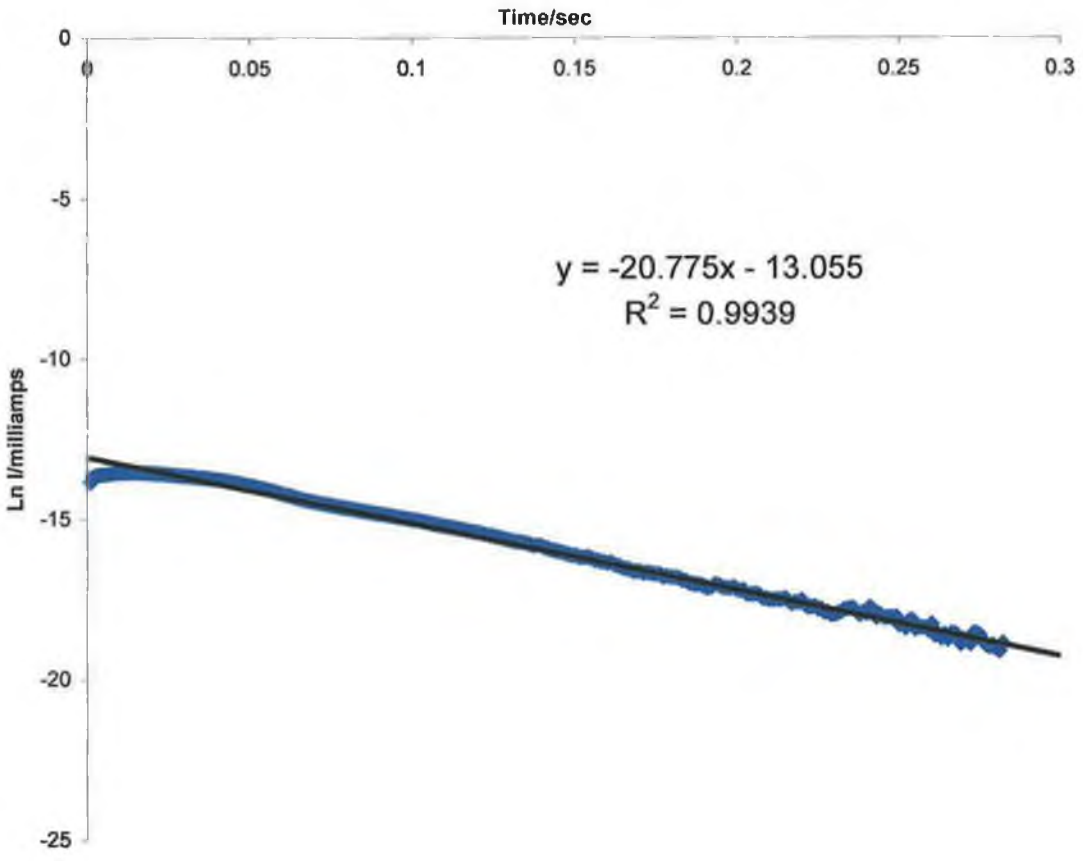

Figure 5.20 Plot of Ln of current versus time for indium electrodeposition on a copper microelectrode substrate. The experimental setup included a 25μm radius copper microelectrode as a working electrode in a solution of 0.4mM $InCl_3$ and 0.1M boric acid.

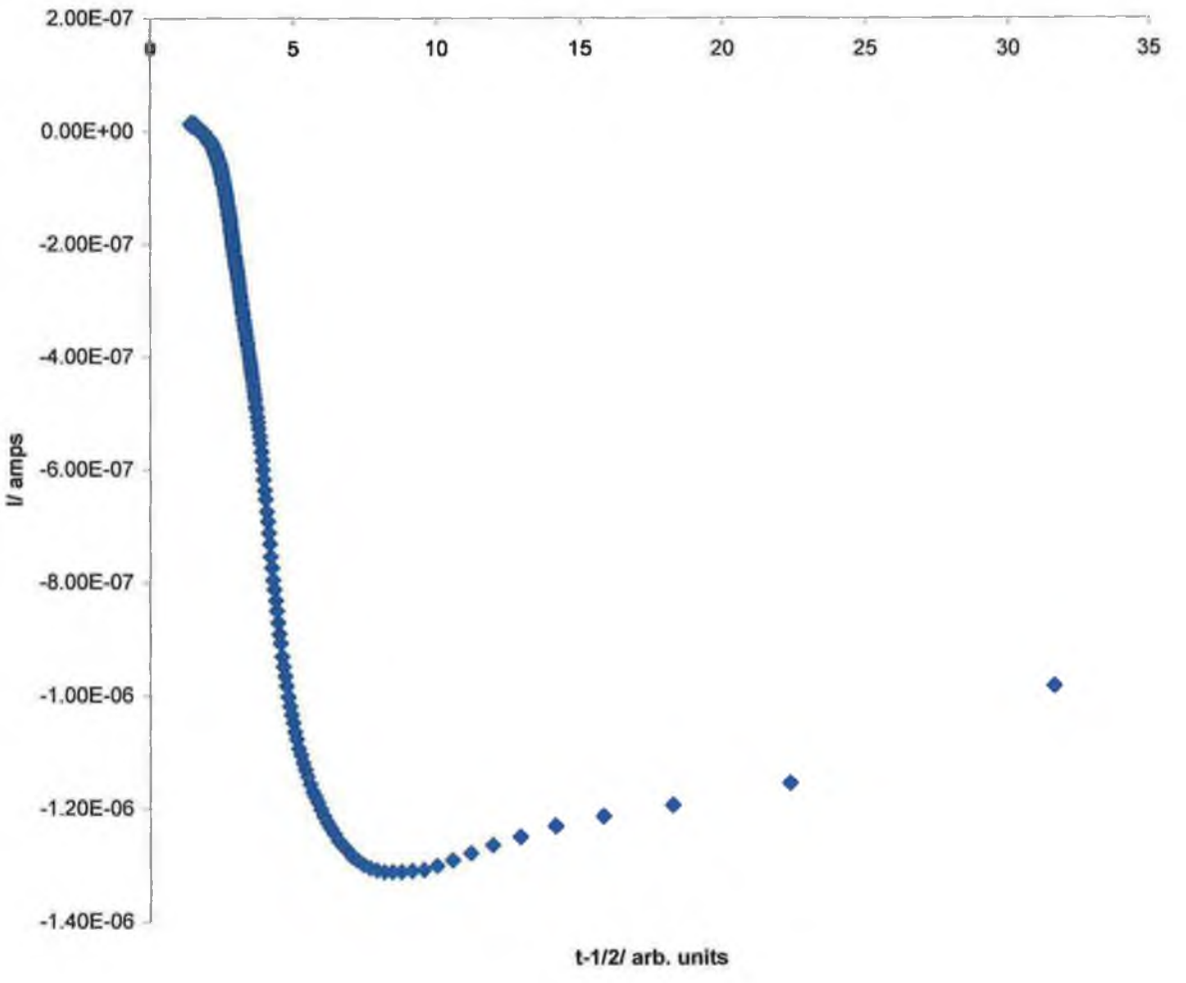

Figure 5.21 Plot of current versus $t^{-1/2}$ for indium electrodeposition on a copper microelectrode substrate. The experimental setup included a 25μm radius copper microelectrode as a working electrode in a solution of 0.4mM $InCl_3$ and 0.1M boric acid.

Both first and second order processes for indium electrodeposition on a copper electrode are illustrated by schematic diagrams in Figure 5.22. Figure 5.22a exemplifies the process of indium electrodeposition according to first order kinetics. In this case the indium diffuses from bulk, accepts electrons from the copper electrode and deposits on the electrode surface. Figure 5.22b illustrates the events occurring if the indium deposition process were second order. Indium firstly diffuses from bulk to the electrode surface where it encounters positively charged cations already adsorbed on the electrode surface. The indium must then substitute for these previously adsorbed cations before electron transfer can take place. Once the surface adsorbed cations are removed the indium can deposit on the surface. In this case there is a two-step approach where firstly the adsorbed cations are removed from the copper electrode surface, followed by the second step of indium deposition. As discussed earlier in this section indium deposits according to first order kinetics, so Figure 5.22a illustrates the indium deposition process.

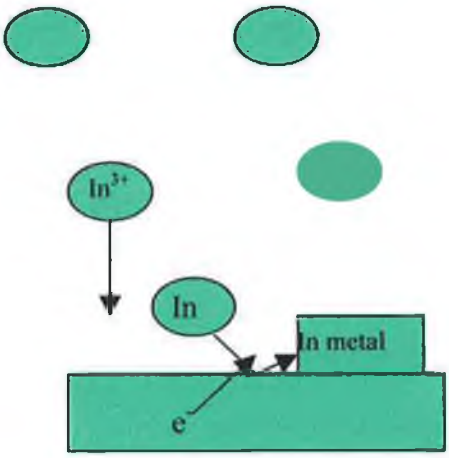

Figure 5.22a Schematic diagram of a first order reaction

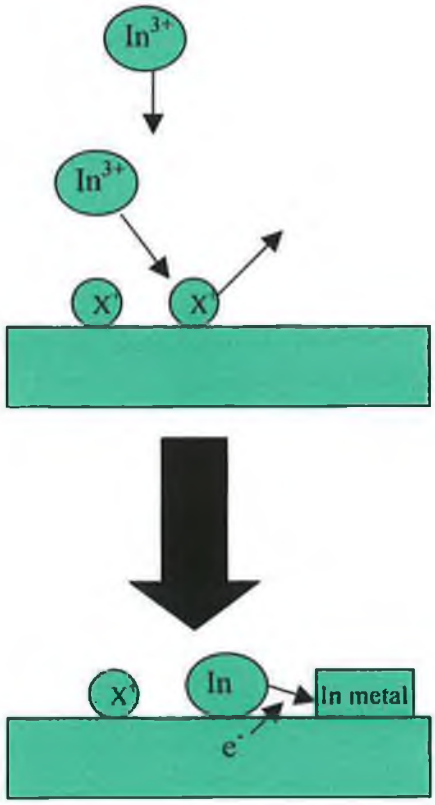

Figure 5.22b Schematic diagram of a second order process

A plot of square root of scan rate versus indium oxidation peak is shown in Figure 5.23. As can be seen from this figure, indium deposition has an optimum scan rate of $0.05Vs^{-1}$. Below this scan rate, indium deposition is inhibited by quantification problems involving peak height measurement, whereas above this scan rate the amount of indium deposited is increased by the amount of time that the potential is kept within the range of –0.658V and –1.0V. Thus, as the scan rate is increased above $0.05Vs^{-1}$ the amount of indium deposition decreases linearly. This is further indication that indium grows progressively on the copper electrode substrate.

Figure 5.24 is a plot of square root of scan rate versus reduction peak, it was expected that this plot would be very similar to the plot of square root of scan rate versus oxidation peak, with the reduction peak larger at slow scan rates and decreasing in size as the scan rate is increased. However, it was discovered that the size of the reduction peak increases with increasing scan rate. In terms of indium deposition this does not make sense particularly when compared to the plot in Figure 5.23. It is thought that the increase in reduction peak with increasing scan rate is evidence of another electrochemical process taking place at the same time as the indium electrodeposition. This accompanying reaction is thought to be either the hydrolysis of water or a hydrogen evolution reaction from the acidic background electrolyte.

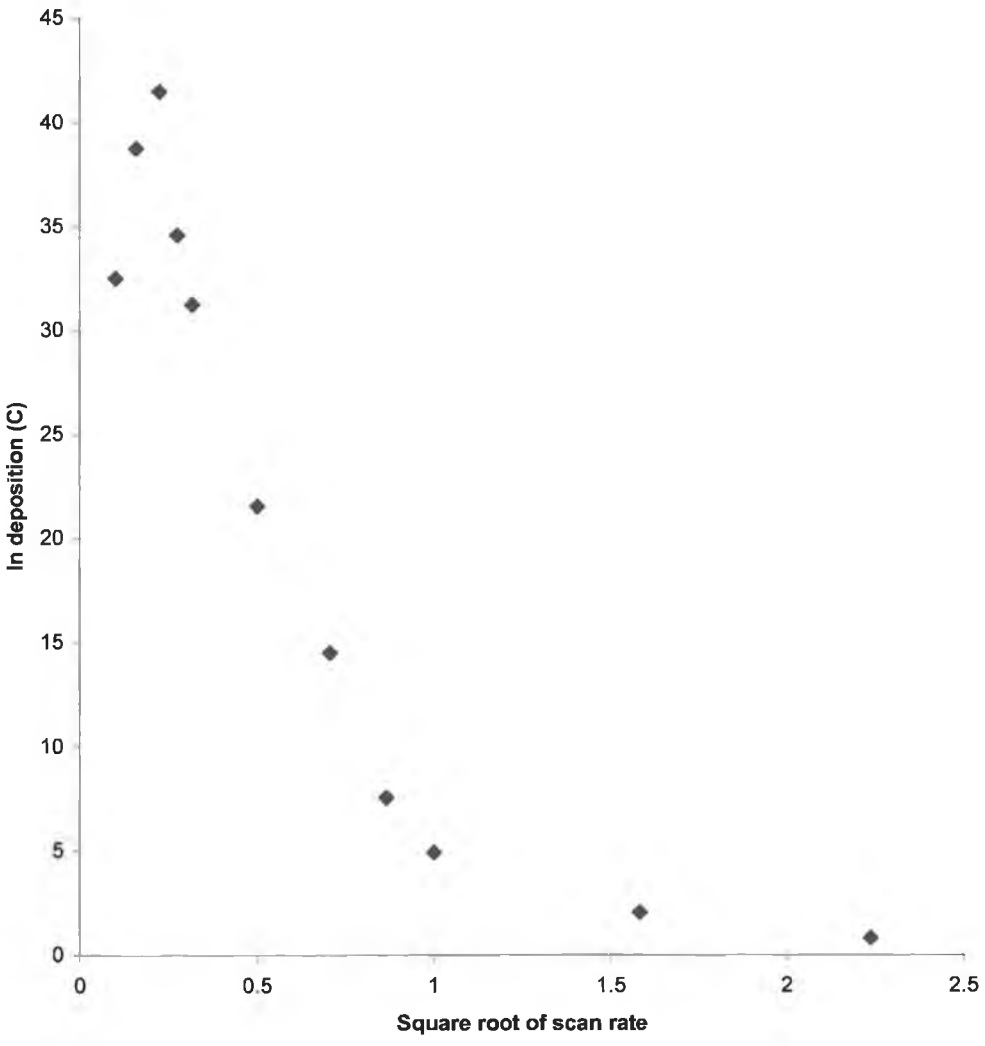

Figure 5.23 Plot of the amount of charge under indium oxidation peak versus √ scan rate.

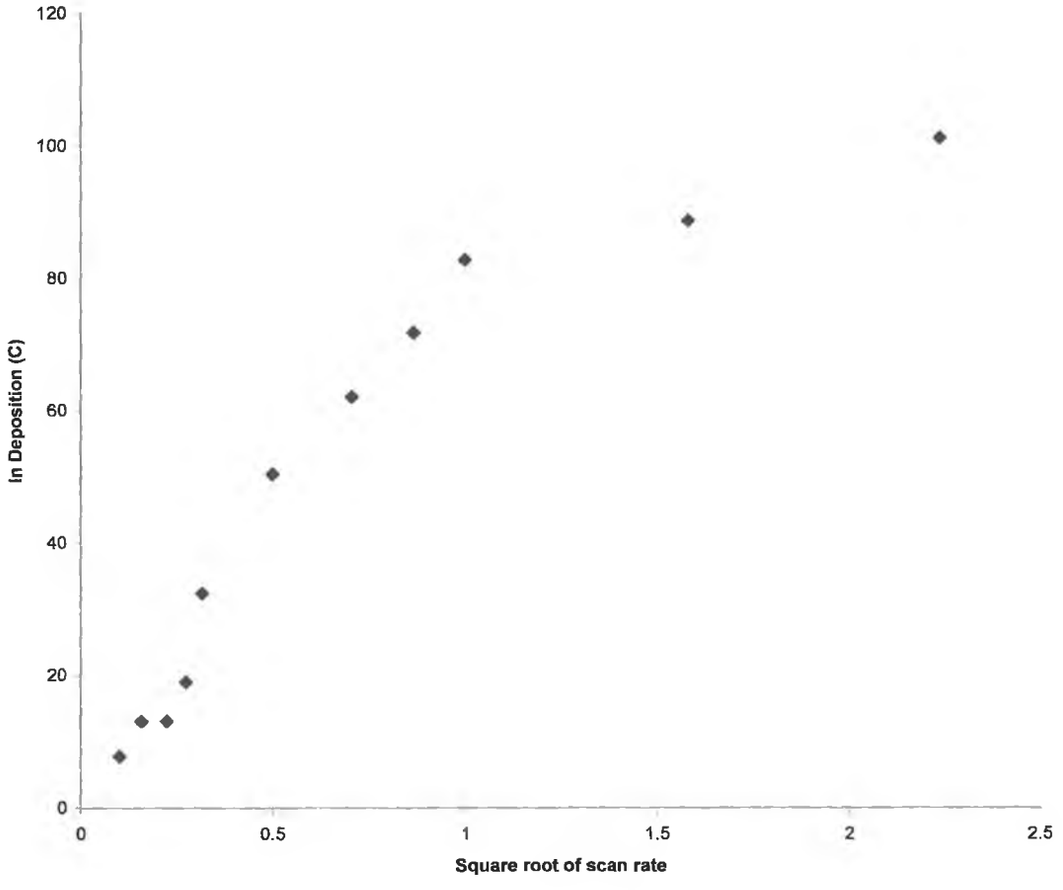

Figure 5.24 Plot of the amount of charge under indium reduction peak versus √ scan rate.

5.3g Electrochemical Stripping of the Copper Microelectrode

The term electrochemical stripping analysis is applied to a family of procedures involving a preconcentration of the analyte onto the working electrode, prior to its direct or indirect determination by means of an electrochemical technique [24]. Such a combination of an effective accumulation step with an advanced measurement procedure results in a very low detection limit and makes striping analysis one of the most important techniques in trace analysis [25].

The term 'stripping' used in naming the original technique, anodic stripping voltammetry, describes exactly the process that is occurring during the voltammetric scan. All of the electroactive species present on the electrode is changed and therefore the term stripping can be considered to be a close approximation to what in effect occurs.

The four main types of stripping voltammetry are:

(i) Cathodic stripping voltammetry (CSV) involves the electrochemical reductive determination of a determinand. This term is used in methods where the determinand is accumulated either anodically (e.g. as a mercury salt) or by direct adsorption (without reduction or oxidation) and is then determined cathodically.

(ii) Anodic stripping voltammetry (ASV) involves the electrochemical oxidative determination of a determinand by stripping voltammetry. This term is used for methods in which the determinand is accumulated either cathodically (in the case of a metal ion) or by direct adsorption (without reduction or oxidation) and is then determined anodically.

(iii) Adsorptive stripping voltammetry (AdSV) in which accumulation is affected by adsorption of (mainly) organic determinands. The term should not be applied when there is a change of oxidation state of the metal ion during the accumulation or in the cases where an organic compound is being accumulated and determined indirectly as a metal salt or complex.

(iv) Potentiometric stripping analysis (PSA) and stripping Potentiometry (SP) are general terms synonymous with stripping chronopotentiometry.

In this experiment the type of electrochemical stripping used was (ii) Anodic stripping voltammetry (ASV), where a potential step is applied such that In^{3+} is electrodeposited on the copper electrode surface and the change in current as it is electrochemically removed is measured versus time.

Information regarding the kinetics of indium stripping from the copper substrate can be garnered by subtracting a plot of current versus time for a potential step above the $E_{½}$ value from a plot of current versus time for a potential step involving indium removal. In Figure 5.25, a plot of current versus time for a potential step from -0.4V to +0.1V is taken as a background as in this potential range no indium has been electrodeposited. This 'background' is subtracted from a plot of current versus time for a potential step from –0.8V to –0.3V to give information solely on the 'stripping' of indium from the copper surface. For a first order reaction, the natural log of this set of values is plotted versus time to give a straight line graph with the slope equal to the kinetic value for electrodeposited indium 'stripping' from a copper electrode. The kinetic value calculated from this graph (Figure 5.25) is 9.11 s^{-1}. This allows us calculate the length of one lifetime for this system, if one lifetime is taken to be 1/k, giving a value of 0.11 seconds.

Figure 5.25 is linear, indicating that the electrochemical 'stripping' of indium from the copper electrode surface involves first order kinetics. For this result to be accepted the graph of log of current versus time must be linear over at least 2 lifetimes. A lifetime for this system can be determined by taking 1/k to be equal to 1 lifetime. This gives a value for 1 lifetime of 0.11 seconds, as can be seen from Figure 5.25 the graph of log of current versus time is linear for just over 4 lifetimes. Thus the kinetics for the electrochemical 'stripping' of indium from the copper electrode substrate is accepted as being first-order.

Figure 5.26 is a graph of current versus $t^{-½}$. In the electrochemical stripping of indium from the copper electrode, the indium can be removed in one of two ways. The first of these would be that indium 'strips' directly from the electrode surface and the second involves indium diffusing across the surface before eventually stripping from the electrode surface. A graph of current versus $t^{-½}$, as seen in Figure 5.26, allows us to determine the method of indium stripping. If Figure 5.26 were linear, this would

indicate that indium strips according to the second method, indicating that the stripping kinetics are dependent on the surface diffusion of the adsorbed indium atoms. However, the plot of current versus $t^{-½}$ is not linear, which indicates that the electrodeposited indium atoms 'strip' directly from the copper electrode surface and diffuse into the bulk solution.

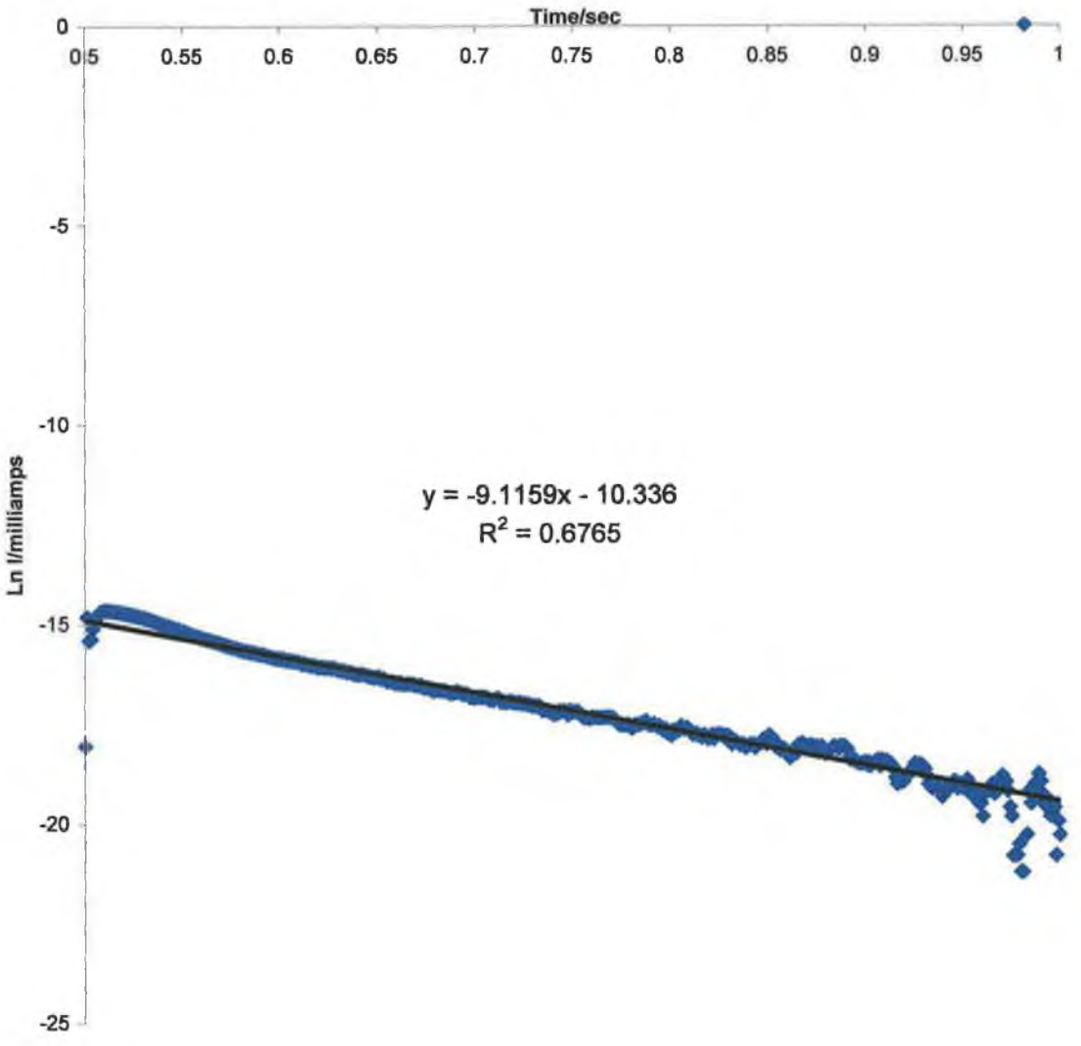

Figure 5.25 Plot of current versus time for the removal of metallic indium from a copper microelectrode substrate. The experimental setup included a 25μm radius copper microelectrode as a working electrode in a solution of 0.4mM $InCl_3$ and 0.1M boric acid.

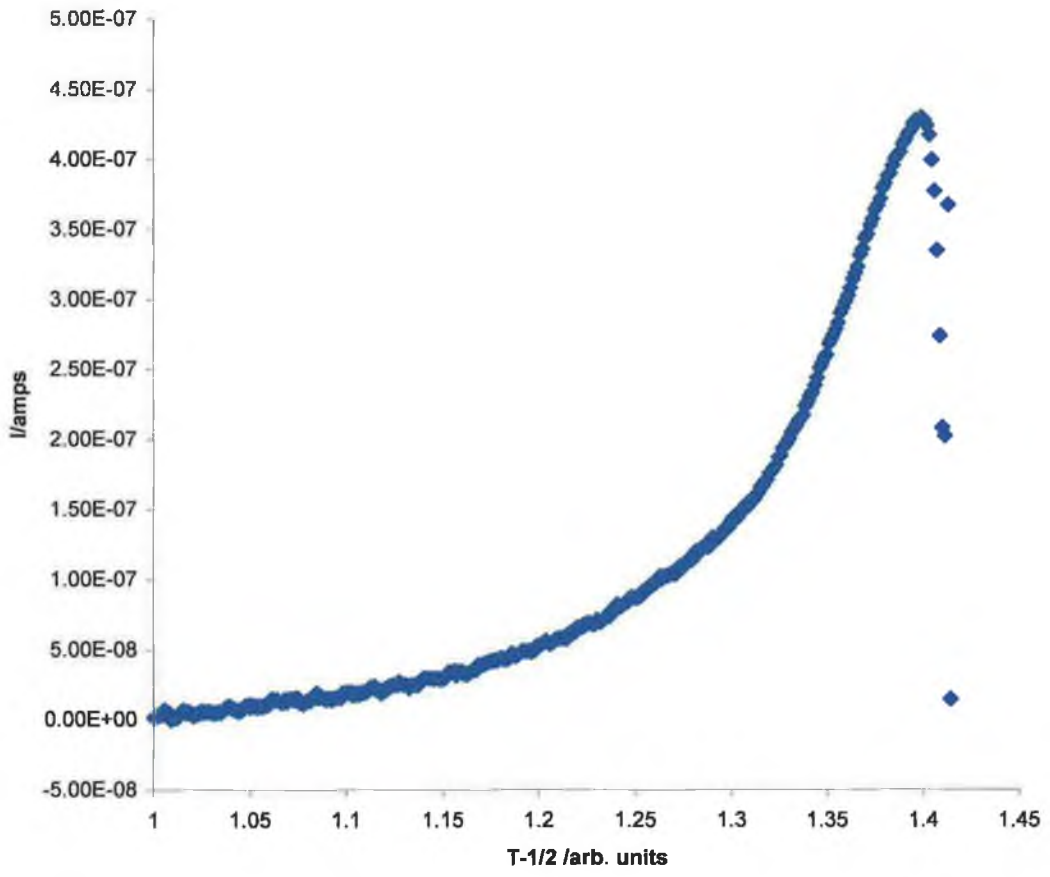

Figure 5.27 Plot of current versus $t^{-1/2}$ for the removal of metallic indium from a copper microelectrode substrate. The experimental setup included a 25μm radius copper microelectrode as a working electrode in a solution of 0.4mM $InCl_3$ and 0.1M boric acid.

5.4 Conclusion

Despite a number of studies being conducted on the co-deposition of indium and copper on numerous substrates particularly as precursors in the formation of solar cells, there has been no previously published work on the electrodeposition of indium on to copper microelectrodes. This study attempted to determine the mechanism and dynamics of the overall process.

The potential window for the electrodeposition of indium on a copper microelectrode substrate was found experimentally to be from –0.08 to –1.0V. From this cyclic voltammogram the experimental $E_{½}$ value for the reduction of In^{3+} was determined to be –0.658V, which compares well with the theoretical value of approximately –0.6V. The experimental limiting current for the reduction of In^{3+} to In can also be determined from this CV and was calculated to be $1.7x10^{-7}$A. The limiting current is an important parameter as it represents the maximum rate at which an electrode reaction can proceed. This experimentally calculated limiting current is compared to a theoretical value of $1.158x10^{-7}$A. This means that the experimentally determined limiting current is nearly 1.5 times larger than the theoretical value and indicates that the electrodeposited indium is rough, which causes the area of the modified electrode to be somewhat larger than the area of the original copper microelectrode.

Cyclic voltammograms were taken over this potential window for increasing scan rates from 0.01 to 5 Vs^{-1}. A comparison of the effect of scan rate on the amount of indium electrodeposited on the copper microelectrode substrate reveals that at lower scan rates increased amounts of indium are electrodeposited, with two oxidation peaks evident, the first thought to be from In previously deposited from the diffusion layer 'stripping' from the electrode surface and the second, larger peak, is thought to be due to indium previously adsorbed due to under potential deposition (UPD) from the bulk solution being 'stripped' from the copper substrate. As the scan rate increases, this UPD peak disappears with the current amplitude of the CV increasing. A further increase in scan rate results in the deterioration of the features of the CV, until at a scan rate of $2.5Vs^{-1}$ the resulting CV exhibiting features of a much deteriorated quality, distorted shape and an unacceptable level of current amplitude. This change

in the amount of electrodeposited indium with increased scan rate provides important information about the indium nucleation process. It means that the nucleation type is likely to be progressive rather than instantaneous. In the progressive nucleation mechanism the amount of indium growth centres on the copper substrate increases with the amount of time the potential is kept within the limits of In^{3+} reduction, while for instantaneous nucleation once the $E_{½}$ value for indium electrodeposition on copper microelectrodes is reached indium growth centres begin to nucleate but the amount of nucleation is independent of the amount of time spent within the potential limits for In^{3+} reduction.

Indium was electrodeposited on 1.25mm copper macroelectrodes. The electrode was emersed under potential control leaving the indium electrodeposited on the electrode surface. This macroelectrode was viewed using SEM, which revealed that at low coverages, indium electrodeposits preferentially at the triple interface of electrode insulator, copper surface and contacting electrolyte. Increasing the magnification reveals that the indium deposits in clusters rather than as a continuous film and these clusters were found to be of varying sizes. EDX results prove that it is indeed indium which is deposited on the copper macroelectrode. As expected the EDX results indicate that there is a much larger concentration of copper than indium on the electrode surface as only a small amount of indium was deposited in comparison to the area of the copper macroelectrode.

Chronoamperometric results were used to elucidate the nucleation type and growth mode for the deposited indium. Two potential steps were taken, one below the $E_{½}$ potential and the second incorporating the $E_{½}$ potential. These were from +0.1 to –0.4V and from –0.3 to –0.8V. A graph of current versus time was plotted for each potential step. The current versus time plot for the potential step from +0.1 to –0.4V was used as background any change in current is due to the RC time constant for the system. This background was subtracted from the plot of current versus time for the potential step from –0.3 to –0.8V to leave a current versus time plot for the metal deposition. From this plot a graph of I/I_{max} and $(I/I_{max})^2$ is constructed versus time. A set of transients was constructed to represent the 4 different nucleation types and growth modes namely 2D progressive, 2D instantaneous 3D progressive and 3D instantaneous, according to formulas taken from a paper by Harrison et al. The plot of

I/I_{max} and $(I/I_{max})^2$ versus time is overlaid on the graph of the 4 transients to elucidate the nucleation type and growth mode. On comparison it was found that indium deposits according to 3D progressive. This means that the longer the potential is held within the potential limits for In^{3+} reduction, the more indium growth centres that nucleate on the copper substrate. In this case nucleation of growth centres occur faster than the rate of growth from these centres. It also means that the indium clusters grow in both vertical and horizontal directions.

A graph of the Ln of current for metal deposition versus time gives a straight line over at least 4 lifetimes. This means that the kinetics for indium deposition are first order, with indium depositing directly onto the surface of the copper microelectrode. The rate constant for indium deposition was calculated to be 20.755 s^{-1}.

A plot of current versus time for the 'stripping' of indium was constructed giving a straight line over more than 4 lifetimes, indicating that the indium 'strips' according to first order kinetics. The rate constant for the removal of indium is 9.1 s^{-1}. A graph of current versus $time^{-½}$ was plotted, which is non-linear. This infers that indium 'strips' directly from the copper surface rather than diffusing across the surface prior to removal.

Overall, indium electrodeposits on copper electrodes according to the 3D progressive model, with In^{3+} moving towards the electrode surface via radial diffusion. Indium deposits preferentially at the triple interface of electrode insulator, copper surface and contacting electrolyte. Indium electrodeposition is a first order reaction and it is thought the rate-determining step in this process is the nucleation of indium growth centres on the copper surface. It was found that the removal of indium from the electrode surface is a first order reaction with indium 'stripping' directly from the electrode surface.

5.5 References

1. Zotti, G., Cattarin, S., Comisso, S., J. Electroanal. Chem., 239 (1998) 387.
2. Duic, Lj., Mandic, Z., Kovacicek, F., J. Polymer Sci. Part A, 32 (1994) 105.
3. Hwang, B-J., Santhanam, R., Chung-Ru, W., Yin-When, T., Electroanalysis, 13 (2001) 37.
4. Southampton Electrochemistry Group, 'Instrumental Methods in Electrochemistry', Horwood, Chichester, 2001.
5. Prosini, P.P., Addonizio, M.L., Antonaia, A., Thin Solid Films, 298 (1997) 191.
6. Prosini, P.P., Addonizio, M.L., Antonaia, A., Loreti, S., Thin Solid Films, 288 (1996) 90.
7. Calixto, E, Sebastian, P.J., Fernandez, A., J. of Crystal Growth, 169 (1996) 287.
8. Huang, C.J., Meen, T.H., Lai, M.Y., Chen, W.R., Solar Energy Materials and Solar Cells, 4 (2004) 553.
9. Nageswara Rao, N., Ramachandrach, G., Solar Cells, 16 (1986) 245.
10. Guillen, C., Martinez, M.A., Herrero, J., Vacuum, 58 (2000) 594.
11. Calixto, M.E., Sebastian, P.J., Solar Energy Materials and Solar Cells, 63 (2000) 335.
12. Nakamura, S., Sugawara, S., Hashimoto, A., Yamamoto, A., Solar Energy Materials and Solar Cells, 50 (1998) 25.
13. Kozlov, V.M., Agrigento, V., Mussati, G., Bicelli, L.P., J. of Alloys and Compounds 288 (1999) 255.
14. Harrison, A., Thirsk, H.R., 'Electroanalytical Chemistry', Academic Press, New York, 1971.
15. http://www.seallabs.com.html.
16. Stranski, I.N., Z. Physik. Chem., 136 (1928) 259.
17. Vetter, K.J., Electrochemical kinetics, Academic press, N.Y., (1967) 283.
18. Conway, B.E., Bockris, J. O'M, Electrochimica Acta, 3 (1961) 340.
19. http://www.uq.edu.au/nanoworld/sem_gen.html.
20. http://www.uksaf.org/tech/edx.html.
21. Armstrong, R.D., Fleischmann, M., Thirsk, H.R., J. Electroanal. Chem., 11 (1966) 205.

22. Hwang, B.J., Santhanam, R, Lin, Y. Electroanalysis 15 (2002) 115.

23. Burgess, J., "Metal ions in solution", Horwood, Chichester, 1978.

24. www.electrochem.cwru.edu/ed/dict.htm.

25. http://pages.pomona.edu/~wsteinmetz/chem160/ASV.doc.

Chapter 6

Conclusions

Auger electron microscopy, low energy electron diffraction and scanning tunnelling microscopy were used to study the ultra high vacuum deposition of indium on a Cu{100} sample at ambient temperature. Indium is deposited up to a surface coverage of 1ML. AES was used to quantify the concentration of indium deposited on the sample surface. AES revealed that indium deposited on the Cu{100} substrate according to the Stranski-Krastanov growth mode, with the first atomic layer of indium growing in a layer-by-layer fashion but following ML point, with subsequent growth occurring in the form of 3-D crystallites.

At indium coverages of up to 0.35ML, indium was found to form a Cu{100}-p(1x1)-In surface alloy. It is thought that indium substitutes into the outermost copper layer, dislocating copper atoms from their lattice and forcing them onto the sample surface. These ejected copper atoms are thought to congregate on the sample surface in island-like formations. This phenomenon was only visible using STM, where a topographic scan was taken of a number of these copper islands and line profiles used to verify their composition. LEED images taken at this coverage were inconclusive, although the bright sharp spots associated with a clean Cu{100} surface became dull and blurred indicating surface disorder, this could be due to the randomness of the locations of the ejected copper islands but it could also be due to mobile indium atoms on the copper surface.

LEED images revealed that at a coverage of 0.4ML of deposited indium, the indium atoms arrange themselves into a $9\sqrt{2}x2\sqrt{2}$ unit cell. This $9\sqrt{2}x2\sqrt{2}$ structure was found to undergo a temperature dependant reversible phase transition to form a c(2x2) unit cell on heating to 373K. LEED images reveal for the low temperature phase a 'box of four' spots are found at each 1/2, 1/2 position with these spots seeming to combine to form a single spot equal in intensity to the sum of the intensities of each of the spots in the 'box of four' conformation on heating to 373K. This is thought to be due to the copper atoms in the lattice relaxing allowing the indium atoms move more freely across the surface to occupy surface positions of higher energy. Unfortunately at this concentration it was found impossible to determine whether the structures formed were overlayers or surface alloys due to the techniques used.

At a surface coverage of approximately 0.6ML, LEED and STM images reveal that indium atoms form a c(4x4) unit cell on the Cu{100} substrate. LEED I(V)'s were taken for each of the integral beams and the more important fractional order spots. From these LEED I(V)'s, a Tensor LEED study was conducted for the c(4x4) structure. Results from the Tensor LEED study revealed that indium forms an overlayer structure consisting of a c(2x2) structure for the In layer closest to bulk, with indium atoms occupying four fold hollow sites with respect to substrate. On top of this layer is a c(4x4) indium layer in which the indium atoms lie at four fold hollow site with respect to the c(2x2) layer.

From a coverage of 0.65ML to ML point indium forms a 'complex' phase on the copper substrate. LEED results reveal a very complex unit cell, possibly a superstructure, which we were unable to conclusively determine. STM results also proved difficult as it is thought at this coverage indium is quite mobile on the copper surface resulting in indium atoms adhering to the STM tip, resulting in a topographic image of very poor resolution.

LEED and STM were used to determine any surface structures formed by antimony on a Cu{100} substrate up to a coverage of 0.45ML deposited antimony. Above this concentration, Aufray et al found antimony formed a $p(\sqrt{3}x\sqrt{3})R30^{\circ}$ surface alloy, however the substrate used in their studies was a Cu{111} surface.

At a concentration of 0.25ML, Sb forms a p(2x2) surface alloy with the Cu{100} substrate. The p(2x2) LEED pattern is characterised by the presence of fractional order spots in the (1/2,0), (1/2,1/2), (1,1/2) and (3/2,0). LEED I(V)s were measured for all integral beams and the most important fractional order spots. The total energy range for this analysis was 1540eV of which 400eV was from fractional order spots. These results were used to conduct a Tensor LEED study of the p(2x2) structure. The analysis produced four different models, 3 overlayer structures and a surface alloy. The best fit structure has a relatively corrugated CuSb surface alloy with Sb atoms being at 0.56Å above the centre of mass of surface Cu atoms. Despite the alloying of Sb with the outermost Cu atoms, it was found that the addition of Sb atoms to the Cu{100} substrate did not produce a significant perturbation of the deeper Cu layers.

The maximum determined buckling was less than 3% relative to the Cu bulk interlayer spacing.

STM images seemed to disagree with this postulation as troughs were only present in the vertical direction intimating that the structure formed may be 2 domains of p(2x1). The figures for the vectors of the lattice fitted represent the sum of the atomic diameters of one Sb and one Cu atom (3.18Å(Sb) and 2.556Å(Cu)) giving a value of 5.7736Å. Both profiles indicate that the surface alloy is a well ordered uniform structure with little or no disorder between unit cells.

At a concentration of 0.32ML Sb on the Cu{100} surface, Sb forms a p(6x6) structure. The p(6x6) LEED pattern is characterised by 5 spots between the (0,0) spot and each of the integral beams, namely the four (1,0) and (1,1) beams, giving a 'grid' of 36 spots in each direction. Due to the complexity and number of spots contained in the LEED pattern, a reasonable set of I(V)s proved too difficult to acquire, making a Tensor LEED study impossible. This made it incredibly difficult to determine whether the Cu{100}-p(6x6)-Sb system is an overlayer or surface alloy.

An STM study of this system confirmed the unit cell as p(6x6), with lattice vectors of 1.53nm and 1.56nm. The height of the step edges was measured to be 0.178+/-0.015nm, which is in good agreement with a value of 0.180nm, which is the expected value for bulk copper and is consistent with a slight relaxation of the topmost layer. Atomic resolution STM images of the Cu{100}-p(6x6)-Sb surface display both double and single rows of atoms which implies that the deposited Sb causes a reconstruction in the selvedge.

It is though that the Cu{100}-p(6x6)-Sb system is a surface alloy as at both lower and higher coverages of deposited Sb, p(2x2) and p($\sqrt{3}$x$\sqrt{3}$)R30° surface alloys are formed respectively.

Copper microelectrodes were fabricated using a vacuum sealing technique to reduce the possibility of oxide formation. 25μm radius copper wire was soldered to a wire assembly consisting of a 'hook up' wire and a tin coated copper wire, which was heat sealed in a soft glass casing using an applied vacuum. Once fabrication was

completed, the copper microelectrodes were characterised in a solution of background electrolyte.

The real surface area of a 25μm radius copper microelectrode is 1.85×10^{-4} with a surface roughness value of 2.3, indicating that the surface of the electrode is relatively smooth.

The potential window for copper microelectrodes in a 0.1M solution of $HClO_4$ was tested. It was discovered that at potentials more positive than –0.08V a large peak is formed due to the formation of Cu_2O at the electrode surface. In the negative direction, the potential window is curtailed by the formation of a large peak below –0.6V, thought to be due to the bulk evolution of hydrogen from the acidic electrolyte, 0.1M $HClO_4$.

The problems of oxide formation on the electrode and bulk evolution of hydrogen from the electrolyte were greatly reduced by an increase in pH of the background electrolyte. At a pH of 4.45 the interference from both reactions is at a minimum giving a potential window of +0.1 to –1.0V. Increasing the pH above 4.45 causes a large increase in capacitance, so it becomes a trade-off between keeping the pH low enough to achieve a good cyclic voltammogram and high enough to avoid the limitations caused by the oxide formation and hydrogen evolution reactions. This is best achieved at a pH of approx. 4.5.

Chronoamperometric measurements were taken for increasing concentrations of $HClO_4$ at potentials from –100mV to –600mV. The RC time constant for Cu microelectrodes in $HClO_4$ was found to be 7.0±0.2μs for 0.1 M $HClO_4$, which compares favourably with values of 11.3±0.3μs and 2.8±0.2μs for Au and Pt microelectrodes under similar experimental conditions.

The performance of copper macro- and microelectrodes for the electrodeposition of indium was investigated. Indium was electrodeposited on the surface of the Cu microelectrodes and characterised using SEM and EDX to elucidate the distribution of indium on the surface. These results reveal that for low indium coverages, deposition occurs preferentially at the triple interface between the electrode insulator,

copper surface and the contacting electrolyte. The contributions from nucleation and growth deposition as well as mass transport to this behaviour were also considered. Cyclic voltammetry revealed that the surface coverage of indium can be varied from sub-monolayer to thick films by controlling the experimental timescale.

Chronoamperometry conducted on the μs to seconds timescale was used to elucidate the growth mechanism of the indium films and suggests that the nucleation and growth mode for electrodeposition of indium on copper is 3D progressive. This compares favourably with the results from Chapter 2, which found the nucleation and growth mode of Indium on Cu{100} under vacuum to obey the Stranski-Krastanov growth model, with the deposited indium firstly grows in a layer by layer fashion until monolayer point is reached and subsequently grows in clusters on the monolayer surface.

Indium was found to deposit and strip according to first order rate constants. This indicates that for indium electrodeposition, indium diffuses towards the electrode surface, accepts electrons from the copper electrode substrate and deposit on the copper surface. Removal of indium is thought to occur by direct stripping of the deposited atoms from the copper surface.

A more accurate comparison of the relevant deposition techniques would be to conduct vapour deposition studies on a polycrystalline sample rather than the single crystal used. Alternatively a electrodeposition could be conducted on a Cu{100} single crystal, this would remove any ambiguity regarding the differences in substrates.

An interesting follow on study from the electrodeposition of indium on copper microelectrodes would be to co-deposit selenium along with indium on the copper electrode substrate. $CuInSe_2$ is a well known photoactive compound which is used extensively in the production of solar cells and although many different methods previously exist for this process, this particular method of $CuInSe_2$ formation has not been previously tested.

Appendices

		$1s_{\frac{1}{2}}$ K	$2s_{\frac{1}{2}}$ L_I	$2p_{\frac{1}{2}}$ L_{II}	$2p_{\frac{3}{2}}$ L_{III}	$3s_{\frac{1}{2}}$ M_I	$3p_{\frac{1}{2}}$ M_{II}	$3p_{\frac{3}{2}}$ M_{III}	$3d_{\frac{3}{2}}$ M_{IV}	$3d_{\frac{5}{2}}$ M_V	$4s_{\frac{1}{2}}$ N_I	$4p_{\frac{1}{2}}$ N_{II}	$4p_{\frac{3}{2}}$ N_{III}
1	H	14											
2	He	25											
3	Li	55											
4	Be	111	*										
5	B	188	*		5*								
6	C	284	*		7*								
7	N	399	*		9*								
8	O	532	24		7*								
9	F	686	31		8*								
10	Ne	867	45		18*								
11	Na	1072	63		31*		1						
12	Mg	1305	89		52*		2						
13	Al	1560	118	74		73	1						
14	Si	1839	149	100		99	8	3					
15	P	2149	189	136		135	16	10					
16	S	2472	229	165		164	16	8					
17	Cl	2823	270	202		200	18	7					
18	Ar	3203	320	247		245	25	12					
19	K	3608	377	297		294	34	18*					
20	Ca	4038	438	350		347	44	26*		5*			
21	Sc	4493	500	407		402	54	32*		7*			
22	Ti	4965	564	461		455	59	34*		5*			
23	V	5465	628	520		513	66	38*		2*			
24	Cr	5989	695	584		575	74	43*		2*			
25	Mn	6539	769	652		641	84	49*		4*			
26	Fe	7114	846	723		710	95	58*		6*			
27	Co	7769	926	794		779	101	60*		3*			
28	Ni	8333	1008	872		855	112	68*		4*			
29	Cu	8978	1096	951		931	120	74*		2*			
30	Zn	9659	1194	1044		1021	137	87*		9*			
31	Ga	10 367	1298	1143		1116	158	107	105	16*			1
32	Ge	11 104	1413	1249		1217	181	129	122	29*			3
33	As	11 867	1527	1359		1323	204	147	141	41*			3
34	Se	12 658	1654	1476		1436	232	168	162	57*			6
35	Br	13 474	1782	1596		1550	257	189	182	70	69	27	5
36	Kr	14 326	1921	1727		1675	289	223	214	89*	24		11
37	Rb	15 200	2065	1864		1805	322	248	239	112	111	30	15 14
38	Sr	16 105	2216	2007		1940	358	280	269	135	133	38	20

Binding energies of elements of atomic number 1-38 in electron volts.

Cu-In

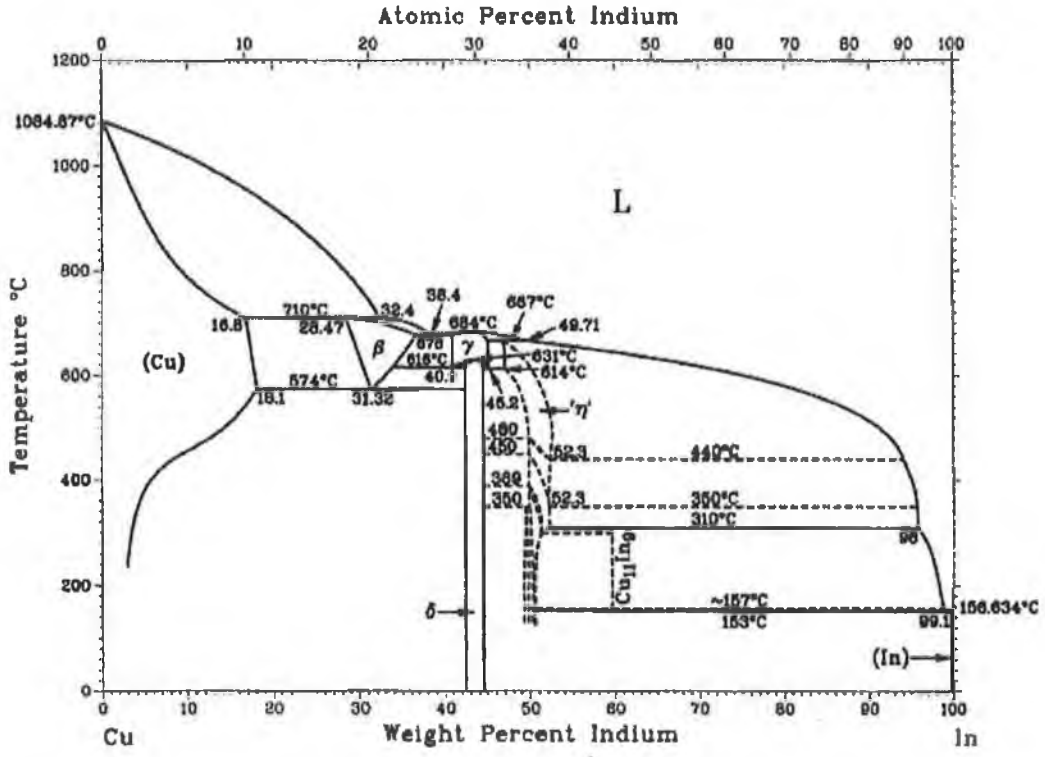

Phase Diagram for Cu-In system.

Phase	Composition, wt% In	Pearson symbol	Space group
(Cu)	0 to 18.1	*cF*4	$Fm\bar{3}m$
β	28.47 to 37.0	*cI*2	$Im\bar{3}m$
γ	40.9 to 45.2	*cP*52	$P\bar{4}3m$
δ	42.52 to 44.3	*aP*40	$P\bar{1}$
"η"	47.00 to 52.3	*hP*4	$P6_3/mmc$
		*hP*6	$P6_3/mmc$
	49.5 to 52.3	*o***	...
$Cu_{11}In_9$	~59	*mC*20	*C*2/*m*
(In)	~100	*tI*2	*I*4/*mmm*

Table summarising each phase and subsequent parameters involved in Cu-In phase diagram.

Cu-Sb

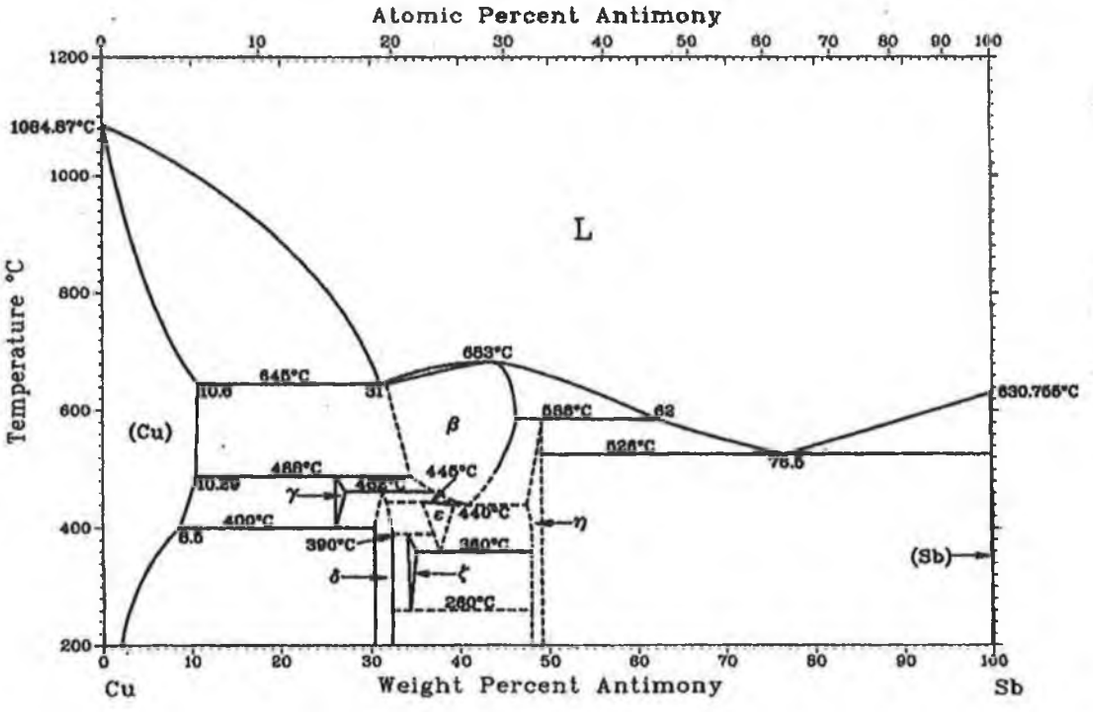

Phase Diagram for Cu-Sb system

P.R. Subramanian, 1990

Phase	Composition, wt% Sb	Pearson symbol	Space group
(Cu)	0 to 10.6	*cF*4	$Fm\bar{3}m$
β	31.6 to 46.0	*oF*16	$Fm\bar{3}m$
γ	~26.0 to 26.7	*hP*2	$P6_3/mmc$
δ	30.3 to 32	*hP*?	$P6_3/mmc$
ε	~36.1 to 39.4	*oP*8	*Pmmn*
ζ	~34.1 to 34.5	*hP*26	$P\bar{3}$
η	~47.4 to 48.9	*tP*6	*P*4/*nmm*
(Sb)	~100	*hR*2	$R\bar{3}m$

Table summarising each phase and subsequent parameters involved in Cu-Sb phase diagram.